X-ray diffraction and X-ray absorption of strained CoO and MnO thin films

Cover: Virtual lizard lost in reciprocal space around the (226) reflection of a relaxing thin film in the low density approximation.

RuG

MSC PhD thesis series 2005-11
ISSN 1570-1530

The work described in this thesis was performed in the group 'Chemistry of Thin Films' (part of the Materials Science Centre) of the University of Groningen, the Netherlands.

Printed by: Febodruk B.V., Enschede, The Netherlands
ISBN: 90-367-2375-2

Rijksuniversiteit Groningen

X-ray diffraction and X-ray absorption of strained CoO and MnO thin films

Proefschrift

ter verkrijging van het doctoraat in de
Wiskunde en Natuurwetenschappen
aan de Rijksuniversiteit Groningen
op gezag van de
Rector Magnificus, dr. F. Zwarts
in het openbaar te verdedigen op
vrijdag 14 oktober 2005
om 14.45 uur

door

Szilard Istvan Csiszar

geboren op 11 september 1976
te Sighetu Marmatiei
Roemenië

Promotores:	Prof. Dr. T. Hibma
	Prof. Dr. L. H. Tjeng
Beoordelingscommissie:	Prof. Dr. T. Palstra
	Prof. Dr. P. Rudolf
	Prof. Dr. J. Goedkoop

Science is the belief in the ignorance of experts.

(R. Feynman)

Contents

Chapter 1

General introduction

1.1 Introduction

The driving force originating from the fast developments of technology motivate today's scientists to search for new compounds or novel structures, built from new or already well known materials, in order to increase the size of the effects and the temperature range at which they appear. These aspirations can become fruitful with less effort if first an understanding of the basic phenomena is reached.

The large variety of physical properties of transition metal oxides, that can be manipulated with only small variation of some parameters such as composition, strain or temperature, attracted a great amount of scientific interest in this field [1]. Another reason for such studies is the link between the high temperature superconductors and simple transition metal compounds. For example, a doubling of the superconducting transition temperature was obtained, as a result of epitaxial strain induced by the underlying substrate [2]. Other interesting phenomena involving substrate effects were obtained in the case of $BiFeO_3$ multiferroic thin film heterostructures, for which an enhancement of almost an order of magnitude in the spontaneous polarization as well as enhanced thickness-dependent magnetism with respect to the bulk was reported [3]. However, there is no consensus reached yet about the origin of the magnetic behavior [4, 5]. A final noteworthy example is the strain induced insulator-metal transition observed in the case of epitaxial VO films [6].

Our goal, in this thesis, is to study the effects of strain on the magnetic structure of transition metal oxides, with and without, single ion anisotropy. Consequently, the present thesis will be dealing with mainly two first row transition metal monoxides: CoO and MnO.

Transition metal oxides constitute a special class of materials. As early as 1928, Bloch [7] was the first to attempt to understand the basic chemical and physical properties of solids in a general way by approximating the total wave-function describing the crystal, with a linear combination of atomic orbitals of the constituents. This single electron band theory was successful in many respects but failed to describe transition-metal oxides (see also ref. [8]). In the following years, up to the present, many other approaches appeared providing increasingly accurate results as compared with experiments. These theories can now disentangle the properties of many solids in a quite exact manner. However it is still impossible to describe the electronic structure of transition-metal oxides only by simple band theory. Even the most sophisticated theories such as Density Functional Theory (DFT) [11, 12] or the G-W approximation [13] are only partially successful. For transition-metal monoxides mainly the appearance of a large insulating gap cannot be explained with such theories. What is causing this high degree of discrepancy, i.e. why can some solids be described by simple theories and why are others such as the transition-metal (TM) oxides so unique? The answer was sought for a long time, and the work of Wilson, Peierls, Mott and Hubbard brought the problem closer to a solution. The answer can be found in the breakdown of the independent-electron approximation, in other words the strong Coulomb correlation effects at the TM cation site, in conjunction with the extended valence orbitals of the anions on the other hand, are responsible for the insulating nature, magnetism and many other physical properties of the TM oxides. The 3d electrons in the incomplete shell on the TM remain localized on the ions due to strong electron-electron interactions. For CoO for example, a comparison of the dispersion curves of the O 2p states, from the Angle-Resolved Photoemission Spectra (ARPES) with the results from the LDA band structure calculations, gives good agreement [9, 10]. This proves the spatially extended nature of the oxygen states. However, for the Co 3d states strong correlation effects have been observed and narrowing of the Co 3d bands was measured. Therefore the localized states of the TM 3d shells must be dealt with in a totally different manner than the extended O 2p states. This discrepancy leaves little room for a *general theory*, which makes these compounds so fascinating and intriguing at the same time.

A general classification of the different kinds of effects that appear for the wide range of TM compounds is given by the Zaanen-Sawatzky-Allen (ZSA) scheme [14]. According to this scheme the insulating compounds can be classified in two regions depending on the relative size of the on-site Coulomb

interaction U and the charge transfer energy Δ. These are defined by:

$$\begin{aligned} U &= E(d^{n+1}) + E(d^{n-1}) - 2E(d^n), \\ \Delta &= E(d^{n+1}\underline{L}) - E(d^n) \end{aligned} \tag{1.1}$$

where n is the occupation of the d shell and $E(d^{n+1}) - E(d^n)$, $E(d^n) - E(d^{n-1})$ and $E(d^n)$ are the electron affinity, the ionization energy and the ground state energy, respectively and $\underline{L}$ denotes a hole in the ligand band. If the hybridization between the ligand anions and the TM cation is small in comparison with the Coulomb interaction U, that is, if the electrons cannot move freely in the solid, the TM compound is either a charge transfer ($U > \Delta$) or a Mott-Hubbard ($U < \Delta$) insulator. CoO and MnO are situated at the border of these two classes and they seem to be a mixture of Mott-Hubbard and charge transfer insulators. Currently the accepted approach to explain the magnetic properties due to the 3d electrons for these TM compound materials, are local models such as crystal-field, ligand field or related cluster calculations. These treatments give very realistic results and they will be used in the last two chapters of the thesis for explaining temperature and polarization dependent soft X-ray absorption spectra at the TM $L_{2,3}$ edges.

There is not only scientific but also technological interest in these materials since they offer a wide range of physical properties. One of the reasons for this lies in their magnetic behavior due to the Hund's rule stabilization of local magnetic moments. In CoO and MnO these localized moments below the so-called Néel temperature will have an antiferromagnetic coupling with each other, mediated via the closed outer shell O^{2-} anions due to the superexchange interaction [15]. This causes every TM ion to be surrounded by six next-nearest neighbor TM ions with antiparallel moments. The magnetic structure of such a monoxide is shown in Figure 1.1. Above the Néel temperature the effects of thermal agitation dominate and the materials turn into paramagnets. For the magnetically ordered phase semi-empirical rules describing superexchange have been developed [16, 17], which are the so-called Goudenough-Kanamori rules. However these rules do not specify the orientation of the spins with respect to the crystallographic axes. The orientation of the magnetic moments in these antiferromagnets in a bulk structure depends on the single ion anisotropy (present in CoO but absent in MnO) as well as on the magnetic dipole-dipole interactions.

The precise magnetic and crystallographic structure of the transition metal oxides was the subject of dispute for many years [18–27]. Latest results from neutron and X-ray scattering measurements show that while CoO undergoes a tetragonal distortion with $c/a<1$, having the magnetic moments along one of

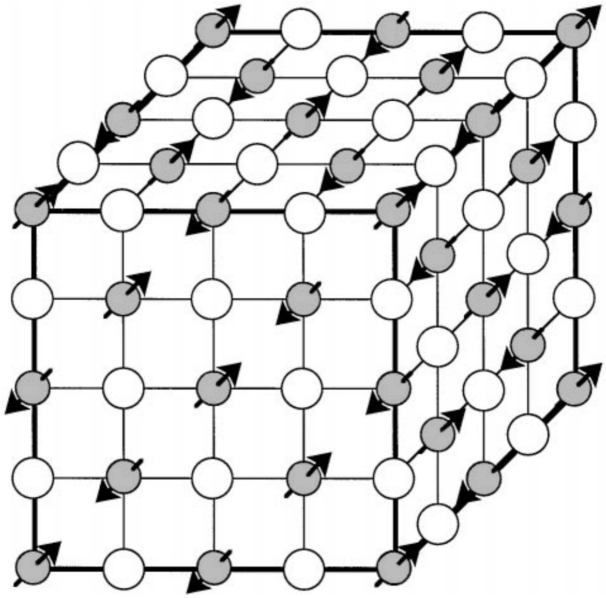

Figure 1.1: Magnetic structure of bulk MnO, CoO and NiO antiferromagnets. Figure taken from ref. [33].

the [117] crystallographic axes, the magnetic transition in MnO is accompanied by a small rhombohedral distortion with $\alpha > 60°$, having the spin moments along one of the [113] directions. In both cases the distortions are very small. For CoO these are mainly the result of magnetostriction, which is associated with an unquenched orbital momentum. This angular momentum which is finite because of the particular 3d orbital occupation of the Co^{2+} ion, aligns the spin momentum through the spin-orbit interaction [28]. Consequently, the single ion anisotropy is very strong in CoO (see also ref. [29]). In the case of MnO, on the other hand, the deformation is caused by the so-called "exchange-striction", which arises from the dependence of the exchange energies on the interionic distances. Here dipole-dipole interaction dominates and determines the spin direction, the ground state being an orbital singlet.

Antiferromagnets have no net magnetization. The two magnetic sublattices, individually having the same direction of the magnetic moments, cancel each other. It is quite difficult to determine the orientation of the magnetic axis by neutron diffraction experiments, apart from the fact that large sized single crystal samples are required. Nevertheless, it is very important to know this orientation in connection with the exchange bias phenomenon which was discovered in 1956 by Mijklejohn and Bean [30–32] (see also for a review [33, 34]).

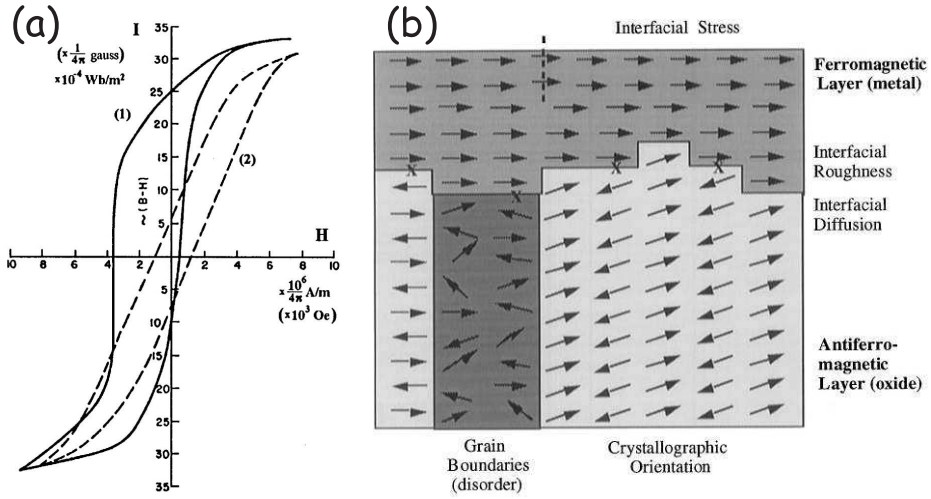

Figure 1.2: (a) Hysteresis loop at T=77 K of partially oxidized Co particles (1) cooled in a magnetic field through the paramagnetic to antiferromagnetic transition temperature of CoO and (2) cooled in zero magnetic field. Figure taken from ref. [30]. (b) Possible scenarios at the antiferro-ferromagnetic interface. Figure taken from ref. [33].

They were the first ones to observe a shift in the field cooled hysteresis loop of partially oxidized Co nanoparticles. The result of their experiments is shown in Figure 1.2 (a). It is seen that when nanoparticles are cooled down though the Néel temperature of CoO with no magnetic field present when crossing this temperature, they behave as normal ferromagnets with a symmetrical hysteresis in the magnetization (I) versus the external magnetic field (H). On the other hand, the hysteresis curve from the sample cooled down in a nonzero magnetic field is displaced along the H axis.

A boom of experimental and theoretical research followed these simple experiments because it was realized that this effect could be used in applications in the information storage area. However, after almost 50 years, there is still no transparent and decisive quantitative description for the exchange bias phenomenon. It is realized nowadays that the exchange-bias phenomenon strongly depends on the interface characteristics of the two materials (see Figure 1.1 (b)), as well as on properties such as the single ion anisotropy and the Néel temperature of the antiferromagnetic layer. It is also accepted that the magnetic structure of the anti-ferromagnet plays a relevant, if not governing, role in the microscopic mechanisms responsible for the effect. Even so,

in most of the experimental and theoretical studies on exchange-bias the bulk antiferromagnetic structure presented earlier, is considered as a starting point. Strangely enough, the effects of misfit strain, which are in fact unavoidable in almost all cases, have been fully neglected up till now. The main purpose of this thesis is to study the effects of epitaxial strain on the spin orientation, single ion anisotropy and magnetic ordering temperature of antiferromagnets with well controlled strain.

While many studies engage in the difficult task of unravelling the fundamental details defining the exchange-bias effect, by using structures that already exhibit the exchange-bias phenomenon, namely antiferromagnetic-ferromagnetic layers [35–38], our approach was slightly different. We concentrated our attention on the effects of strain without any magnetic coupling with a ferromagnetic substrate material. This way one can clearly determine whether the changes in the magnetic structure of the transition-metal oxide layer are the result of strain only, without being confused by the presence of a coupling with another magnetic material.

To mimic the possible strains that might appear in these antiferromagnetic layers one simply has to grow these films on a suitable non-ferromagnetic substrate. Depending on the lattice parameters of such a substrate, different expitaxial strains can be produced in the films. One impediment in these kinds of structures is the so-called relaxation process. At the initial stages of growth the deposited film will adopt a structure that matches the in-plane lattice parameters of the substrate. This happens until the so-called critical thickness, where the elastic energy incorporated in the film due to this deformation will be too high and the appearance of dislocations in the lattice becomes energetically more favorable than the completely strained state. The relaxation process is a well studied phenomenon, in particular in the case of semiconductors [39, 40] where the research was motivated by the possibility of engineering band structure and thus altering the electrical properties of these materials. However, semiconductors relax in a slightly different manner than ionic crystals because the type of dislocations by which they release the strain is different for the two. The determination of the exact thickness at which the film relaxes its epitaxial strain depends not only on the misfit between the lattice parameters but also on the elastic properties of the layer. The critical thickness can be estimated using the well known Matthews-Blakeslee [41] formula if equilibrium conditions are assumed. However, in reality critical thicknesses are found to be much larger, because the relaxation process is delayed due to kinetic barriers. Currently there is no definite formula that can predict the critical thickness for an arbitrary system. It is therefore necessary

to conduct a detailed experimental survey for a certain substrate-overlayer combination to gain an insight in the relaxation process. The technique by which one can extensively examine the relaxation in films is X-ray diffraction. The commonly used procedure is to follow the position of the specular and off-specular diffraction spots for films having different thicknesses, in order to detect the deviation from coherent growth as soon as the relaxation process starts. As we will show, diffuse X-ray scattering contains very valuable information about the nature of the relaxation process. The appearance of misfit dislocations will produce considerable intensity at places in the reciprocal space where a perfect crystalline film would not scatter. The investigation of the shape and intensity of such diffuse scattering gives insight into the type of dislocation through which the relaxation takes place and the dislocation density in the film. There are in fact, a number of theories which debate the mechanisms by which the diffuse X-ray scattering appears and which predict the distribution in reciprocal space as a function of dislocation type and density. In addition to the previously mentioned strain effects on the magnetic structure of CoO layers, this thesis also contains a detailed analysis of the diffuse scattering observed around the coherent scattering from CoO and MnO epitaxial layers at different stages of relaxation [42].

1.2 Scope of this thesis

This thesis is devoted to unravel the magnetic properties of epitaxially strained CoO layers as well as the effects of such layers on other antiferromagnets having no single ion anisotropy (MnO). To achieve this, high quality samples were grown, the strains were measured and the spin orientation determined.

The samples were characterized by X-ray and electron diffraction as well as soft X-ray absorption spectroscopy. These (indispensable) measurements discovered new, unexpected phenomena such as the observation of diffuse scattering originating from the dislocations caused by the strain relaxation process as well as the magnetic interlayer coupling between the CoO and the MnO layers. The thesis is roughly divided in two parts. The first part contains the growth and structural characterization of the films and buffer layers and the second part is dealing with the change in the magnetic structure as a consequence of epitaxial strain. These findings will be presented in the following way:

In *Chapter 2* the growth details, using the Molecular Beam Epitaxy (MBE) technique, of CoO and MnO thin films on different substrates is discussed. Epitaxial CoO thin films were grown on different substrates imposing com-

pressive strain by the underlying substrate (MgO, $MgAl_2O_4$, $SrTiO_3$ and Ag) and tensile strain using underlying MnO buffer layers. The growth was monitored using *in-situ* electron diffraction techniques such as Reflection High Energy Electron Diffraction (RHEED) and Low Energy Electron Diffraction (LEED). In this chapter the principles and limitations of these techniques are also explained.

In *Chapter 3* the structural characterization of the films is presented. Here, special interest is devoted to the strain relaxation as a function of the thickness of the films. The aim was to determine the maximum thickness at which CoO films are in the coherently strained state on MgO substrates and MnO buffer layers. Different alternative methods for creating the strain state of the films are outlined as well as the experimental observation and modelling of diffuse scattering due to dislocations.

In *Chapter 4* the theory of X-ray absorption is presented. As this technique has been the subject of many publications, we focus only on the most significant results obtained throughout the years that are necessary to understand our results in the following last two chapters.

In *Chapter 5* a temperature dependent X-ray magnetic linear dichroism study of two differently strained CoO layers is discussed. Here, we focus on the changes in the spin orientation of these antiferromagnetic oxides as a function of the sign of the epitaxial strain.

Finally, in *Chapter 6* we report on the effects of strained CoO layers on the magnetic structure of adjacent MnO layers. It turns out that such MnO layers couple magnetically with the underlying CoO layers and this coupling results in a stabilization of those magnetic domains in the MnO films that are parallel to the magnetic domains of the underlying CoO films. It is therefore inferred that the control over the spin orientation in the CoO layers can be extended into an adjacent antiferromagnet.

References

[1] W.E. Picket, Rev. Mod. Phys., **61**, 443 (1989)

[2] J.-P. Locquet, J. Perret, J. Fompeyrine, E. Mächler,J. W. Seo and G. Van Tendeloo, Nature **394**, 453 (1998)

[3] J. Wang, J. B. Neaton, H. Zheng, V. Nagarajan, S. B. Ogale, B. Liu, D. Viehland, V. Vaithyanathan, D. G. Schlom, U. V. Waghmare, N. A. Spaldin, K. M. Rabe, M. Wuttig, R. Ramesh, Science, **299**, 1719 (2003)

[4] W. Eerenstein, F. D. Morrison, J. Dho, M. G. Blamire, J. F. Scott, and N. D. Mathur, Science **307**, 1203a (2005)

[5] J. Wang, A. Scholl, H. Zheng, S. B. Ogale, D. Viehland, D. G. Schlom, N. A. Spaldin, K. M. Rabe, M. Wuttig, L. Mohaddes, J. Neaton, U. Waghmare, T. Zhao, and R. Ramesh, Science **307**, 1203b (2005)

[6] A.D. Rata, *Strain-induced properties of epitaxial VO_x thin films*, Ph.D. thesis, University of Groningen, The Netherlands, (2004)

[7] F. Bloch, Z. Physik, **52**, 555 (1928)

[8] J.C. Slater, G.F. Koster, Phys. Rev. **94**, 1498 (1954)

[9] Z.X. Shen, J. W. Allen, P. A. P. Lindberg, D. S. Dessau, B. O. Wells, A. Borg, W. Ellis, J. S. Kang, S.J. Oh, I. Lindau and W. E. Spicer, Phys. Rev. B, **42**, 1817 (1990)

[10] Z.X. Shen, C.K. Shih, O. Jepsen, W.E. Spicer, I. Lindau, J.W. Allen, Phys. Rev. Lett. **20**, 2442 (1990)

[11] P. Hohenberg, W. Kohn, Phys. Rev. **136**, B864 (1964)

[12] W. Kohna, L.J. Sham, Phys. Rev. **140**, A1133 (1964)

[13] L. Hedin, Phys. Rev. **139**, A796 (1965)

[14] J. Zaanen, G.A. Sawatzky, J.W. Allen, Phys. Rev. Lett. **55**, 418 (1985)

[15] P.W. Anderson, Phys. Rev. **115**, 2, (1959); Solid State Physics, **14**, 99 (1963)

[16] J.B. Goodenough, *Magnetism and Chemical Bond*, Wiley and Sons, New-York, (1963)

[17] J. Kanamori, J. Phys. Chem. Solids **10**, 87 (1959)

[18] N.C. Tombs, H.P. Rooksby, Nature (London) **165**, 442 (1950)

[19] C.G. Shull, W.A. Strauser, and E.O. Wollan, Phys. Rev. **83**, 333 (1951)

[20] S. Greenwald, Acta Crystallogr. **6**, 396 (1953)

[21] J. Kanamori, Prog. Theoret. Phys. (Japan) **17**, 177 (1957); **17**, 223 (1957)

[22] W.L. Roth, Phys. Rev. **110**, 1333 (1958); Phys. Rev. **111**, 772 (1958)

[23] B. Van Laar, Phys. Rev. **138**, A584 (1956)

[24] S. Saito, K. Nagahigashi, Y. Shimomura, J. Phys. Soc. Jpn. **21**, 850 (1966)

[25] K.H. Germann, K. Maier, E. Srauss, Phys. Status Solidi B **61**, 449 (1974)

[26] D. Herrmann-Ronzaud, P. Barlet, and J. Rossat-Mignod, J. Phys. C **11**, 2123 (1978)

[27] W. Jauch, M. Reehuis, H.J. Bleif, F. Kubanek, P. Pattinson, Phys. Rev. B, **64**, 052102 (2001)

[28] D. Alders, R. Coehoorn, and W.J.M. de Jonge Phys. Rev. B **63**, 054407 (2001)

[29] J.B. Goodenough, Phys. Rev. **171**, 466 (1968)

[30] W.H. Mijklejohn, C.P. Bean, Phys. Rev. **102**, 1413 (1956)

[31] W.H. Mijklejohn, C.P. Bean, Phys. Rev. **105**, 904 (1957)

[32] W.H. Mijklejohn, J. Appl. Phys. Suppl. **33**, 1328 (1962)

[33] A.E. Berkowitz and K. Takano, J. Magn. Magn. Mater. **200**, 552-570 (1999)

[34] J. Nogués, I.K. Schuller, J. Magn. Magn. Mater. **192**, 203-232 (1999)

[35] H. Ohldag, A. Scholl, F. Nolting, S. Anders, F. U. Hillebrecht, and J. Stöhr, Phys. Rev. Lett. **86**, 2878 (2001)

[36] H. Ohldag, T.J. Regan, J. Stöhr, A. Scholl, F. Nolting, J. Lüning, C. Stamm, S. Anders, and R. L. White, Phys. Rev. Lett. **87**, 247201 (2001)

[37] H. Ohldag, A. Scholl, F. Nolting, E. Arenholz, S. Maat, A.T. Young, M. Carey, and J. Stöhr, Phys. Rev. Lett. **91**, 017203 (2003)

[38] A. Scholl, M. Liberati, E. Arenholz, H. Ohldag, and J. Stöhr, Phys. Rev. Lett. **92**, 247201 (2004)

[39] Jeffrey Y. Tsao, *Materials Fundamentals of Molecular Beam Epitaxy*, Academic Press, INC, San Diego (1993)

[40] K-N. Tu, J.W. Mayer, L.C. Feldman, *Electronic Thin Film Science for Electrical Engineers and Material Scientists*, New York (1992)

[41] J.W. Matthews, A.E. Blakeslee, J. Cryst. Growth, **27**, 118 (1974)

[42] V.M. Kaganer, R. Köhler, M. Schmidbauer, R. Opitz, B. Jenichen, Phys. Rev. B, 1793, **55** (1997)

Chapter 2

Growth details of CoO and MnO films and multilayers on different substrates

2.1 Introduction

As already explained in the previous chapter, the major issue in this thesis will be to explore the effects of epitaxial strain on the electronic and magnetic structure of CoO thin films. To this aim, samples were grown by the Molecular Beam Epitaxy (MBE) technique, and the size and sign of the epitaxial strain in the films was controlled by a suitable choice of substrate materials or buffer layers. *In-situ* characterization of these films was carried out by means of surface sensitive techniques, such as Reflection High-Energy Electron Diffraction (RHEED) and Low Energy Electron Diffraction (LEED) to follow the morphology and structure during and after growth, and X-ray Photoemission Spectroscopy to check its chemical composition. In the present chapter the epitaxial growth of CoO and MnO films on different substrates will be presented.

2.2 Substrates and preparation

The substrate most often used for oxide growth is MgO. This is primarily due to, the ease with which one can prepare a clean, crystallographically almost perfect surface. The substrates ($10 \times 10 \times 10$ mm^3 cubes and $1 \times 10 \times 10$ mm^3 polished crystals) were purchased from Crystal GMBH. The polished (001) oriented substrates usually have a finite miscut i.e. the angle between the normal to the surface and the crystallographic [001] direction is in the range of 0.5 °. This can be easily measured with X-ray diffraction. Because of its abundant use in thin film growth, MgO attracted a lot of scientific attention and therefore good recipes for preparing well ordered surfaces were developed [1–3]. MgO surfaces are known to be hydrophylic (adsorb water). Therefore, immediately after cleaving the substrates were clamped on stainless steel sample holders in order to achieve good thermal contact, and inserted into the vacuum chamber. This operation took on average less than 30 minutes. Polished substrates were first cleaned in pure acetone and methanol. The samples were then introduced in Ultra High Vacuum (UHV) and subjected to a heat treatment of about 60 minutes at 650 °C in P=10^{-6} mbar O_2 atmosphere. O_2 has the role of oxidizing agent reacting mainly with the carbon on the surfaces and producing CO which is pumped away. It was previously demonstrated that such a treatment results in crystallographically and spectroscopically good surfaces [4]. The use of conductive glue such as silver paint instead of stainless steel strips, turned out to be inefficient and caused bad pressure upon heating. $SrTiO_3$ and $MgAl_2O_4$ crystals were also used as substrates and the preparation procedure described above was successfully applied in both cases, resulting in well ordered surfaces giving well resolved RHEED and LEED patterns. The preparation of Ag single crystals was performed by cycles of Argon sputtering in $P_{Ar}=5\times10^{-5}$ mbar atmosphere and annealing at 400-450 °C until the XPS spectra showed no contamination.

2.3 Techniques used at growth

A short overview of the two main techniques RHEED and LEED used *in-situ* before, during and after growth of the films will be given. For a more comprehensive treatment of these techniques the reader is referred to [7].

2.3.1 Reflection High-Energy Electron Diffraction (RHEED)

RHEED is widely used in crystal growth because of its potential of delivering vital information about the quality and crystallographic nature, as well

as the morphology and growth mode of the films, such as layer-by-layer or island growth. The only requirement for its use is the existence of a fairly good vacuum (although with some modifications, this impediment was also circumvented [5, 6]).

Since the probing particles are electrons the technique is very surface sensitive. A major advantage is that the technique can be used during growth of the films. The electrons that probe the surface, are accelerated to a certain energy by the gun, the most used values being in the region of 15-25 keV, which is equivalent to a k vector given by:

$$k_0 = \frac{1}{\hbar}\sqrt{2m_0E + \frac{E^2}{c^2}}, \tag{2.1}$$

In this equation the relativistic correction, which is about 3% at 20 keV, is included [7]; m_0 is the rest mass of the electron. Using E=20 keV Eq. 2.1 gives a momentum k_0, of the order of 73.4 Å^{-1}, which is about 50 times larger than the reciprocal-lattice vector ($2\pi/a_{MgO}$) of MgO.
A schematic view of the RHEED setup, together with the Ewald sphere construction for the RHEED case, is presented in Fig. 2.1.

The streaks (or spots) produced on the screen are the result of the interference of the electrons which suffered elastic collisions with the surface atoms. The interference of these electrons gives Bragg maxima if the surface is ordered. As there is a limited depth which the electrons reach inside the surface before they are inelastically scattered [13], only two of the three Laue conditions are satisfied. Due to the relaxation of the third Laue condition we may use a set of reciprocal lattice rods perpendicular to the surface plane instead of reciprocal lattice points as in the 3D case. For a fixed angle of incidence of the electron beam, the Bragg condition is fulfilled at the points of intersection of the rods and the Ewald sphere. The resulting Bragg spots lie on circles. In practice the reciprocal lattice rods have a finite width due to the finite size of the lateral domains and a finite coherence length of the electron beam (Fig 2.1). The coherence length, defined as the distance along the surface over which the diffracted electron beams still interfere constructively, determines the upper limit of the long range order that can be studied with this technique.

The intensity of the RHEED spots oscillates if the crystal is growing in a layer-by-layer fashion. This intensity oscillation can be measured by recording a movie of the RHEED pattern during film growth. The details of the mechanism causing the growth oscillations are not yet clear. The most common explanation is based on the periodic change of the surface roughness.

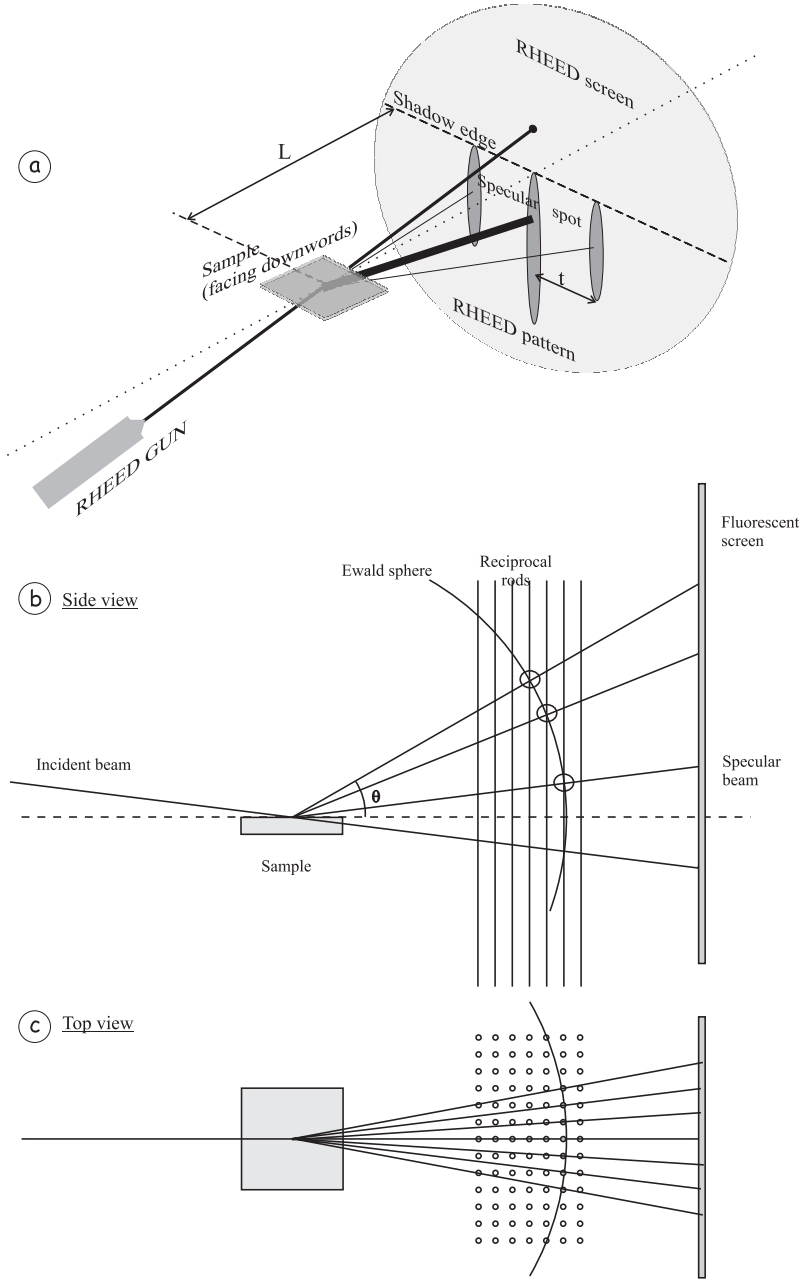

Figure 2.1: (a) Schematic view of the **RHEED setup** in the growth chamber together with the Ewald sphere construction for the RHEED case. (b) **Side view** The circles represent the position where the Ewald sphere intersects the reciprocal lattice rods. (c) **Top view**. The observed pattern is the one projected on the screen.

When the coverage of the growing film reaches 0.5 ML, the step density is maximum and the specularly reflected electron beam has the lowest intensity due to diffuse scattering by the steps. A second explanation which was often used shortly after the discovery of the RHEED oscillations, is based on the (destructive) interference between the electrons scattered by the growing top-layer and the fully developed layers below. This effect is largest at the so-called anti-Bragg condition. It is, in fact, the predominant mechanism in the case of growth oscillations in reflected X-rays. In the case of electrons, however, the kinematic approach is too simple. The most disturbing discrepancy between the above models and experiment is the commonly observed phase shift of the RHEED oscillation with respect to the maxima in the step density or occupation of the top-layer, which can only be explained in the framework of dynamical scattering theory. The simplest model predicting these phase shifts is one in which the reflectivity of the top layer changes periodically. Also this model is not capable of a reliable and quantitative description of the growth oscillations. Nevertheless, the RHEED oscillations are very useful in growth characterization. Whether the oscillations are caused by the variations in top-layer occupation, step-density or refraction effects, the period of the oscillations is in all cases an accurate measure of the time necessary to grow a crystalline monolayer (see Section 2.4.1 for an example).

While smooth surfaces with a limited amount of defects produce a streak-like pattern, rough surfaces produce a spot-like pattern also known as transmission pattern. This is so because the impinging electrons in the latter case "feel" the crystalline periodicity not only in the lateral but also in the vertical direction. In this case one would expect a square-like pattern for a relaxed crystal. This, however, is not what is observed in experiment, see Fig. 2.2. In this figure the in-plane spots are equidistant (dotted line) but the distance between the out of plane spots is the same only at high angles and becomes smaller as the diffracted beam approaches grazing angles. This effect is entirely due to the existence of an inner potential of the order of 10-20 V, inside the film, giving rise to refraction.

Because of the inner potential Φ, the electrons from the RHEED gun, arriving at the surface of the crystal will have a higher perpendicular momentum inside the crystal. The difference in their momentum is due to the gain in kinetic energy due to the inner potential of the crystal. The same phenomenon is obviously also active if the electrons leave the crystal, thus electrons emerging under grazing incidence will be affected more than those diffracted to higher angles with respect to the crystal surface. There exists even a fraction of electrons which will be unable to escape at all due to total reflection. Writing

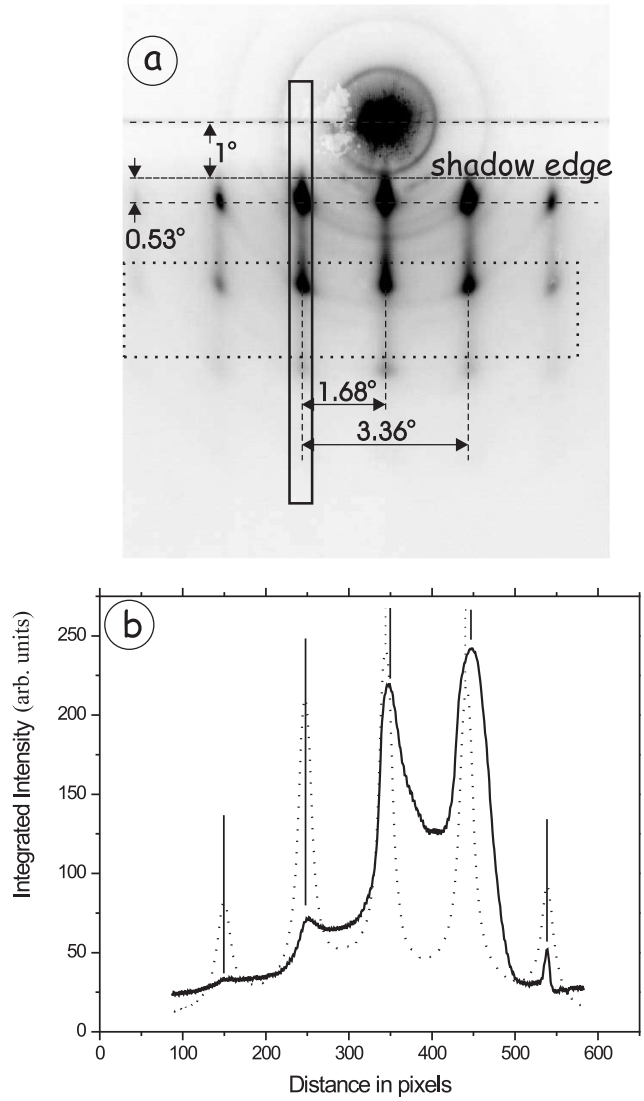

Figure 2.2: (a) 25kV RHEED pattern of 100 monolayer thick $Sr(O_xN_{1-x})$film grown on cleaved MgO. The film is relaxed (in-plane and out-of-plane lattice parameters are equal due to the large mismatch and therefore the fast relaxation) and produces a 3D-like pattern. The rectangles show two cross sections: parallel (dotted) and perpendicular (solid) to the surface of the film. (b) Integrated intensity from the two rectangles taken along the short side of the rectangles in function of position (pixels). The position of the peaks in the two scans coincides only for the first two peaks whereas last two peaks of the vertical section are not regularly spaced.

down the conservation of energy, neglecting relativistic effects, one can derive a simple formula for the angular dependence of the outgoing electron beam:

$$\sin^2(\alpha_f) = \sin^2(\alpha_i) + \frac{\Phi}{U} \tag{2.2}$$

where U is the RHEED accelerating voltage, α_f and α_i are the angles between the electron beam and the surface, inside and outside the material respectively. Taking $\Phi = 10V$ and $U = 25kV$ one gets for the limiting case of $\alpha_i = 0$, a value of $\alpha_f = 1.146°$, which is a considerably large angle. In Figure 2.3 is shown how α_f varies with α_i. At angles lower than the critical angle no beam is escaping due to the total reflection, whereas well above the critical angle α_i the escape angle does not deviate much from the internal angle α_f. Therefore, as expected, the strongest distortion is caused at very grazing emergence angles. The value of the inner potential is calculated for the case depicted in Figure 2.2 (b) where also the relevant distances (in degrees) are displayed. The calculation of the inner potential can be done by solving equation 2.2 for the two refraction events, namely at incidence and at escape, together with the Bragg condition inside the crystal. These equations using the approximation $\alpha \approx \sin(\alpha)$, that is valid at such small angles, become:

$$\begin{aligned} \alpha_{1f}^2 &= \alpha_{1i}^2 + \frac{\Phi}{U}, \\ \alpha_{2f}^2 &= \alpha_{2i}^2 + \frac{\Phi}{U}, \\ \theta &= \alpha_{1f} + \alpha_{2f}, \end{aligned} \tag{2.3}$$

The most expected scenario is when θ is taken equal to the distance between two consecutive reflections, namely (0 0 2) and (0 0 4), consequently one presumes that the spots laying closest to the shadow edge, illustrated in Figure 2.1, are the (h 0 2) reflections. Having from Figure 2.2 the angles $\alpha_{1i} = 1°$, $\alpha_{2i} = 0.53°$, and $\theta = 1.68°$ and solving the above equations, one gets $\Phi = 0.84V$. However, this value for Φ is an order of magnitude lover than the inner potential determined in the available literature which is in the region of 5-20 V [8] (for MgO Φ ∼15 V [9]). The explanation is that the first row of reflections lying nearest to the shadow edge is not the (h 0 2) but the (h 0 4). In fact the (h 0 2) reflections are approaching the surface, from inside the crystal, under such a grazing angle that they cannot escape from the material. This case is represented by the white line in Figure 2.3 (a). It is therefore the (h 0 4) reflections that can only escape in the present example and thus are visible in the transmission pattern closest to the shadow edge in Figure 2.2, therefore $\theta = 3.36°$ which results in $\Phi = 16.7$V. This value of

the inner potential is more plausible and the present example illustrates the huge effect of the inner potential on the position of the diffraction peaks in the perpendicular direction. One should be aware of this effect when calculating lattice constants from RHEED patterns even if the film is poly-crystalline and the spots turn into rings. These rings will deviate from a regular circle having a different curvature close to the shadow edge. The same effect is visible in the case of Kikuchi lines, which turn perpendicular to the shadow edge when close to grazing emergence angles. The lateral distance between the RHEED streaks is not affected by the inner potential and, as will be shown in the following sections, this distance can provide us with important information regarding the change in the in-plane lattice parameter of the film during growth.

2.3.2 Low Energy Electron Diffraction (LEED)

In the present study LEED was used as a qualitative tool mainly for structure identification purposes. Our experimental setup uses a beam of low energy (50-500 eV) electrons impinging perpendicularly on a surface of a single crystal having a well ordered surface. The electrons accelerated at these low energies will have a de Broglie wavelength of the order of Ångstoms ($\lambda \approx \sqrt{\frac{150}{V}}$ Å) and are diffracted by a thin layer of surface atoms and imaged on a fluorescent screen which has the shape of a hemisphere centered on the crystal surface and is situated around the electron gun. The spots on the screen, projected onto the viewing plane correspond to the reciprocal lattice of the surface. In comparison with RHEED, the advantage here is that while RHEED produces an image from a vertical cut in reciprocal space, LEED provides us with a snapshot of the 2D reciprocal lattice seen from above. It is therefore much easier to recognize the symmetry of the reciprocal lattice and no rotation of the sample is necessary in order to determine the surface structure.

2.4 CoO under compressive strain

2.4.1 CoO growth on MgO

Epitaxial films of CoO were grown by Molecular Beam Epitaxy (MBE) on cleaved and epi-polished MgO substrates. The growth was performed at the following conditions: base pressure P_{base}=3×10^{-10} mbar, and substrate temperature ∼260-290 °C. Elemental Co of 99.99 % purity was evaporated from alumina crucible kept at 1270-1300 °C, onto the substrate positioned at ∼ 50 cm from the crucibles, the result being a metal flux in the range of 1-3 Å/min at the sample position. The metal flux was checked with a crystal monitor

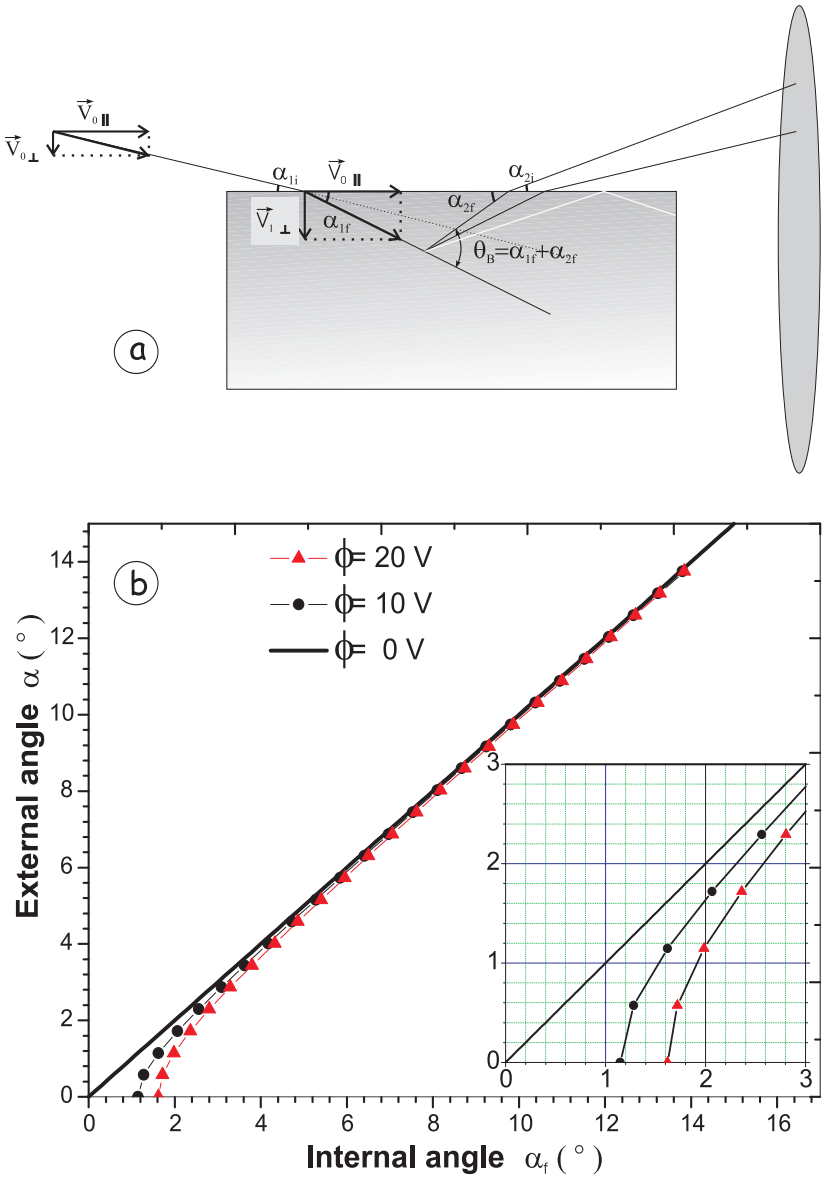

Figure 2.3: (a) Schematic picture of the possible electron paths in the RHEED setup viewed from the side. The relevant angles are also presented. (b) Solution of Equation 2.2 for several values of inner potential. It is visible that at low angles the deviation of the internal angle (α_f) from the external angle (α_i) is larger than at higher angles. At higher incidence angles $> 5-6°$ the deviation is vanishingly small.

prior the growth. O_2 was supplied from a 35 cm long and 1 cm diameter pipe, positioned at 2-8 cm from the sample (see also [10]). A baratron was used to measured the oxygen pressure in a buffer volume separated from the chamber by the above mentioned pipe. The O_2 gas was introduced in the growth chamber via a special leak-valve, so that the baratron voltage was maintained at $U_{baratron} \approx 0.2V$ ($P_{baratron} \propto U_{baratron}$). The oxygen flux arriving at the sample surface can be calculated using the Hertz-Knudsen formula:

$$F_{O_2} = \frac{P_{baratron}}{\sqrt{2\pi m k_B T}} \tag{2.4}$$

where m is the atomic mass of the gas, k_B is the Botzmann constant ant T is the absolute temperature of the gas. This resulted in O_2 background pressure of $\sim 10^{-7}$mbar, for more details see the dissertation thesis of F.C Voogt [4]. The growth was monitored by RHEED with a CCD camera, recording a movie in digital form on the hard drive of a PC. This allowed us to analyze the growth mode and crystallographic nature of the film with the help of a home made computer program [11]. Fig.2.4 shows the recorded RHEED pattern (U=20 kV) of the MgO substrate before growth, and of a 26 ML ($\sim$ 55 Å) CoO film grown on the MgO crystal, with the incident electron beam along the [100] direction. At 260 °C both the substrate MgO and the film CoO have the same cubic rock-salt structure in bulk form i.e. the Bragg condition will be satisfied for all odd or all even indices.

During growth, intensity oscillations of the specularly reflected spot were observed. As already stated, these oscillations signify a layer-by-layer type of growth and they can be used to determine the exact thickness of the films. In this way, a growth rate of 2.3 Monolayer (ML)/min, and from the time of growth of $\sim$ 980 s, a thickness, of 26 ML was determined. From the final RHEED figure 2.4 of the CoO film the streaked pattern as well as the RHEED intensity oscillations during growth in Figure 2.5 suggest the presence of a smooth surface after the CoO deposition. The RHEED oscillations in Fig 2.5 were recorded during growth of a similar CoO film (where we used almost the same growth conditions) but the incidence angle of the electron beam was set at an optimum value in order to record RHEED oscillations with high amplitude. Having an insulating substrate and also an insulating film these conditions, involving highly grazing geometries, are sometimes difficult to realize due to charging effects. In order to solve these problems, an electron flood-gun was employed to compensate for the excess electrons emitted from the sample.

The crystals MgO and CoO, having lattice constants of 4.212 Å and 4.267 Å respectively, constitute a system with a considerable lattice mismatch,

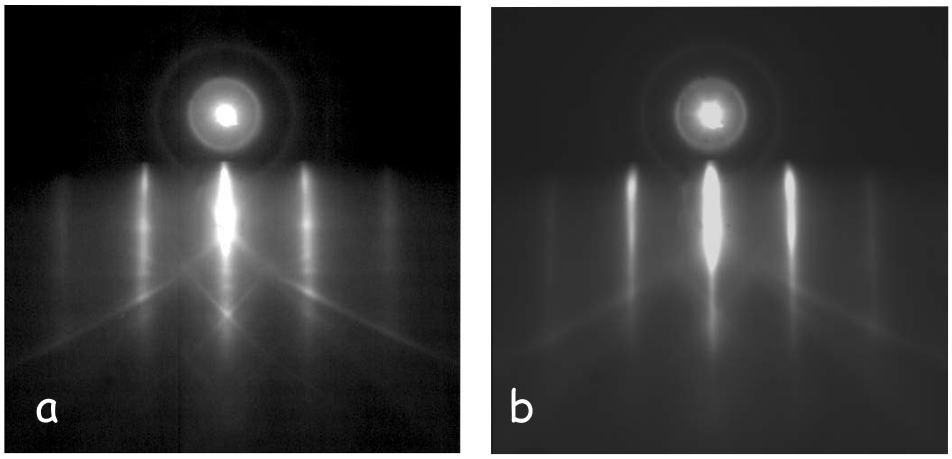

Figure 2.4: RHEED pattern of (a) cleaved MgO crystal before growth, (b) 26 ML of CoO film grown at 260 °C, with a rate of 2.3 ML/min. Both pictures were made at the same electron energy of 20 keV. The film growth was in a layer-by layer fashion since RHEED oscillations could be recorded see Figure 2.5. In both cases the electron beam is incident in the [100] direction.

f, producing a misfit strain, ϵ_0, in a thin, unrelaxed CoO layer:

$$f = \frac{a_{CoO} - a_{MgO}}{a_{MgO}} \approx 0.0129 \tag{2.5}$$

$$\epsilon_0 = \frac{a_{MgO} - a_{CoO}}{a_{CoO}} \approx -0.0128 \tag{2.6}$$

Because of the small difference in the absolute value of these two quantities, for low misfit systems the equality $\epsilon_0 = -f_0$ is often used. At very small thicknesses (several tens of ML), coherent growth is expected during which the in-plane lattice constant for the CoO film equals the lattice constant of the MgO. Beyond a certain critical thickness, misfit dislocations relieve the strain in the film. The substrate temperature has proven to be an important parameter in many growth studies which influences not only the type of growth but also the relaxation behavior of the films. On the one hand, it is expected that the layer-by-layer type of growth is promoted by the high temperatures due to the increase in diffusivity [12]. On the other hand it is obvious, that the increase in temperature promotes the gliding of the dislocations [14, 15] which favors the relaxation of the strain by the multiplication of dislocations. The substrate temperature of 260-290°C was a compromise, namely high enough

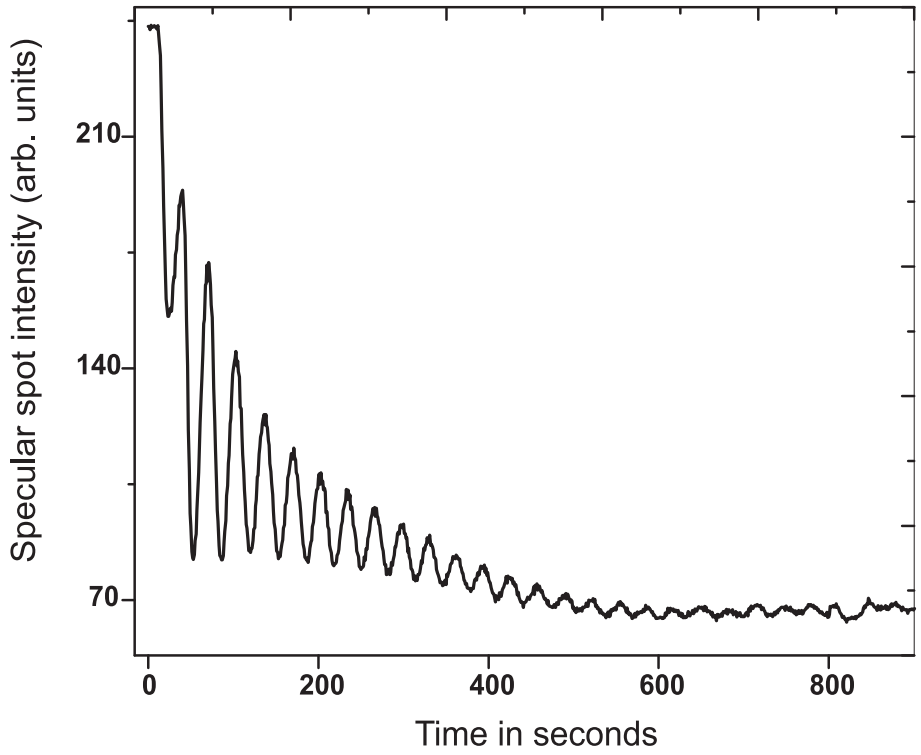

Figure 2.5: RHEED oscillations of the specularly reflected electron beam during growth of a CoO film on cleaved MgO crystal. Every oscillation corresponds to a ML of CoO. These oscillations can be utilized to grow submonolayer thicknesses with high accuracy.

for having smooth films (promote layer-by-layer growth) and low enough to inhibit high dislocation velocities ($v_{disloc} \sim exp\left(-\frac{U}{kT}\right)$ where U is the activation energy and T is the absolute temperature).

As described in section 2.3.1, the position of the streaks appearing in RHEED are directly related to the *in-plane* lattice parameter of the surface. Thus one should be able to measure the relaxation during film growth. However, due to the relatively small lattice mismatch between CoO and MgO it was not possible to produce conclusive results by RHEED since the CCD camera resolution was too low for this substrate-film system. The effective displacement of the (02) RHEED lines was of the order of 1 pixel. This disadvantage is compensated by the fact that the relaxation of the layer will occur at higher thicknesses (110-130 Å), therefore it allows the measurement of relaxation using X-ray diffraction. Chapter 3 will deal entirely with this

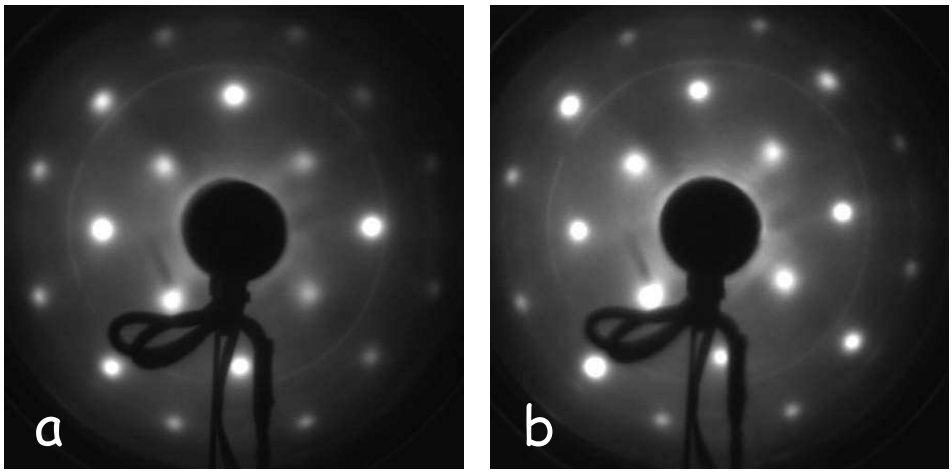

Figure 2.6: LEED pattern of (a) thin CoO film grown on MgO and, (b) 220 ML of CoO film , both films grown at 250 °C, with a rate of 0.84 ML/min. Both pictures were made at the same electron energy of ∼143.6 eV. No difference is visible although the thin film is under and the thick film is above the critical thickness (discussed in more detail in chapter 3)

problem including different models describing also the relaxation behavior for other substrate-film systems. In Figure 2.6 we present two LEED patterns at 143.6 eV incident beam energy, recorded below (a) and well above (b) the experimentally and theoretically found critical thicknesses for CoO on MgO. Due to the small mismatch there is no dissimilarity between the two patterns, attesting the perfect crystalline nature of the films in both cases. But, in order to observe an convincing quantitative difference between the relaxed and unrelaxed films one should use a camera with a higher resolution.

2.4.2 CoO growth on Ag

There are many papers describing the growth of CoO on metal surfaces such as Ag (001) [17, 18], Au (111) [19, 20], bct Co (001) [21], and even semiconductors [22] and Fe_3O_4 [23]. Therefore, in this chapter we refer to these papers and only mention details on the expected relaxation behavior of CoO on Ag (001). Starting with a base pressure of p_{base}=3×10^{-10} mbar before deposition, the growth was performed in an O_2 pressure set to p_{O_2}=3×10^{-7} mbar by leaking it in the growth chamber through the previously described pipe, kept at 4 cm

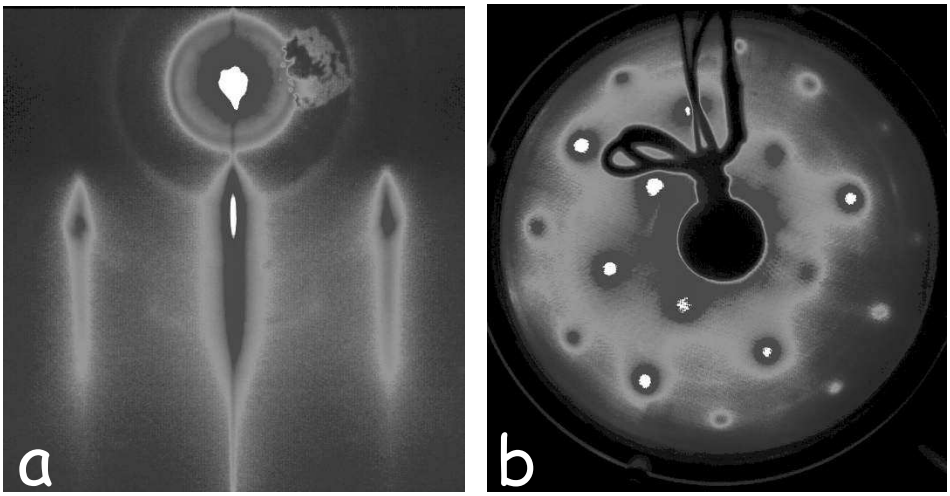

Figure 2.7: (a) RHEED pattern of 105 ML thick epitaxial CoO on Ag (001) taken immediately after growth, having the electron beam in the [001] direction. (b) LEED pattern taken at an electron beam anergy of 222 eV of the 105 ML CoO.

distance from the sample. The Co metal flux was 0.91 Å/min and the Ag substrate temperature was kept at 150 °C. Figure 2.7 presents the RHEED and LEED pattern of a 105 ML CoO film immediately after growth, proving the good quality of the CoO films grown on a Ag (001) single crystal prepared as described in section 2.2.

Due to the large misfit of ~ 4.3 %, between the bulk CoO lattice parameter and the Ag substrate, and the fact that Ag is a relatively soft metal (the shear modulus of silver $G_{Ag} \approx 1.53 \cdot 10^{10}$ Pa as compared to the one of MgO $G_{MgO} \approx 10.13 \cdot 10^{10}$ Pa), the relaxation observable from RHEED is virtually immediate. Part of the strain is relieved in the Ag substrate and part in the film by the appearance of a network of misfit dislocations. This relaxation is not complete and even after ∼200 ML, the film is still partially strained. The values of the in-plane and out-of-plane lattice parameters of such films are $a_{\perp CoO}$=4.285 Å , $a_{\parallel CoO}$=4.235 Å. Chapter 3 will give more insight into the theoretically predicted values for the strain.

2.4.3 CoO growth on $MgAl_2O_4$ and $SrTiO_3$

In order to impose higher compressive strain to the CoO layer we decided to attempt the growth on $MgAl_2O_4$ substrates. $MgAl_2O_4$ has the spinel-type

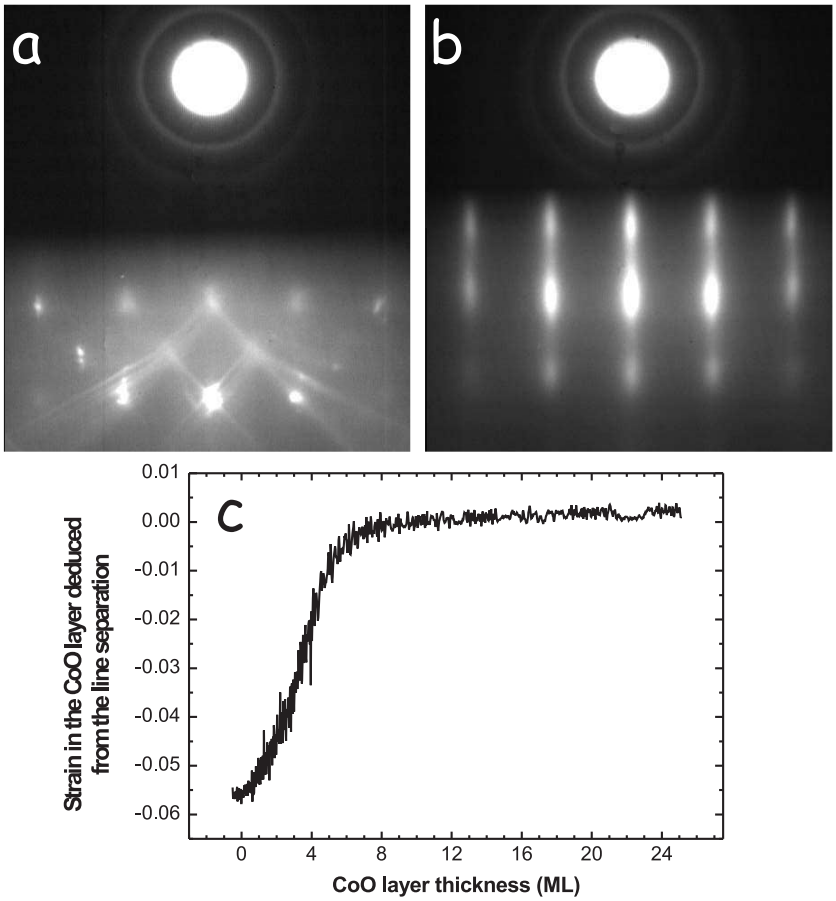

Figure 2.8: (a) RHEED pattern and of $MgAl_2O_4$ and (b) a 25 ML CoO layer grown under conditions explained in detail in the text. (c) Strain relaxation during growth as derived from RHEED. The immediate relaxation of strain is visible as well as the final relaxed layer well above 5-7 ML of CoO.

crystal structure and consists of a cubic close packed O^{2-} sublattice having the Mg^{2+} in the tetrahedral and the Al^{3+} in octahedral interstitial sites. The lattice constant of spinel is 8.083 Å and therefore the mismatch with the CoO lattice is $f \sim 0.056$, the two structures having identical oxygen lattices [16]. Figure 2.8 presents the recorded RHEED pattern of (a) the substrate and (b) a ∼25 ML CoO film grown at 270 °C substrate temperature using a CoO growth rate of 39 sec/ML. The oxygen flux, delivered by the above described

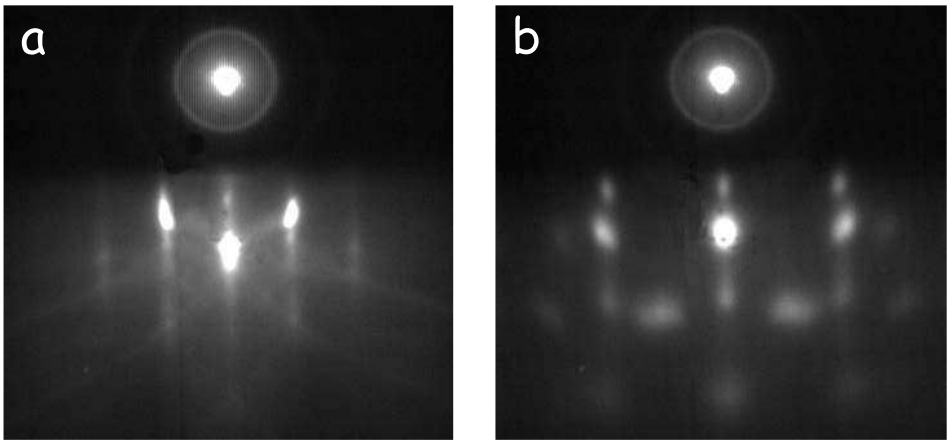

Figure 2.9: (a) $SrTiO_3$ (001) surface. The barely visible RHEED lines close to the side of the figure are the (02) and $(0\bar{2})$ whereas the more intense lines aside of the central line are the (01) and $(0\bar{1})$ lines respectively. (b) CoO_x layer. The extra spots visible between the (02) and $(0\bar{2})$ lines are due to some unwanted crystallites having different orientation than the expected epitaxial layer. The growth is therefore not single crystalline, this is most probably caused by the high mismatch between substrate and film.

pipe, 4 cm away from the substrate, was kept high enough to fully oxidize the Co. The RHEED pattern originating from the 25 ML CoO layer suggests a rough surface which actually appears immediately after the first monolayers. RHEED intensity oscillations were not observed. The thickness of the film is estimated by knowing the Co flux, beforehand, from RHEED oscillation periods recorded during CoO on MgO growth and X-ray reflectivity measurements. Because $MgAl_2O_4$ is an insulator, it was necessary to make use of a flood-gun in order to be able to record a movie of the growth process without the disturbing charging effects. These charging problems sometimes arose also in the case of MgO and other insulating substrates, and are caused by the emission of secondary electrons in numbers exceeding the flux of the primary beam, thereby creating positively charged areas. In conductive materials charging can be avoided by grounding the sample. In the case of insulating substrates flood guns are commonly used to compensate for the charge imbalance.

In the case of CoO on MgO the limited resolution of the CCD camera prevented us from acquiring information about the relaxation of the layer during growth by measuring the spacing of the RHEED diffraction lines. In the present case of CoO on $MgAl_2O_4$, this is not a problem anymore because

the misfit is a lot larger (∼5.58 %). Thus also the image of the reciprocal lattice projected on the fluorescent screen is expected to change considerably during relaxation. In calculating the strain we make the approximation that the separation of the RHEED lines is inversely proportional to the lattice parameter. This approximation is valid if the measurement geometry is such that the sample to screen distance is a lot larger than the line separation and that the radius of the Ewald sphere is much larger than the reciprocal lattice spacing [29]. In this case λ/2d=sin(θ_{Bragg}) $\approx \frac{1}{2}\tan(2\theta_{Bragg})$=t/2L (see Figure 2.1 for the abbreviations). Figure 2.8(c) shows the instantaneous strain derived from the separation of the RHEED lines. The strain starts to decrease immediately as the shutter is opened (0 ML) and the film is totally relaxed after about 5-7 monolayers. This is just as expected from theory. A full derivation of relaxation behavior and the dependence of the critical thickness (h_c) for different misfits and substrate elastic constants will be given in the following chapter, section 3.5.

An attempt was made also to grow CoO thin films on $SrTiO_3$ substrates. The growth conditions were identical to the CoO on $MgAl_2O_4$ case. The corresponding RHEED patterns are depicted in Figure 2.9. Since the mismatch is more than 9 % the growth is not coherent. Although not studied in detail, the extra diffracted intensity appearing in between the (02) and (0$\bar{2}$) lines, see Figure (b), might be due to the presence of domains being rotated 45° with respect to the [010] direction.

2.5 CoO under tensile strain

2.5.1 MnO growth on MgO

The main reason of pursuing this subject was the need of a suitable and easily obtainable substrate, having a larger lattice spacing than CoO. Due to difficulties in attaining an adequate, well oriented and ordered surface of an *ex-situ* cleaved MnO crystal as well as the elevated price of these single crystals, successful attempts were made in epitaxially growing MnO buffer-layers on MgO which could be used as substrates for CoO growth.

MnO crystalizes also in the rock-salt structure above its Néel temperature ($\sim 120K$), with a lattice spacing of 4.445 Å at room temperature. The misfit between bulk MnO and MgO is $f = 0.0553$. MnO grows layer-by-layer on MgO, although the appearance of misfit dislocations occurs theoretically after only a few monolayers and fast roughening of the surface is expected. Figure 2.10 displays a comparison of the 20kV RHEED pattern of an MgO substrate together with a 480 ML thick MnO film, grown at 400 °C substrate

temperature in $P_{O_2} = 1 \times 10^{-7}$ mbar oxygen pressure delivered from a 35 cm long, 1 cm diameter pipe 8 cm away from the sample. The growth rate used for all samples was in between 5 and 7.5 ML/min. This increased growth rate in comparison with the growth of the CoO films was adopted for the following reasons:

- CoO/MnO multilayers were grown consisting of thin strained CoO layers sandwiched between thick relaxed MnO layers. In comparison to Co, the Mn is easily oxidizable to Mn_3O_4, or in other words, MnO is less stable than CoO at higher partial O_2 pressures. Increasing the Mn deposition rate relative to the Co rate it is possible to maintain the necessary oxygen fluxes only by adjustment of the *sample to oxidizing pipe distance*. The latter can be adjusted very precisely and this process requires approximately 3 seconds, which is much less than the time needed to grow 0.5 ML MnO.

- the usual thicknesses of MnO buffer layers for the growth of stretched CoO layers, were of the order of 0.1-1 μm. Adopting this high growth rate decreased the growth time appreciably.

As it is often the case for epitaxial oxide growth, the substrate temperature is decisive not only for the growth mode adopted by the layer but also for the

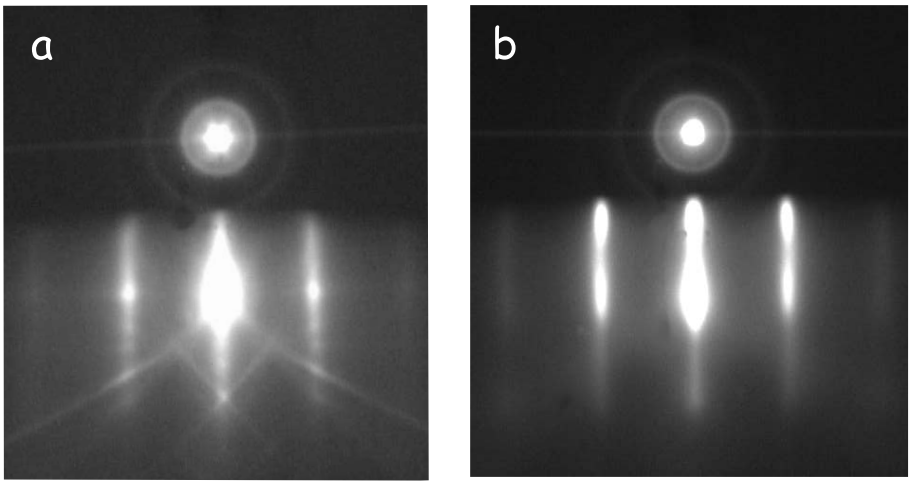

Figure 2.10: (a) RHEED pattern of MgO (001) surface before deposition of MnO film. (b) 480 ML of MnO grown under the conditions specified in the text. The simple "clean" pattern reflects the good single crystalline quality of the film. These kind of films will further be used as substrates for CoO films.

stoichiometry of the *as-grown* material [3, 4, 24, 25]. The stoichiometry of MnO is highly responsive to the substrate temperature during growth as well as after growth, if the film is kept at a certain nonzero O_2 background pressure.

To illustrate how the stoichiometry can be affected by the substrate temperature, we grew MnO films on MgO and Ag, at different substrate temperatures. The growth was performed at a fixed Mn evaporation rate of 7 Å/min (measured by a quartz crystal monitor) by heating elemental Mn in an alumina crucible. The O_2 was delivered by a pipe as described before at a distance of approximately 10 cm from the sample. These experiments were performed at ESRF Grenoble at the ID8 beamline, in order to find a recipe for growing stoichiometric MnO by using X-ray absorption spectroscopy as a tool to detect Mn^{3+} ions. The conclusion from these experiments is, that while films grown at substrate temperatures of 270 °C were stoichiometric for an oxygen partial pressure range of 2-8 $\times 10^{-7}$ mbar, the samples grown at lower substrate temperatures such as 200 °C were metallic below, and the presence of Mn^{3+}, indicating the presence of Mn_3O_4, was detectable above 3×10^{-7} mbar partial oxygen pressure. Figure 2.11 presents the O K edge as well as the Mn $L_{2,3}$ edge X-ray absorption spectra of two MnO films, with (upper) and without (lower) the presence of Mn^{3+} ions. The only clear difference in the spectra is observed at the pre-edge of the oxygen absorbtion.

The O K edge absorption process is a transition from the ground state consisting of mainly d^n states with some $d^{n+1}\underline{\mathrm{L}}$ states mixed in, to an excited state, consisting of an oxygen ligand core hole and no ligand hole in the valence band. The decay products of this excitation are measured: $d^{n+1}\underline{\mathrm{L}} \rightarrow \underline{\mathrm{c}}d^{n+1}$, where n represents the number of electrons in the d shell, $\underline{\mathrm{L}}$ denotes an oxygen ligand hole and $\underline{\mathrm{c}}$ is an O *1s* core hole. In the case of Mn^{2+}, n=5 and for Mn^{3+}, n=4. It is obvious that in a purely ionic picture having O^{2-} ions as ligands and if there would be no hybridization, the transition $1s \rightarrow 2p$ would not be possible since there would be no O 2p holes ($\underline{\mathrm{L}}$). The absorption process is observed because there *is* hybridization between O^{2-} an Mn^{2+} thus the Mn d states are responsible for the first part of the O 1s absorption spectrum ($\sim$4 eV) while the Mn $4sp$ states are involved at higher photon energies [26–28] at the unoccupied DOS close to the Fermi energy. The pre-peak appearing in the presence of Mn^{3+} is a consequence of a missing majority spin electron in the e_g orbital, which due to the exchange and the ligand field, will produce dipole accessible states by hybridization with the O 2p orbitals at lower photon energies. It was shown by de Groot et al. [28] that defects in the crystal are not so critical for the shape of this spectrum. Thus defects can not be considered as causes of the appearance of this pre-peak.

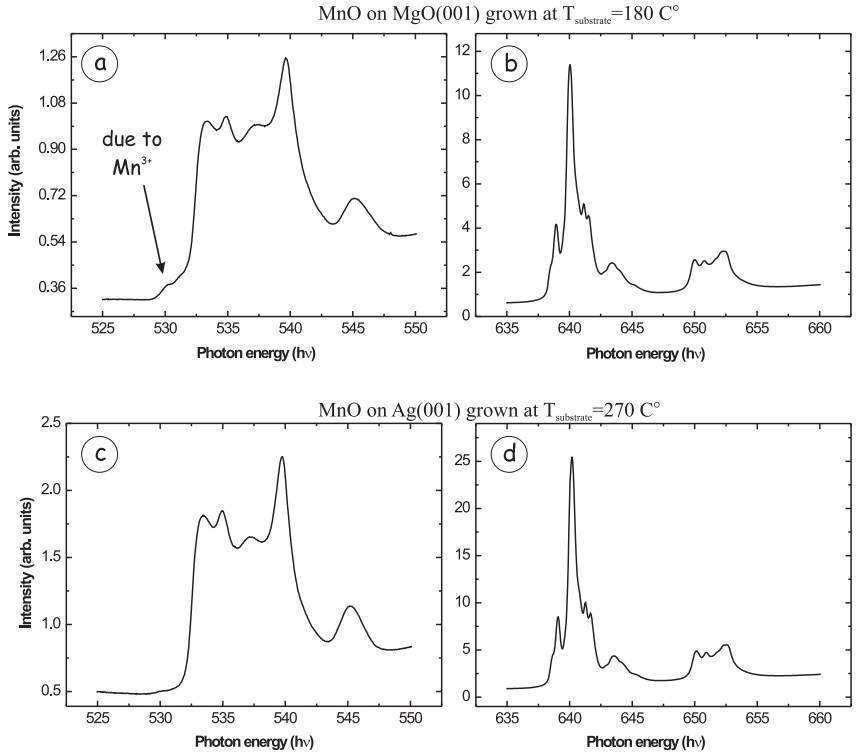

Figure 2.11: (a) O_{1s} X-ray absorbtion spectra recorded in the total electron yield mode of epitaxial MnO films grown on an MgO (001) cleaved crystal containing Mn^{3+} ions (a) The presence of Mn^{3+} ions is evident from the small shoulder just before the edge jump at $\sim$ 530 eV and (c) O_{1s} XAS spectra of stoichiometric MnO of the film grown at higher substrate temperatures where no shoulder is visible. (right side plots, (b) and (d)) In the Mn $L_{2,3}$ XAS spectra, almost no difference is visible in the two spectra.

We conclude from the above experiment that spectroscopically, good quality MnO films can be grown at substrate temperatures that are higher than 270 °C, in a relatively large oxygen partial pressure range.

To illustrate how the films behave from a crystallographic point of view if the samples are cooled down in a nonzero oxygen background pressure, we studied the surfeca structure using RHEED. Figure 2.12 presents the result of a short experiment done on a 110 ML MnO film on MgO. After growth at 320 °C substrate temperature the RHEED pattern in Figure 2.12 (a) indicates a relatively rough, but crystallographically perfect MnO surface. If the Mn

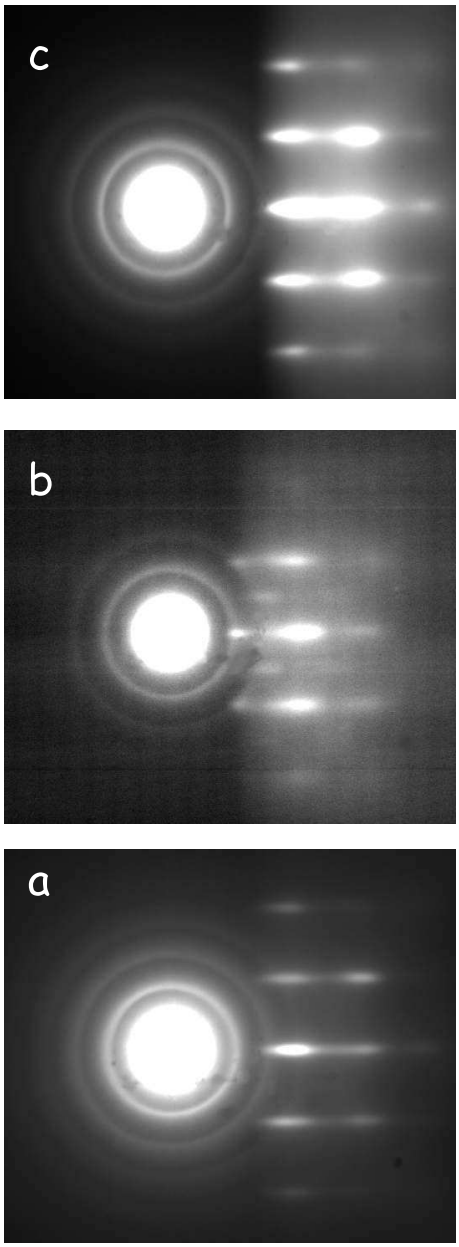

Figure 2.12: (a) RHEED pattern of as-grown MnO (110 ML) film. (b) RHEED pattern of the same MnO film cooled down in $P_{O_2} = 3.5 \times 10^{-7}$ mbar O_2 base pressure for $\sim$ 20 minutes. The extra streaks are the consequence of surface oxidation of rock-salt MnO into Mn_3O_4 having a spinel structure. (c) After annealing the film at 400 °C for 20 minutes the original RHEED pattern is regained which suggests the reduction of Mn_3O_4 to MnO.

metal evaporation is now stopped and the sample is kept a low ($p_{O_2} = 3.5 \times 10^{-7}$ mbar) oxygen pressure while cooling down for $\sim$ 20 minutes, the RHEED pattern changes into the one shown in the middle picture. The extra lines emerging between the former rocksalt MnO (0$\pm$2) diffraction lines are due to the oxidation of the MnO layer to M_3O_4 (hausmanite) which has a spinel crystal structure. If the sample is then kept in vacuum at 400 °C temperature for $\sim$ 20 minutes, the layer transforms back to the original rock-salt structure, as is evident from the RHEED pattern of Figure 2.12 (e). This shows that the process is reversible.

Figure 2.13 summarizes the relaxation behavior detected with the use of the separation of the RHEED lines in the case of the MnO/MgO growth. The film was grown at a substrate temperature of $\sim$400 °C which is the optimal temperature at which the film grows in a layer-by-layer fashion for the first 8-9 monolayers as confirmed by the intensity oscillations in fig 2.13(b) (dotted graph). The strain is deduced from the separation of the RHEED lines and is also shown in fig 2.13(b) (continuous line). After a sudden decrease of $\sim$ 20% during the first 1-2 monolayers from the initial totally strained value ($\epsilon \sim 0.055$) the film reaches a metastable state until a thickness of $\sim 5-6$ ML, after which it quickly relaxes towards the fully unstrained (relaxed) state. This is usually reached after 40-45 ML. The strain data displayed in the figure are calculated from the position of the maxima of the Lorentzian fits of the integrated intensities along the diffraction streaks of the RHEED patterns recorded every 0.5 s during growth, as shown by the thick arrow in the dashed rectangle in Figure 2.13 (a). Figure 2.13 (c) and (d) represent the time evolution (in the direction of the white arrow) of the above described integrated pattern originating from the solid rectangle from Figure 2.13 (a). One can see that not only the specularly reflected intensity undergoes oscillations but also the (02) and ($0\bar{2}$) Bragg intensities. The oscillations in the strain calculated from the line separation could be due to this intensity oscillations since not only the intensity of the lines oscillates but also the width which, due to its superposition on a nonconstant background across the pattern, can produce small, artificial displacements in position. The initial decrease of $\sim$ 20% for the first 1-2 ML could also be connected to this change in background. For other systems such as FeO_x on Al_2O_3 (0001) this jump in separation is considerably larger, exceeding the expected separation for the relaxed film, suggesting an increase of the strain in the opposite sense [30, 31]. It is also clearly visible from fig (d) that the intensity oscillations disappear when the separation of the lines decreases. In addition we observed a change of the RHEED pattern from a streaky to a more spotty pattern (like the one of Figure 2.12 **bottom**):

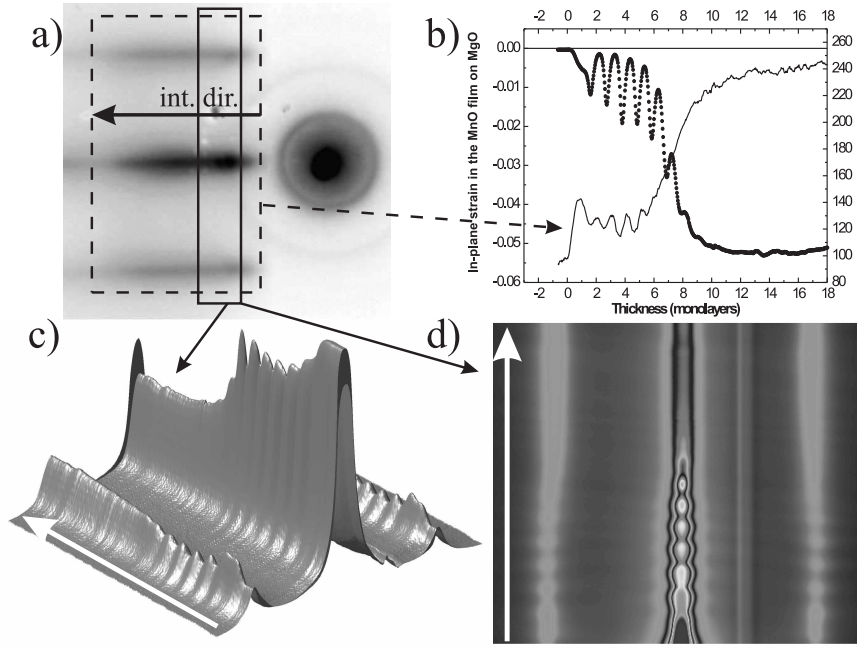

Figure 2.13: (a) Snapshot of the RHEED pattern of an MnO film during deposition by MBE on MgO. (b) Intensity oscillations of the specularly reflected electron beam during film growth at 400 C° substrate temperature (circles right vertical axis), as well as strain evolution calculated from the separation of the (02) and (0$\bar{2}$) RHEED lines during growth of the film (solid line, left vertical axis). The position of the lines was obtained by fitting the intensity (integrated in the direction shown by the arrow in (a)), with a "triple Lorentzian" profile and taking the position of the two extreme maxima.(c) Time evolution of the integrated intensity from the solid box in (a), the white arrow showing the time. (d) The change in separation of the lines is observable after ∼8 ML.

the pattern immediately after this transition is shown in Figure 2.13(a). The disappearance of the intensity oscillations together with the change into the spot-like pattern is a result of a change in growth mode from a two-dimensional layer-by-layer type to a three-dimensional island type which is related to the lattice mismatch between the MgO substrate and MnO film. Although Figure 2.13 represents the situation at 400°C, from our measurements we concluded that the overall relaxation behavior of MnO on MgO growth, namely the appearance of the *intermediate strain phase* and a *virtually full relaxation* after

30-40 ML, is similar for lower (300 °C) and higher (480 °C) substrate temperatures. The intensity oscillations revealing the layer-by-layer growth are most pronounced at a substrate temperature of 400 °C and they are *less intense but still present* for lower and higher substrate temperatures. At lower temperatures they persist also after the metastable state is overgrown. Therefore, in order to prepare MnO films for buffer layer applications one must keep in mind two limiting substrate temperatures: the low temperature being responsible for good stoichiometry for a larger oxygen partial pressure window and the high temperature bing responsible for roughening of the surface at lower film thicknesses (see also [32]).

2.5.2 CoO grown on MnO buffer layers

In the previous section we demonstrated that good quality stoichiometric MnO buffer layers can be grown on MgO substrates. These layers relax to their natural lattice spacing of 4.445 Å after about 40 monolayers. In this section we will show, that these MnO buffer layers can be used as substrates for CoO films. The positive mismatch between this buffer layer and CoO (f=0.041) will induce a considerable tensile strain in the CoO films. Figure 2.14 shows an overview of diffraction patterns recorded by RHEED and LEED in order to prove the possibility of realizing these structures. The RHEED patterns were collected with the electron beam incident along a [100] direction and the LEED patterns were recorded at an incident electron beam energy of ∼200 V. Except for Figure 2.14(f), all images show sharp lines in RHEED and sharp spots in LEED. Figure 2.14 (f) is taken from a 10 ML CoO film on MnO. The shape of the LEED spots is not circular but has a cross-like envelope, which is the consequence of the appearance of misfit dislocations in the CoO layer releasing the tensile strain. This kind of LEED images were reported also in the case of MgO grown on Fe (001) [33, 34]. The effect of misfit dislocations can also be observed in X-ray diffraction. The next chapter is almost entirely devoted to the explanation and simulation of these features. As discussed in the previous section, RHEED can be used to relate the diffracted intensity positions to the in-plane strain in the layer during epitaxial growth. The in-plane strain derived for the case of CoO on MnO is presented in the Figure 2.15(a). The horizontal scale shows the number of mono-layers of CoO. After a small jump in the opposite sense (which is most probably related to a fit artifact explained in the previous section), the lattice constant relaxes slowly towards the bulk value. We observed repeatedly that the first 4-5 ML of CoO had very little or no relaxation of the *in-plane* lattice parameter. Figure 2.15(b) shows the evolution of the distance between the (02) RHEED lines

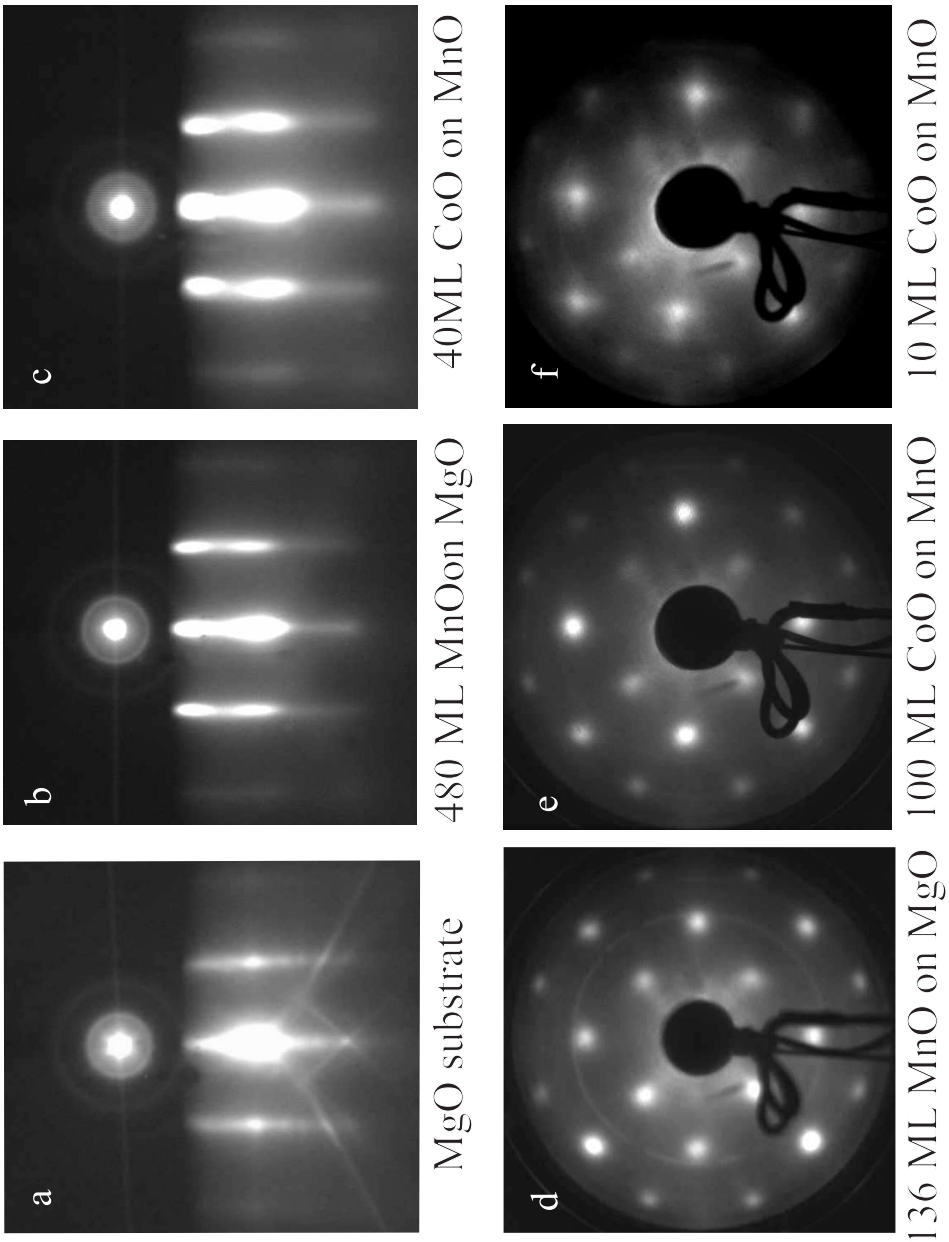

Figure 2.14: (a-c) RHEED patterns recorded during growth of MgO, MnO as well as CoO on thick MnO buffer layers. (d-f) LEED patterns of MnO as well as thick and thin layers of CoO on MnO buffer layers. In figure (f) cross-like shapes spot can be observed due to of the appearance of misfit dislocations.

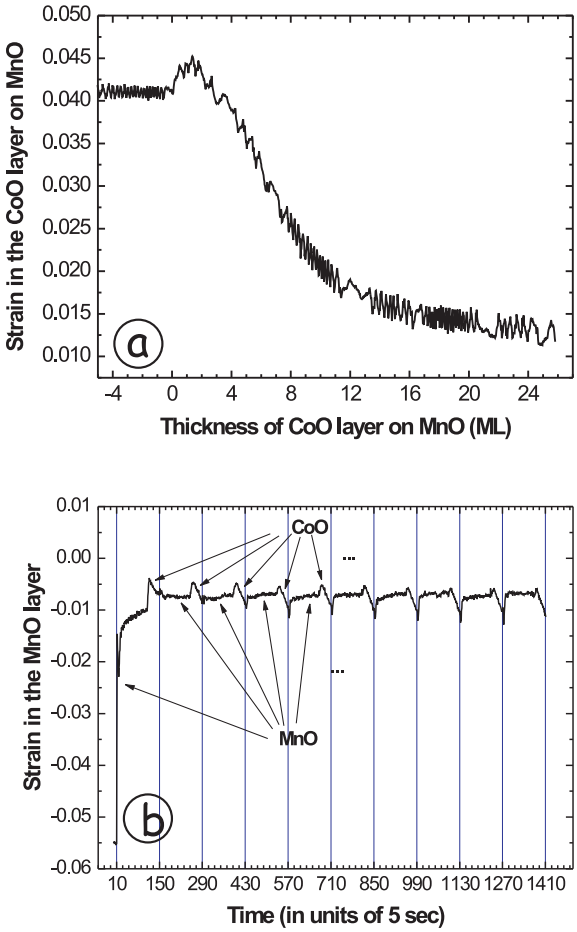

Figure 2.15: Relaxation behavior from the streak separation in RHEED. (a) After a thick MnO layer was grown on MgO, CoO is deposited on MnO and the observed separation of the RHEED streaks was translated into a numeric value of the tensile strain. This is plotted as a function of thickness during growth of the layer. (b) The in-plane strain variation in the case of a multilayer consisting of 10 double layers of composition (∼4 ML CoO on ∼80 ML MnO) is presented as a function of time during growth. The relaxed state of the MnO layer imposes a considerable tensile strain on the CoO layers which after 4 ML have almost entirely the same in-plane lattice constant as the relaxed MnO layers. By the use of the repeated sequence one can hope to build up enough material to allow the measurement of the structure with the use of X-rays (see next chapter).

for this sample. The values derived from the RHEED pattern after 5 ML are of particular interest because they cannot be determined using XRD. If one assumes that they are representative for the whole depth of the layer, $a_{in-plane}$=4.424 Å. From this value $a_{out-of-plane}$=4.15 Å can be calculated using a Poisson ratio of ν=0.27 derived from X-ray diffraction results (see next chapter). From these values it is obvious that the tetragonal distortion is considerable ($\sim$ 6.2 %).

In order to unravel whether the above derived values are indeed representative for the entire film or wether they are just values characteristic for the top layer, we decided to grow ten-fold multilayers having as repeat unit a thick ($\sim$80 ML) MnO layer and a thin ($\sim$4 ML) CoO layer. An attempt was made to measure such multilayers having a ten fold increased CoO diffracting volume using X-ray diffraction the results of such measurement are presented in the following chapter. In the graph in Figure 2.15 (b) the vertical lines separate the ten repeat units having the above described composition. It should be noted that the growth rate of CoO was $\sim$9.4 times slower than the growth rate of MnO. As explained before, the reason for this is two fold. Firstly MnO requires less O_2 flux than CoO and secondly, the time of the growth could be reduced by increasing the growth rate of MnO. Similar multilayers have also been grown having as constituent units thicker layers of CoO and thinner layers of MnO as well as the opposite configuration with thin MnO and thick CoO. For details of the X-ray diffraction studies on such multi-layer structures we refer to Chapter 3.

2.6 Conclusions

In this section the growth behavior of CoO on different substrates such as MgO, MnO, Ag, $SrTiO_3$, $MgAl_2O_4$ as well as buffer layers of MnO on MgO and Ag was discussed. It was shown that ordered single crystal epitaxial CoO films can be grown on all of the above mentioned substrates, except on $SrTiO_3$ which is highly unsuitable as a substrate for CoO because of their large (~ 9 %) mismatch.

The relaxation behavior, as derived from the *in-situ* RHEED measurements, was presented for large mismatches whereas for the relaxation of the other systems such as CoO on MgO X-ray diffraction will give the answer (see following chapter). Besides this, anticipating the need of X-ray diffraction for larger diffracting volume for determining the strain state of the CoO films, the growth of CoO on MnO multilayers was also discussed.

It was demonstrated that surface temperature and oxygen partial pressure are of crucial importance for the case of MnO growth. A growth recipe was set forth for the latter case by the employment of O 1s X-ray Absorption Spectroscopy (XAS), which proved to be a highly sensitive technique for identifying the valence state of the transition metal ion.

References

[1] S.S. Perry, P.B. Merrill, Surf. Sci. **383**, 268 (1997)

[2] Claudine Noguera, *Physics and Chemistry at Oxide Surfaces* Cambridge University Press 1996 Great Britain

[3] P. A. Cox, *Transition metal oxides*, Clarendon Press, Oxford (1995).

[4] F.C Voogt, *NO_2-assisted molecular beam epitaxy of iron oxide films*, PhD. thesis, Department of Chemical Physics and Nuclear Solid State Physics, University of Groningen, The Netherlands, (1998)

[5] G. Rijnders, G. Koster, D.H.A. Blank, and H. Rogalla, Appl. Phys. Lett. **70** (1997) 1880

[6] G. Koster, G. Rijnders, D.H.A. Blank, and H. Rogalla, Appl. Phys. Lett. **74** (1999) 3729

[7] Hans Lüth, *Surfaces and Interfaces of Solids*, Springer-Verlag, Heidelberg (1993)

[8] W. Braun *Applied RHEED*, Springer, Berlin (1999)

[9] T. Gotoh, S. Murakami, K. Kinosita, J. Phys. Soc. Jpn. **50**, 2063 (1981)

[10] S. Peacor and T. Hibma, Surf. Science, **301**, 11-18 (1994)

[11] T. Hibma *Viewall64.pro*, data collection and analysis program written in IDL 6.0

[12] K-N. Tu, J.W. Mayer, L.C. Feldman, *Electronic Thin Film Science for Electrical Engineers and Material Scientists*, New York (1992)

[13] M.P. Seah and W.A. Dench, Surf. Interface Anal. **1**, 2 (1979).

[14] B. W Dodoson and J Y. Tsao, Appl. Phys. Lett. **51**, 1325 (1987)

[15] G. J Whaley and P. I Cohen, Appl. Phys. Lett. **57**, 144 (1990)

[16] Anthony R. West, *Solid State Chemistry and its Applications*, John Wiley & Sons (1985)

[17] I. Sebastian, T. Bertrams, K. Meinel, H. Neddermeyer, Faraday Discuss., 129, **114** (1999)

[18] I. Sebastian, H. Nedermeyer, Surf. Sci., 771, **454** (2000)

[19] I. Sebastian, M. Heiler, K. Meinel, H. Neddermeyer, Appl. Phys. A, 525, **66** (1998)

[20] I. Sebastian, M. Heiler, K. -M. Schindler, H. Neddermeyer, Surf. Sci. 197, **541** (2003)

[21] G.C. Gazzadi, A. Borghi, A. di Bona, S. Valeri, Surf. Sci. 632, **402** (1998)

[22] S. Entani, M. Kiguchi, K. Saiki, A. Koma, J. Crystal Growth, 110, **247** (2003)

[23] R.M. Wolf, A.E.M. De Veirman, P. van der Sluis, P.J. van der Zaag, J.B.F. aan de Stegge, MRS, 23 **341**, (1994)

[24] D. Rata, *Strain-induced properties of epitaxial VO_x thin films*, PhD thesis, University of Groningen, The Netherlands, (2004)

[25] O.C Rogojanu, *Stabilizing CrO by epitaxial growth*, PhD thesis, University of Groningen, The Netherlands, (2002)

[26] F.M.F de Groot, *X-ray absorption of transition metal oxides*, PhD thesis, Nijmegen University, The Netherlands, (1991)

[27] J. Park, *Electron spectroscopy study of 3d transition metal oxides and metal-insulator transitions*, PhD thesis, University of Michigan, USA, (1994)

[28] F.M.F de Groot, M. Grioni, J.C Fuggle, J. Ghijsen, G. A Sawatzky, H. Petersen, PRB, **40**, 117 (1989)

[29] M. Prutton, *Surface physics*, Oxford University Press, New York, (1983)

[30] E. Guiot, *Epitaxie assistée par plasma d'oxygene de couches minces d'oxydes de fer sur α-Al_2O_3*, PhD thesis, University of Paris, (1998)

[31] S. Gota, E. Guiot, M. Henriot, M. Gautier-Soyer, Surf Science, **454**, 796 (2000)

[32] M. A Herman, Cryst. Res. Thechnol, **34**, 583 (1999)

[33] M. Klaua, D. Ullmann, J.Wulfhekel, J. Kirschner, R. Urban, T. L Monchesky, J. F Cochran and B. Heinrich PRB, **64**, 134411 (2001)

[34] M.Dynna, J. L Vassent, A. Marty, B. Gilles, J. Appl. Phys., **80**, 2650 (1996)

[35] F.M.F. de Groot, M. Abbate, J. van Elp, G.A. Sawatzky, Y.J. Ma, C.T. Chen and F. Sette, J. Phys.: Condens. Matter 2277, **5** (1993)

[36] J. van Elp, J.L. Wieland, H. Eskes, P. Kuiper, G.A. Sawatzky, F.M.F. de Groot, T.S. Turner, Phys. Rev. B, 6090, **44** (1991)

[37] P.W. Tasker, J. Phys. C **12**, 4977 (1979)

[38] P.W. Tasker, Phil. Mag. A, **39**, 119 (1979)

[39] J. Chenavas, J.C. Joubert, Solid State Commun., **9**, 1057 (1971)

Chapter 3

X-ray diffraction on thin films and multilayers

3.1 Introduction

In this section we present *ex-situ* X-ray diffraction measurements as well as their numerical simulations for epitaxial CoO and MnO thin films and multilayers.

In the first half of this chapter we show how information about thickness, strain and structure is obtained using conventional methods. The second half is devoted to the discovery of rather complicated diffuse scattering patterns near reciprocal lattice points, which are characteristic of the presence of misfit dislocations appearing in partially relaxed films of strained CoO and MnO films. Up till now such patterns have been reported in literature only in the case of semiconductors. Numerical simulations of the recorded diffracted intensity are presented, comparing a simple "block model" with more realistic models comprising the full displacement field of the misfit dislocations responsible for relaxation.

It will become clear that X-ray diffraction is not only a sensitive tool to detect order, but, if carefully used, can give insight into the nature and magnitude of disorder related to the presence of misfit dislocations in strained epitaxial layers.

3.2 X-ray diffraction versus RHEED

In the previous chapter we were mainly concerned with the characterization of surfaces of crystalline substrates and thin films by the use of electron diffraction. We have seen that for these techniques a good vacuum environment is necessary which is an advantage in the case of thin films that are reactive in air (see for example the oxidation of MnO in oxygen atmosphere 2.12). In this chapter we will mainly focus on *ex-situ* characterization of surfaces by X-rays, therefore this is a good opportunity to shortly compare the two complementary techniques.

With RHEED, diffracted electrons are easily detectable by the use of a fluorescent screen, and the small wavelength allows the visualization of a large area of the reciprocal lattice but restricts at the same time the precise determination of small differences in lattice constants. X-rays on the other hand can easily be monochromatized and the larger wavelength ($\sim$1.54 Å) allows the precise determination of the lattice constants as well as the strain state of the thin films. The coherence length, the penetration depth as well as the dynamic range for detection are higher for X-rays than for RHEED. Hence X-ray diffraction is a valuable tool for the study of thin films and multilayers as long as the films are inert or can be capped with a protective layer which prevents the deterioration of the films in contact with air. While for electrons, which interact strongly with matter, only complicated dynamical theory calculations can be used to attain insight into material properties, for hard X-rays a simple kinematical approach is in most of the cases sufficient to fit the measured diffraction spectrum because their interaction with matter is weak.

Table 3.1 presents an overview of the two techniques.

Property	Electrons in RHEED	X-rays in diffractometer
Interaction	Strong	Weak
Dynamic range	10^3 (CCD)	10^6
Focusing	Yes	Yes
Wavelength (λ (in Å))	0.1-0.04	1.54 (Cu)
Environment	vacuum	vacuum or air
Theory	Dynamic	Kinematic

Table 3.1: Overview of similarities and differences between the RHEED and X-ray diffraction techniques.

3.3 X-ray diffraction by crystals

The interaction of hard X-rays with matter happens through the scattering by the electrons of the atomic constituents. Assuming the dipole approximation, the scattered wave with amplitude A_1 from an electron at position r_e observed at a distance R_0, is given by the formula:

$$A_1 = A_0 \frac{e^2}{mc^2} \frac{1}{R_0} e^{[i(k_f - k_i)r_e]} \tag{3.1}$$

where e is the charge, m is the mass and k_i and k_f are the incident and the scattered wave vectors respectively. The quantity $e^2/mc^2 \sim 2.85 \times 10^{-15}$ m is the Thomson scattering length (also called the classical radius of the electron: its small value is the reason why the interaction is so weak) and the $1/R_0$ represents the decay of the scattered wave with distance. Going through all the steps of the theory presented in many general textbooks [1, 3, 4] where first the interaction of a single electron, than that with an atom and finally with all the atoms in a unit cell are considered one can derive a formula for the amplitude of the wave scattered by a crystal of the form:

$$A_{cryst} = A_0 \frac{e^2}{mc^2} \frac{1}{R_0} F(q) \sum_{n_1=0}^{N_1-1} \sum_{n_2=0}^{N_2-1} \sum_{n_3=0}^{N_3-1} \exp\left(i \overrightarrow{q} \cdot (n_1 \overrightarrow{a}_1 + n_2 \overrightarrow{a}_2 + n_3 \overrightarrow{a}_3)\right) \tag{3.2}$$

where $\overrightarrow{q} = \overrightarrow{k}_f - \overrightarrow{k}_i$ is the momentum transfer and in the case of elastic scattering $| \overrightarrow{k}_i | = | \overrightarrow{k}_f | = 2\pi/\lambda$, and

$$F(q) = \sum_{j=1}^{N_c} f_i(q) \exp(i \overrightarrow{q} \cdot \overrightarrow{r}_j) d^3r, \tag{3.3}$$

is the structure factor of the unit cell and N_c is the number of atoms in the unit cell, defined by the vectors $\overrightarrow{a}_1$, $\overrightarrow{a}_2$, $\overrightarrow{a}_3$, all atoms of the unit cell having their own atomic scattering factors $f_i(q)$. Setting now the size of the crystal equal to 0 in the direction of $\overrightarrow{a}_2$ and $\overrightarrow{a}_3$ it is worthwhile to study what kind of diffraction pattern one gets from a simple one dimensional crystal. In order to get an idea of how the scattered intensity would look like, one must focus on the modulus squared of the only sum remaining from equation 3.2. Disregarding for the moment the quantity F(q), we get:

$$|S_{N_1}(q_1 a_1)|^2 = \left| \sum_{n_1=0}^{N_1-1} \exp(i q_1 a_1 n_1) \right|^2 = \left| \frac{1 - \exp(i q_1 a_1 N_1)}{1 - \exp(i q_1 a_1)} \right|^2 = \frac{\sin^2(N_1 q_1 a_1/2)}{\sin^2(q_1 a_1/2)} \tag{3.4}$$

This function, called *"N-slit interference function"* (due to it's use in optics), is plotted in Figure 3.1 in the case of N_1=10, for $q_1 a_1 \in [-1, 8]$. This function is responsible for many of the features that we will deal with in the present chapter, such as the Scherrer formula and the intensity oscillations close to the Bragg peaks of perfect crystalline films [4]. In the limit of a very long chain of atoms (N_1 large) this function transforms into a series of delta functions centered at multiples of 2π. In reality though, the crystal is not infinite but it has to end somewhere. If one would only consider a free standing monolayer, namely N_1=1, equation 3.4 gives $|S_{N_1=1}(q_1 a_1)|^2 = 1$. This would mean that the diffraction from the monolayer will be independent of q_1 and will take on a finite, constant value whereas in the other two directions the Laue conditions are satisfied. In reciprocal space this will produce rods that are perpendicular to the surface of the monolayer.

In reality the N_1 is larger than 1 and finite, therefore in this case the diffraction profile transforms into the so-called *crystal truncation rod*. Considering for N_1 a high, finite value, the numerator of equation 3.4 is a rapidly varying function of q_1 and therefore in a real experiment it is smeared out. In this limit the diffracted intensity will be inversely proportional to $\sin^2(\overrightarrow{\mathbf{q}} \cdot \overrightarrow{\mathbf{a}_1})$. This means that the diffracted intensity is not 0 between the $(00l)$ Bragg points, but [2]:

$$|S(\overrightarrow{\mathbf{q}} \cdot \overrightarrow{\mathbf{a}_1})|^2 = \left| \sum_{j=0}^{\infty} \exp(-(i\overrightarrow{\mathbf{q}} \cdot \overrightarrow{\mathbf{a}_1} + \epsilon) \cdot j) \right|^2 \tag{3.5}$$

where ϵ is a small quantity that describes the absorption from one layer and therefore the above formula gives only significant value close to the Bragg peaks and does not diverge to ∞ where the Bragg condition is satisfied.

Therefore the diffracted wave from a crystal that is built up by $N_1 \times N_2 \times N_3$ unit cells using the *N-slit interference functions* is:

$$A_{cryst} = A_0 \frac{e^2}{mc^2} \frac{1}{R_0} F(q) S_{N_1}(q_1 a_1) S_{N_2}(q_2 a_2) S_{N_3}(q_3 a_3) \tag{3.6}$$

the diffracted intensity being the absolute square of this amplitude ($I_{cryst} = | A_{cryst} |^2$). In the limit of a *large crystal* there will only be nonzero diffracted intensity if the Laue conditions are satisfied, or if:

$$\begin{aligned} q_1 \cdot a_1 &= 2\pi h \\ q_2 \cdot a_2 &= 2\pi k \\ q_3 \cdot a_3 &= 2\pi l \end{aligned} \tag{3.7}$$

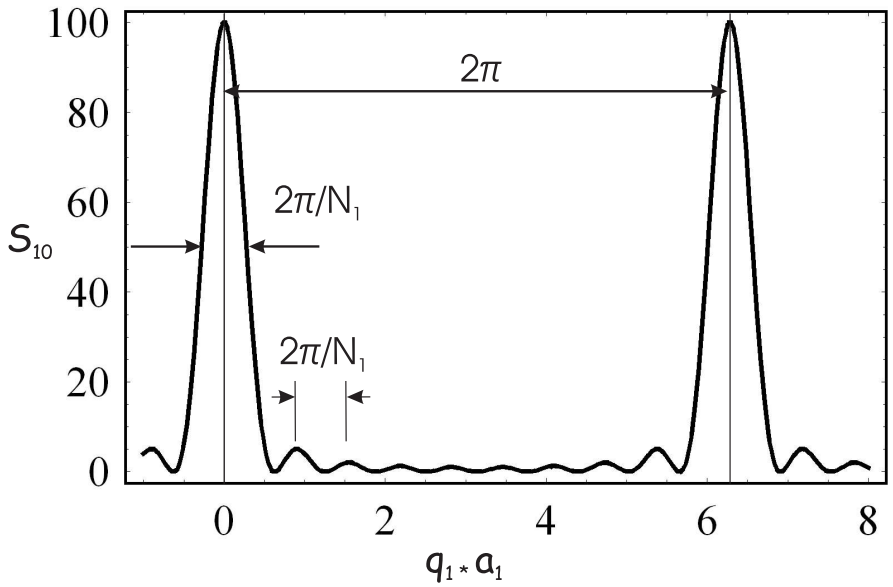

Figure 3.1: Graphical representation of Equation 3.4 with N_1=10. The separation of the main peaks is 2π. It is of major importance that the width of this main peak is inversely proportional with N_1, namely with the number of atoms in the one-dimensional chain and that besides the main peaks subsidiary maxima exist, the spacing of which is $2\pi/N_1$.

where *h, k, l* are the Miller indices. The conditions can be simultaneously satisfied if $\overrightarrow{q}$ is equal to a reciprocal lattice vector $\overrightarrow{g} = h \cdot \overrightarrow{g}_1 + k \cdot \overrightarrow{g}_2 + l \cdot \overrightarrow{g}_3$ where $\overrightarrow{g}_1 = 2\pi \frac{\overrightarrow{a}_2 \times \overrightarrow{a}_3}{\overrightarrow{a}_1 \cdot (\overrightarrow{a}_2 \times \overrightarrow{a}_3)}$ and similarly $\overrightarrow{g}_2$ and $\overrightarrow{g}_3$, by cyclic permutation. Because epitaxial films studied here are extremely thin in comparison with the penetration depth of X- rays, besides the diffracted intensities originating from the films, an intense peak as a result of the diffraction from the substrate will always be visible. Fortunately however this substrate peak will appear usually at a different position in reciprocal space.

Additionally to the crystallographic information derived from X-ray diffraction there is one other, simple, but very useful application one can profit from by the use of well focused, monocromatic X-rays, namely the so called reflectivity curve. The reflectivity measurements are possible due to the contrast in electronic density between two layers (or many in the case of multilayers) lying on top of each other. Due to the interference between the X-ray beams scattered from the different interfaces one is able to record a scan consisting of

so-called thickness fringes i.e. intensity maxima corresponding to constructive interference and minima due to destructive interference. The position of these features is directly related to the thickness of the layers.

In the hard X-ray region the refractive index n of the materials is smaller than unity. This is a consequence of the repeated resonant behavior of many possible electronic transitions up to the X-ray region. The refractive index can be represented as follows:

$$n = 1 - \delta + i\beta \tag{3.8}$$

where the two real numbers δ and β, have the following material and wavelength dependencies:

$$\begin{aligned} \delta &= \frac{2\pi\rho_a f^0(0) r_0}{k^2} \\ \beta &= \frac{\mu}{2k} \end{aligned} \tag{3.9}$$

δ is a reduction due to the binding of the electrons in the atom, which is proportional to the electron density ($\rho_a \cdot f^0(0)$) of the material and inversely proportional with the square of the wavevector k. The imaginary part is related to the absorbtion of X-rays, β being proportional with the absorbtion coefficient. The refractive index is directly related to the real and imaginary components of the dispersion corrections (f' and f") in the following way:

$$n = 1 - \frac{2\pi\rho_a r_0}{k^2} \cdot (f^0(0) + f' + i \cdot f'') \tag{3.10}$$

where ρ_a is the atomic density, $f^0(0)$ is the number of electrons in the atoms and f' and f" are related to each other through the Kramers-Kroning relations. Using the values for f' and f" tabulated in crystallographic tables [6] and calculating the overall electron density of the individual layers and the substrate from the knowledge of the lattice parameters and the atomic constituents, one can have a good starting point for the refractive index profile responsible for the shape of the reflectivity curve. The reflectivity from a slab of material can be calculated using the following equations relating the angular dependence of the reflected X-rays through the phase factor p to the layer properties such as electron density, roughness and thickness:

$$\begin{aligned} R = |r|^2 &= \left| \frac{\tilde{r}_{01} + \tilde{r}_{12} p^2}{1 + \tilde{r}_{01}\tilde{r}_{12} p^2} \right|^2 \\ \text{with} \qquad \tilde{r}_{ij} &= r_{ij} \cdot \exp\left(\frac{-k^2 \sigma_j^2 \sin\alpha_i \sin\alpha_j}{2} \right) \end{aligned}$$

$$\text{and} \qquad r_{ij} = \frac{\alpha_i - \alpha_j}{\alpha_i + \alpha_j} \tag{3.11}$$

where the α_i and α_j are related through the generalized Snell equation

$$n_i \cos \alpha_i = n_j \cos \alpha_j \tag{3.12}$$

and p^2 being given by:

$$p^2 = \exp(i2k \cdot \sin \alpha_1 \cdot \Delta) \tag{3.13}$$

where Δ represents the thickness of the layer and σ_i represents the roughness parameter of the i'th interface. In Figure 3.2 we show two reflectivity curve simulations of a 150 Å and 400 Å layer of CoO on a gold (upper graph) and a MgO substrate (lower graph) respectively. At small angles one can see that the reflected intensity in the case of Au substrate decreases in two steps which for the MgO substrate only one decrease is discernable. This difference clearly illustrates the effect of electron density. Gold being a heavy element, has a electronic density ~ 2.5 times higher than the electronic density of CoO, whereas MgO, being composed of light elements, has an electronic density which is lower than the one of CoO. Making an analogy with the visible light escaping from an optically denser medium (such as water) into air there will be a critical angle under which the total reflection phenomenon inhibits the emergence of light from the water. One has the same phenomenon for the X-rays with condensed matter. Because the refractive index inside the material is now smaller than the one of air ($n_{air} = 1$), there will be an angle under which the X-rays are totally reflected. This angle is called the critical angle and it is dependent on the electronic density as:

$$\alpha_{crit} = \sqrt{\frac{4\pi\rho_{el}r_0}{k^2}} \tag{3.14}$$

The electronic density ρ_{el} is the only material property appearing in this equation, thus a good fit of the reflectivity curve can give information about the stoichiometry of the layer. This is a commonly used technique in the case of novel films with unknown stoichiometry [5].

Another characteristic feature of the reflectivity curve is the so-called thickness or Kiessig fringes also pointed out in Figure 3.2. The period of these fringes gives an immediate approximate value of the thickness d, the separation of two maxima being inversely proportional with d (for small angles $d = \lambda/2 \cdot \Delta\alpha$ where $\Delta\alpha$ is the difference in angular position between two consecutive maxima or minima). More sophisticated methods of simulating

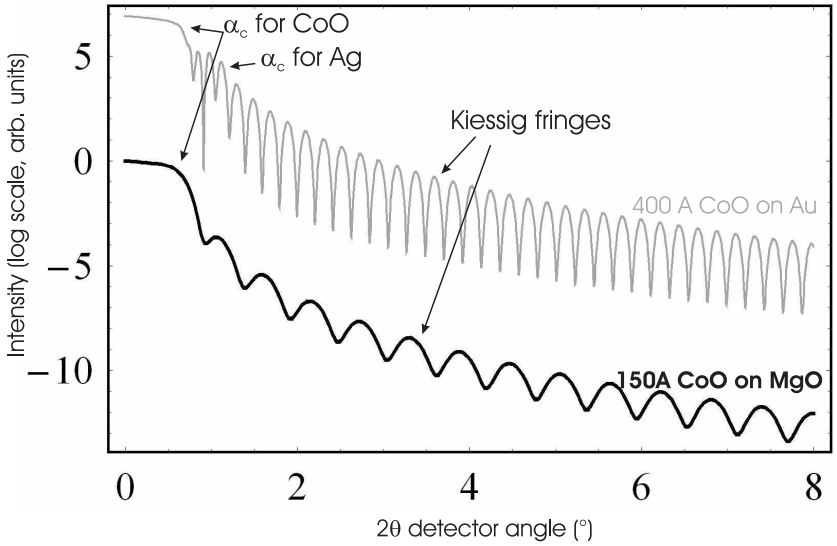

Figure 3.2: Simulated reflectivity curve for (top) 400Å CoO on a Au substrate. The gold having a high electronic density, its critical angle α_{crit} is higher than the one for the CoO over-layer and therefore both can be visible. (bottom) 150 Å of CoO on MgO, where only the critical angle of the CoO is observable. The reflected intensity oscillations are called Kiessig fringes and are a consequence of the interference of X-rays reflected from the top and the bottom of the thin film

the reflectivity curves give more accurate values for the thickness and give also information about the size of the inter-layer roughnesses (σ_i) or possible correlations in height fluctuations [3]. Reflectivity measurements can also be done for multilayers and the approximate formula describing the phenomenon was given by Parratt [3, 20]. In Section 3.11 an example of a measurement and a simulation is presented. To give a numerical picture for the reader, Table 3.2 shows the numbers used for the simulation of the reflectivity curve in Figure 3.2. The values for f' and f" were taken from [6] and are specific for Cu Kα radiation.

A last important X-ray diffraction measurement method which is worth mentioning before turning to the experimental results in this chapter, is the so called Reciprocal Space Mapping (RSM). This mapping is done by transforming a series of one dimensional radial scans taken with slightly different offsets, into a 2 dimensional image. In Figure 3.3 the execution of such a RSM is shown. The radial scans are so called 2θ-ω scans (2θ is the detector angle,

Parameter	O	Mg	Co	Au	MgO	CoO
Z=$f^0(0)$	8	12	27	79	20	35
f'	0.0492	0.1719	-2.464	-5.096	0.2211	-2.4148
f"	0.0322	0.1771	3.608	7.297	0.2093	3.6402
σ_1, σ_2	-	-	-	$1{\cdot}10^{-10}$	$1 \cdot 10^{-10}$	$1 \cdot 10^{-10}$
Re(n)	-	-	-	0.999954	0.999988	0.999982
-Im(n)$\cdot 10^{-7}$	-	-	-	45.409	1.1942	19.953
α_{crit}	-	-	-	0.541°	0.262°	0.339°

Table 3.2: Parameters used for simulation of the reflectivity curves in Figure 3.2

and ω is the angle between the sample and the incident beam), whereby only the *length* of the momentum transfer vector ΔK is changed but not the direction in the reciprocal space. The *omega* scans are scans whereby the direction of ΔK is changed but not the length. By combining these two motions and recording the scattered intensity as a function of these two angles (ω and θ), one can produce a 2 dimensional map of the spanned reciprocal space. The transformation of the recorded angles (2θ and ω) to $K_\perp$ and $K_\parallel$ is done using the following simple transformations:

$$\begin{aligned} K_\perp &= \Delta K \cdot \cos(\delta) \\ K_\parallel &= \Delta K \cdot \sin(\delta) \end{aligned} \tag{3.15}$$

where $\delta = \theta - \omega$ is called the *offset* and $\Delta K = 2k_0 \cdot \sin(\theta)$. Reciprocal lattice maps around non-specular Bragg peaks will prove to be useful measurements in determining the relaxation state of strained layers and they also serve as tools for *understanding* diffuse scattering from partially relaxed epitaxial layers.

3.4 Measurement setup

The measurement setup used to collect diffraction data for the present thesis was a Philips X'pert four axes diffractometer equipped with primary and secondary optics suited for epitaxial thin film analysis. In this section we will present some of the accessories that are specific for this configuration.

X-rays characteristic of Copper are generated by a PW-3373/00 (Cu LFF DK 127355) X-ray tube operated at U_{acc}=40 kV and I_{emis}=40 mA in the line focus mode, the beam size being $\sim$ 12 mm $\times$ 0.4 mm. This beam is made

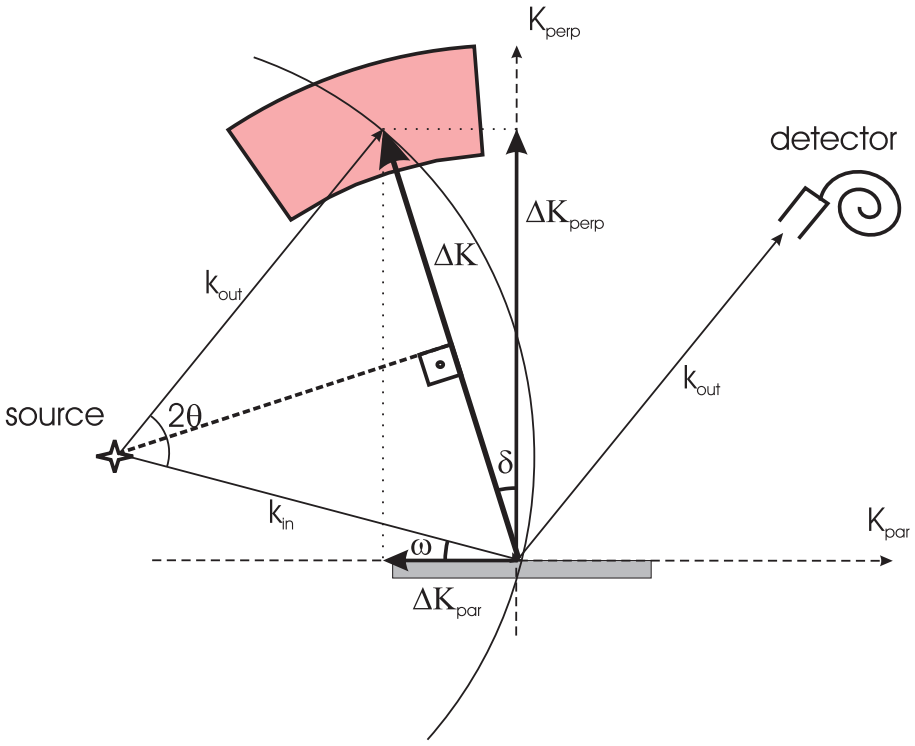

Figure 3.3: Reciprocal Space Mapping with X-rays. By a controlled motion of the sample and detector one can span the shaded area with the momentum transfer vector (ΔK), recording the diffracted intensity. The collected data are plotted in a 2D graph where the color of every pixel will represent the diffracted intensity. Usually the horizontal axis will correspond to the $K_{\parallel}$ and the vertical axis to the $K_{\perp}$ directions.

parallel (horizontal divergence $\sim 0.05°$) and monochromatic by the hybrid X-ray mirror sketched in Figure 3.4. The spectral range of this monocromator is larger than the so-called four-crystal monochromator but delivers a much more intense beam. Because the K_{β} component is almost completely suppressed by the monochromator, the remaining beam is monochromatic composed mainly of $K_{\alpha 1}$ (λ=1.54059 Å) the $K_{\alpha 2}$ radiation being suppressed to less than 0.1 %. The divergence slit commonly used was the 1/8 ° fixed slit which produced a beam of 12 × 0.3 mm after the monochromator a vertically divergent and horizontally parallel beam. After diffraction or reflection from the sample follows the secondary optics. Here the antiscatter slit is meant to reduce the amount of scattered X-rays by other objects than the sample itself (usually

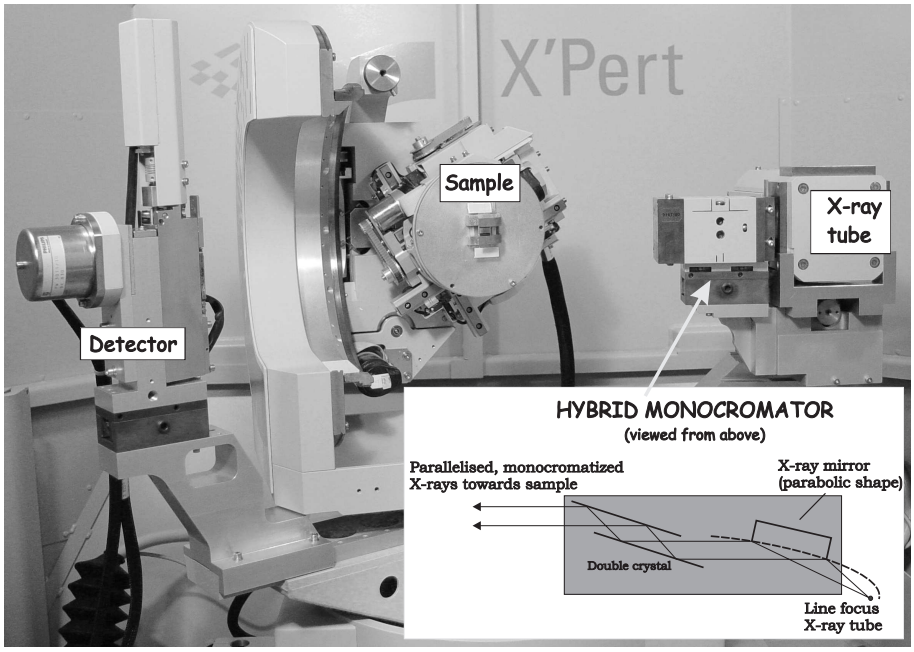

Figure 3.4: Picture of the inside of the Philips X'pert diffractometer. The X-ray source is fixed, the sample can be rotated around the vertical (ω), horizontal (ψ) and around the azimuth (ϕ) axes. The detector at the left of the picture rotates around the vertical axis positioned at the center of the sample (2θ). Also presented is a schematic drawing of the hybrid monochromator if the mirror is viewed from above.

taken to be 1/4 °). The next important element is the 0.04 rad Soller slit consisting of horizontally closely spaced metal foils, which reduces the vertical divergence of the scattered beam to some extent. Although it reduces the intensity by a factor of ~ 2, the noise level is also drastically reduced. The last element positioned before the detector is the Programmable Receiving Slit, which is a slit that can be controlled by software and is meant to define the resolution of the apparatus (since the current configuration contained no analyzer crystals). The detector used to count the number of photons at a certain detector angle (2θ) is a proportional detector, fabricated as a sealed chamber filled with a xenon/methane gas mixture. These detectors have a 99 % linearity range of 0-500,000 cts/s and a 84 % efficiency for Cu radiation [8, 9].

3.5 Strain relaxation in epitaxial layers

Before entering into the details of our experimental findings on the relaxation of epitaxial transition metal oxides on different substrates and buffer layers it seems appropriate to first give a flavor of more than 50 years of research committed to reveal the intricate mechanisms through which homogeneous layers relax the epitaxial strain imposed by the substrate. Obviously, since this thesis is not devoted to conceive a new, more precise theoretical description of relaxation, we will just present what we think are the most important details in some of the easily comprehensible theories developed throughout the years.

This research area developed so rapidly mostly because of the advances in semiconductor industry in the direction of manipulation of electronic properties of thin films deposited on mismatched substrates. These developments required quantitative theories relating values for the strain in these films with known quantities such as thickness, mismatch and elastic constants. The theoretical research started in year 1949 with the work of F.C. Frank and J.H. van der Merwe [10] who developed their original equilibrium theories which showed that only below a certain critical thickness the film will accommodate the mismatch despite the strain in the film (see also [12]). Layers having thicknesses above this critical value relieve their strain by formation of misfit dislocations.

The theory named after their discoverers Frank-van der Merwe usually gives an underestimate of the critical thickness. Matthews and Blackeslee [11] came up with a more realistic formula for the thickness dependent strain based on the energy minimization of the sum of the elastic energy of the film and the energy of an edge dislocation. This formula is also designated after their names (M-B model):

$$\mid \epsilon(h) \mid = \frac{G_s b}{(G_s + G_f) \cdot 4\pi(1+\nu)h} \cdot [\ln(\frac{h}{b}) + 1], \tag{3.16}$$

for layers having the dislocation in the interface plane, and

$$\begin{aligned} \mid \epsilon(h) \mid \;\; = \;\; & \frac{(1-\nu)}{2G_f h \cos(\lambda)(1+\nu)} \cdot \\ & \cdot \left[\frac{G_f G_s b(1-\nu\cos^2(\alpha))}{2\pi(G_f+G_s)(1-\nu)} \cdot \left[\ln(\frac{h}{b}) + 1 \right] + \sigma \sin(\alpha) + \frac{\gamma h}{b\cos(\phi)} \right] \end{aligned} \tag{3.17}$$

assuming the more general case of dislocations, *not* lying in the interface plane,

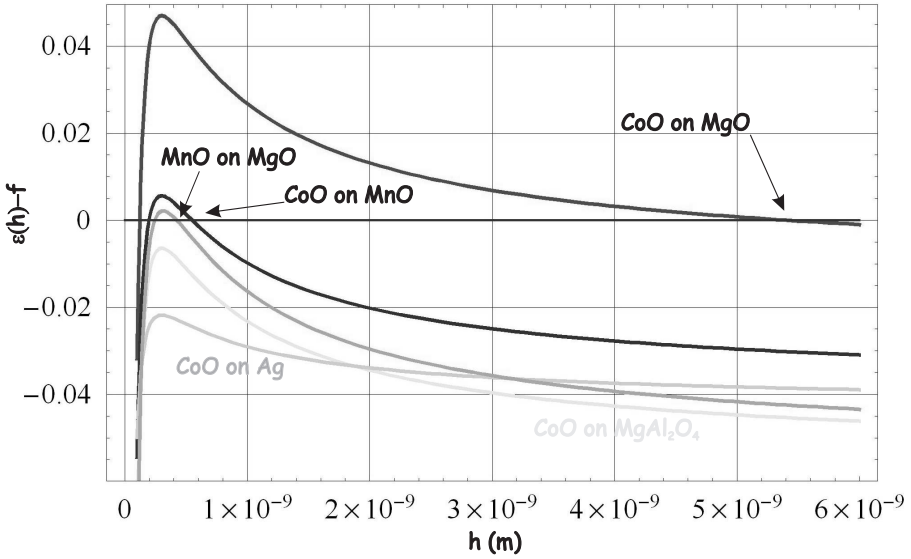

Figure 3.5: Determination of critical thickness from Equation 3.17 as explained in the text. For some cases the curve does not cross the y=0 line and therefore, the mismatch is too high for any nonzero critical thickness. In this case dislocation are supposed to appear instantaneously in the first monolayer. This is in reality not true as explained further in the text, because for very thin films one must redefine the core energy of the dislocation.

where $\epsilon(h)$ is the thickness dependent strain, G_s and G_f are the shear modulus for the substrate and the film respectively, α is the angle between the dislocation line and its Burgers vector, λ is the angle between the slip direction and the line in the interface plane which is normal to the line of the intersection between the slip plane and the interface, and ϕ is the angle between the normal to the slip plane and the sample surface, σ is the surface tension of the film and γ the stacking fault energy.

We plotted the results of this prediction (eq. 3.17) in Figure 3.5 for most of the films discussed in this chapter. The critical thickness is the second intersection of the curve with the y=0 axis (pointed at by the arrows). We plotted the function $(\epsilon(h) - f_0)$ where f_0 is the coherent mismatch defined by Equation 2.5 in the previous section $f_0 = (a_{film} - a_{substrate})/a_{substrate}$. It is important to note that while the CoO is predicted to relax at ∼55 Å on an MgO substrate, it relaxes after only a few monolayers on MnO and that the mismatch is so large that one can no longer define a critical thickness for CoO

on Ag and $MgAl_2O_4$[1]. Table 3.3 contains the material parameters used for the calculation of critical thickness displayed in Figure 3.5.

Material	Lattice parameter (Å)	ν	G (N/m^2)
MgO	4.212	-	$10.13 \cdot 10^{10}$
Ag	4.09	-	$1.54 \cdot 10^{10}$
$MgAl_2O_4$	4.04	-	$6.18 \cdot 10^{10}$
MnO	4.445	0.31	$5.15 \cdot 10^{10}$
CoO	4.267	0.27	$4.85 \cdot 10^{10}$

Table 3.3: Parameters used for Figure 3.5.

Theory which takes into account also dislocation multiplication and therefore includes also the temperature and time as an important factor is the model of Dodson and Tsao [13–15]. Their model was a breakthrough towards understanding the reasons why the usual experimental data showed an increased value of the critical thickness compared to the values given by the Frank-van der Merwe and Matthews-Blackeslee (M-B) models. They propose a differential equation describing the strain relief $\gamma(t)$ of the form:

$$\frac{d\gamma(t)}{dt} = CG^2[f_0 - \gamma(t) - \epsilon(h)]^2 \cdot [\gamma(t) - \gamma_0] \tag{3.18}$$

here f_0 is the coherent mismatch, γ_0 is a dislocation source term and $\epsilon(h)$ is the residual strain at equilibrium given by:

$$\epsilon(h) = \frac{1}{4\pi} \frac{(1-\nu)\cos^2(\alpha)}{1+\nu} \frac{\ln(\frac{\xi h}{b})}{(\frac{h}{b})} \tag{3.19}$$

with $\xi \in [1, 8]$ being a parameter accounting for the core energy of the dislocation. This model predicts a more sluggish relaxation of the misfit strain.

Finally we want draw your attention to a more recent observation of K. Wiesauer and G. Springholtz [16] who pointed out that the factor ξ, which is usually taken as a constant when determining the strain with the M-B model, should in fact be considered to be thickness dependent. They also pointed out that ξ accounts for the energy of the dislocation at the dislocation core and

For the angles in Equation 3.17 we used $\alpha = \pi/2$, $\lambda = \pi/4$, $\phi = \pi/4$, specific for the edge dislocations occurring in ionic solids and $\sigma = \gamma = 0$ thus neglecting surface tension and staking faults.

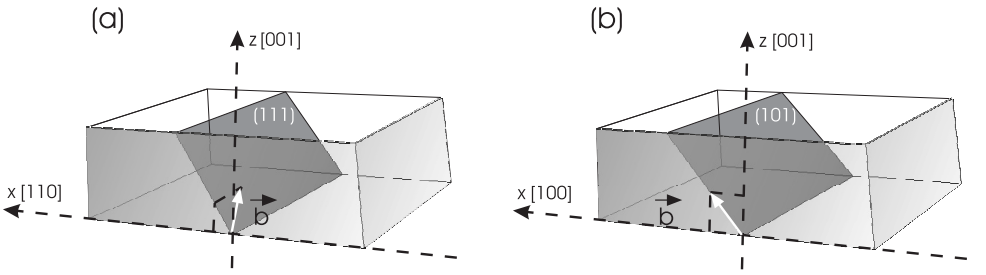

Figure 3.6: Dislocation system in the case of (a) diamond structures $\mathbf{b}=\frac{1}{2}<1\bar{1}0>\{111\}$ and in the case of (b) rock-salt structure $\mathbf{b}=\frac{1}{2}<1\bar{1}0>\{110\}$. The white arrows represent the Burgers vectors and the dark shaded areas are the slip planes.

at very low thicknesses this parameter should have different values which also depend on the material. Based on this uncertainty they treated $\xi \in [1, 8]$ as an adjustable parameter and succeed to fit quite well the strain relaxation of $PbTe_{1-x}Se_x$ layers on PbSe (001).

As a closure of this section we must mention that the kinds of misfit dislocations which relieve the strain are different for oxides and semiconductors (there are very few studies dealing with the relaxation behavior of epitaxial strain in thin films of binary oxides). To illustrate the difference, the usual dislocation system in semiconductors and in rock-salt oxides are compared in Figure 3.6. In covalent solids such as Si and Ge with strong directional bonds and having a diamond structure [17], the strain is relieved by the appearance of dislocations of the type $\mathbf{b}=\frac{1}{2}<1\bar{1}0>$, with slip planes $\{111\}$ as shown in the figure. For binary oxides the relaxation occurs though the $\mathbf{b}=\frac{1}{2}<1\bar{1}0>$ with the $\{110\}$ slip planes [17].

Because the dislocation is quite different in the two structures, the displacement field, by which the atoms of the structure rearrange, will also be different. This will become clear in the sections concerned with diffuse scattering where we will show that the two dislocation types produce a different diffuse intensity profile.

3.6 X-ray specular scans from CoO on MgO

Tn this chapter we shall refer to scans having offsets in the range of $\delta \in (-1^\circ, +1^\circ)$ (see Figure 3.3), these are the so-called specular scans. In fact the miscut, i.e. the angle between the surface normal and the (001) crystallo-

graphic direction of the substrate is responsible for the often nonzero values of δ. This miscut appears as an error in the polishing direction in the case of epi-polished substrates and as an unavoidable effect when the crystals are cleaved. Specular scans produced by scanning the size of the momentum transfer perpendicular to the substrate give information about the lattice spacing of the film and the substrate perpendicular to the surface. Figure 3.7 presents two such specular scans for two different CoO layer thicknesses epitaxially grown on MgO cleaved substrates. Both films were covered by a thin ($\sim$10 Å) MgO layer to avoid oxidation of the surface. In both figures two groups of peaks are visible and they correspond to the (002) (at $\theta \sim 21°$) and (004) (at $\theta \sim 46.5°$) reflections of the MgO and CoO FCC lattice. The absence of any other peaks than the (002) and (004) is a proof (besides the RHEED results) that the films are perfectly epitaxial. The position and the width of the peaks gives information about the $c(\neq a=b)$ value of the lattice constant and the thickness of the film. In the inserts of the upper figure intensity oscillations are observable, they appear as a consequence of the limited thickness of the film ($\sim$150 Å CoO on MgO) as debated in section 3.3, the subsidiary maxima originating from the *N-slit function* (see Figure 3.1). In the bottom figure which is a specular scan of a $\sim$450 Å CoO film, these oscillations are only vaguely visible. As we will demonstrate later in this chapter, these oscillations disappear because of the inhomogeneities of the out-of plane lattice constant, caused by the multiplication of misfit dislocations in the film.

In Figure 3.7 simulations of the scans are also presented at the bottom of the graphs as well as in the inserts (gray lines). These kinematic calculations take into account not only the complex refractive indices of the substrate and the film (see section 3.3) but also the angular dependent scattering factors of the atomic components [6, 7]. A reasonably good fit can be achieved using this kinematical approach in the case of thin (40 -210 Å) CoO films, but as one can observe in the insert of the bottom figure, these simulations do not fit the measured data at large thicknesses. This limitation is mainly due to the multiplication of the above mentioned inhomogeneities in the c lattice parameter at higher film thicknesses.

Another effect may be noticed if one compares the width of the peaks in the simulation with the experimental curve. In the case of the thin (150 Å CoO) film the width of the two are equal but in the case of the thicker (450 Å CoO) films the experimental curve has a wider (002) Bragg peak than the simulation. This is again a consequence of the inhomogeneities of the c lattice parameter and the broadening will be explained by means of diffuse scattering from networks of misfit dislocations.

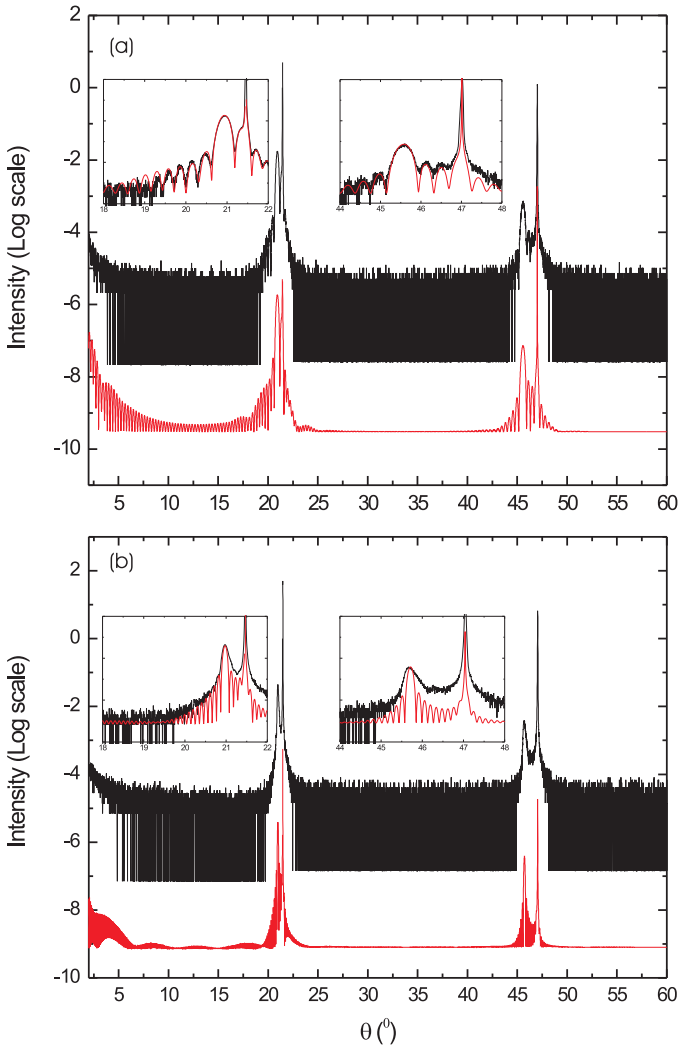

Figure 3.7: Specular scans from (a) ∼150 Å and (b) ∼450 Å CoO films on MgO (001) together with the simulation (below) using a kinematical approach. The inserts show a magnification of the (002) and (004) Bragg peaks. The thin film can be almost perfectly fitted with the simple approach but the thick film has broader Bragg peaks than the simulation and the expected thickness fringes are mostly vanished.

In the following we show how the *out-of-plane* lattice parameter c, determined from these types of specular scans, depends on the CoO layer thickness. Figure 3.8 shows this dependence for films having increasing thicknesses. The dashed line represents the bulk value of the lattice constant for CoO, namely 4.267 Å. Because of the compressive strain of the substrate this value is not reached for the thickest films we prepared (860 Å). Therefore up to a value of ∼350 Å the c parameter stays constant at a value of 4.305 Å. Knowing the c parameter and using the result (discussed later) that the in-plane lattice parameter of CoO coincides with a_{MgO}=4.212 Å (coherent growth) one can determine the Poisson ratio of CoO, defined as the negative ratio between the lateral and longitudinal strain under uniaxial longitudinal stress. In our case of biaxial stress:

$$\epsilon_{\perp} = -\frac{2 \cdot \nu}{1 - \nu} \cdot \epsilon_{\parallel} \tag{3.20}$$

where $\epsilon_{\perp} = (c - a_{CoObulk})/a_{CoObulk} \approx 9 \cdot 10^{-3}$ and $\epsilon_{\parallel} = (a_{MgO} - a_{CoObulk})/$ $/a_{CoObulk} \approx 1.3 \cdot 10^{-2}$, From this we determine the Poisson ratio for CoO: $\nu_{CoO} \approx 0.27$.

The out-of-plane lattice constant c remains 4.305 Å up to a thickness of 350-400 Å , plastic relaxation occurs and the reduction of strain evolves through the appearance of suitable dislocations at the layer substrate interface. This will influence not only the the position of the peaks but also their shape.

The Figure 3.8 (b) shows the width of the (002) Bragg reflections measured from the specular scans of CoO films grown on MgO having increasing thickness. As explained in section 3.3 the width of the peaks should be inversely proportional with the number of monolayers. This effect is used also in interpreting the X-ray diffraction spectra from polycrystals to determine the grain size and is given by the Scherrer formula:

$$w = \frac{k \cdot \lambda}{d \cdot \cos(\theta_{Bragg})} \tag{3.21}$$

where w is the full width half maximum (in θ) of the peak, d is the thickness of the film and k is called the shape factor, in the present case of thin films taking a value of $k = 0.88$ [3].

Therefore, not only from the position in $2\theta_{Bragg}$ but also from the width of these peaks results that the critical thickness of CoO on MgO (having a misfit of $f_0 \sim 0.013$) is 350 Å. This conclusion is drawn only on the basis of the specular scans described in this section. In the following we show that off-specular scans give a different value for this critical thickness.

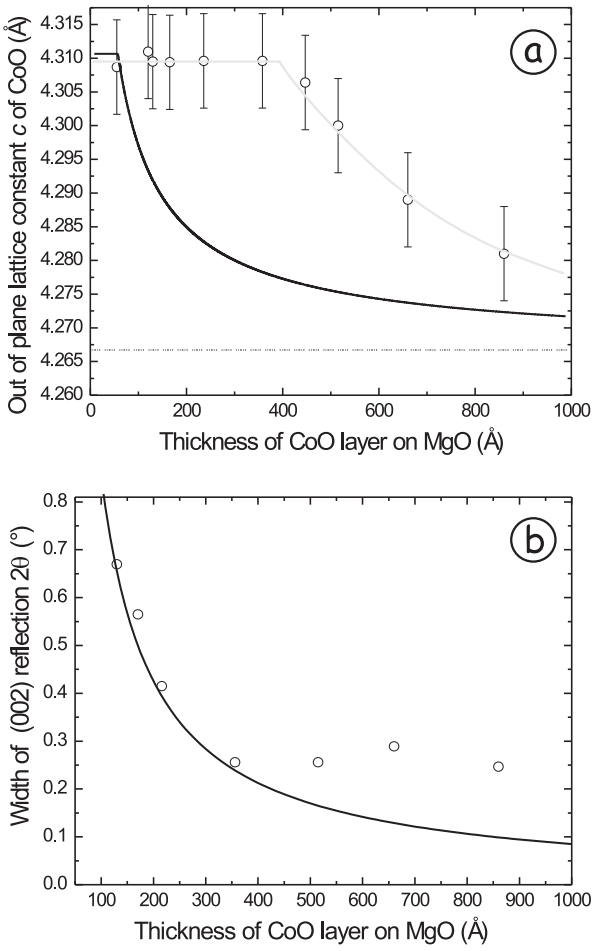

Figure 3.8: (a) The points represent the thickness dependence of the out-of-plane c lattice constant measured by means of specular scans from the position of the (002) Bragg reflection. The thick solid line gives the lattice parameter evolution as predicted by the M-B formula from Section 3.5 and the dashed line represents the bulk lattice parameter of CoO. (b) Peak width of the (002) reflections from the specular scans as a function of layer thickness (points). The drawn line is a fit using the Scherrer equation. At thicknesses higher then $\sim$360 Å, the widths are considerably larger than expected, the cause being the diffuse scattering produced by the dislocations.

3.7 Reciprocal space maps from CoO on MgO

In the following we will be concerned with the type of scans described in detail in Section 3.3. These **R**eciprocal **S**pace **M**aps (RSM) can be produced around specular or non-specular reflections. In the present section we will only present off-specular RSM's and deal in more detail with the specular RSM's in the following section.

In the case of coherent growth, the in-plane lattice parameter of the film will be coincident with the one from the substrate, whereas the out-of-plane lattice parameter will increase according to equation 3.20. In reciprocal space this is equivalent with having the *in-plane* Bragg reflections of the film at the same position as the substrate but at a displaced position in the *out-of-plane* direction. Figure 3.9 shows a schematic picture of the off-specular RSM's for the case of CoO on MgO. From the positions of the intensities in reciprocal space one can calculate both the out-of-plane and in-plane lattice parameters. Figures 3.10 and 3.11 show RSM's around the (224) reflection of CoO and the MgO substrate measured from films of different thicknesses. The axes in these maps are in so-called **R**eciprocal **L**attice **U**nits (RLU) which are reciprocal space units normalized to the theoretically achievable maximum distance from the origin for a certain X-ray wavelength. The normalization constant is equal to the diameter of the Ewald sphere ($2k_0=2\cdot(2\pi)/\lambda$). At low thicknesses (125 Å) the growth seems to be coherent, and the off-specular Bragg reflection is situated straight below the substrate reflection as expected from the previous reasoning. This is not the case anymore for thicker films and starting from a thicknesses of 170 Å of CoO, there appears to be extra intensity extending outside this value in the $k_{\|}$ direction as can be seen in the bottom RSM in Figure 3.10 (b). Although from the data presented in Figure 3.8 we deduced that the growth remains coherent up to 356-400 Å, this RSM shows evidence for the contrary. Therefore, the two measurements i.e. specular scans and RSM around off-specular Bragg peaks seem to give inconsistent results. These differences substantiate that Reciprocal Space Mapping is a more sensitive tool for detecting the appearance of the relaxation of thin films, than the simple specular scans.

Figure 3.11 presents RSMs of thicker samples. Here one observes that with increasing thickness the maxima of the intensity distribution moves away from the homogeneously strained position towards the relaxed position situated at $k_{\perp}=0.722$, $k_{\|}=0.5106$ for relaxed CoO in units of $2k_0$. This intensity distribution is produced by the dislocations which multiply with increasing thickness [18–22, 24, 31] and we call it the dislocation induced diffuse scattering.

One would obviously like to quantify, in some manner, the peak position

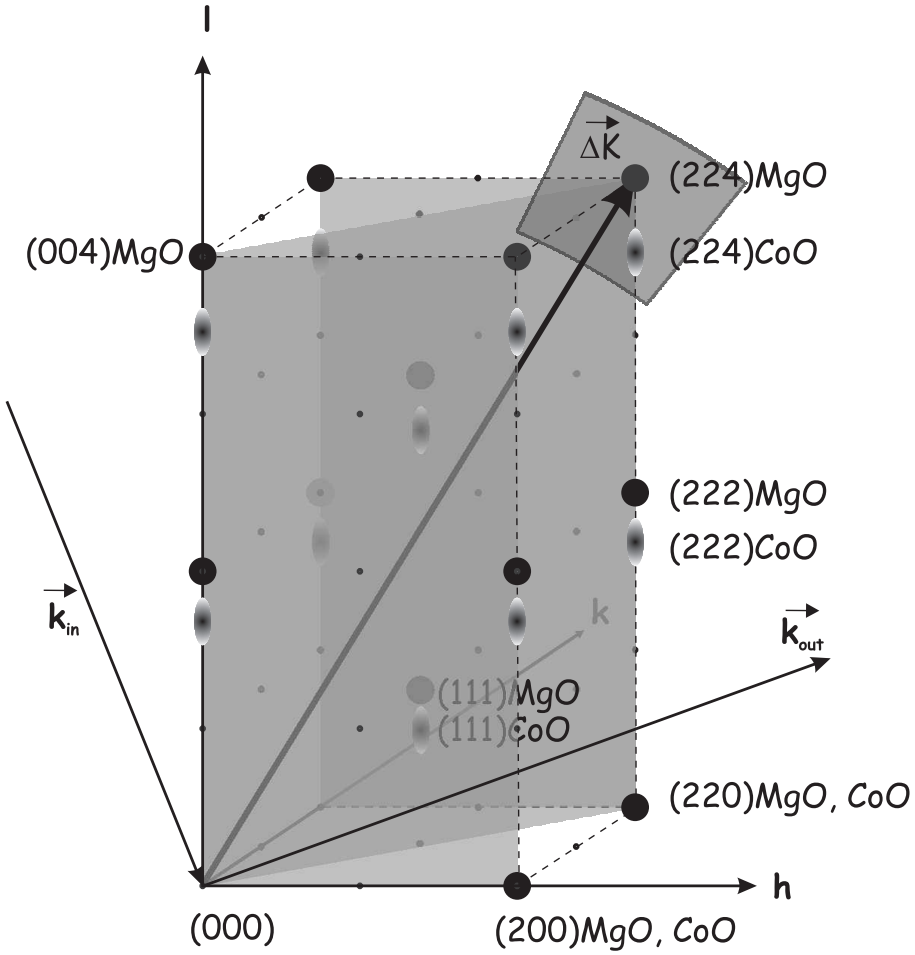

Figure 3.9: Schematic representation of the RSM for off-specular reflections of CoO on MgO. Due to the compressive strain, the c parameter of the CoO will increase, which corresponds to a decrease in the vertical direction in the reciprocal space. The unrelaxed CoO would have its (hkl) reflection straight below the MgO reflections, whereas the relaxed CoO would produce the diffracted intensity to be situated along the X-ray momentum transfer ΔK. The surrounding of the (hkl) reflections of the MgO and CoO is the RSM described in section 3.3.

and the intensity distributions of these reflections. One way of doing so is to select the intensity from the rectangular area displayed in Figure 3.11 and to determine the position of the maxima ($k_\perp$, $k_\parallel$) of the integrated intensity in

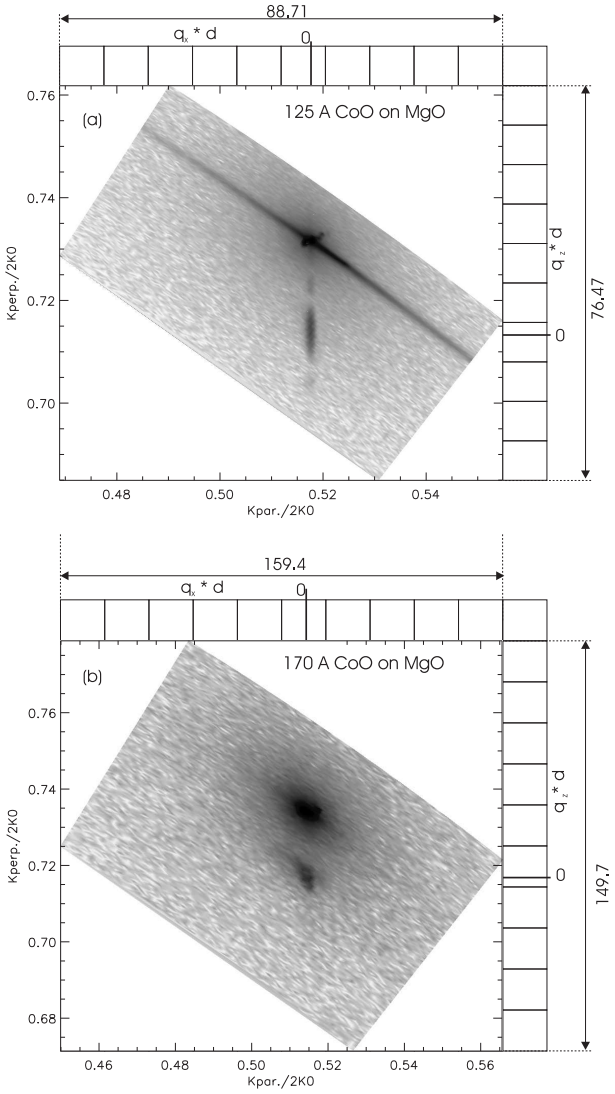

Figure 3.10: Area scans around the (224) Bragg reflections of CoO and the substrate MgO measured for samples of different CoO thicknesses. As explained in the text and schematically in Figure 3.9, the thin films which grow homogeneously on the substrate will have their Bragg reflection straight below the substrate peak. In the upper picture an example of this behavior is shown (125 Å CoO on MgO). At a thickness of 170 Å (b) the Bragg reflection of the film moves towards the relaxed bulk value. The intensity scale (the darkness of the pixels) is logarithmic because of the high intensity ratio between the scattering from the substrate and overlayers.

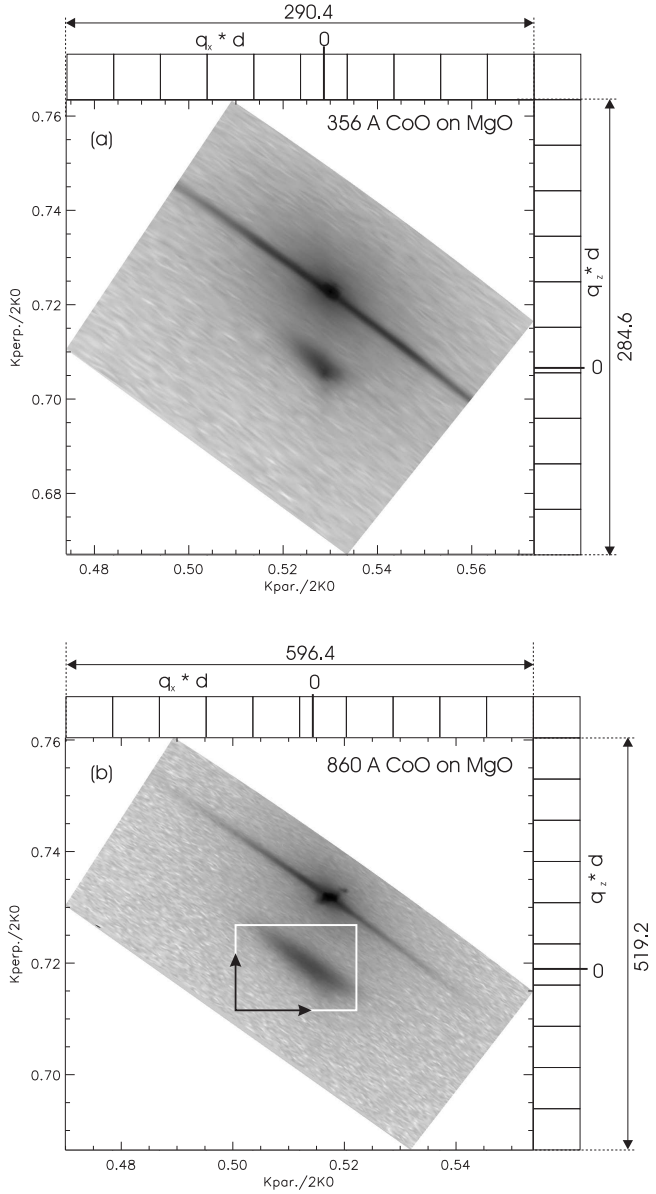

Figure 3.11: Like the previous picture but with higher thicknesses of the films. According to the specular scans 3.8 (a) the layer responsible for the upper graph is still in the unrelaxed state, which is obviously not the case from this figure. The bottom figure is a RSM from the thickest CoO film grown on MgO. The rectangular box around the CoO (224) reflection is the area from which we determined the lattice parameters as explained in the text.

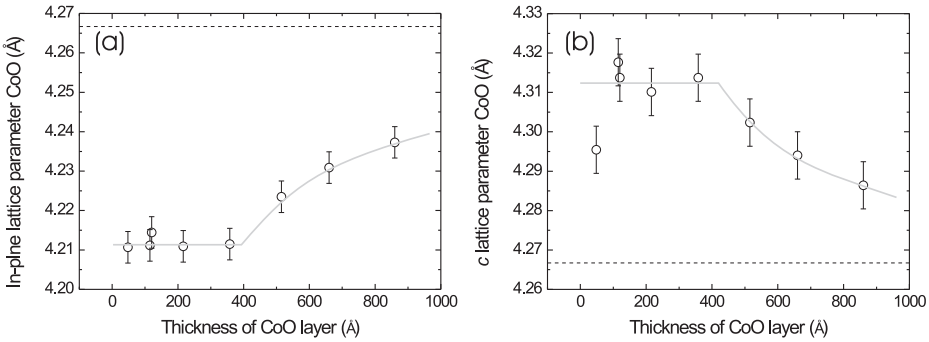

Figure 3.12: Lattice parameters measured from the position of the maxima of the integrated intensity along the $k_{\parallel}$ and $k_{\perp}$ of the CoO (224) reflections on MgO. The data was corrected by shifting the values such that the MgO (224) is situated at it's theoretical position. This was necessary due to the occasional misalignment caused by the surface miscut.

the directions indicated by the arrows. The lattice parameters obtained in this way are shown in Figure 3.12. Although the values of the out-of-plane lattice parameter are much more scattered, they compare well with the values already discussed in Section 3.6, Figure 3.8 (a), suggesting the same critical thickness. Therefore, although visible, the diffuse intensity around these reciprocal lattice points is not intense enough to change the position of the maxima originating from the coherently strained lattice. However, since the critical thickness is defined as the thickness at which dislocations start to appear, the thickness at which this diffuse scattering appears around these off-specular spots represents the *true critical thickness* that can be determined with this technique.

We therefore can reevaluate our experimental critical thickness for CoO on MgO of being round 170 Å. As a short preliminary conclusion of this section one can say that although we could observe the diffuse scattering produced by the dislocations in the film, this intensity was not high enough to displace the measured maximum position. Therefore, the thickness at which diffuse scattering appears, is defined as being the borderline between homogeneous and relaxing regions. As a consequence, two obvious questions arise, namely:

1. Will the diffuse intensity around Bragg peaks having higher intensity such as the (002) also be higher and therefore more easily observable ?

2. Is it possible to simulate the diffuse scattering due to dislocations?

The answers to these questions will be given in the following sections.

3.8 Diffuse scattering around the (002) reflection of CoO on MgO

In this section we shall consider the first point mentioned at the end of the previous section and we will therefore search for diffuse intensity around Bragg spots having higher intensity such as the (002) reflections. These measurements can easily be done by performing RSM's around these areas in the reciprocal space. Results are shown in Figures 3.13, 3.14 and 3.15 for samples of increasing CoO thickness. As in Figures 3.10 and 3.11 the axes are in units of the Ewald sphere diameter ($2k_0$) but to the right of the RSM's also another scale is drawn, namely (q·d), a scale by which all the figures can be compared. Such a scale will become useful in the following section when we deal with the simulations of diffuse scattering.

These maps contain three important regions: the MgO substrate (002) reflection situated around ($k_\perp = 0.365, k_\parallel = 0$), the CoO film (002) Bragg reflection at ($k_\perp = 0.358$, $k_\parallel = 0$) which is very sharp in the $k_\parallel$ direction but elongated in the $k_\perp$ direction, and finally the diffuse scattering situated to the left and to the right of the film (002) Bragg peak, which is not very intense for the thinnest sample, but clearly visible for thicker samples. To the left of every RSM two intensity profiles are plotted. They represent the integrated intensity along the $k_\parallel$ from the boxes surrounded by the rectangles in Figure 3.13 (a): The continuous line corresponds to the intensity profile of the coherent part of the scattering, the broken line corresponds to the diffuse part of the scattering. The intensity scale is set to logarithmic since the intensity of the substrate peak is orders of magnitude higher than the intensity scattered by the film.

There are several features one observes. Firstly, the line scan represented by the solid line corresponding to every RSM is equal to a specular scan as discussed in Section 3.6 (see also Figure 3.7). The relaxation of the c lattice parameter of Figure 3.8 (a) can therefore be determined from such kind of RSM's. Secondly, the scans originating from the diffuse scattering (dashed box and lines) have their maxima displaced with respect to the (002) peaks originating from coherent scattering. The maxima are located at higher $k_\perp$ value which imply a lower, relaxed, c value. Thirdly, weak diffuse intensity is already present for the thinnest (130 Å) sample Figure 3.13 (a). Therefore dislocation formation already has started at this low thickness.

It is thus true that the diffuse scattering expected around higher intensity peaks is more pronounced. Defining as before the "true" critical thickness as

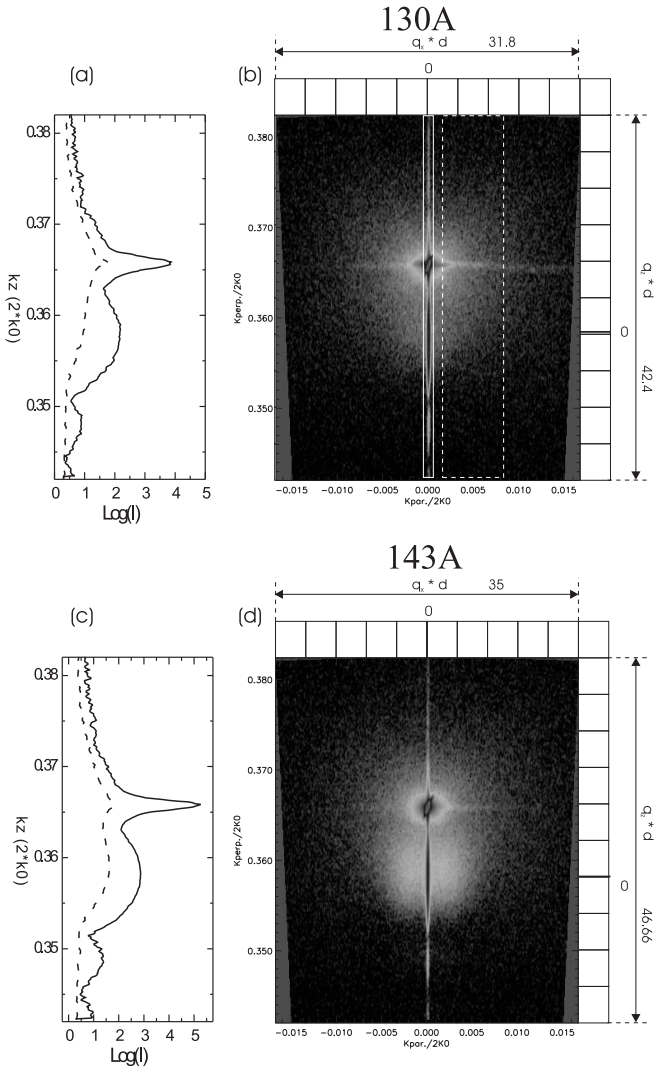

Figure 3.13: Reciprocal Space Maps around the (002) reflections of the MgO substrate and the CoO film having increasing thicknesses. The axis on the left side of the RSM's are in units of Ewald sphere diameter ($4\pi/\lambda$) and the axis on the right side is in ($q_x \cdot d$), i.e. dimensionless units centered on the CoO (002) peak. On the left-hand side of every RSM are graphs presenting integrated intensity scans corresponding to the boxes depicted in the area scan. Graphs on the left side correspond to selections from the boxes exemplified in the upper figure with corresponding line types.

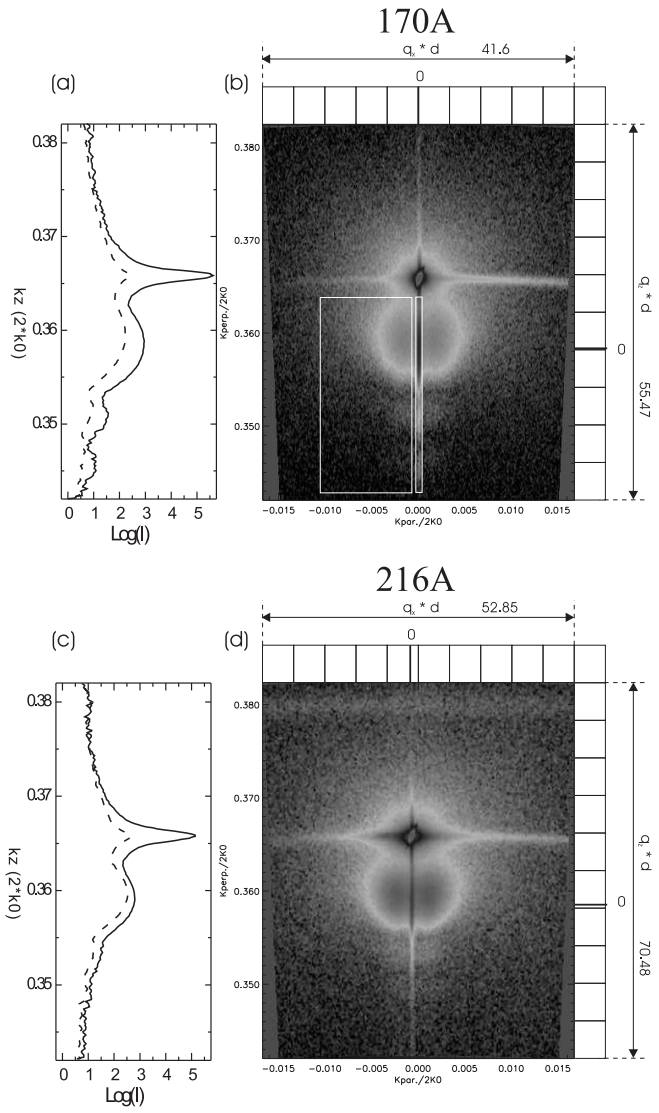

Figure 3.14: Diffuse intensity appears already at films of 130 Å thickness (at $k_{\parallel} \neq 0$). The maximum of this diffuse intensity (dashed line) is shifted to higher $k_{\perp}$ values in comparison with the coherent scattering situated at $k_{\parallel}=0$ (solid line). This situation corresponds to the low density limit (see text in next section). The boxes in the RSM in figure (b) are selections wherefrom the diffuse (wide box) and coherent (narrow box) intensity was determined presented later in this Chapter in Figure 3.22.

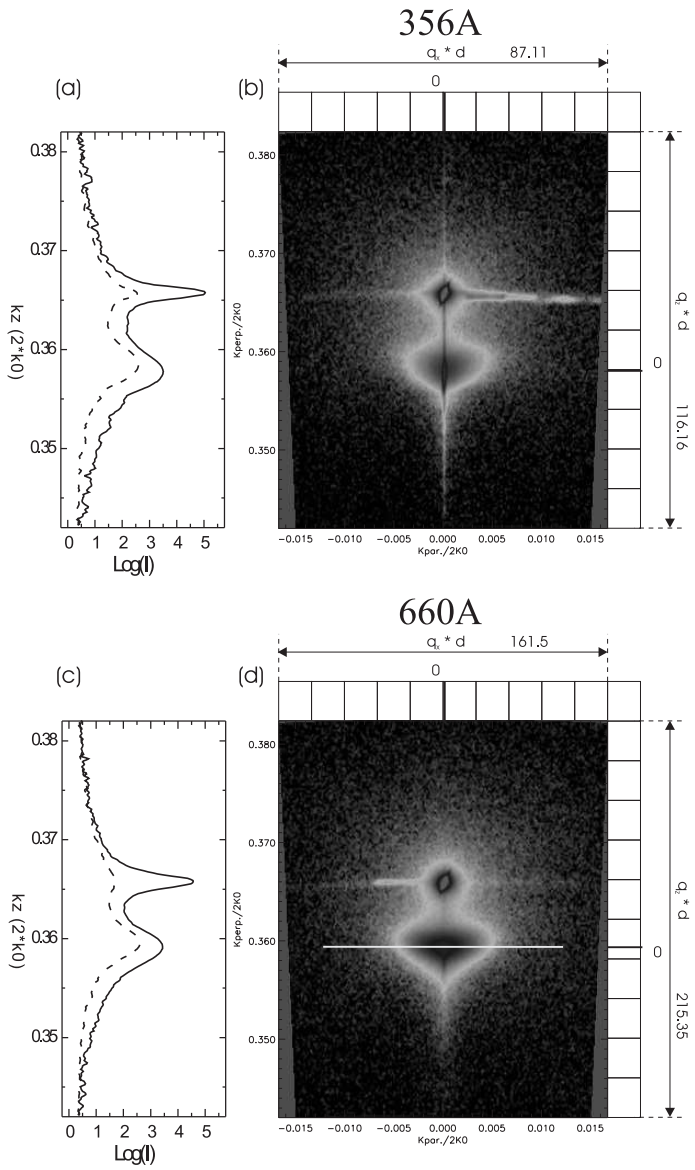

Figure 3.15: At very high thicknesses the specular peak position (collected from $k_{\|}$=0 (solid line)) will move more towards the diffuse intensity maxima (collected from $k_{\|} \neq 0$, dashed line). This corresponds already to the intermediate-to-high density limit (see text).

the value at which diffuse scattering appears for a film-substrate system the relaxation for CoO grown on MgO already sets in at ∼130 Å.

In the following we will try to numerically simulate the observed diffuse scattering around specular and of-specular reflections.

3.9 Modelling of the diffuse scattering

In this section we will focus our attention on the discussion of the main hypothesis and predictions of some models explaining the appearance of diffuse scattering from epitaxial layers.

The simplest model was envisaged by V. Srikant *et al.* [25] and was meant to explain in a very simple manner the relaxation of epitaxial layers having a large lattice mismatch. The width of the (002) or (004) specular reflection (the "omega" scan) perpendicular to the crystal truncation rod was for long recognized as a quality factor for epitaxial films. It was interpreted by Srikant and co-workers as mosaic spread of the films, namely as a mis-orientation of the grains and sub-grains of the film with respect to each other and to the substrate. This mosaicity was described by two parameters: the tilt range and the twist range (expressed as the full width half maximum (FWHM)) of the film with respect to the sample normal. Others such as Chierchia and co-workers [26] used four parameters in their analysis, the *lateral* and *vertical coherence* length being the other two in addition to the ones of Srikant *et al.* The mosaic of the films is explained by the appearance of, what they call, *geometrically necessary* misfit dislocations to fill the space and to account for the sub-grain mis-orientation distributions.

The next model worth mentioning in the present context is the one developed by P. Kidd, N.L. Andrew and P.F. Fewster [27, 31]. They studied RSM's around the (004) specular reflection from different thickness of $In_{0.1}Ga_{0.9}As$ layers on [001] oriented GaAs substrates. The layers having this composition produced a small misfit between the substrate and the film lattice parameters of ~ 0.63 %. They explained their observations, which were very similar with our RSM's taken from films of CoO on MgO substrates, by supposing that the dislocations appearing at the interface, after the start of the relaxation, produce a lateral region having a different lattice parameter than the rest of the strained film (see Figure 3.16(a)). These regions around the dislocation lines are extending to distances that is proportional to the thickness of the film (TEM observations). These regions give also rise to the diffuse intensity next to the strained Bragg peaks, as they were able to prove by the use of X-ray topography technique [5, 28–30]. In their model, the diffuse peaks are

interpreted as the square of the Fourier transform of the constant strain field having a finite lateral extent proportional to the film thickness centered on the dislocation line. This approach was to some extent successfully used by Großmann *et al.* [32] (Figure 3.16(b)) and H.R. Relß *et al.* [33]. It is evident from the data of Großmann *et al.* (reproduced here for the sake of clarity) that the diffuse peaks can be properly fitted by the above described model but as the dislocation density increases due to annealing, the model does not provide a good description anymore.

The schematic representation of this model is presented in Figure 3.16 (a) together with the above mentioned Fourier transform :
$I_{diffuse}(k,s) \propto [\sin(k \cdot s/2)/(k \cdot s/2)]^2$, s being the lateral extent of the strain field and k the parallel momentum transfer of the X-rays. In addition to the fact that the model cannot fit the high density limit, it cannot properly describe the RSM's around non-specular reflections either.

More elaborate and more realistic models describing the diffuse scattering were developed independently by Kaganer [21] *et al.* and Holý *et al.* [18–20]. Their approach is virtually the same except for some details. Below we shall give a short description summarizing Kaganer's model which we consider to be the most valid one of the two, as we shall discuss at the end of this section.

Kaganer took into account the total displacement field of the strain relieving misfit-dislocations which are expected for a certain crystal structure (see section 3.5 Figure 3.6). The necessity to do this becomes obvious if one observes the displacement field, noted as u_s, originating from a 45° tilted edge dislocation (referred to as *normal type of dislocation* for rock-salt from here on) plotted in Figure 3.17 as given in the appendix of ref [21] and first solved by A.K. Head [38]. It is also clear from this picture that the displacement field is only appreciable close to the dislocation. The extent is indeed comparable to the thickness of the film. It is also obvious, however, that the approximation of a constant displacement in the most affected region is a very crude (and unnecessary) oversimplification of reality.

The intensity scattered by such a film is calculated using the kinematical approximation taking into account a random distribution of dislocations starting at the substrate layer interface. It is given by $I(Q) = \langle \mid A(Q) \mid^2 \rangle$ averaged over the random positions of the defects, where $A(Q) = \sum_s \exp[iQ(R_s + u_s)]$ is the amplitude of the wave and the sum is taken over all the atoms of the crystal. By writing it out in more detail the intensity becomes:

$$I(Q) = \sum_{s,s'} \exp[iQ \cdot (R_s - R_{s'})] \cdot G(R_s, R_{s'}) \tag{3.22}$$

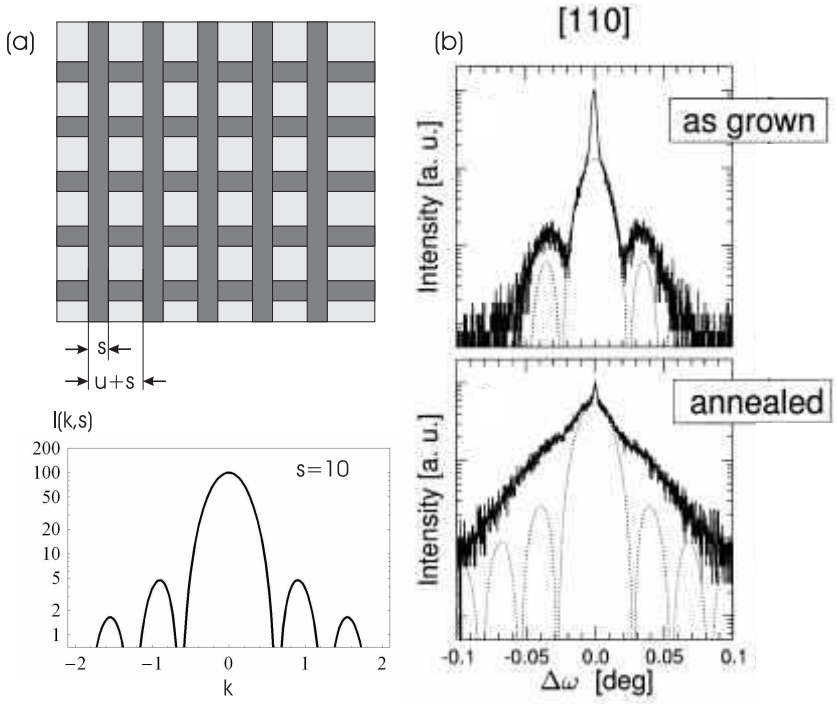

Figure 3.16: (a) Schematic drawing of the Kidd-Andrew-Fewster (KAF) model. The dark-gray areas are dislocation affected regions having a lattice constant which is slightly different from the one of the light-gray areas which are assumed to be homogeneously grown. The graph shows a representation of the square of the Fourier transform from such a step function with limited width *s=10*, plotted against $k_{||}$ (the X-ray momentum transfer parallel to the surface). (b) Experimental (solid line) and fitted (dashed line) is an ω scan taken from reference [32] of an as grown ZnSe layer on GaAs (upper graph) and the same for an annealed film (lower graph). The KAF model seems to fit very well the diffraction pattern before heat treatment but not after, in other words at high dislocation densities the model does not give satisfactory results.

where G is the correlation function:

$$G(R_s, R_{s'}) = \langle \exp[iQ \cdot (u_s - u_{s'})] \rangle = exp[T \cdot (R_s - R_{s'})] \tag{3.23}$$

Depending on the density of defects (dislocations), one can distinguish two limits: the spatially independent (low density limit) and the spatially correlated case. In the first case the defects are so rare that they do not interact with

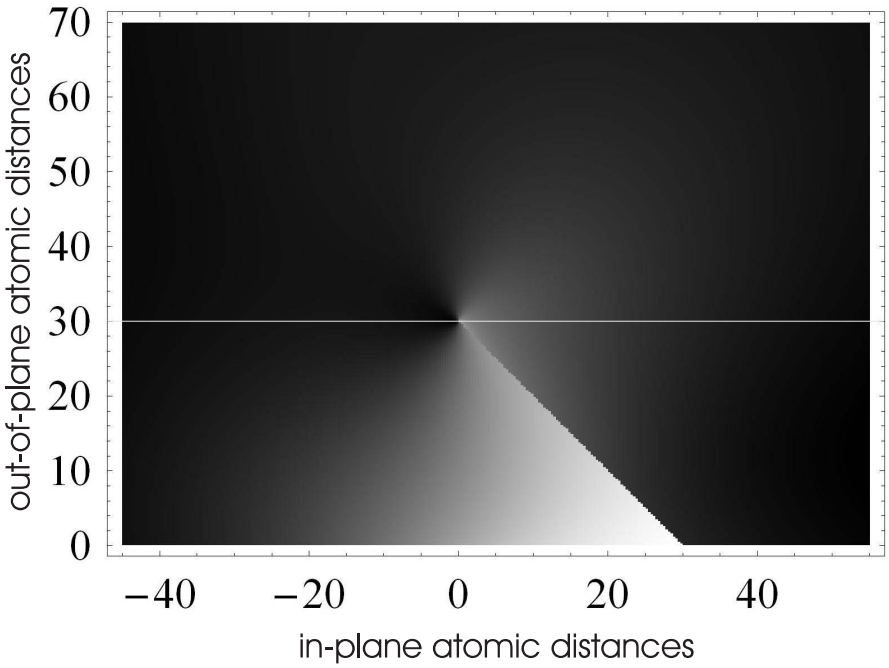

Figure 3.17: Displacement field due to a *normal type* edge dislocation. The horizontal line represents the borderline between the substrate (top) and film (below the line). The numbers represent atomic positions parallel (horizontal) and perpendicular (vertical) to the surface. The displacement is represented as brightness of the pixels, the maximum displacement being equal to one atomic distance (displayed as white), i.e. one lattice constant, the entirely black pixels indicating no displacement at all. (After the formulas given by Kaganer *et al.* [21].)

each other and the only parameter is their density $c \ll 1$. This is the limit we are considering in this section. In this case, after some approximations valid in this limit, one can write:

$$T(R_s, R_{s'}) = c \sum_t \{1 - \exp[iQ(u_{st} - u_{s't})]\} \tag{3.24}$$

where, $u_{s,t} = u(R_s - R_t)$ is the displacement at the position R_s due to a dislocation at position R_t. $T(R_s, R_{s'})$ is also sometimes referred to as the correlation function. Equation 3.24 is the correlation function used in this section.

The case of spatially correlated defects has to be considered when dis-

locations are so close that they are no longer independent from each other. Therefore, in order to minimize the energy they tend to redistribute. At these high densities, dislocations are almost equidistant, for further examples see references [16, 34, 35].

Returning to the Kaganer model, and assuming spatially uncorrelated dislocations we distinguish two limits: the *low* and *high* density limit.

In the general case the diffuse intensity can, as presented in Kaganer's paper, be calculated by numerically evaluating the following expression:

$$I_{diffuse}(q_x, q_z) = \int_{-\infty}^{+\infty} dx \int_0^d \int_0^d dz_s dz_{s'} \cdot e^{q_x x + i q_z (z_s - z_{s'})} \cdot \{ e^{-T(x, z_z, z_{s'})} - e^{-T_\infty (z_s, z_{s'})} \} \tag{3.25}$$

where (q_x, q_z) is a vector around a certain reciprocal lattice point Q, and $T_\infty(z_s, z_{s'}) = \lim_{x \to \infty} T_x(z_s, z_{s'})$ is the non-vanishing limit of the correlation function.

This diffuse intensity is superimposed on the coherent intensity

$$I_{coherent}(q_x, q_z) = 2\pi\delta(q_x) \int_0^d \int_0^d dz_s dz_{s'} \cdot e^{q_z (z_s - z_{s'})} \cdot e^{-T_\infty (z_s, z_{s'})} \tag{3.26}$$

i.e. the sum of the two is the total intensity. The diffuse intensity here was calculated by performing a Fast Fourier transform, corresponding to the integral over *dx*, of the following two integrals over *dz* and *dz'* evaluated as simple sums in equation 3.25.

In the low density limit the dimensionless parameter $\rho \cdot d$ is smaller than unity. Since dislocations are very distant, the correlation function $G(r_1, r_2)$ vanishes for $(r_2 - r_1) \to \infty$. The Bragg reflection will still be visible but decreases in intensity with increasing density and thickness. A surprising result is that the Bragg peak does not follow the mean distortion. This is so, because the displacement field which is large close to the dislocation line, contributes largely to the mean distortion ($Q \cdot u(r)$) but since the displacements are comparable to the Burgers vector (which is by definition a lattice vector) they do not change much the Bragg position ($\sin(Q \cdot u(r))$). In this case the correlation function $T(x, z_s, z_{s'})$ is small and one can use the expansion for the exponential function $\exp(T) \approx 1\text{-}T$ in equation 3.25, and the diffuse intensity becomes:

$$I_{diffuse}(q_x,q_z)=\sum_{\alpha}\rho_{\alpha}\left|\int_{-\infty}^{\infty}dx\int_{0}^{d}dze^{iq_xx+iq_zz}\cdot[e^{iQu_{\alpha}(x,z)}-1]\right|^2 \tag{3.27}$$

This is the expression we used in calculating the low density limit ($\rho\cdot d\ll 1$). The integral over dz was calculated as a sum while the integral over dx was performed by a Fourier transform of the sum. The results of these calculations will be presented in the next section.

The other limiting case is the high dislocation density limit which corresponds to the case where only points close to each other are correlated and contribute to G. Here the mean distortion determines the position of the diffraction peak. The phase factor is $Q\cdot(u(r_2)-u(r_1))\approx(r_2-r_1)\nabla(Q\cdot u(r))$. Consequently the peak position depends on $\langle\nabla(Q\cdot u(r))\rangle$ and the peak width depends on the mean square distortion $\langle[\nabla(Q\cdot u(r))]^2\rangle$. In this situation the coherent Bragg intensity is exponentially small and the diffuse intensity is given, in the simplest case of specular reflections, by:

$$I(q_x,q_z)=\pi\int_{0}^{d}\frac{dz}{\sqrt{w_xw_z}}\cdot\exp[-\frac{q_x^2}{4w_x}-\frac{q_z^2}{4w_z}], \tag{3.28}$$

where

$$\begin{aligned} w_x(z) &= \frac{\rho}{2}\cdot Q_z^2\int_{-\infty}^{+\infty}dx[u_{z,x}^{(x)2}+u_{z,x}^{(z)2}],\\ w_x(z) &= \rho\cdot Q_z^2\int_{-\infty}^{+\infty}dx[u_{z,z}^{(x)2}+u_{z,z}^{(z)2}], \end{aligned} \tag{3.29}$$

using $u_{i,j}=\frac{\partial u_i}{\partial x_j}$ and $(i,j)=(x,z)$. *u(x,z)* is the above mentioned displacement field and the symbols in the parentheses represent which type of Burger's vector is responsible for this displacement field ((x) for b_x, (y) for b_y and (z) for b_z). The case of off-specular reflections is slightly more complicated:

$$I(q_x,q_z)=\pi\int_{0}^{d}\frac{dz}{\sqrt{det\hat{w}}}\cdot\exp[-\frac{1}{4}w_{ij}^{-1}(\mathbf{q}-\mathbf{q_0})_i\cdot(\mathbf{q}-\mathbf{q_0})_j], \tag{3.30}$$

where w_{ij} is a matrix having elements given by:

$$
\begin{aligned}
w_{xx}(z) &= \frac{\rho}{2} \cdot \sum_{\sigma=x,y} \int_{-\infty}^{+\infty} dx (Q_x^2 u_{x,x}^{(\sigma)2} + Q_z^2 u_{z,x}^{(\sigma)2}), \\
w_{xz}(z) &= \frac{\rho}{2} Q_x Q_z \cdot \sum_{\sigma=x,y} \int_{-\infty}^{+\infty} dx (u_{x,x}^{(\sigma)} u_{z,z}^{(\sigma)} + u_{x,z}^{(\sigma)} u_{z,x}^{(\sigma)}), \qquad (3.31) \\
w_{zz}(z) &= \frac{\rho}{2} \cdot \left\{ \sum_{\sigma=x,y} \int_{-\infty}^{+\infty} dx (Q_x^2 u_{x,z}^{(\sigma)2} + 2 Q_z^2 u_{z,z}^{(\sigma)2}) + \int_{-\infty}^{+\infty} dx Q_x^2 u_{x,z}^{(y)2} \right\}
\end{aligned}
$$

A more insightful description of the theory can be found in reference [21]. We numerically simulated RSM's and one dimensional scans using these two limits with the above presented formulas. Calculations using the model of Kaganer are very few [36, 37] although its results, as will be visible in the following sections, are surprisingly good, and the only fitting parameter is $(\rho \cdot d)$. Of course one has to know in advance what type of dislocations can be present in the layer. The type of dislocation can also be identified by comparing the simulations with the experiment.

It is convenient to plot the numerical calculations as a function of the dimensionless parameter q·d. For the purpose of comparison between theory and experiment these axes were also drawn for RSMs in Figures 3.10, 3.11, 3.13, 3.14 and 3.15.

As mentioned before, Holý *et al.* developed also a model to describe the diffuse scattering in mismatched epitaxial layers. There is, however, a fundamental difference between the initial assumptions of the two theories. Holý starts by assuming that the differences $(u(r_2) - u(r_1))$ consist of displacements $u(r_i)$ behaving as Gaussian random variables, Kaganer makes use of the results of Krivoglaz based on Poisson statistics for uncorrelated dislocations [39]. The simplified consideration of Holý is based on the ease with which one can arrive at a simplified form of the correlation function using the Baker-Hausdorff theorem (see appendix of ref. [3])
$< \exp[iQ(u(r_2) - u(r_1))] >= \exp\{-\frac{1}{2} < [iQ(u(r_2) - u(r_1))] >\}$ or for further details see reference [19]. We believe that Kaganers treatment is the correct one. However, probably because of the rather involved mathematics it is not much used in the literature.

Finally we want to mention a number of LEED studies of diffuse scattering i.e. the one by M. Dynna *et al.* [22] as well as the one by M. Klaua *et al.*

[23]. In simulating the spot profile of thin MgO films on Fe(001) surface they also considered the full displacement field $u(r)$. Because of the surface sensitivity of the LEED technique only the displacement of the surface has to be taken into account. Their calculations were done in the low density limit neglecting the correlation of the dislocations although the misfit of the films with the substrate was high. Nevertheless, their calculations fitted quite well the experimental profile.

3.10 Fitting the experimental diffuse scattering data

In the previous section we have presented some of the models which were developed to explain and simulate the experimentally measurable diffuse scattering originating from misfit dislocations. In the following two sections we will use the method of Kaganer described in some detail in the previous section and apply this model to our measured diffuse scattering. We will separate the very low to intermediate dislocation density case from the high density case since these are the two regions applicable to the thin CoO layers on MgO and the thick MnO buffer layers on MgO respectively.

3.10.1 Low and intermediate density limit

We have already shown RSM's around the (002) reflection of CoO layers of increasing thickness on MgO. In the following we will turn our attention to specific cross-sections from these area scans, namely scans parallel to the surface (so-called q_x scans). The scans measured for CoO layers on MgO are plotted in Figure 3.18 and, as mentioned before, the horizontal axis is plotted in units of $(q_x \cdot d)$ so that all the scans can pe represented by the same axis. In this figure there are roughly 4 distinct regions visible.

1. The first region is represented by the 115 Å CoO on MgO and smaller thicknesses (not shown). Apart from one single sharp peak at $q_x \cdot d$=0 which is entirely due to coherent scattering , almost no diffuse scattering is visible.

2. The second region is comprises the 130-216 Å thick CoO films on MgO where a separate, distinct feature is visible at both sides of the, still present, coherent peak. One should note that as the thickness increases, the coherent peak is becoming smaller in comparison to the diffuse lobes. Also interesting to note is that the side lobes stay at the same position in the $q_x d$ plot as the thickness of the film is increasing and that the center coherent peak remains sharp at higher thicknesses.

3. The third region is limited to the 356-660 Å thick films of CoO on MgO. Although the center peak is still present, the diffuse features have a different shape than the previous region. These diffuse lobes now become more smeared out invading the middle coherent peak and extending to higher values on the $q_x \cdot d$ scale.

4. Finally the last region is made up by the very thick films (880 Å and thicker) of CoO on MgO. The peak is entirely diffuse in character although according to some authors this is because the grain and sub-grain mis-orientations. This limit will be discussed in more detail in the following subsection 3.10.2.

In Figure 3.19 we present the best fits we could achieve using the procedure outlined in Section 3.9 with the Equations 3.25 and 3.27. Here we made the approximation that the values of q_x around a certain reciprocal lattice point (Q_x, Q_y, Q_z) are so small that the integral over *dx* could be replaced by the Fast Fourier Transform of the remaining two integrals over *dz* and *dz'*, which were calculated by evaluating the integrals as finite sums. The fits are not perfect but they mimic quite well the main features of the experimental scans. As can be seen in Figure 3.19 the (002) reflections are surrounded by one satellite on both sides of the peak while the (004) peaks have two such satellite peaks. To our knowledge these scans and simulations are unique in the case of epitaxial oxides.

In many studies of thin oxide films, the width of the reflections in the q_x direction is considered a measure of the quality of the films, sharper peaks representing better quality. Therefore, in the investigations published in the literature the films are either completely coherent so the q_x scans are extremely sharp (and are determined by the resolution of the X-ray apparatus), or the large widening of the peak is considered as an effect of grain or sub-grain mis-orientations due to misfit. As disclosed in the next section, this broadening can be treated in the high dislocation density limit.

It is also interesting to note that we did not use analyzer crystals in front of the detector. Our resolution was around of $5 \cdot 10^{-4}$ Å^{-1} in the neighborhood of the CoO (002) reflection. Even so, the diffuse scattering surrounding these reflections is clearly visible.

As shown in Figure 3.18, after the appearance of diffuse intensity in the second region between 130 Å and 216 Å of CoO on MgO, the shape and separation of the side bumps is independent of the thickness *d*. Therefore, in Figure 3.19 we only present the fit for the 170 Å sample which should be representative for this group. The next region corresponds to the intermediate

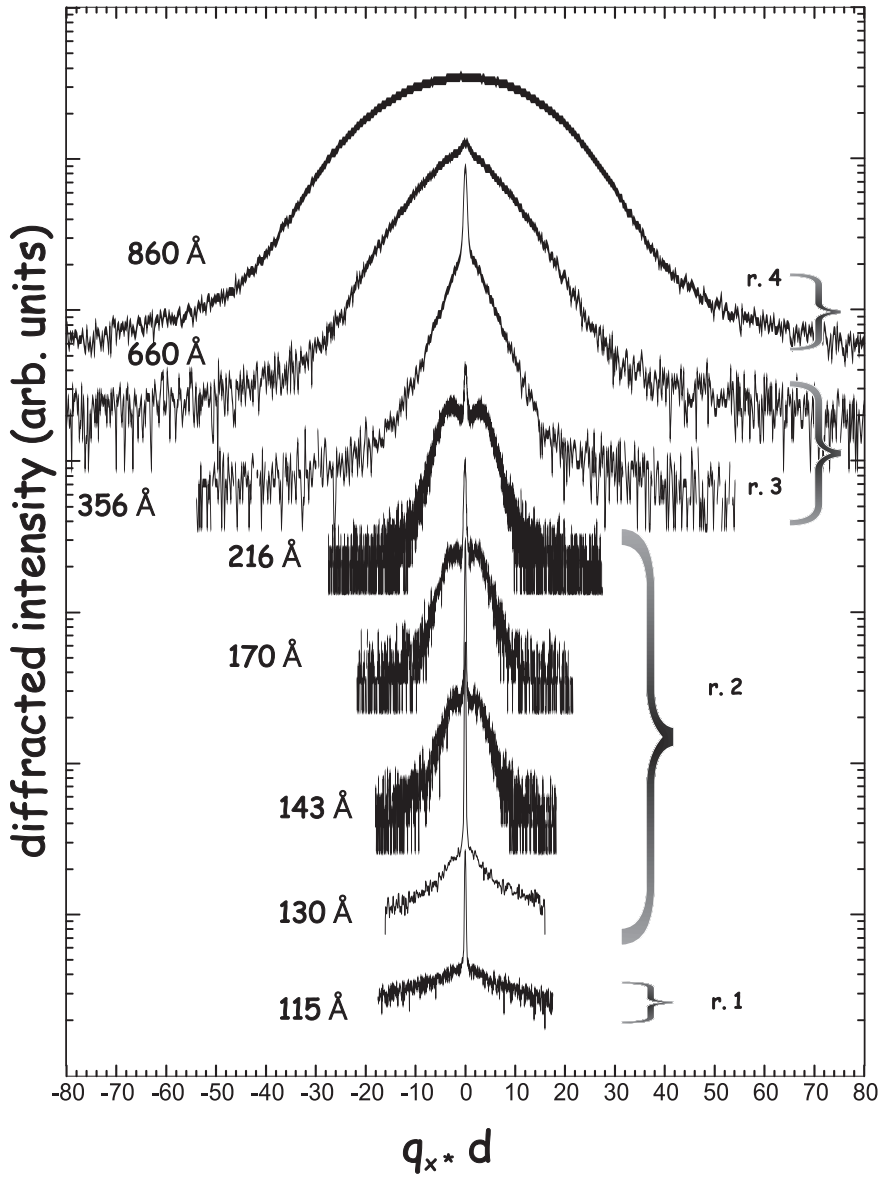

Figure 3.18: $q_x \cdot d$ scans, as shown by the horizontal line in Figure 3.15, for CoO layers on MgO for increasing thickness. The thinnest (115 Å) film shows almost no diffuse scattering. For increasing thickness the central sharp coherent peak disappears, while the diffuse scattering gets more and more pronounced.

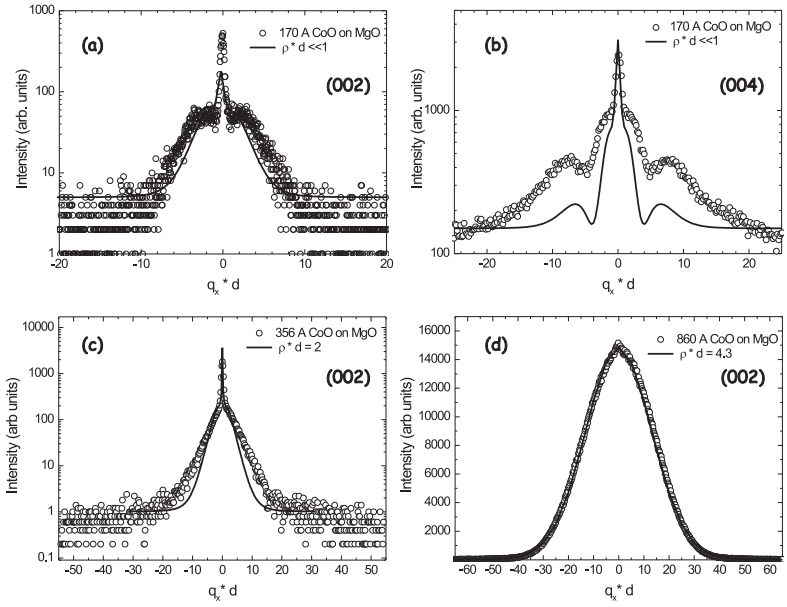

Figure 3.19: Comparison of the experimental with simulated $q_x \cdot d$ scans calculated using Kaganer's approach in the low density approximation. (a) and (b) Scans trough the (002) and (004) reflection from the 170 Å CoO on MgO can be fitted using the low dislocation density approximation. This region is a meta-stable region where the multiplication of dislocations is hindered by kinetic barriers. (c) At the intermediate density region the side lobes start to disappear. The fit here was done using the intermediate density model. At these thicknesses the film is relaxing and the density of dislocations is rapidly increasing with further increase in thickness. (d) The same scans but for the thickest 860 Å CoO on MgO film. The thick film belongs to the high density region. The fit was done using the high density approximation described in section 3.9 and exemplified in more detail in the following section. From this last fit the linear dislocation density $\rho = 0.011$ was deduced.

density where $\rho \cdot d \approx 1$ for which the fit for the 356 Å CoO on MgO sample is displayed. This intermediate limit can only be fitted well with $\rho \cdot d = 2$. This means that we overestimate the dislocation density, because this results in $\rho \sim 0.012$, and this value is almost equal with the misfit f=0.015 for the CoO/MgO system. Possible reasons for this discrepancy are discussed below. The best fit was achieved for the thickest CoO film using the high dislocation

density limit, for which the value of $\rho \cdot d = 4.3$ was found. Knowing that the thickness of the film d is almost 400 ML, this resulted in a linear dislocation density of ρ=0.011. This is a value smaller than the misfit (f=0.015) for the CoO/MgO system which suggests that the film is not entirely relaxed and a small compressive strain remains in the film. This result is in accordance with the out-of-plane c lattice parameter value, measured from the specular scans represented by the last data point in Figure 3.8 (a).

The values shown for our best fits are not entirely correct, since one should also take into account the threading dislocations as well as the correlations with other dislocations which this model does not account for. It is very probable that these values are slightly overestimating the real linear dislocation density. Note that in the simulations only the diffuse scattering was calculated. These calculations can be extended also in the perpendicular direction and thus for every q_z value a q_x scan can be calculated. In this way it is easy to compare the shape of the simulated and measured diffuse scattering. The calculated and measured RSM are presented in Figure 3.20 not only for the specular but also for the (224) off-specular reflection. One can see that although the overall shape is comparable, the number of visible features in the simulation is higher than in the measurement. One of the reasons for this is the insufficient intensity of the X-ray beam of our apparatus.

Finally in Figure 3.21 we present another RSM from an off specular reflection and the corresponding calculation, as well as some further simulations of other achievable reflections using the $\lambda = 1.54$ Å X-ray wavelength. One should also note that by decreasing the wavelength and thus increasing the diameter of the Ewald sphere, other specular and off-specular reflections can be measured where according to our simulations more structure is expected in the diffuse scattering.

An important point, almost always overlooked in reports studying relaxation is concerning the position of the specular Bragg peaks of a partially relaxed film. It is inferred by these authors, without any proof, that the position of the coherent peak follows the mean distortion in the crystal. Kaganer *et al.* [21] proved though, that this is the case only for the high density limit. At low dislocation densities, although the intensity of the coherent peak decreases exponentially by increasing ρd, the position of the coherent part of the diffracted intensity is not affected by the mean distortion. This is the reason for the discrepancies of the critical thickness resulting from Figures 3.12 and 3.8, and the presence of diffuse scattering because of the dislocations relieving strain already at lower thicknesses. Knowing that the sum of the coherent and diffuse part of the diffracted intensity has to be constant if normalized

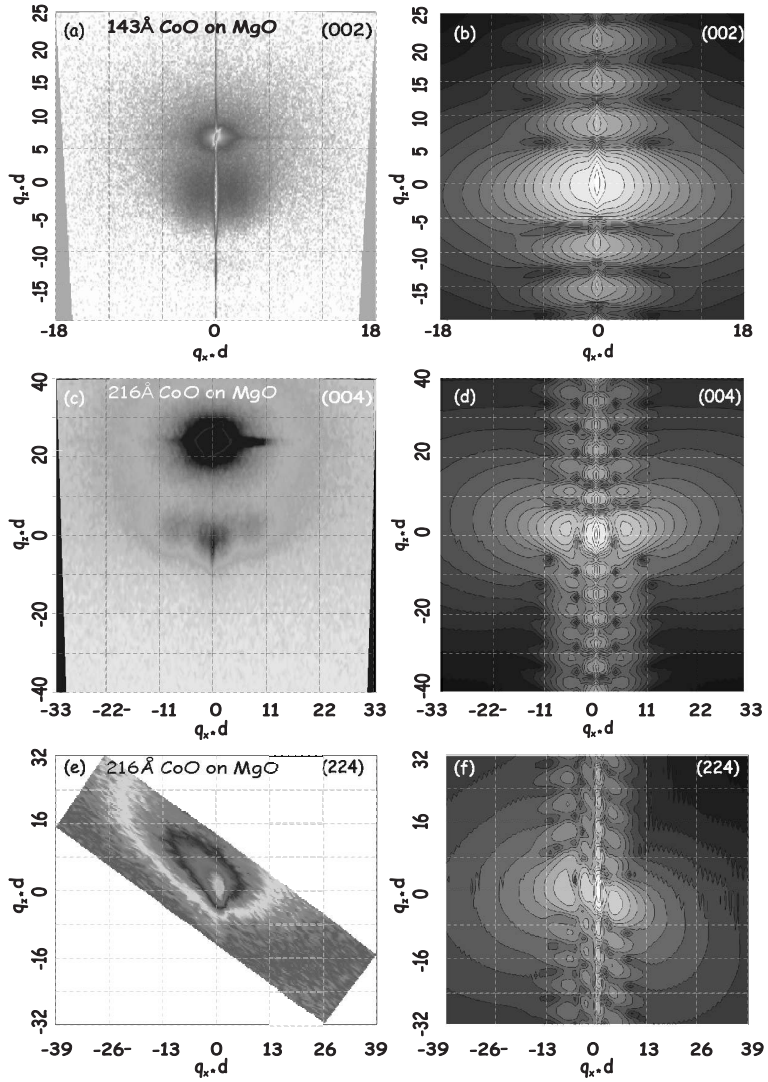

Figure 3.20: Measured and simulated RSMs around specular or off-specular reflections of CoO on MgO. (a) and (b) RSM around the (002) of a 143 Å CoO film on MgO and a simulated RSM using the low density limit (eq. 3.27 discussed in section 3.9). (c) and (d) RSM around the (004) reflection of a 216 Å CoO film on MgO, and a simulated map using the same equation. Finally a RSM around an off-specular reflection, namely the (224) of the 216 Å CoO film on MgO (e) in this case we zoomed in on the film reflection so the substrate MgO (224) is not visible and the corresponding calculated spectra (f).

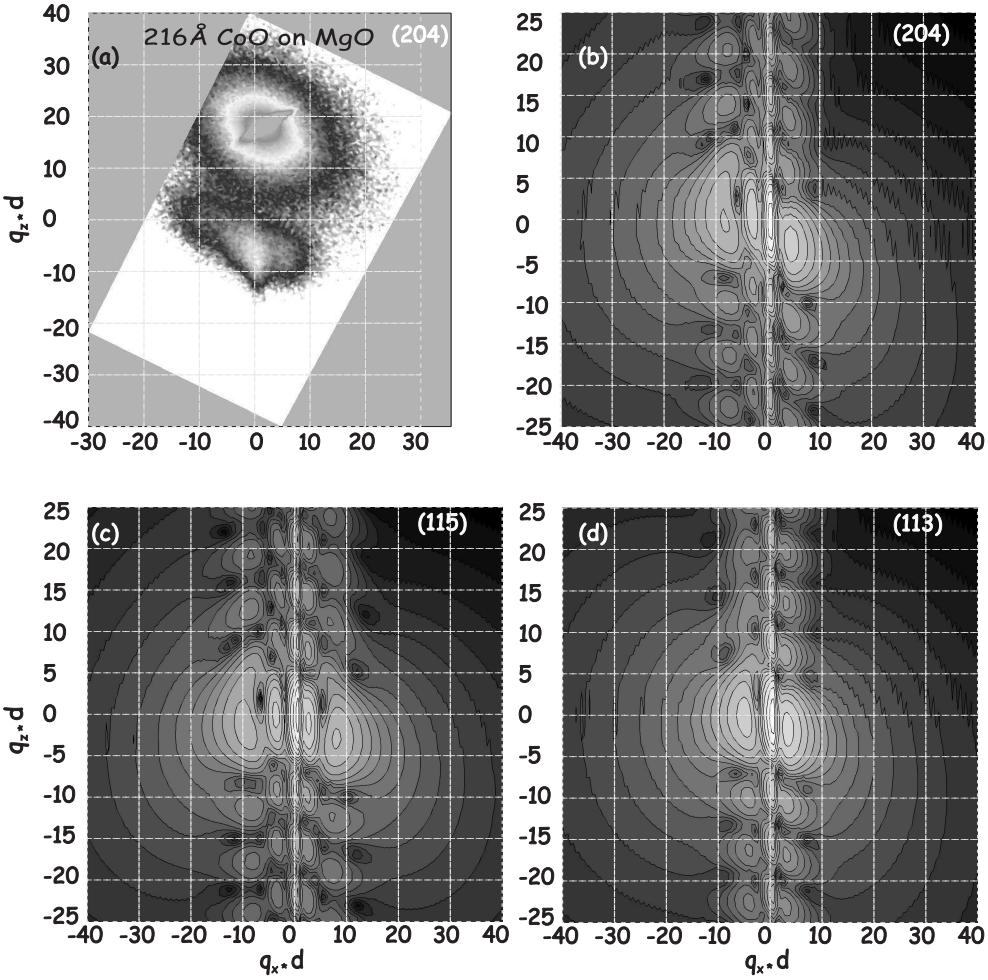

Figure 3.21: Measured and simulated RSMs around off-specular reflections of CoO on MgO. (a) and (b) RSM around the (204) of a 216 Å CoO film on MgO and a simulated RSM using the low density limit eq. 3.27 discussed in section 3.9. (c) and (d) simulated RSM around the (115) and (113) reflections calculated in the low dislocation density limit.

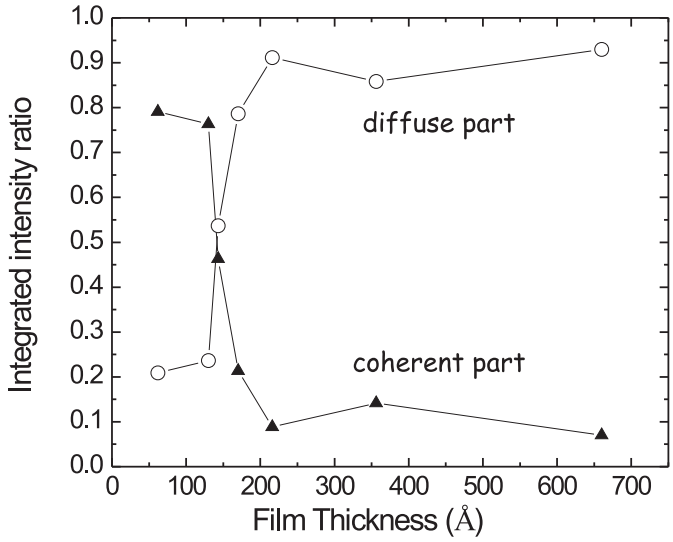

Figure 3.22: Ratio of integrated intensities from the boxes shown in Figure 3.14 for all thicknesses. the diffuse scattering increases rapidly above ∼125 Å, and becomes higher than the coherent part after about ∼ 130 Å thickness of the CoO layer on MgO.

to the thickness of the film, we compare in Figure 3.22 how these intensities develop as a function of thickness. The data points represent integrated intensities from the two boxes depicted in Figure 3.14 normalized to the sum of the coherent and diffuse intensities.

Because the intensity scattered in the specular direction (into the narrow box represented in Figure 3.14) is not entirely made of coherently scattered X-rays, this simple integration procedure is not entirely correct. However, the error made is not extremely large, since at low dislocation densities the diffuse intensity in this position of the reciprocal space is vanishingly small. The figure therefore represents just a guideline. If the diffuse scattering was correctly separated, the shape of the curve would be just slightly altered at low thicknesses and the last two points, representing the diffuse and coherent part, would be very close to one and zero, respectively. However, from this analysis one can clearly see that the diffuse scattering becomes a significant fraction of the total intensity for a thickness of 130 Å or higher of the CoO layer on MgO. The sudden change in the intensity distribution above ∼ 125

Å comes as an additional prove confirming that the relaxation process started already between 125-130 Å thickness of the CoO layer on MgO and that a single specular scan is not sufficient to deduce the state of the relaxation.

Data taken with synchrotron radiation would improve very much the statistics, and since, judging from the calculations, off-specular spots have increased number of features around the reflections, the high intensity combined with an increased resolution would be useful for achieving better correspondence between experiment and simulation.

3.10.2 High density limit

In the following we will illustrate the high density limit ($\rho \cdot d \gg 1$). The experimental XRD data was collected from thick layers of MnO epitaxially grown on MgO. The films were covered by a thin CoO layer in order to prevent oxidation. The misfit between bulk MnO and MgO is of the order of 5 %. This large misfit makes this system a good candidate for the high density limit since the relaxation of the strain is rapid, thus ρ is large. Figures 3.23 and 3.24 present two RSM's around the (113) and (224) reflections of the MgO substrate and MnO film, respectively, of a sample having the following composition: 540 ML MnO on MgO covered with 40 ML CoO.

The figures show the experimental data, the calculated RSM's as well as the horizontal and vertical line scans presented by the symbols (measured) and by the solid lines (calculated). The calculation of the diffuse scattering was done as explained in Section 3.9. The parameters for the two reflections were the same ρ=0.416, d=60, and ν=0.33. The values of the three quantities w_{xx}, w_{xz} and w_{zz} were evaluated for every z ($\in [0, d]$) by transforming the integrals from equations 3.31 into simple sums which run from $(-\frac{length-1}{2}) = -100$ to $(\frac{length-1}{2}) = 100$ for x. Increasing the value of "*length*" did not change the calculated profiles. The integral over z was also transformed into a sum from 0 to d, and evaluated for every (q_x, q_z) pair. From the fits at the bottom of these figures it becomes clear how well the theory describes the experimental measurements for the high density case, although the only parameter which is used is the product $\rho \cdot d$, in our case $\rho \cdot d = 25$. Knowing now the thickness of our sample of 540 ML, which was deduced from the Mn metal flux and also from the fit of the reflectivity curve, one can deduce the real linear dislocation density $\rho = 25/540 = 0.046$, which corresponds to one dislocation per 21.6 lattice units. This value of ρ is slightly lower than the misfit of the MnO with the substrate, which suggests that the film is not entirely relaxed. This fact is in agreement with the value of the out-of-plane lattice parameter c=4.453 Å, being slightly larger than the bulk value ($a_{MnO} = 4.445\mathring{A}$). In order to

fit the data a trial and error method was used. For this the following general predictions were kept in mind:

- The shape and orientation of the calculated diffuse intensity will strongly depend on the type of dislocations which are considered in the calculation. Three types of dislocations were considered: *Lomer type* edge dislocations (b_x=1, b_y=0, b_z=0) which can occur in oxides but only at high temperatures (∼800-1000 C°), *normal type* edge dislocations (as shown in figure 3.17) (b_x=1, b_y=0, b_z=-1) and *60°* dislocations which occur in semiconductors such as Si or Ge ($b_x = \frac{\sqrt{2}}{2}$, $b_y = \frac{\sqrt{2}}{2}$, b_z=-1).

- The peak widths $\Delta q_{x,z}$ are proportional to $\sqrt{\rho/d}$ and the aspect ratio $\Delta q_x/\Delta q_z$ is representative of a particular reflection (Q_x, Q_y, Q_z) for a particular type of dislocation, or a mixture of dislocations.

- The aspect ratio q_x/q_z as well as the orientation of the ellipse shaped diffuse intensity profile is strongly dependent on the value of the Poisson ratio (ν) for a certain type of dislocation or mixture of dislocations.

This way one is able to find a particular parameter set in order to simulate, with a certain precision, not only the *shape* of the diffuse peaks but also their *orientation*.

It is worthwhile to turn our attention towards the orientation of the peaks in the reciprocal space. In the most rudimentary picture, one would imagine the layer as composed of regions having different in-plane stress profiles, whereas the corresponding out-of-plane c lattice parameters are given by the material specific Poisson ratio (ν). In this case one would expect that the scattered diffuse intensity profile generated by such a strained film follows the line connecting the position of the completely strained state with the position of the entirely relaxed state. These points in the reciprocal space are depicted in Figure 3.25 (a). The angle α formed by the horizontal and the line connecting these two points can be calculated once one knows the position of these points as shown in the figure for the case of the (224) reflection:

$$\alpha = \arctan\left(\frac{4(a^*_{MnO} - c^*_{MnO})}{2\sqrt{2}(a^*_{MgO} - a^*_{MnO})}\right) \tag{3.32}$$

where $a^*_{MnO} = 2\pi/a_{MnO}$, and c^* is given by the Equation 3.20 (in which one should read MnO instead of CoO and which contains the dependence on the Poisson ratio). This behavior is illustrated in the following two graphs in Figure 3.25 by the *gray squares* as a function of ν for the (113) and (224)

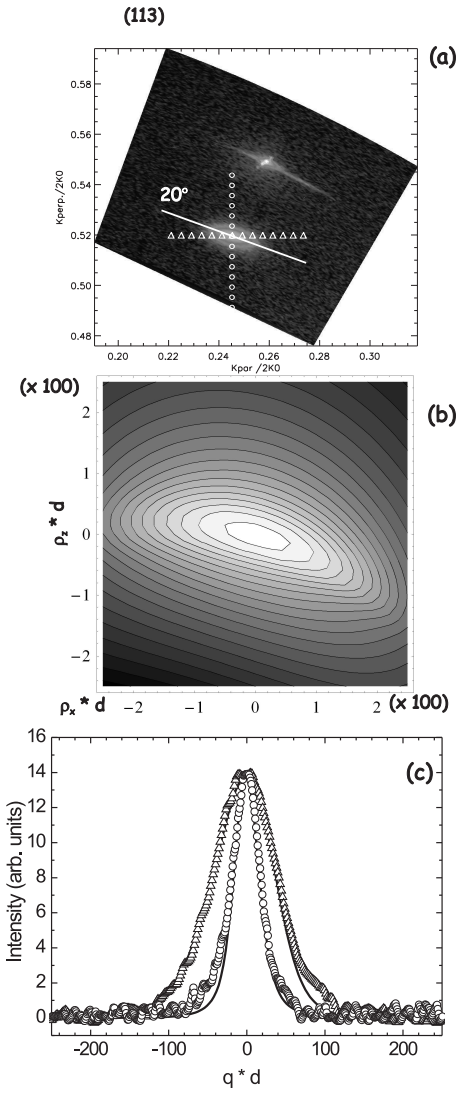

Figure 3.23: (a) Reciprocal Space Map around the (113) reflection from a 45 ML CoO on 540 ML MnO bilayer grown on MgO substrate. (b) Calculated RSM using the high density limit method described in Section 3.9. The parameters used for this simulation were $\nu_{MnO} = 0.33$, d=60, $\rho = 0.416$. (c) Experimental and simulated scans as presented by the patterns crossing the (113) peak in the top figure, solid lines represent the corresponding simulations. The match is virtually perfect.

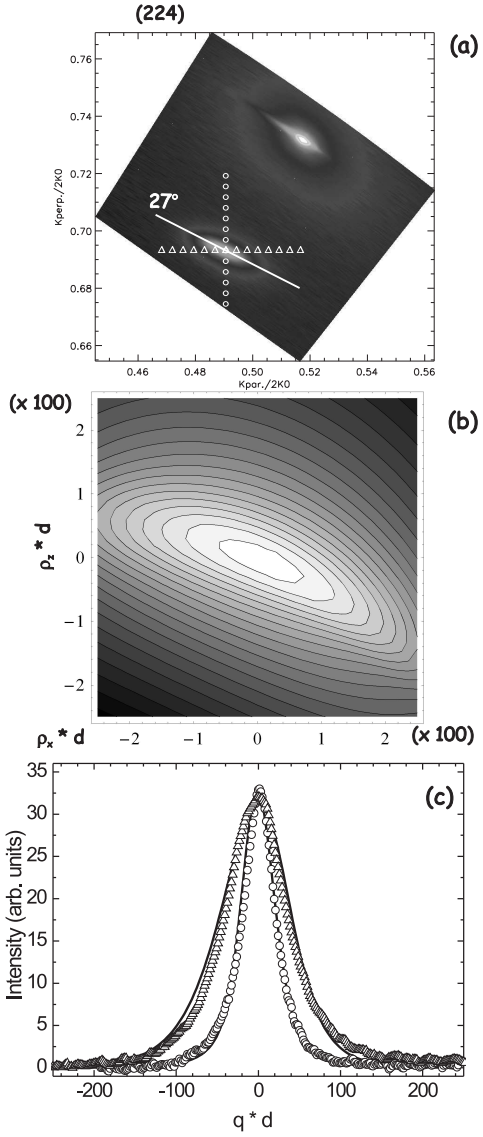

Figure 3.24: (a) Reciprocal Space Map around the (224) reflection from a 45 ML CoO on 540 ML MnO bilayer grown on MgO substrate. (b) Calculated RSM using the high density limit method described in Section 3.9. The parameters used for this simulation were $\nu_{MnO} = 0.33$, d=60, $\rho = 0.416$. (c) Experimental and simulated scans as presented by the patterns crossing the (224) peak in the top figure, solid lines represent the corresponding simulations. The match is virtually perfect.

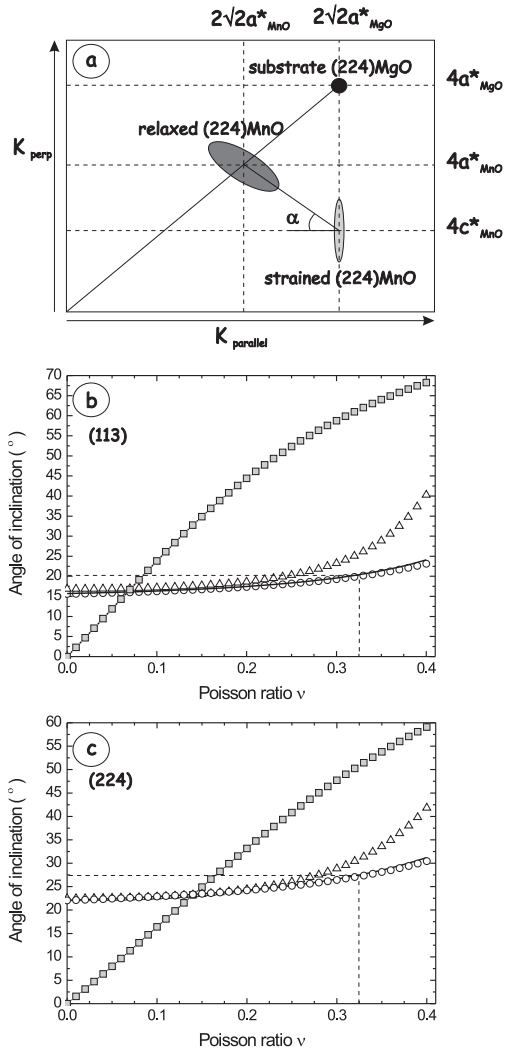

Figure 3.25: (a) Schematic drawing in reciprocal space of the relaxed and unrelaxed (224) reflection of MnO film on an MgO substrate. (b) Calculated rotation angle α of the ellipse shaped intensity distribution for the case of the (113) reflection. The line with square symbols represents the angle between the line connecting the relaxed and entirely strained positions with the horizontal, as a function of the Poisson ratio. The solid line, the triangle and the circle symbols represent the rotation of the principal axis of the ellipse with respect to the horizontal as calculated from Equation 3.33 for the case of *normal type*, *Lomer type* and the *60°* dislocations respectively, as a function of the Poisson ratio. (c) Same as (b) but for the (224) reflection.

reflections of the MnO on MgO. The other three lines in the graphs represent the values of the angle as calculated by the formula given by Kaganer, which relates the angle formed by the short axis of the ellipse with the vertical direction (basically equal to our α):

$$\alpha = \frac{1}{2}\arctan\left(\frac{2w_{xz}}{w_{zz} - w_{xx}}\right) \tag{3.33}$$

This is the orientation of the main axis of the $\hat{w}^{-1}$ with respect to the horizontal. Kaganer realized that the functions w_{xx}, w_{zz} and w_{xz} are increasing functions of z and since their contribution to the diffuse intensity decreases exponentialy (see the simple case of specular reflections Eq. 3.28), the width of the scattered intensity can be estimated using their values at z=0 (at the interface). By calculating these functions for the three different dislocation types we can plot how the orientation of the main axis of the diffuse intensity changes as a function of ν using the above formula 3.33. These curves plotted in Figure 3.25 for the two most frequently used off-specular reflections, (113) and (224). One can see that there is a strong deviation between the angle predicted by the Kaganer model and the angle calculated using the naive model given by the Equation 3.32. It is also clear that the *Lomer type* of dislocations produces a larger rotation than the *normal type* or the *60°* dislocations as a function of the Poisson ratio. The best fit to our experimental data was achieved using an approximative value of the Poisson ratio $\nu = 0.33$ and a *normal type* (b_x=1, b_y=0, b_z=-1) of dislocation. These findings are in agreement with the experimentally found values for ν calculated by the formula:

$$\nu = \frac{c_{12}}{c_{12} + c_{11}} \tag{3.34}$$

using the values found in literature , $c_{12} = 22.3 \cdot 10^{10}\ N/m^2$, $c_{11} = 12 \cdot 10^{10}\ N/m^2$, [40] which give $\nu = 0.349$, or with the values published for $\nu = 0.301$ from ref. [41] and assuming that the active dislocation is of the type expected to appear in ionic solids. The simulations using the same parameter set can fit not only the peaks shown in the above figures but also the rest of the measured diffraction profiles such as the (002), (004) or the (115) (not shown here). This perfect agreement between theory and experiment is a proof that the present interpretation chosen to explain the diffuse scattering originating from the dislocations in the strained layers is quite rigorous. (Nevertheless, far too few authors follow the model of Kaganer).

3.11 Multilayers

Up to now we only dealt with X-ray diffraction studies of two different compressively strained systems. For the low misfit CoO on MgO system intense complex diffuse features were observed near the (002) and (004) reflections while for the large misfit MnO on MgO system we found broad anisotropic lines. As we shall outline in the course of this thesis, the tensile strain in CoO thin films induces an interesting phenomenon causing a change in the magnetic structure of CoO. The relaxation of CoO ($a_{CoO} = 4.267$ Å) on MnO films ($a_{MnO} = 4.445$ Å) was already mentioned in Section 2.5.2 where we discussed the *in-situ* RHEED investigation. As we mentioned in the beginning of the current chapter the interaction of hard X-rays with matter is very weak. One might be able to overcome this problem by growing multilayers in order to increase the diffraction volume. Note that by sandwiching the CoO between MnO layers also the critical thickness should increase.

In Figure 3.26 we present RSM's around the (113) off-specular reflection of three multilayer samples designed to have compositions such that the strain imposed by one of the layers (MnO or CoO) surmounts the other one (CoO or MnO).

In the first figure a RSM is presented for a sample having the composition 10× (80 ML MnO / 4 ML CoO) on MgO (001). The series of fringes in the vertical direction is due to the finite thickness perpendicular to the surface. The intense peak at the bottom with coordinates ($k_{\parallel}$=0.245, $k_{\perp}$=0.517 in units of $(2 \cdot 2\pi/\lambda)$ represents the MnO (113) reflection, and the distance between the subsidiary maxima is inversely proportional to the thickness of one double layer (MnO with CoO). This can be exemplified by measuring the distance between two subsidiary maxima $\Delta k_{\perp} = 3.957 \cdot 10^{-3}(2 \cdot 2\pi/\lambda)$, and using the prediction from Section 3.3 that $\Delta k = 2\pi/D$, results in $\Delta k_{\perp} \cdot (2 \cdot 2\pi/\lambda) = \frac{2\pi}{D}$ and D=194.6 Å, which is approximately the thickness of a double layer (CoO and MnO).

Although the sample was designed such that one could extract information about the out-of-plane lattice parameter of thin (4 ML) CoO strained on MnO, there is no peak observable which can be assigned to CoO [2]. This suggests that there is no fixed lattice parameter of the CoO layer, thus the relaxation process

---

If one assumes a Poisson ratio of ν=0.27 for CoO the diffraction peak for such a completely strained layer should lie almost outside (above) the area shown in figure ($a_{CoOstrained}$ = 4.135 Å) at $k_{\perp} \sim 0.5586 \cdot (2 \cdot \frac{2\pi}{\lambda})$. Therefore a long vertical scan (called **Q** scan) was performed at $k_{\parallel} = 0.2450$ since one expected a very wide peak (width of the peak is inversely proportional with the thickness which here was only 4 ML) but still there was no trace of any peak there.

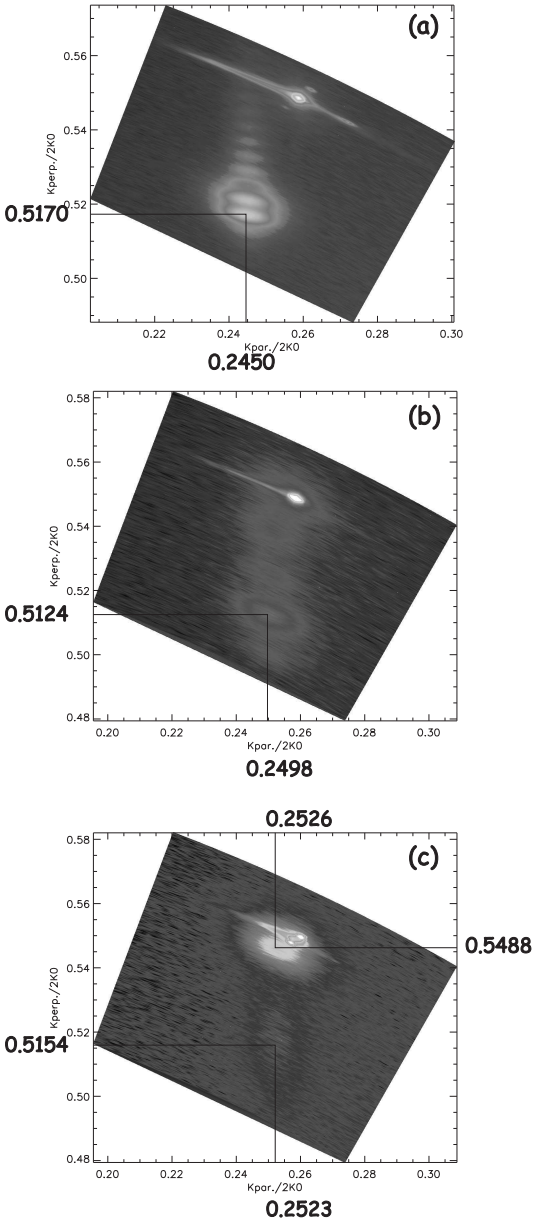

Figure 3.26: (a) RSM around the (113) reflection of a multilayer grown on a polished MgO substrate having the composition 10 × (80 ML MnO / 4 ML CoO), the first layer being in all of the samples the MnO layer on MgO. (b) Same as (a) but from a multilayer with composition 5 × (30 ML MnO / 10 ML CoO). (c) Same as (a) but from a multilayer with composition 3 × (11.7 ML MnO / 50 ML CoO).

already starts at 4 ML of CoO and the diffraction peak is so much smeared out that it is not noticeable (at least not with our apparatus). On the other hand the MnO layer is about 20 times thicker and thus under very small, almost unobservable, compressive strain. The lattice parameters are $a_{MnO\perp} = 4.468$ Å, $a_{MnO\parallel} = 4.445$ Å.

In order to observe what happens if one increases the CoO thickness and decreases the MnO thickness, such that the film thicknesses are comparable, we fabricated a sample with the following composition 5 × (10 ML CoO / 20 ML MnO) on MgO (001). The RSM is presented in Figure 3.26 (b). From the position of the MnO reflection one can deduce a lattice parameter set $a_{MnO\perp} = 4.508$ Å, $a_{MnO\parallel} = 4.359$ Å. From the separation of the subsidiary maxima $\Delta k_\perp = 0.0131(4\pi/\lambda)$ one gets D=58.55 Å for the double layer thickness which agrees with the reflectivity measurement results. It is interesting to observe that the CoO peak is still not present, probably if one would have grown a thicker MnO layer the CoO peak would also be visible.

Finally the last multilayer discussed here is the one with thick CoO and thin MnO layer: 3 × (11.7 ML MnO / 50 ML CoO). In this sample (Figure 3.26 (c)) the CoO reflection as well as the MnO reflection are visible. The lattice parameters are for the MnO film $a_{MnO\perp} = 4.482$ Å, $a_{MnO\parallel} = 4.318$ Å and for the CoO film $a_{CoO\perp} = 4.209$ Å, $a_{CoO\parallel} = 4.312$ Å. It is thus possible to achieve tensiley strained CoO films even for such high thicknesses. However, although almost 5 times thinner, the MnO layer is imposing a high tensile strain on the thick CoO film and the thin MnO film is just slightly compressed by the underlying CoO film. To understand this one can compare the shear modulus G of the two materials: $G_{CoO} \sim 4.85 \cdot 10^{10}\ N/m^2$, and $G_{MnO} \sim 5.15 \cdot 10^{10}\ N/m^2$, where G was calculated with the approximate formula $G = (c_{11} - c_{12})/2$ [42], but this difference is not high enough to explain this effect. Therefore the most plausible explanation for this effect is the asymmetry in the potential curve of the interatomic interaction. Due to this asymmetry compressive strain will relax earlier than a same amount of tensile strain. For this we refer the reader to the study of relaxation of single monolayers which is discussed in reference [43], for both, positive and negative misfits.

In order to check the thickness of these multilayers, reflectivity curves were measured. An example of one of these curves together with the theoretical fit is presented in Figure 3.27. The thickness of the sample is close to the upper limit of what can be measured with our apparatus using this technique because of the divergence of the X-ray beam and (or) the limited resolution. The fit was performed using the same procedure outlined in Section 3.3, but

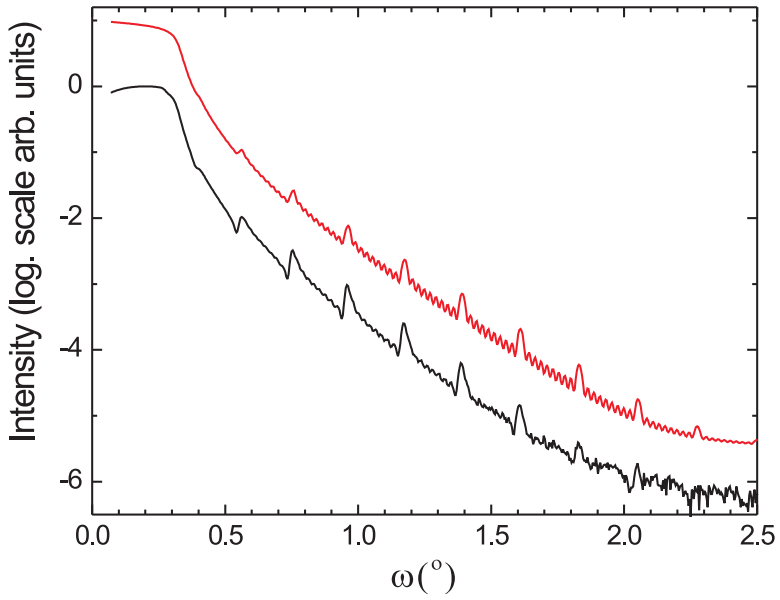

Figure 3.27: Reflectivity measurement (below) and fit (above) of the 10 double layer (CoO and MnO) described in the text. It should be noted that the very fine low amplitude oscillations are originating from the total thickness of the sample and the distance between the large peaks is inversely proportional to the thickness of one double layer composed of one CoO and one MnO layer. The fit was performed using the procedure described in Section 3.3

involving all interfaces between all the layers. The layer thicknesses used for the fit were 10 × (188 Å MnO and 8 Å CoO).

We have seen that using diffraction we were not able to get out useful information about the relaxation state of the ultra-thin CoO layers and therefore we have resorted to another surface sensitive technique, namely the Rutherford Back Scattering. Figure 3.28 shows the channelling measurements for three samples all consisting of epipolished MgO substrates with a thick (∼540 ML) MnO buffer layer and covered with CoO layers of different thicknesses. The graphs show the backscattering yield as a function of the angle of the incoming beam with respect to the sample. The dips are caused by channelling. The

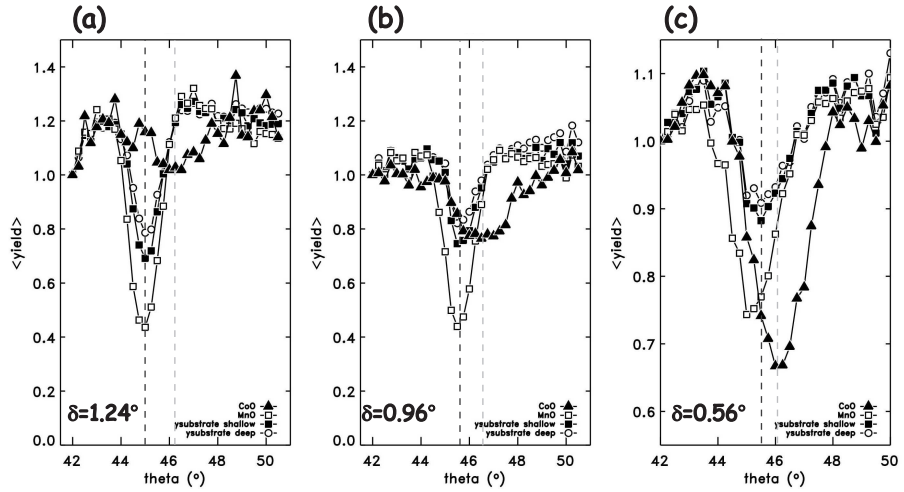

Figure 3.28: Rutherford Back Scattering Channelling measurements performed by Wim Arnold-Bik (University of Utrecht) on three samples, all grown on polished MgO substrates and all having the same 540 ML thick MnO buffer layer on top of which (**a**) 10 ML CoO, (**b**) 40 ML CoO and (**c**) 100 ML CoO was deposited. The dark dashed vertical line represents the value for the maximum channelling for the MgO substrate and the light dashed line the channelling position for the CoO layer.

two vertical dashed lines represent the positions for the maximum channelling for the substrate (dark line) and the CoO films (gray line). One would expect that the substrate MgO, because it is unstrained, has the channelling direction at $\phi = 45°$. This is not true in our case due to the miscut of the crystal and since the calibration of $\phi = 90°$ was made with respect to the surface of the film (see Section 2.2). As expected one observes that the difference between the two changeling directions, δ, decreases with increasing thickness due to the enhanced relaxation, however, even at thicknesses of 100 ML CoO the effect of the tensile strain from the underlying MnO layer is detectable. These deviations between the two channelling directions are also displayed in the figures. They give the following c/a ratios: for the 10 ML CoO film ($\delta = 1.24°$) c/a=0.96, for the 40 ML CoO film ($\delta = 0.96°$) c/a=0.97 (very much comparable with the value determined from diffraction for case of the multilayer presented in Figure 3.26 (**c**) for which is $c/a = a_{CoO\perp}/a_{CoO\parallel} = 0.976$), and finally for the 100 ML CoO ($\delta = 0.56°$) c/a=0.98. Note that the channelling from the 10 ML film is very poor (see Figure 3.28 (**a**)), which is in agreement with the absence of a clear diffraction peak in the first multilayer case,

suggesting also a large disorder in the film.

We have demonstrated that relaxation of strain in CoO layers grown on MnO buffer layers probably appears already at very small thicknesses, smaller than 4 ML of CoO. However one can produce tensiley strained CoO films having c/a ratios smaller than unity on MnO buffer layers. This finding will become a necessary ingredient in the last two chapters of this thesis, where the magnetic structure of CoO layers with different c/a ratios will be studied.

3.12 Is the diffuse scattering unique to CoO and MnO?

This thesis is mainly concerned with thin epitaxial layers of MnO and CoO for which, as discussed in the previous sections, diffuse scattering originating from stress relieving dislocations was observed and simulated. Since there are no reports in literature, except those concerning the priviously mentioned LEED studies [22, 23], dealing with the appearance of diffuse scattering in oxides, we may ask ourself wether the case of CoO and MnO are unique. Judging from the origins of this scattering, there should be no reason why other epitaxial thin films having sufficient misfit to cause misfit dislocations at the interface, would fail to produce the same phenomenon. We therefore turned our attention on samples produced earlier in our laboratory.

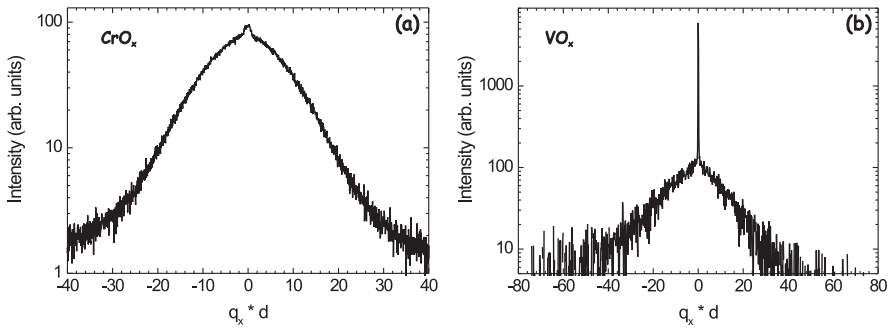

Figure 3.29: (a) ω scan across the (002) reflection of CrO_x on MgO (sample from ref [44]). The shape of the scan looks very much like the scan presented in Figure 3.18 660 ÅCoO on MgO. (b) ω scan across the (002) reflection of VO_x on MgO(sample from ref [45]). The diffuse scattering beside the central peak can be a consequence of not only dislocations but also of V and O vacancies. To find the real cause more diffraction data is needed.

Samples left over from previous PhD. students were remeasured, but now using the knowledge on the phenomenon of diffuse scattering originating from the appearance of these misfit dislocations. We present without special analysis two examples for the cases of a $\sim$ 325 Å CrO_x film on MgO [44] and a $\sim$ 100 Å VO_x film on MgO [45]. Figure 3.29 shows two q_x scans measured on the above samples across the films (002) reflections. The measurement done on the CrO_x film looks very much like the scan presented in Figure 3.18 from the 660 Å CoO film grown on MgO. This makes sense since the misfit of CrOx on MgO is higher than CoO on MgO, although the film thickness is half of the CoO film thickness.

The other example, VO_x on MgO, is comparable to the unrelaxed CoO on MgO case. Although the film is very thin (50 ML) there is a considerable amount of diffuse scattering around the coherent peak. This scattering may be due to the high concentration of vacancies (up to 15 %) present in VO_x since the displacement field due to vacancies can produce diffuse scattering as well. Thus this method combined with high intensity synchrotron measurements could give insights in a possible vacancy ordering in these types of systems.

3.13 Conclusions

By the use of Reciprocal Space Maps around specular and off-specular reflections, diffuse scattering originating from arrays of misfit dislocations were detected. These dislocations appear as a result of epitaxial strain in thin films when the elastic energy, which is proportional to the film thickness, exceeds the energy required for the appearance of dislocations that relieve the strain. Through careful measurements we were able to find the threshold value of the thickness where the diffuse scattering first appears, which we identified as the experimental critical thickness of CoO on MgO, namely ∼125 Å. This value is higher than the ∼55 Å, value predicted by the Matthews-Blakeslee model and very much smaller than the value of ∼ 360 Å given by the value of the c lattice parameter measured from specular scans.

In order to simulate the diffuse scattering we adopted the model of Kaganer *et al.* and applied it to the case of CoO and MnO. These oxides grown on MgO crystals proved to be adequate model systems for low to intermediate and high dislocation density, respectively. The results of these simulations were in accordance with the experimental findings if 45° tilted edge dislocations were considered as the cause of diffuse scattering. The presence of this type of dislocations is in agreement with earlier findings for the case of ionic solids.

The diffuse scattering is not only specific for the case of CoO and MnO but appears as a result of dislocations or other defects in the case of most epitaxial films such as semiconductors or other transition metal oxides such as CrO_x or VO_x.

References

[1] I.K. Robinson, D.J. Tweet, Rep. Prog. Phys. **55**, 599 (1992)

[2] I.K. Robinson, Phys. Rev. B, **33**, 3830 (1986)

[3] Jens Als-Nielsen, Des McMorrow, *Elements of Modern X-Ray Physics*, England (2001)

[4] B.D. Cullity and S.R. Stock, *Elements of X-ray Diffraction*, Prentice Hall (2001)

[5] P.F. Fewster, *X-ray scattering from semiconductors*, Imperial Colege Press, London, (2003)

[6] *International Tables for X-ray Crystallography* vol. 1-4, Birmingham (1974)

[7] T. Hibma *XRDFit8*, XRD data simulation program written in IDL 6.0

[8] http://web.utk.edu/ xling/main.htm

[9] http://www-lam.stanford.edu/xlab/Main.htm

[10] F.C. Frank, J.H. Merwe, Proc. Roy. London A **198**, 205, 216 (1949) and 125 (1949)

[11] J.W. Matthews, A.E. Blakeslee, J. Cryst. Growth, **27**, 118 (1974)

[12] Helmut Fll, http://www.tf.uni-kiel.de/matwis/amat/defen/index.html

[13] B.W. Dodson and J.Y. Tsao, Appl Phys. Lett., **51**, 1325 (1987)

[14] B.W. Dodson and J.Y. Tsao, Appl Phys. Lett., **52**, 1325 (1987)

[15] Jeffrey Y. Tsao, *Materials Fundamentals of Molecular Beam Epitaxy*, Academic Press, INC, San Diego (1993)

[16] Karin Wiesauer and G. Springholz, PRB, **69**, 245313 (2004)

[17] B. Henderson, *Defects in Crystalline Solids*, Crane, Russak & Comp. Inc. New York 1972

[18] V. Holý, K. Wolf, M. Kastner, H. Stanzl, W. Gebhardt, J. Appl. Cryst, 551, **27** (1994)

[19] V. Holý, J.H. Li, G. Bauer, F. Scheffler, H.-J. Herzog, J. Appl. Phys., 5013, **78** (1995)

[20] V. Holý, U.Pietsch, T. Baumbach *High Resolution X-Ray Scattering from Thin Films and Multilayers*, Springer, (1999) Berlin

[21] V.M. Kaganer, R. Köhler, M. Schmidbauer, R. Opitz, B. Jenichen, Phys. Rev. B, 1793, **55** (1997)

[22] M. Dynna, J.L. Vassent, A. Marty, J. Appl. Phys. 2650, **80**, (1996)

[23] M. Klaua, D. Ullmann, J.Wulfhekel, J. Kirschner, R. Urban, T. L Monchesky, J. F Cochran and B. Heinrich PRB, **64**, 134411 (2001)

[24] R. Chierchia, T. Böttcher, H. Heinke, S. Einfeldt, S. Figge, D. Hommel, J. Appl. Phys., 8918, **93** (2003)

[25] V. Srikant, J.S. Speck, D.R. Clarke, J. Appl. Phys. 4286, **82** (1997)

[26] R. Chierchia, T. Böttcher, S. Figge, M. Diesselberg, H. Heinke and D. Hommel, phys. stat. sol. (b) **228**, No. 2, 403406 (2001)

[27] P. Kidd, P.F. Fewster and N.L. Andrew, J. Phys. D. Appl. Phys. 133, **28** (1995).

[28] P.F. Fewster, N.L. Andrew, J. Appl. Cryst. 812, **26** (1993)

[29] P.F. Fewster, J. Appl. Cryst., 714, **25** (1992)

[30] P.F. Fewster, N.L. Andrew, J. Appl. Phys., 3121, **74** (1993)

[31] P.F. Fewster, Semicond. Sci. Techn., 1915, **8** (1993)

[32] V. Großmann, H. Heinke, K. Leonardi, D. Hommel, Journal of Crystal Growth, 447, **214** (2000)

[33] H.R. Relß, W. Spahn, R. Ebel, J. Niirnberger, M. Keller, H. Schtifer, M. Korn, M. Ehinger, W. Faschinger, G. Landwehr, Journal of Crystal Growth, 90, **184** (1998)

[34] A. Rockett, C.J. Kiely, Phys. Rev. B, 1154, **44**, (1991)

[35] G. Springholz and K. Wiesauer, Phys. Rev. Lett. 015507, **88** (2002)

[36] G. Alexe, H. Heinke, M. Klude, V. Kaganer, and D. Hommel, phys. stat. sol. (b) **229**, No. 1, 193196 (2002)

[37] A. Yu Babkevich, R.A. Cowley, N.J. Mason, S. Sandiford, A. Stunault, J. Phys.: Condens. Matter, 7101, **14** (2002)

[38] A.K. Head, Proc. Phys. Soc. London Sect. B **66**, 793 (1953)

[39] M.A. Krivoglaz, *X-ray and Neurton Diffraction in Nonideal Crystals*, Springer, Berlin (1996)

[40] S.B. Palmer and A. Waintal, Solid. State. Com. 663, **34** (1980)

[41] Orson L. Anderson and Donald G. Isaak, *Mineral Physics and Crystallography, A Handbook of Physical Constants*, (1995) American Geophysical Union.

[42] K-N. Tu, J.W. Mayer, L.C. Feldman, *Electronic Thin Film Science for Electrical Engineers and Material Scientists*, New York (1992)

[43] T. Hibma, in *Proceedings of the 2nd International Conference on the structure of Surfaces (ICSOS II)*, p419, Amsterdam (1987)

[44] O.C Rogojanu, *Stabilizing CrO by epitaxial growth*, University of Groningen, The Netherlands, (2002)

[45] A.D. Rata, *Strain-induced properties of epitaxial VO_x thin films*, University of Groningen, The Netherlands, (2004)

Chapter 4

Probing the electronic and magnetic structure of transition-metal oxide thin films

4.1 Introduction

The use of synchrotron radiation based high energy spectroscopies such as linearly and circularly polarized soft-x-ray absorption spectroscopy is relatively new [1]. This type of spectroscopy has been developed into full maturity only in the last 15 years, both in terms of instrumentation as well as in terms of a quantitative theoretical analysis of the spectra, which are often dominated by multiplet structures [2–4]. In fact, it all started with the pioneering work of Fink, Thole, Sawatzky and Fuggle, who used high energy electron-energy-loss spectroscopy to study narrow band and impurity systems, and recognized that the observed multiplet structures can provide an extremely detailed information about the local electronic structure of systems involving transition-metal and rare-earth atoms [5–8]. The underlying principle is the fact that the core hole produced has a strong attractive Coulomb interaction with the valence electrons. For strongly correlated oxides, this interaction is much larger than the one-electron band width of the valence electrons. The absorption process is therefore strongly excitonic and the spectra can then be understood in a straightforward manner in terms of atomic-like transitions.

These spectra are not only element specific, but above all, their multiplet structures are extremely sensitive to the charge, spin and orbital state of the ion due to the very effective dipole selection rules associated with the K ($1s \rightarrow 2p$), $L_{2,3}$ ($2p \rightarrow 3d$), and $M_{4,5}$ ($3d \rightarrow 4f$) transitions for the oxygen,

transition metal and rare-earth ions, respectively. In fact, the specificity to the initial state symmetry is so large, that one does not need a very good energy resolution in order to measure which of the possible initial state symmetries is occupied, since different symmetries lead to completely different multiplet structured spectra. In other words, an experimental energy resolution of 500 meV is often enough to distinguish initial states that are different by not more than a few meV or less in energy, making the technique extremely valuable for the study of electronic and magnetic phase transitions which usually occur in the temperature range up to roughly room temperature (kT_c = 25 meV). This is clearly demonstrated in later experiments using synchrotron radiation in the soft-x-ray region [2, 9–30].

Very important in this context was the development of sum rules, by which the separate orbital and spin contributions to the total magnetic moment in ferromagnetic materials can be deduced directly from the integrated circularly-polarized x-ray absorption spectra, without having to rely on simulations of the spectra [31–33]. This provides a considerable simplification for the use of the technique for the study of (multi-element) magnetic materials.

In addition, soft X-ray absorption spectroscopy is a surface sensitive technique. This aspect makes it extremely suitable to characterize the chemical composition, magnetic properties and electronic structure of surfaces, thin films and multilayers. In fact, there are not many spectroscopic tools that have the sensitivity to deal with such minute amounts of material.

Finally, it is worthwhile to mention that soft-x-ray absorption spectroscopy may be the only technique that has sufficient contrast for the orbital symmetry of the electrons, yielding information that is crucial to unravel the interplay between spin and orbital degrees of freedom in correlated oxides. This is a necessity for the understanding of, for instance, the magnetic properties of transition metal oxides with a high magnetocrystalline anisotropy.

4.2 Synchrotron radiation

First observed as an energy loss in electron storage rings, synchrotron radiation turned out to be a very useful source of electromagnetic radiation. Synchrotrons originally developed for the study of elementary particles are nowadays mostly used as powerful photon sources. These facilities are capable of generating electromagnetic radiation ranging from infra-red to hard X-rays. The principle is based on the radiation of electromagnetic waves from charged particles (electrons) undergoing an accelerated motion when passing through a magnetic field. Three types of magnet structures that are commonly used to generate synchrotron radiation are: bending magnets, undulators and wigglers. For more details about the synchrotron radiation we refer the reader to [34, 35].

Our soft X-ray absorption measurements were carried out at National Synchrotron Radiation Research Center (NSRRC) Taiwan. The beamline used for this purpose was the original Dragon beamline built by C.T. Chen and F. Sette at the National Synchrotron Light Source, Brookhaven National Laboratory and later moved to Taiwan. It delivers soft X-rays from a bending magnet in an energy range of 90-1200 eV [36–38]. This beamline and the NSRRC storage ring fulfilled completely the needs of our experiment which were a high degree of linear polarization, extreme intensity and energy stability as well as high resolution. Figure 4.1 sketches the layout of the Dragon monochromator.

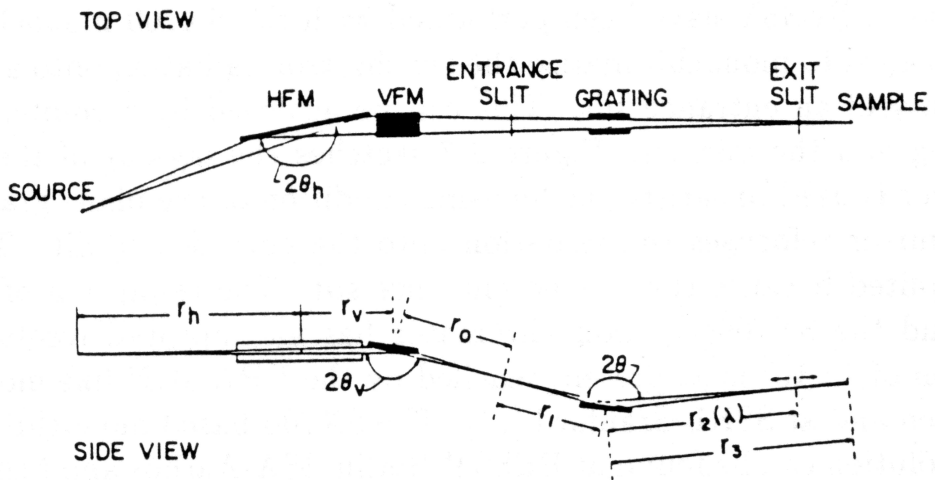

Figure 4.1: Dragon monochromator taken from ref [38].

The idea of designing a monochromator with a simple arrangement of spherical optical elements [36] turned out to be a great success, achieving an unprecedented high resolution of $1{:}10^4$ in the soft X-ray range. The horizontal and vertical focusing mirrors (HFM and VFM), which direct the radiation from the bending magnet and to allow the selection of linear or circular polarized light are followed by the entrance slit. This slit improves the resolution by making the monochromator less dependent on the source size. The grating which diffracts and focuses the photon beam is followed by a movable exit slit in order to follow the focus at different wavelengths. The overall photon energy resolution was usually set to 0.3∼0.4 eV for photon energies between 600-800 eV.

4.3 Principles of soft X-ray absorption

The absorption of X-rays arises as a result of a photoelectron process, which transfers an electron from a core level (1s, 2s, 2p) to the empty valence levels above the Fermi level. This is exemplified in Figure 4.2(a) where we use a one electron picture to describe the process. Later we will show that this picture is actually quite incorrect due to strong electron-electron correlation effects. The detection of the absorption process can be done in many ways. These possibilities are depicted in Figure 4.3. The most straight-forward method one can think of, is by measuring the number of incident photons and the number of transmitted photons trough a thin foil, this method is the so-called *transmission mode*. The ratio between the two numbers will be an exponential function of the absorption coefficient. Although this measurement method would be intuitively the most reliable one, the realization of the actual measurement is quite a challenge. The reason for this is that soft X-rays are strongly absorbed by matter. Just to give an example the absorption of X-rays for Ni is almost two orders of magnitude higher at 1 keV than at 8 keV photon energy (see for example ref. [39]). Therefore, in order to be able to measure the transmission in the soft X-ray energy region, the samples must be made extremely thin and homogeneous.

Another way of measuring the absorption coefficient is by detecting the decay products of the absorption process itself. In Figure 4.3 beside the transmission mode two other ways of measuring the absorption process are depicted: the fluorescent yield and the total electron yield.

In the *fluorescent yield mode* one detects the electromagnetic radiation resulting from the radiative decay of the electrons from the occupied Density Of States (DOS) to refill the core hole created by the X-ray absorption process.

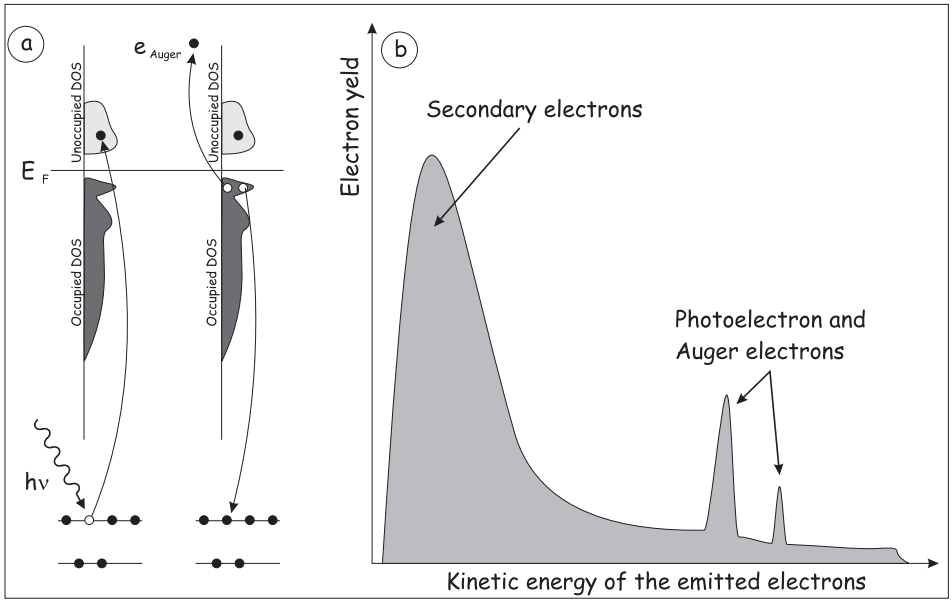

Figure 4.2: (a) Schematic figure of the absorption process. An core electron is excited by the incident X-rays into the unoccupied density of states (DOS) above the Fermi level. The measurement proceeds by detecting the decay products which can be photons, Auger electrons, photoelectrons or secondary electrons. (b) The energy distribution of these are decay products is presented.

The number of photons is proportional with the number of core holes created by the absorption process. This detection method proved to be more efficient and less demanding as far as the type of sample is concerned, since there is no limitation on the thickness of the sample contrary to the transmission mode nor has the sample to be conducting as is the case for the total electron yield mode (discussed later in this section). It is also important to note that this detection method is quite bulk sensitive since at these low photon energies there are almost no photon scattering processes: the probing depth of this technique is $\sim$2000 Å [15]. The drawback of this technique is that the mean free path of the fluorescent photons could be comparable to that of the incoming photons, hence self-absorption effects can take place, with the result that the fluorescent yield will no longer be proportional to the absorption coefficient. Moreover, the fluorescent process itself can be strongly dependent on the multiplet state that is created in the absorption process, making this technique less suitable for accurate quantitative measurements.

The last but most used detection method for the X-ray absorption process

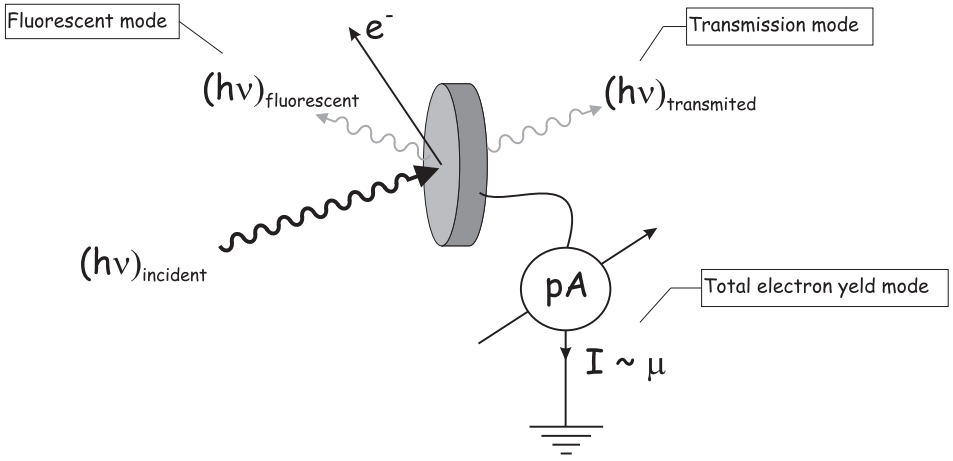

Figure 4.3: Measurement of the XAS spectra in the Total Electron Yield (TEY) mode. The absorbed photon creates a photoelectron which is emitted from a core level. The resulting core hole is later on occupied by a valence electron. The gained energy is transferred by Auger process to another electron which is emitted from the surface. The absorption is proportional to the number of electrons emitted thus also to the electrical current which neutralizes the sample. This drain current is measured as a function of photon energy and gives our XAS spectra.

is the *total electron yield mode* (TEY). What is measured here is the photoelectrical current which is supplied from the ground in order to neutralize the sample. Thus, as is depicted in Figure 4.3, the sample is grounded through a pico-amperemeter. Figure 4.2(a) exemplifies the processes that cause the "charging" of the sample: the unfilled core hole left behind by the X-ray absorption process is filled by an electron which decays from the occupied DOS, but in this case the process is not a radiative, but an Auger process. The energy gained from this decay is transferred to an other electron which can escape from the material. The leaving electron will conserve its kinetic energy only if is originating from not very deep under the surface, and this is due to the small elastic mean free path of the electrons in this energy region. Electrons originating from deeper regions of the sample will most probably suffer inelastic collisions and therefore will loose some of their kinetic energy. The photoemission spectrum of the electrons escaping from the irradiated surface is shown schematically in Figure 4.2(b). The amount of the so-called secondary electrons is orders of magnitude larger than the amount of the original Auger electrons, so experimentally it becomes very easy to measure

the decay products of the absorption process: the total electron yield can simply be measured by using a pico-amperemeter. However, it has been shown that the total electron yield signal is proportional to the absorption coefficient. The probing depth for this method is about 40-100 Å depending on material.

These two characteristics made TEY detection ideal for our purposes: the proportionality to the absorption coefficient allows for an accurate quantitative analysis of the spectra and the surface sensitivity is a necessity for ultra thin film samples.

In some cases when the material is very dense and the absorption is very high like in rare-earth elements, so that the escape depth of the electrons is comparable to the mean free path of the photons saturation effects may appear in the spectra. These effects were not of much importance for our transition metal oxide thin films and for further debate the reader is referred to [51].

In order to describe the XAS process one must know the ground state, the final state, and the matrix elements governing the transition cross section. Obviously, our aim is to find the ground state of the transition metal oxide film. The final state will be comprised by a core hole and an extra electron in the valence state. For the 2p-3d ($L_{2,3}$) transition the X-ray absorption process can be schematically represented as follows: $2p^6 3d^N + h\nu \rightarrow 2p^5 3d^{N+1}$. The probability of the electronic transition which actually gives us the absorption cross section is given by the Fermi golden rule:

$$\sigma \sim |\langle f|P|i\rangle|^2 \, \delta(E_f - E_i - \hbar\omega) \tag{4.1}$$

here $\langle f|P|i\rangle$ is the matrix element for the interaction between the *initial state* $|i\rangle$ and the *final state* $|f\rangle$. δ represents the requirement that the photon energy must match the energy difference between the possible electronic states. The operator P that couples the initial and final states can be written as:

$$P = e^{ik(\overrightarrow{\mathbf{n}}\cdot\mathbf{r})}\mathbf{p}\cdot\overrightarrow{\mathbf{e}} \tag{4.2}$$

where $\overrightarrow{\mathbf{e}}$ is the polarization vector and $\overrightarrow{\mathbf{n}}$ represents the propagation direction of the light and $\mathbf{r}$ is the electron position operator. Using the dipole approximation this operator is customary written as $P = \mathbf{p}\cdot\overrightarrow{\mathbf{e}}$, since only the first term is considered when expanding in series the exponential, here $\mathbf{p}$ is the momentum operator [40, 41]. The operator $\mathbf{p}$ can be replaced by the position operator $\mathbf{r}$ since $[\mathbf{r}, H] = (ih/m)\mathbf{p}$ [2]. It must be noted that the dipole approximation is valid since in this energy region since the wavelength of the soft X-ray radiation is much larger than the size of the atoms ($h\nu \in [100 - 1500]eV \Rightarrow \lambda \in [125 - 8.6]\mathring{A}$).

The final state, as shown in Figure 4.2(a) contains a core hole. However this core hole created by the incident photon will strongly interact with the valence electrons through the Coulomb interaction. Therefore, the process cannot be described in a one electron picture. In the case of transition metal oxides which are narrow band systems [42] the X-ray absorption is strongly excitonic since these strong Coulomb interactions are larger than the one electron bandwidth of the valence electrons, the electronic transition caused by the absorption process can be well described in an atomic-like picture [3, 5, 43, 46, 59]. A successful method to calculate the 2p-3d ($L_{2,3}$) spectrum is to consider a small cluster built up by a central transition metal atom surrounded by oxygen atoms located in such a way that they reflect the point symmetry of the transition metal atom in the crystal.

The number of existing initial and final multiplet states is a function of the number of d electrons, and this number can be very high already in the ionic limit (for the $2p^5 3d^5$ final state the number of possible terms is 1536). Figure 4.4 shows all available final states depending on the number of d electrons at the transition metal site. It is important to note that since the position operator $\mathbf{r}$ is an odd operator, the initial and the final states must have different parity, otherwise the integral in Equation 4.1 vanishes. The selection rules for the dipole transitions are:

$$\begin{aligned} \Delta l &= \pm 1 \\ \Delta m &= 0, \pm 1 \\ \Delta j &= 0, \pm 1 \\ \Delta L &= 0, \pm 1 \\ \Delta J &= 0, \pm 1 \\ \Delta S &= 0 \end{aligned} \tag{4.3}$$

All these rules are the so-called *dipole selection rules*. Satisfying these rules results in the pleasant surprise, namely, that not all possible final states presented in Figure 4.4 will be available and that the resulting XAS spectra will not be structure less.

The initial and final states of the atom are described by multiplets, which are multielectronic wavefunctions arising as a result of couplings of spin and angular momenta of the constituent electrons. For example the Russel-Saunders coupling results in such LS multiplet having terms of the form $^{2S+1}L_J$ with (2S+1) multiplicity. Each multiplet state has a certain atomic angular momentum quantum number J. Thus for an isolated atom each state is (2J+1)

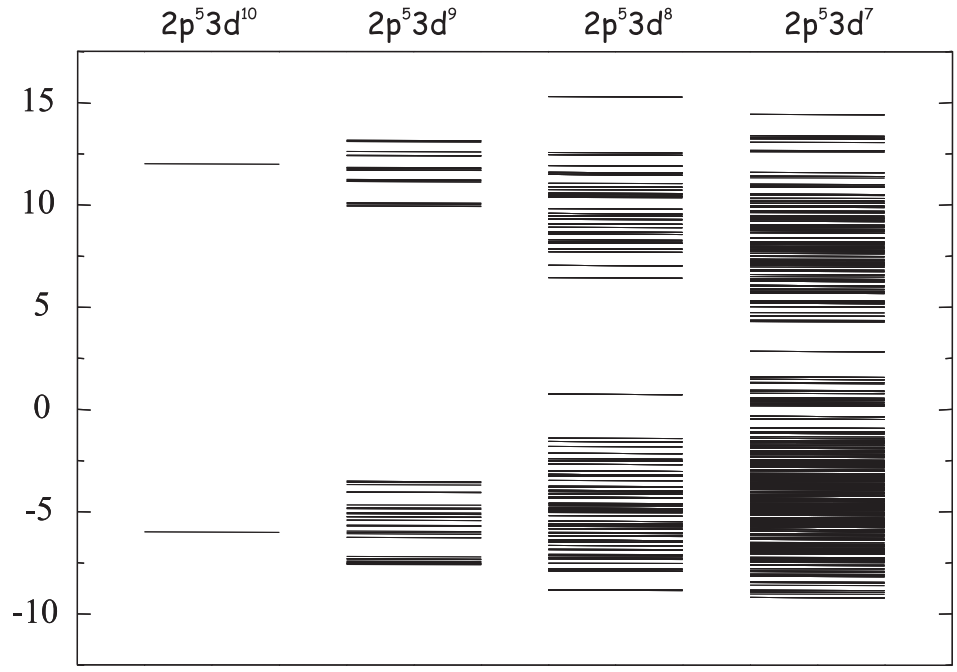

Figure 4.4: Multiplet structure in the final state $2p^5 3d^{N+1}$. Without the dipole selection rules all transitions to these states would be possible. Figure taken from ref. [46].

degenerate having $M_J = (-J, -J+1, \ldots, J-1, J)$ if there is no external magnetic field present. Taking in consideration all possible initial state multiplets ($2p^6 2d^N$) and final state multiplets ($2p^5 3d^{N+1}$), the transition probability can be calculated with Equation 4.1.

In the following we will present relevant examples illustrating some essential effects taken from the immense literature that appeared in the last 25-30 years after the prediction in 1985 [43] and experimental proof in 1986 [44] of strong magnetic X-ray dichroic effects.

4.4 Examples from literature

4.4.1 XAS of free atoms and solids

The first example presented here will be based on the findings of P. Gambardella *et al.* [45]. They reported XAS measurements on transition metal impurities on K and Na films. Here they were able to show that if transition

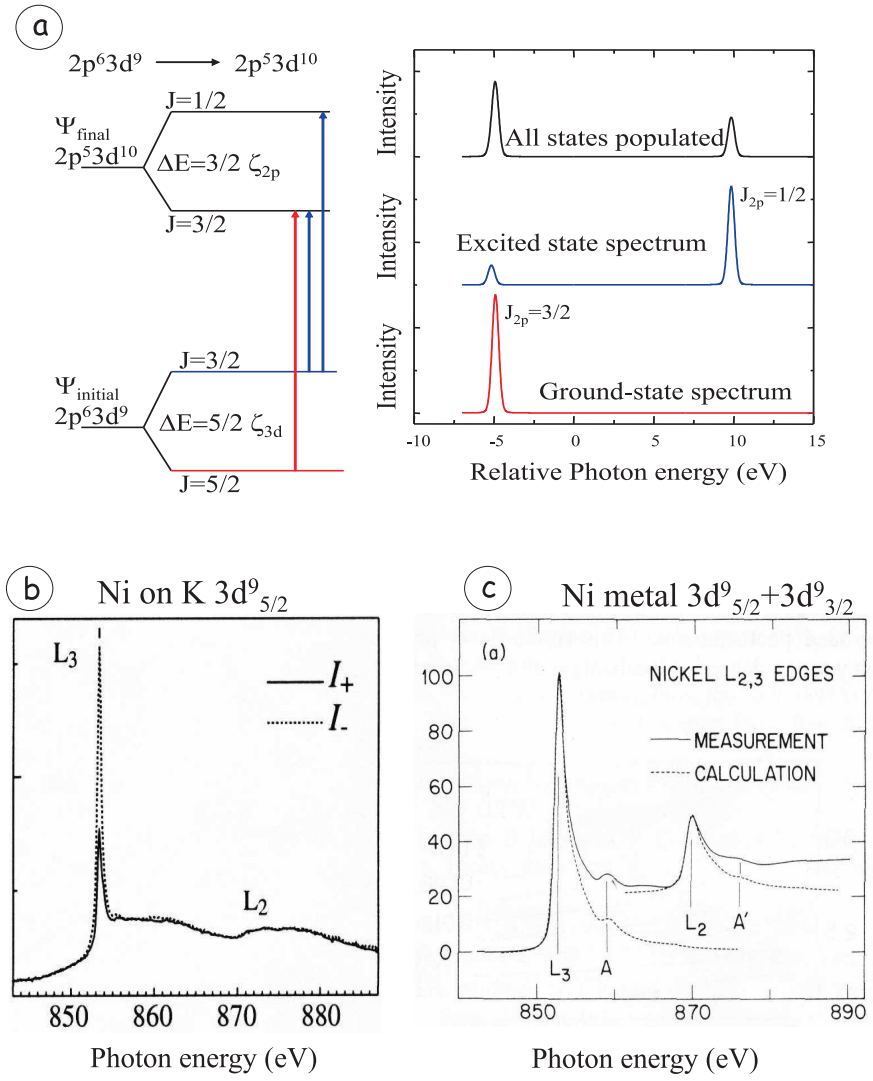

Figure 4.5: (a)(taken from ref [46]) (left) energy level diagram with initial and final states of the 2p-3d absorption process of Cu^{2+} or Ni $3d^9$. The initial state is the 3d spin orbit split ground state of which only the lowest part is occupied at very low temperatures in the atomic state. The final state is split by the core hole spin orbit interaction (several electronvolts in magnitude), (right) Calculated spectra depending on the population of the ground state.(b)(taken from ref [45]) XAS spectrum of Ni impurities on K film, only the L_3 edge is visible because in the ground state only the J=5/2 is populated and the dipole selection rules allow only $\Delta J = 0, \pm 1$. (c)(taken from ref [47]) XAS spectrum of Ni metal where both initial states are populated.

metal atoms are evaporated on these surfaces, such that they don't form clusters, they will exhibit atomic like character. The simplest example is Ni d^9. The XAS process is described by $2p^6 3d^9 \left|\alpha J M\right\rangle \rightarrow 2p^5 3d^{10} \left|\alpha' J' M'\right\rangle$ transition where the important quantum numbers are J and M, whereas α represents other quantum numbers. This example is convenient since in the final state only the p shell is unfilled since the d shell is complete. In this situation, for a free ion, according to Hund's rules, the ground state is described by a $^2D_{5/2}$ term. At an energy of $5/2{\cdot}\xi_{3d}$ above this ground level, where ξ_{3d} is the 3d spin-orbit coupling, lies the $^2D_{3/2}$ atomic level. For the final state the possible levels are $^2P_{3/2}$ and $^2P_{1/2}$ separated by $3/2{\cdot}\xi_{2p}$, where ξ_{2p} represents the 2p spin-orbit coupling (see also Figure 4.5(a)). In the atomic state, at very low temperatures, only the lowest lying level will be populated, therefore, taking into account the dipole selection rule $\Delta J = 0, \pm 1$, from the $^2D_{5/2}$ ground state only the $\Delta J = -1$ transition is possible hence only the $^2P_{3/2}$ state can be reached. This is represented by the bottom spectrum in Figure 4.5(a). The actual measurements are presented in Figure 4.5(b), one sees that only the transition from J=5/2 to J=3/2 occurs and that the L_2 edge is almost entirely suppressed.

In Ni metal both the states with J=5/2 and J=3/2 are instead populated due to both band formation and covalency. Therefore the transitions shown in Figure 4.5(a) (upper graph) are possible and the XAS spectrum of Ni metal has two peaks as seen in Figure 4.5(c), taken from ref [47].

4.4.2 X-ray circular dichroism

The use of synchrotron radiation provides not only a wide range of photon energies from which to choose, but it allows also to select of the light polarization. Therefore, one can use polarized light to probe only a specific part of the possible transitions. This is attainable since the photons have an angular momentum, namely q=±1 for circular and q=0 for linear polarized light. The polarization of the light is expressed in the $\vec{\mathbf{e}}$ vector of the dipole operator. Circularly polarized light is expressed as $\vec{\mathbf{e}}_{q=\pm 1} = \mp 1/\sqrt{2}(\vec{\mathbf{e}}_x + i\vec{\mathbf{e}}_y)$, and linearly polarized light as $\vec{\mathbf{e}}_{q=0} = \vec{\mathbf{e}}_z$. The dipole operator P can be thus expressed in spherical harmonics and this simplifies the calculation of integrals of the form of Equation 4.1. Depending on the polarization of the light, the dipole operator therefore be written as [48]:

$$P_{q=\pm 1} \quad = \quad r\sqrt{\frac{4\pi}{3}}Y_1^{\pm 1} \qquad \text{or,}$$

$$P_{q=0} = r\sqrt{\frac{4\pi}{3}}Y_1^0 \tag{4.4}$$

The magnetic quantum number M is changed according to the polarization of the impinging X-rays, such that $\Delta M = q$. The angular dependence of the absorption cross-section can be separated from the radial part such that the dependence of the absorption process on the light polarization becomes apparent. This is done using the Wigner-Eckart theorem (see for example the book of R.D. Cowan [49]), and σ becomes from Equation 4.1:

$$\sigma \sim \left|\left\langle f|P^{(1)}|i\right\rangle\right|^2 \cdot \begin{pmatrix} J & 1 & J' \\ -M & q & M' \end{pmatrix}^2 \tag{4.5}$$

where $\begin{pmatrix} J & 1 & J' \\ -M & q & M' \end{pmatrix}$ is the Wigner $3j$ symbol and $\left\langle f|P^{(1)}|i\right\rangle$ is the reduced matrix element of the dipole operator and gives the linestrength of the transition.

Shortly after the prediction and the experimental confirmation of the polarization dependent X-ray absorption, J.B. Goedkoop *et al.* published calculations of spectra for rare-earth compounds [50]. Figure 4.6 illustrates the energy levels involved in the absorption process for the simplest case: Yb^{3+}. The Ytterbium ion has 13 electrons in the 4f shell. According to Hund's rules this will result in ${}^2F_{7/2}$ ground state. The absorption process will excite a 3d electron to the only empty state in the 4f shell, thus the final state will become $3d^9 4f^{14}$, which again according to Hund's rules is the ${}^2D_{5/2}$. In the atomic state, without any magnetic field present, the transition with $\Delta J = -1$ is the only possible one. This case is depicted in the left side of Figure 4.6. When the ion is placed in a nonzero magnetic field the $2 \cdot 7/2 + 1 = 8$ fold degeneracy is lifted and the sub-levels are split by the Zeeman energy of $E_M = -\mu g_J \mathbf{H} M$. Depending on the polarization of the incident photons, three different groups of transitions exist as depicted in the right side of the energy-level diagram. Since the splitting of the Zeeman levels is of the order of $\sim$1 meV at high temperatures all levels will be equally populated, thus no effect of the dichroism will be visible. At low temperatures, however, the effect of the Boltzmann distribution on the occupation of these levels will cause an unequal absorption for different ΔM_j groups. At T=0K only the M=-7/2 will be populated therefore only absorption of light with polarization q=1 is possible. At the bottom of the figure the relative intensity is plotted as calculated from the squared values of the 3j symbols for the specific transitions. Formulas giving this dependence on the specific values of J and M can be found in many references [40, 50, 52, 54].

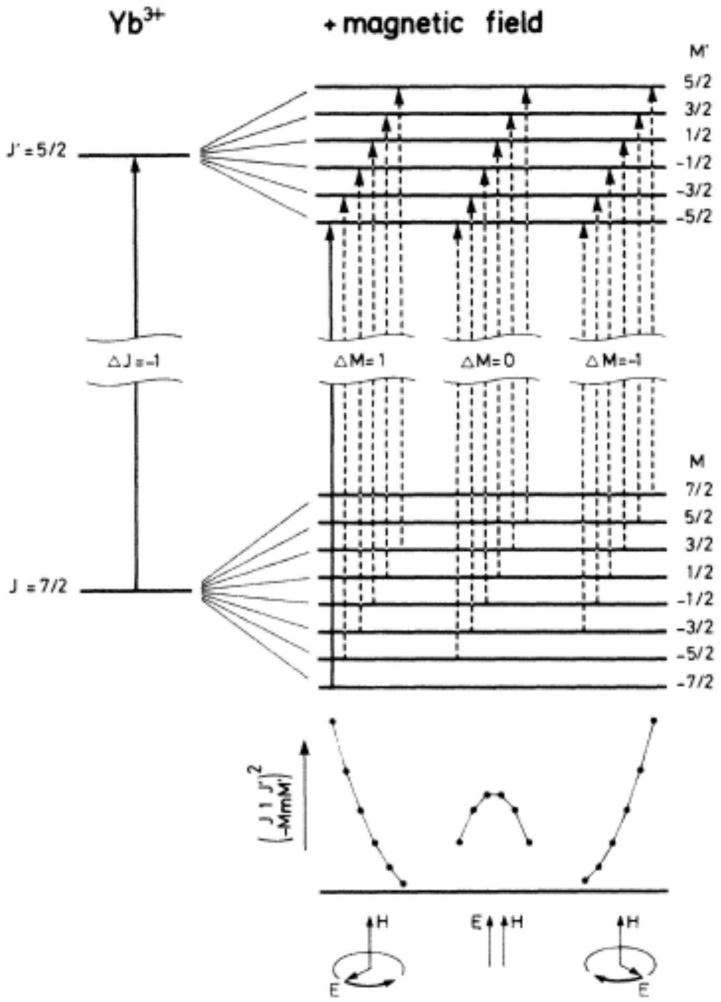

Figure 4.6: Energy level diagram for trivalent Ytterbium. On the left side the free ionic levels involved in the absorption process are shown , while on the right side the splitting due to the magnetic field becomes apparent. The energy scale in the figure is not on scale, the Zeeman splitting being very small, of the order of $\sim$ 1 meV. Figure taken from ref. [50].

Historically, after these developments focusing only on rare earth compounds, the first experimental circular dichroic experiment on 3d transition metals was done by C.T. Chen and co-workers [9] who studied the circular dichroism of Ni metal, presented in Figure 4.7.

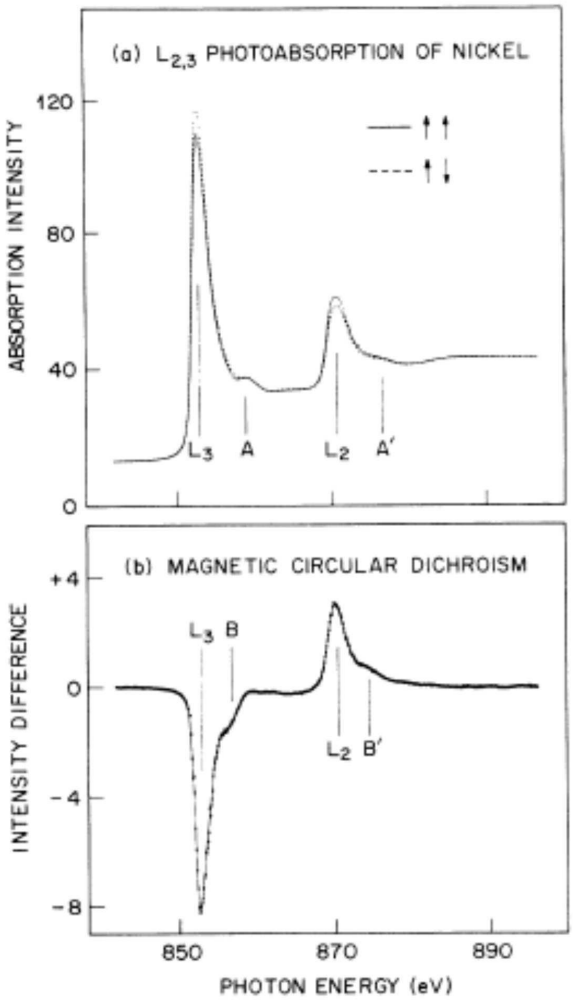

Figure 4.7: (a) X-ray absorption spectra of Ni metal taken with two different polarizations of the X-ray photons with respect to the spin direction. (b) Difference spectrum (Magnetic Circular Dichroism). Figure taken form ref. [53].

In ferromagnets the net magnetization is caused by lowering of the energy by parallel alignment of neighboring spins (*exchange energy*). Therefore, electronic states with m_j corresponding to a certain spin orientation will be preferentially occupied (the highest unoccupied state being the $m_j = 3/2$). Thus, considering the absorption cross-section from the calculation of the square of

the 3j symbols, one would expect the following ratios: $\sigma_{L_3tot}/\sigma_{L_2tot} = 2:1$ and $\frac{MCD_{L_3}}{MCD_{L_2}} = -1:1$. In reality the ratios measured were 2.6:1 and -1.6:1, respectively. Subsequent analysis has shown that these deviations from the statistical expectations are caused by the spin-orbit interaction active in the Ni 3d shell, i.e. that the Ni carries an orbital momentum. These results clearly show that the dichroic signal is sensitive to small details of the electronic and magnetic structure.

As we have seen, the line shape and intensity of the X-ray absorption spectrum depend on relative orientation of the photon angular momentum and the magnetization direction. This can be achieved for ferromagnetic samples where the net magnetic moment of the material is nonzero: $\langle \mathbf{M} \rangle \neq 0$. On the other hand, for antiferromagnets where the net magnetization is zero (or very small even in high external magnetic fields) there will be no (or very little) circular dichroism. However, linear dichroism, which is the difference in intensity or shape of the spectrum with the antiferromagnetic axis aligned *parallel* or *perpendicular* with the polarization axis, exists also in the case of antiferromagnets. Here the important quantity is the mean of the square of the magnetization ($\langle \mathbf{M}^2 \rangle \neq 0$). Thus in the following sections we will give some examples that deal with different linear dichroic effects.

4.4.3 X-ray magnetic linear dichroism

In this section we focus on the two classic experimental papers by Kuiper *et al.* [19] and Alders *et al.* [21] which constitute important milestones in the field on linear dichroism of antiferromagnetic materials.

In Figure 4.8 is presented the XAS spectrum of Fe_2O_3 antiferromagnet taken below and above the so-called Morin transition which occurs at ∼263 K. This magnetic phase transition manifests itself as a change of direction of the magnetic moments with respect to the trigonal c axis of the corundum structure of Fe_2O_3. In both cases the spectra are taken with the c axis parallel to the polarization direction of the incident X-rays and thus the difference in the spectra is entirely due to the change in orientation of the magnetic moments on the Fe sites. Fe_2O_3 with the Fe^{3+} ions having 5 high spin electrons in the 3d orbitals, has an atomic ground state $^6S_{5/2}$. This is an orbital singlet (L=0), thus the ground state has A_{1g} symmetry. Hence such a high polarization dependence can not be the result of a deformation of the oxygen octahedra (final state effects). At very low temperatures in a magnetic field, the J=5/2 level of the free ion is split into six Zeeman sub-levels and the ground state level m_j=-5/2 is occupied. Using linearly polarized light with the electric field vector aligned along the magnetic moments, the selection rule

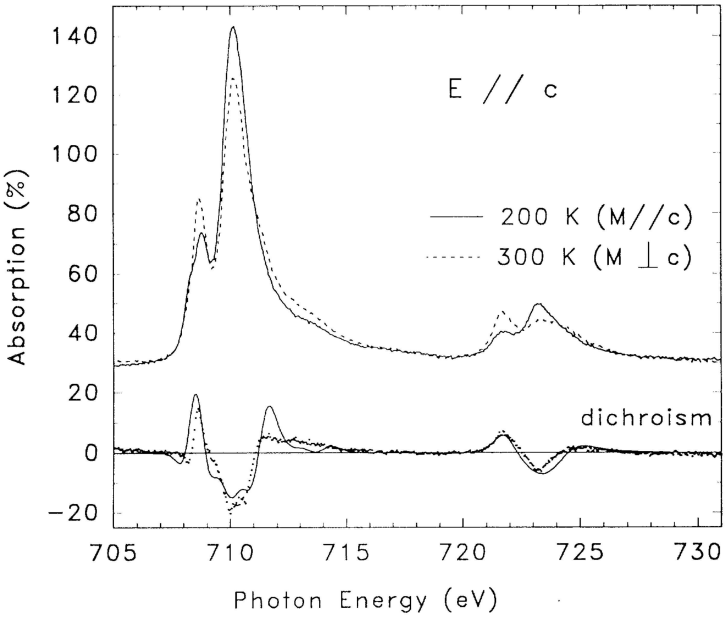

Figure 4.8: X-ray absorption spectra taken below (T=200K) and above (T=300K) the Morin transition (T=$\sim$ 263K) using polarized X-rays with the electric field vector parallel with the c axis. Figure taken form ref. [19].

Δm=0 restricts the transitions from the initial J=5/2, to states having J'=7/2 and J'=5/2 since only these have m'_j=5/2 sub-levels. When the electric field vector of the linearly polarized X-rays is perpendicular to the magnetic moments also the J'=3/2 levels can be reached, since this polarization carries Δm=-1. This causes the large difference observed between the spectra taken below and above the Morin transition.

The other classical example is the work of D. Alders *et al.* [21, 54]. Here the authors present a detailed analysis of thickness as well as temperature dependent X-ray magnetic linear dichroism of NiO thin films.

In NiO thin films epitaxially grown on MgO (001) the largest changes in the spectrum as a function of polarization were observer at the Ni L_2 edge (see Figure 4.9(a)). By comparing the calculated spectrum with the experimental one it was further shown that the ratio of the two components of the L_2 edge scales linearly with the exchange field. Therefore, this ratio of the two peaks served as a measure for the nearest neighbor spin-spin correlation function. The spectrum which for the sake of clarity is normalized to the first peak of the L_2 edge shows a change of the ratio of the order of 40 %. The variation of

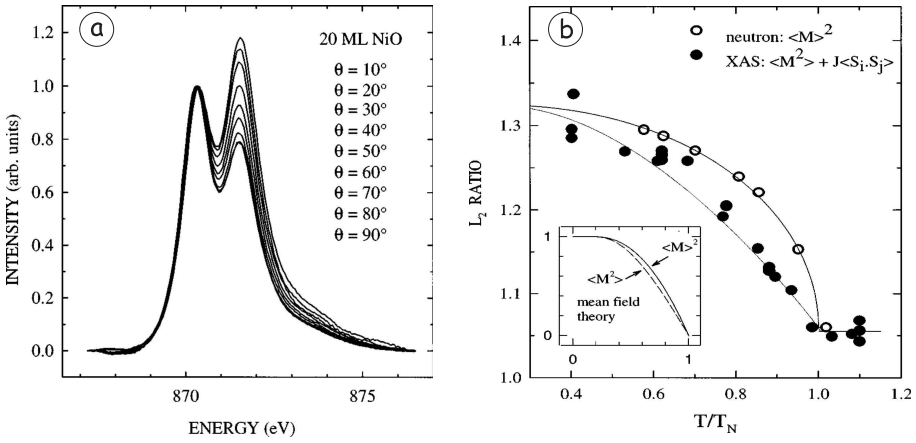

Figure 4.9: (a) Angular dependent Ni L_2 edge spectrum of 20 ML NiO thin film on MgO (100). (b) Ratio of the two peaks as a function of temperature, compared with neutron diffraction data taken from ref. [55]. Figure taken form ref. [21].

this ratio of the two peaks as a function of temperature, is presented in Figure 4.9 (b) and compared with the neutron diffraction data taken from ref [55]:

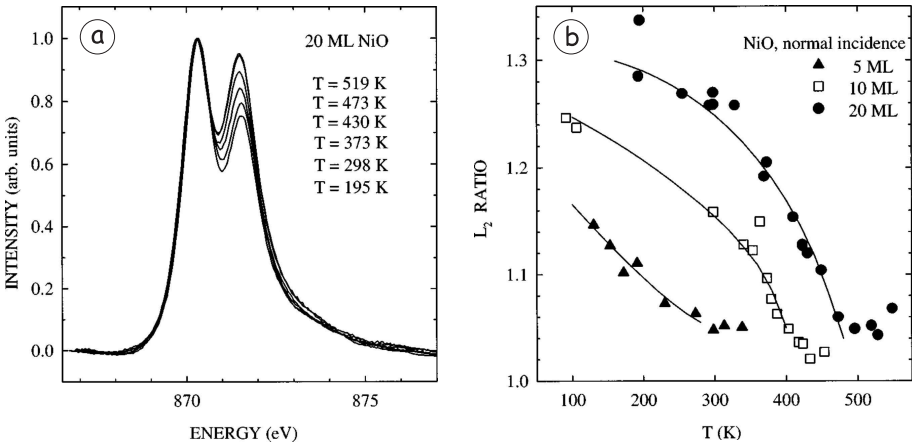

Figure 4.10: (a) Temperature dependent Ni L_2 edge spectrum of 20 ML NiO thin film on MgO (100). Ratio of the two peaks at the L_2 edge for films having different thickness. The 5 ML film has a Neél temperature close to room temperature. Figure taken form ref. [21].

while neutron diffraction measures the mean of the local magnetization $\langle \mathbf{M} \rangle$, XAS technique measures the mean of the square of the magnetization $\langle \mathbf{M}^2 \rangle$ plus the exchange field from the nearest neighbor spin-spin correlation function $J \langle \mathbf{S}_i \cdot \mathbf{S}_j \rangle$. From the comparison of the experimental with the calculated spectrum, it was also determined that for the NiO films, the easy axis of the spins on the Ni site is parallel to one of the [±2,±1,±1] crystallographic directions. Here we must note that spin-orbit coupling is crucial for the appearance of magnetic linear dichroism. In fact for O_h symmetry no orbital ordered state is expected (*no initial state effects*) and the absorption cross-section is independent of polarization. Therefore, MLD can occur only by some coupling of the electronic part with the spin part of the wavefunction. This coupling is exactly the spin-orbit coupling (see for more ref. [46]).

The temperature dependence of the spectrum also changes with the thickness of the NiO film as shown in Figure 4.10. For thinner films the temperature at which antiferromagnetic order is still present is lower. For the 5 ML NiO films on MgO the Néel temperature is only ∼295 K, i.e. less than 2/3 of the bulk value of 520 K. As we will show in Chapter 6 such an effect is not observed, for identically thin layers of CoO on MnO where the Néel temperature is the same as for the bulk.

4.4.4 The effects of the crystal fields

The electronic and magnetic properties of the materials are a direct consequence of the behavior of the outermost uncomplete electronic shells. Transition metals have open d shells while rare earths have open f shells. Therefore, the main interest focuses on these electrons. A change in environment, like a change in the atomic distances or a deformation of the distribution of the closest lying anions, will result in a change of the electron configurations of these ions. Since this electron configuration determines the electronic and magnetic properties of these materials, we are mainly interested in how, by altering the natural environment, we are able to change or even control of these properties. In order to achieve this, a closer look at this anion environment is appropriate.

In the rock-salt transition metal oxides such as CoO and MnO, studied in the following chapters, the metal cation is surrounded by an octahedra formed by the six oxygen anions as presented in Figure 4.11. In a free atom the atomic d levels are all degenerate, (they have the same energy and they are spherically symmetric), but once embedded in this cubic environment some d orbitals will be energetically more favorable than others. Figure 4.11 exemplifies this statement. Depending on their orientation with respect to the anions, the

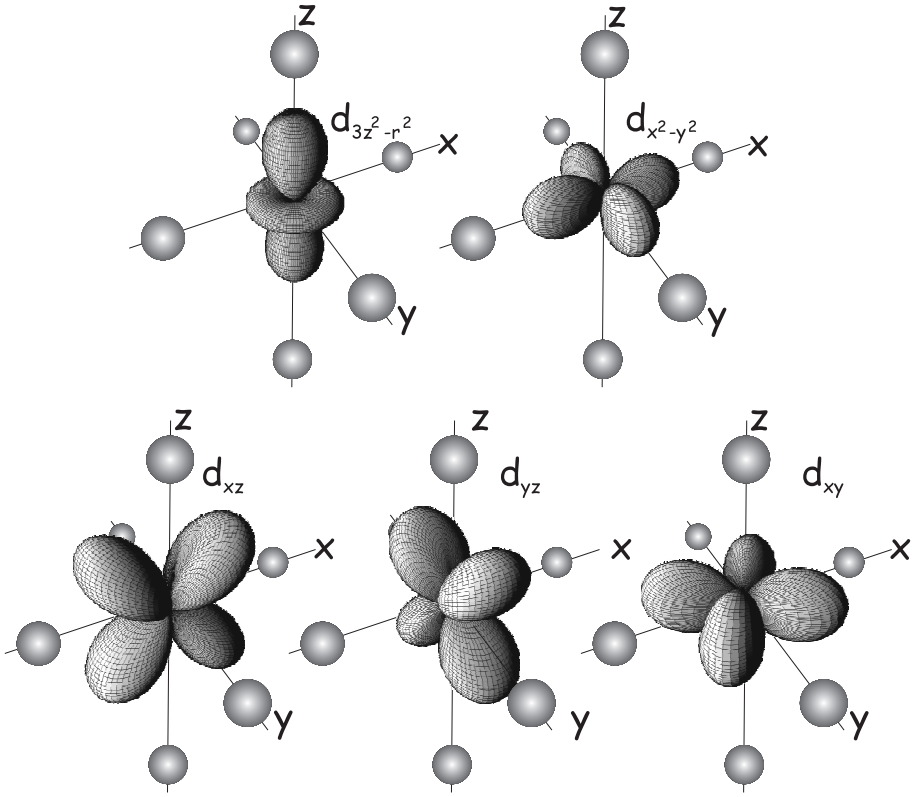

Figure 4.11: Schematic figure of d orbitals in an octahedral field of anions. It is here visible that the $d_{3z^2-r^2}$ and the $d_{x^2-y^2}$ orbitals point toward the anions while the d_{xy}, d_{xz} and d_{yz} orbitals point in between the anions. This is the reason for the energy splitting between the upper group and the lower group, namely between the e_g and the t_{2g} energy levels.

d orbitals will split into the lower lying triply degenerate t_{2g} orbitals, which point *in between* the anions, and the higher lying e_g orbitals which point *towards* the anions. The occupation of these orbitals will proceed in such a way that the overall energy will be minimal. In a simple picture there are two concurring effects which play a role in the population of these orbitals, the exchange interaction which minimizes the energy if two electrons are parallel and the crystal field splitting which favors the occupation of the lower t_{2g} orbital. If the crystal field splitting is small, the electrons will arrange as to maximize the spin. If the crystal field is large, the electrons will tend to stay in the lower t_{2g} orbitals, i.e. in the low spin configuration. In some cases the

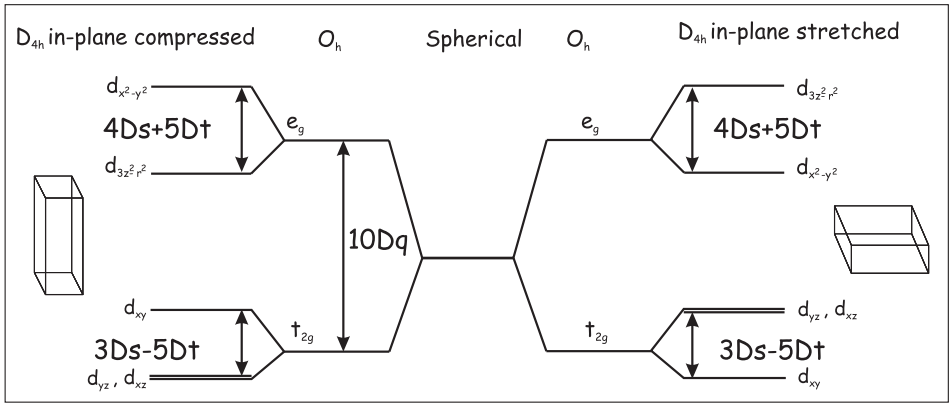

Figure 4.12: Energy level diagram of the d levels for a transition metal atom in an octahedral filed (middle) or in a tetragonally distorted octahedra (left and right).

so-called intermediate spin state is possible where both effects are comparable in size (see for details ref. [51]).

If the octahedra are tetragonally distorted, the symmetry decreases from O_h to D_{4h} and results in a further splitting of the initially so-called t_{2g} and e_g levels. Two extra parameters Ds and Dt are needed for describing this splitting. The reason why they are called parameters is because they are used together with Dq as empirical parameters when fitting the measurements. Theoretical calculations of these parameters were not very successful. All these quantities depend on the radial part of the wavefunctions and therefore the covalent mixing of the metal and ligand orbitals have a major contribution to them also. Figure 4.12 presents a simple overview of the energetics if the levels as a cause of the two kinds of tetragonal distortion of the octahedra.

4.4.5 Initial state effects

X-ray absorption using linearly polarized light is very sensitive also to orbital occupation. This is easily put in evidence by the following example regarding the dipole allowed K edge absorption from s orbital to p orbital. With linearly polarized light the absorption process which is given by Equation 4.1, is described by the integral of the form $\left\langle i \left| r\sqrt{\frac{4\pi}{3}}Y_1^0 \right| f \right\rangle$, which, by replacing $Y_1^0 = \sqrt{\frac{3}{4\pi}}\frac{z}{r}$, results in the simple integral $\langle i|z|f\rangle$. This integral can only be nonzero if the product of the three functions is even. Being now concerned

with the absorption from an s orbital (which is even) to a p orbital (which is an odd function in x, y or z variables), the product of the three will only be even if the polarization of the X-rays matches the orientation of the p orbital. Therefore, one can excite from an s level into a p_z orbital only with z polarized light and into a p_x orbital with x polarized light. A generalization of this example is the statement: *since the dipole operator* $\boldsymbol{r}$ *is a vector with components (x, y, z), the dipole transition will be allowed if the direct product of the irreducible representations of the initial and final states is or contains the irreducible representations to which x, y, or z belongs* [41].

A revealing result for a slightly different case, namely the case of specific type of holes in the 3d orbitals, is presented in Figure 4.13. Here polarization dependent X-ray absorption of $La_{1.85}Sr_{0.15}CuO_4$, a high T_c superconductor, is reproduced from ref. [15]. The authors (C.T. Chen *et al.*) were able to elucidate the controversy that appeared around the amount of O $2p_z$ versus the O $2p_{x,y}$ character as well as the Cu $3d_{3z^2-r^2}$ versus the Cu $3d_{x^2-y^2}$ hole character in these high temperature superconductive compounds which attracted much interest. The specific measuring geometry allowed for an easy and transparent procedure for data analysis and we shall follow a similar procedure for our experiments as detailed in the following two chapters. Until the appearance of this paper there was no transparent way of deriving what percentage of Cu 3d holes (which are responsible for the conduction), are $d_{3z^2-r^2}$ in character.

In Figure 4.13 is very clear that there is a strong difference in absorption as a function of the orientation of the electric field vector with respect to the c axis. The latter is perpendicular to the CuO_2 planes in this material. While the electrical field vector is parallel with the c axis (perpendicular to the CuO_2 planes) the absorption is almost entirely suppressed which clearly suggests that the 3d holes lie in the plane. The holes therefore reside mainly in the Cu $3d_{x^2-y^2}$ orbitals. The calculated value for the Cu $3d_{3z^2-r^2}$ hole character was determined to be $\sim$1.5%.

4.4.6 Final state effects

In one of the previous sections we shortly discussed the results of D. Alders *et al.* about MLD of NiO epitaxial thin films on MgO. We pointed out that thinner films have lower Néel temperatures than thicker films ($\sim$ 20 ML) which had Néel temperatures close to the bulk value. In this final section we want to turn the reader's attention to an instructive example discussed by M.W. Haverkort *et al.* [60]. These authors report XAS measurements from 1 ML NiO epitaxial film grown on Ag (100) single crystals, the film being capped by a 10 ML MgO (100) layer. As it was already discussed in Chapter 3 of

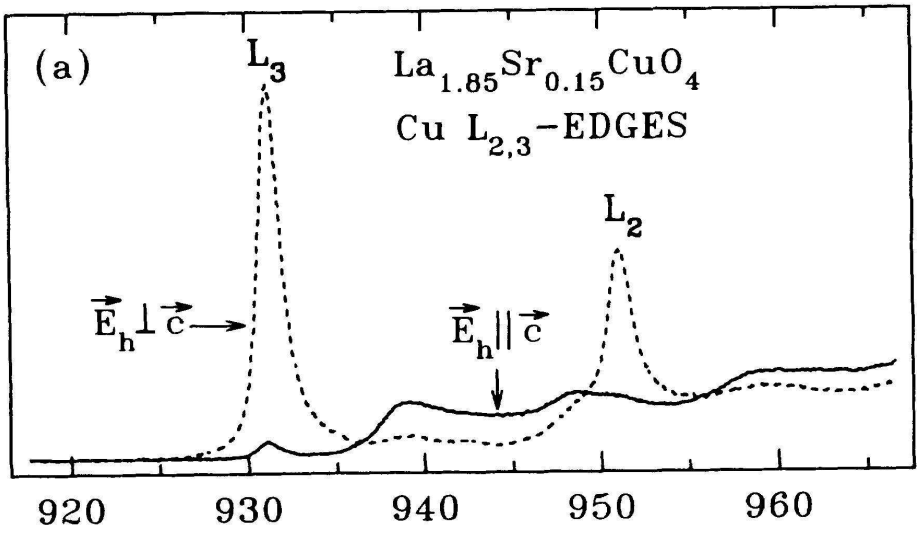

Figure 4.13: Cu $L_{2,3}$ XAS spectra showing immense difference in absorption for the two polarizations. The 3d hole in the Cu $3d^9$ ion resides almost entirely in the $d_{x^2-y^2}$ orbitals. Figure taken form ref. [15].

this thesis, very thin epitaxial films, with a certain amount of misfit, will grow homogeneously on the substrate and they will contain a considerable amount of tetragonal distortion imposed by the substrate. Observing the trend of the Neel temperature with decreasing thickness of the films, one would expect, as the authors also confirm, that the ordering temperature, if any, of 1 ML NiO is lower than room temperature. Even so, for this very thin film a clear linear dichroism was observed at room temperature as well as an energy shift of the peak at the Ni L_3 edge, as can be seen from Figure 4.14(a).

The linear dichroism observed was attributed entirely to the lowering of the symmetry of the Ni atoms, from a perfect octahedron (O_h point group symmetry) to a tetragonally deformed one (in-plane compressed and out-of-plane elongated D_{4h}). This scenario was illustrated in detail in the previous section 4.4.4, in the left side of Figure 4.12. A very simple explanation of the energy shift as well as the slight change in intensity is the following. In a one electron picture, Ni^{2+} has 8 d electrons, thus the high-spin ground state will consist of two holes occupying the $3d_{x^2-y^2}$ and the $3d_{3z^2-r^2}$ orbitals. The absorption process using z-polarized light will promote a 2p electron to the $3d_{3z^2-r^2}$ orbital but not to the $3d_{x^2-y^2}$ orbital because of reasons explained in Section 4.4.5. Changing the polarization of the X-rays to x, mainly the $3d_{x^2-y^2}$

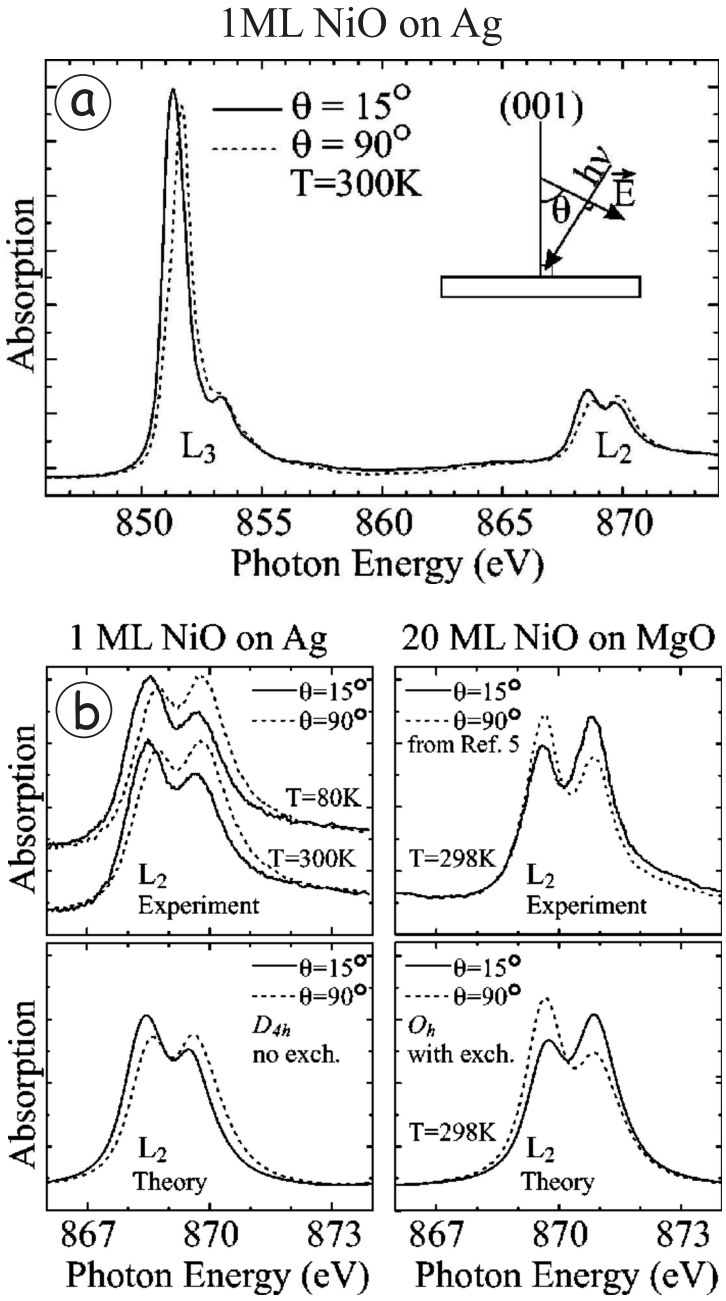

Figure 4.14: (a) Linear dichroism detected at the Ni $L_{2,3}$ edge from 1 ML NiO film on Ag (100). (b) Comparison of linear dichroism at the Ni L_2 edge of 1 ML NiO on Ag and 20 ML NiO on MgO. Figures taken form ref. [60].

orbitals will be reached. The exact final state in this case will be $2p^5\underline{3d}_{z^2-y^2} = \sqrt{3/4}(2p^5\underline{3d}_{3z^2-r^2}) + \sqrt{1/4}(2p^5\underline{3d}_{x^2-y^2})$ where the underline represents a hole. However, one can see from Figure 4.12 that the $3d_{3z^2-r^2}$ energy level is lower than the $3d_{x^2-y^2}$ thus the $2p^5\underline{3d}_{x^2-y^2}$ final state will be $4Ds + 5Dt$ lower than the $2p^5\underline{3d}_{3z^2-r^2}$ state. This is exactly the energy difference that is measured by the difference of the position of the peak at the Ni L_3 edge in Figure 4.14(a). Moreover, the authors have also presented theoretical spectra with and without the inclusion of an exchange field simulating the existence and the absence of magnetic ordering. They found that the spectra from 1 ML NiO on Ag can be described very well using only a D_{4h} point group and no exchange, thus without any magnetic ordering present in the film.

This study exemplifies very convincingly that final state effects can also produce strong dichroism, thus one must be careful when attributing the observed dichroic effects as results of magnetic ordering. There is a similar situation for the case of epitaxial MnO layers on Ag (100), as will be presented in more detail in Chapter 6.

4.5 Conclusions

In this chapter we discussed the X-ray absorption technique by the use of examples from the available literature. We have demonstrated that XAS can give insight not only in ferromagnets but also in antiferromagnets. We have also shown that one-electron picture can be very useful in qualitative explanations but eventually one has to use the full atomic cluster calculations in order to get quantitative results. For more details about such calculations we refer the reader to the PhD thesis of M.W. Maurits [46]. This chapter was ment to be an introductory chapter for the rest of this thesis where we will deal with the changes in the magnetic structure of CoO and MnO as a result of strain and interlayer coupling.

References

[1] For a review see: 'Unoccupied Electronic States', 'Fundamentals for XANES, EELS, IPS, and BIS', edited by J.C. Fuggle and J.E. Inglesfield, Topics in Applied Physics, Vol. 69 (Springer Verlag, Berlin 1992)

[2] See review by F. M. F. de Groot, J. Electron Spectrosc. Relat. Phenom. **67**, 529 (1994).

[3] A. Tanaka and T. Jo, J. Phys. Soc. Jpn. **63**, 2788 (1994).

[4] See review in the Theo Thole Memorial Issue, J. Electron Spectrosc. Relat. Phenom. **86**, 1 (1997).

[5] B.T. Thole, R.D. Cowan, G.A. Sawatzky, J. Fink, J.C. Fuggle, Phys. Rev. B **31**, 6856 (1985)

[6] J. Fink, Th. Müller-Heinzerling, B. Scheerer, W. Speier, F.U. Hillebrecht, J.C. Fuggle, J. Zaanen and G.A. Sawatzky, Phys. Rev. B **32**, 4899 (1985)

[7] J. Fink, Advances in Electronics and Electron Physics **75**, 121 (1989)

[8] J. Fink, in 'Unoccupied Electronic States', 'Fundamentals for XANES, EELS, IPS, and BIS', edited by J.C. Fuggle and J.E. Inglesfield, Topics in Applied Physics, Vol. 69 (Springer Verlag, Berlin 1992), p. 203

[9] C.T. Chen and F. Sette, Phys. Scripta **T31**, 119 (1990)

[10] G. van der Laan, B.T. Thole, G.A. Sawatzky, and M. Verdaguer, Phys. Rev. B **37**, 6587 (1988)

[11] C. Cartier dit Moulin, P. Rudolf, A.-M. Flank, and C.-T. Chen, J. Phys. Chem. **96**, 6196 (1992).

[12] M. Abbate, J.C. Fuggle, A. Fujimori, L.H. Tjeng, C.T. Chen, R. Potze, and G.A. Sawatzky, Phys. Rev. B **47**, 16124 (1993)

[13] M. Abbate, R. Potze, G.A. Sawatzky, C. Schlenker, H.J. Lin, L.H. Tjeng, C.T. Chen, D. Teehan, and T.S. Turner, Phys. Rev. B **51**, 10150 (1995)

[14] H.F. Pen, L.H. Tjeng, E. Pellegrin, F.M.F. de Groot, G.A. Sawatzky, M.A. Veenendaal, and C.T. Chen, Phys. Rev. B **55**, 15500 (1997)

[15] C.T. Chen, L.H. Tjeng, J. Kwo, H.L. Kao, P. Rudolf, F. Sette, and R.M. Fleming, Phys. Rev. Lett. **68**, 2543 (1992)

[16] N.L. Saini, S. Venkatesh, P. Srivastava, B.R. Sekhar, K.B. Garg, L.H. Tjeng, C.T. Chen, A. Menovsky, and J.J.M. Franse, J. Phys.:Condens. Matter **8**, 2467 (1996)

[17] J.-H. Park, L.H. Tjeng, J.W. Allen, C.T. Chen, P. Metcalf, J.M. Honig, F.M.F. de Groot, and G.A. Sawatzky, Phys. Rev. B **61**, 11506 (2000)

[18] T. Mizokawa, L.H. Tjeng, P.G. Steeneken, N.B. Brookes, I. Tsukada, T. Yamamoto, and K. Uchinokura, Phys. Rev. B. (accepted)

[19] P. Kuiper, B.G. Searle, P. Rudolf, L.H. Tjeng, and C.T. Chen, Phys. Rev. Lett. **70**, 1549 (1993)

[20] D. Alders, J. Vogel, C. Levelut, S.D. Peacor, T. Hibma, M. Sacchi, L.H. Tjeng, C.T. Chen, G. van der Laan, B.T. Thole, and G.A. Sawatzky, Europhys. Lett. **32**, 259 (1995)

[21] D. Alders, L.H. Tjeng, F.C. Voogt, T. Hibma, G.A. Sawatzky, J. Vogel, M. Sacchi, S. Iacobucci, and C.T. Chen, Phys. Rev. B **57**, 11623 (1998).

[22] P. Rudolf, F. Sette, L.H. Tjeng, G. Meigs, and C.T. Chen, J. Magn. Magn. Mater. **109**, 109 (1992)

[23] L.H. Tjeng, Y.U. Idzerda, P. Rudolf, F. Sette, and C.T. Chen, J. Magn. Magn. Mater. **109**, 288 (1992)

[24] J. van Elp, S.J. George, J. Chen, G. Peng, C.T. Chen, L.H. Tjeng, G. Meigs, H.-J. Lin, Z.H. Zhou, M.W.W. Adams, B.G. Searle, and S.P. Cramer, Proc. Natl. Acad. Sci. USA **90**, 9664 (1993)

[25] Y.U. Idzerda, C.J. Gutierrez, L.H. Tjeng, H.-J. Lin, G. Meigs, and C.T. Chen, J. Magn. Magn. Mater. **127**, 109 (1993)

[26] Y.U. Idzerda, L.H. Tjeng, H.-J. Lin, C.J. Gutierrez, G. Meigs, and C.T. Chen, Phys Rev. B **48**, 4144 (1993)

[27] C.T. Chen, Y.U. Idzerda, C.-C. Kao, L.H. Tjeng, H.-J. Lin and G. Meigs, Mat. Res. Soc. Symp. Proc. Vol. **375**, 59 (1995)

[28] C.T. Chen, Y.U. Idzerda, C.-C. Kao, L.H. Tjeng, H.-J. Lin, and G. Meigs, Materials Science and Engineering B **31**, 49 (1995)

[29] Y.U. Idzerda, C.T. Chen, H.-J. Lin, L.H. Tjeng, and G. Meigs, Physica B **208&209**, 746 (1995)

[30] E. Pellegrin, L.H. Tjeng, F.M.F. de Groot, R. Hesper, G.A. Sawatzky, Y. Moritomo, and Y. Tokura, J. Electron Spectrosc. Relat. Phenom. **86**, 115 (1997)

[31] B.T. Thole, P. Carra, F. Sette, and G. van der Laan, Phys. Rev. Lett. **68**, 1943 (1992)

[32] P. Carra, B. T. Thole, Massimo Altarelli, and Xindong Wang, Phys. Rev. Lett. **70**, 694 (1993)

[33] C.T. Chen,Y. U. Idzerda, H.-J. Lin, N. V. Smith, G. Meigs, E. Chaban, G. H. Ho, E. Pellegrin, and F. Sette, Phys. Rev. Lett. **75**, 152 (1995)

[34] K. Wille, Rep. Prog. Phys. **54**, 1005 (1991)

[35] D. Attwood, *Soft x-rays and extreme ultraviolet radiation: Principles and applictaions*, Cambridge University Press, Cambridge (1999)

[36] C.T. Chen, Nucl. Instrum. Methods, **256**, 595 (1987)

[37] C.T. Chen and F. Sette, NSLS Annual Report, 2-16 (1987)

[38] C.T. Chen and F. Sette, Rev. Sci. Instrum. **60**, 1616 (1989)

[39] *X-ray data booklet*, University of California, California (2001)

[40] J. Goedkoop, *X-ray dichroism of rare earth materials*, PhD thesis, Nijmegen (1989)

[41] J. Stöhr, *NEXAFS Spectroscopy*, Springer-Verlag, Berlin (1992)

[42] P.A. Cox, *Transition Metal Oxides*, Oxford (1995)

[43] B.T. Thole, G. van der Laan, J.C. Fuggle, G.A. Sawatzky, R.C. Karnatak, J.-M. Esteva, Phys. Rev. B, **32**, 5107 (1985)

[44] G. van der Laan, B.T. Thole, G.A. Sawatzky, J.B. Goedkoop, J.C. Funggle, J.-M. Esteva, R. Karnatak, J.P. Remeika, H.A. Dabkowska, Phys. Rev. B, **34**, 103 (1986)

[45] P. Gambardella, S.S. Dhesi, S. Gardonio, C. Grazioli, P. Ohresser, and C. Carbone, Phys. Rev. Lett. **88**, 047202 (2002)

[46] M.W. Maurits, *Spin and orbital degrees of freedom in bulk and thin film transition metal ixides studied by 2p core level X-ray absorption spectroscopy*, PhD thesis, Köln (2005)

[47] C.T. Chen, N.V. Smith, F. Sette, Phys. Rev. B, **43**, 6785 (1991)

[48] R. Nakajima, *X-ray magnetic circular dichoism spectroscopy in transition metal thin films*, PhD. thesis, Stanford University (1998)

[49] R.D. Cowan *The theory of atomic structure and spectra*, University of California Press, Berkeley (1981).

[50] J.B. Goedkoop, B.T. Thole, G. van der Laan, G.A. Sawatzky, F.M.F. de Groot, J.C. Fungle, Phys. Rev. B, **37**, 2086 (1988)

[51] F.M.F. de Groot, *X-ray absorption of transition metal oxides*, PhD. thesis, Nijmegen (1991)

[52] E. Arenholz, *Magnetic Dichroism in Photoemission from Lanthanide Matherials: Basic Concepts and Applications*, PhD thesis, Berlin (1996)

[53] C.T. Chen, F. Sette, Y. Ma, S. Modesti, Phys. Rev. B, **42**, 7262 (1990)

[54] D. Alders, *Epitaxial transition metal oxide films studied by high energy spectroscopy*, PhD. thesis, Groningen (1996)

[55] W.L Roth, Phys. Rev. **111**, 772 (1958)

[56] M. Gerloch, R.C. Slade, *Ligand-field Parameters*, Cambridge (1973)

[57] B.N. Figgis, *Introduction to ligand fields*, John Wiley & Sons, Inc (1966)

[58] C.J. Ballhausen, *Introduction to ligand field theory*, McGraw-Hill, New York (1962)

[59] M.W. Maurits, *Near-ground state symmetries and x-ray absorption spectra of transition metal thin films*, Master thesis, Groningen (2002)

[60] M.W. Haverkort, S.I. Csiszar, Z. Hu, S. Altieri, A. Tanaka, H.H. Hsieh, H.-J. Lin, C.T. Chen, T. Hibma and L.H. Tjeng, Phys. Rev. B, **69**, 020408(R) (2004)

Chapter 5

Controlling orbital moment and spin orientation in CoO layers by strain

5.1 Introduction

The discovery of the exchange bias phenomenon in surface-oxidized cobalt particles about 50 years ago [1] marks the beginning of a new research field in magnetism. Since then several combinations of antiferromagnetic (AFM) and ferromagnetic (FM) thin film materials have been fabricated and investigated [2, 3], motivated by their potential for applications in information technology. Numerous theoretical [4–8] and experimental [9–14] studies have been devoted to unravel the mechanism(s) responsible for exchange biasing. However, no conclusive picture has emerged yet. A major part of the problem lies in the fact that there is insufficient information available concerning the atomic and magnetic structure of the crucial interface between the AFM and FM material. The important issue of, for instance, spin reorientations in the AFM films close to the interface is hardly considered [15–19], and the role of epitaxial strain herein has not been discussed at all.

In this chapter we study the magnetic properties of CoO thin films epitaxially grown on MnO(100) and on Ag(100), as model systems for an AFM material under either tensile or compressive in-plane stress. Our objective is to establish how the magnetic anisotropy as well as the spin and orbital contributions to the magnetic moments depend on the lowering of the local crystal field symmetry by epitaxial strain. We will use polarization dependent x-ray absorption spectroscopy (XAS) at the Co $L_{2,3}$ ($2p \rightarrow 3d$) edges,

to determine the magnitude and orientation of the magnetic moments in the CoO/MnO(100) and CoO/Ag(100) systems. [1]

Part of this chapter was submitted to Phys. Rev. Lett. as *"Controlling orbital moment and spin orientation in CoO layers by strain"* S. I. Csiszar, M. W. Haverkort, Z. Hu, A. Tanaka, H. H. Hsieh, H.-J. Lin, C. T. Chen, T. Hibma and L. H. Tjeng

5.2 The sample compositions and experimental details

The actual compositions of the CoO/MnO(100) and CoO/Ag(100) systems are (14Å)MnO/(10Å)CoO/(100Å)MnO/Ag(001) and (90Å)CoO/Ag(001), respectively. The two samples were grown by molecular beam epitaxy (MBE), evaporating elemental Mn and Co from alumina crucibles in a pure oxygen atmosphere of 10^{-7} to 10^{-6} mbar. The base pressure of the MBE system is in the low 10^{-10} mbar range. The thickness and epitaxial quality of the films are monitored by reflection high energy electron diffraction measurements. Since the lattice constant of bulk Ag (4.09Å) is smaller than that of bulk CoO (4.267Å) and MnO (4.445Å), we find from x-ray diffraction that CoO on Ag is slightly compressed in-plane ($a_{\parallel} \approx 4.235$Å, $a_{\perp} \approx 4.285$Å), and from reflection high energy electron diffraction (RHEED) that CoO sandwiched by MnO is about 4% expanded in-plane ($a_{\parallel} \approx 4.424$Å). The sandwich structure was used to maximize the CoO thickness with full in-plane strain. Details about the growth can be found in Chapter 2.

The XAS measurements were performed at the Dragon beamline of the NSRRC in Taiwan using *in-situ* MBE grown samples. The spectra were recorded using the total electron yield method in a chamber with a base pressure of 3×10^{-10} mbar. The photon energy resolution at the Co $L_{2,3}$ edges ($h\nu \approx 770 - 800$ eV) was set at 0.3 eV, and the degree of linear polarization

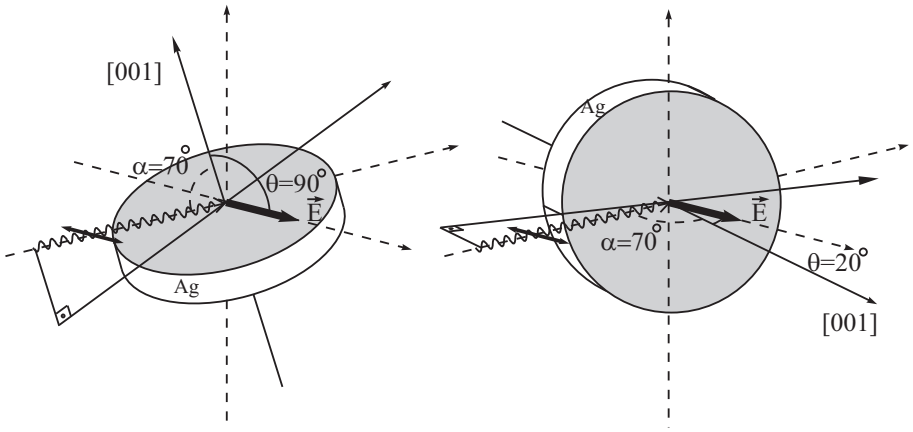

Figure 5.1: Experimental XAS geometry, with polarization of the light in the horizontal plane. θ is the angle between the electric field vector $\vec{E}$ and the [001] surface normal, and α the tilt between the Poynting vector and the surface normal.

was $\approx 98\%$. The sample was tilted with respect to the incoming beam, so that the Poynting vector of the light makes an angle of $\alpha = 70^\circ$ with respect to the [001] surface normal. To change the polarization, the sample was rotated around the Poynting vector axis as depicted in Fig. 5.1. θ, the angle between the electric field vector $\vec{E}$ and the [001] surface normal, can than be varied between 20° and 90°. This measurement geometry allows for an optical path of the incoming beam which is independent of θ, guaranteeing a reliable comparison of the spectral line shapes as a function of θ. A CoO single crystal is measured *simultaneously* in a separate chamber to obtain a relative energy reference with an accuracy of better than 0.02 eV.

5.3 Polarization dependence

Fig. 5.2 shows the polarization dependent Co $L_{2,3}$ XAS spectra of the CoO/MnO(100) (left panels) and CoO/Ag(100) (right panels) systems, taken at temperatures both far below (top panels) and far above (bottom panels) the Néel temperature of the CoO thin film, which is about 290 K for CoO/MnO(100) and 310 K for CoO/Ag(100) as we will show below. The angle θ between the electric field vector $\vec{E}$ and the [001] surface normal, is varied between 20° and 90°. The spectra have been corrected for electron yield saturation effects [21]. The general line shape of the spectra shows the characteristic features similar to that of bulk CoO [22], ensuring the good quality of our CoO films. Very striking in the spectra is the clear polarization dependence, which is stronger at 77 K than at 400 K. Important is also that the polarization dependence of the CoO/MnO(100) system is opposite to that of the CoO/Ag(100): for instance, the intensity of the first peak at $h\nu = 777$ eV is always higher for $\theta = 20^\circ$ than for $\theta = 90^\circ$ in CoO/MnO(100), while it is always smaller in CoO/Ag(100).

We also present here the the temperature dependence of the XAS spectra for all the temperatures measured for the two samples. Figure 5.3 shows this temperature dependence for both normal and grazing incidence for the sandwiched CoO layer, whereas the same is shown for the 90 Å thick CoO on Ag in Figure 5.4.

5.4 Temperature dependence of the dichroism

In order to resolve the origin of the polarization dependence in the CoO spectra, we have investigated the temperature dependence in more detail. Figure 5.5 (a) depicts the polarization contrast of the peak at $h\nu = 777$ eV, de-

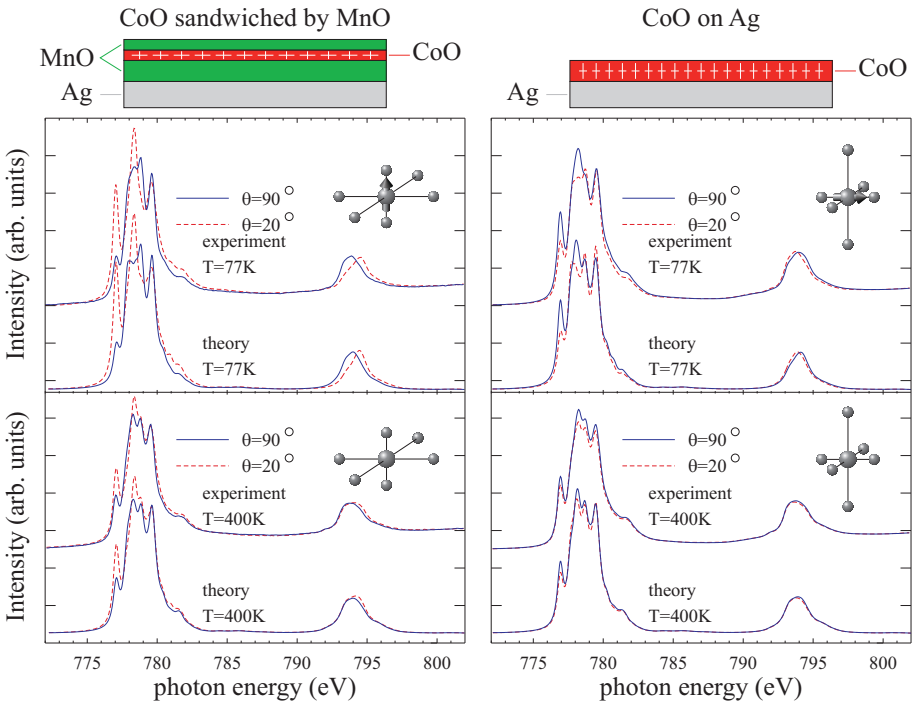

Figure 5.2: Experimental and calculated Co $L_{2,3}$ XAS spectra of: **left panel** CoO in (14Å)MnO/(10Å)CoO/(100Å)MnO/Ag(001) at $\theta = 20°$ and $\theta = 90°$, far below (top panel, T=77K) and far above (bottom panel, T=400K) the Néel temperature of the CoO thin film; **right panel** the same for CoO in (90Å)CoO/Ag(001)

fined as the difference divided by the sum of the peak height in the spectra taken with the $\theta = 20°$ and $\theta = 90°$ polarizations. One can clearly see a significant temperature dependence for both systems, and a closer look also reveals the presence of a kink at about 290 K for CoO/MnO(100) and 310 K for CoO/Ag(100), which can be associated with the Néel temperatures of the CoO thin films as we will show below. We therefore infer that at high temperatures the polarization contrast are caused solely by crystal field effects, and that at low temperatures the magnetism must also contribute to the contrast. In other words, we are observing crystal field induced linear dichroism at high temperatures and a combination of crystal field induced and magnetic linear dichroism at low temperatures. Important is to note that the opposite sign in the dichroism for the CoO/MnO(100) and CoO/Ag(100) systems implies that the orientation of the magnetic moments is perpendicular to each other and

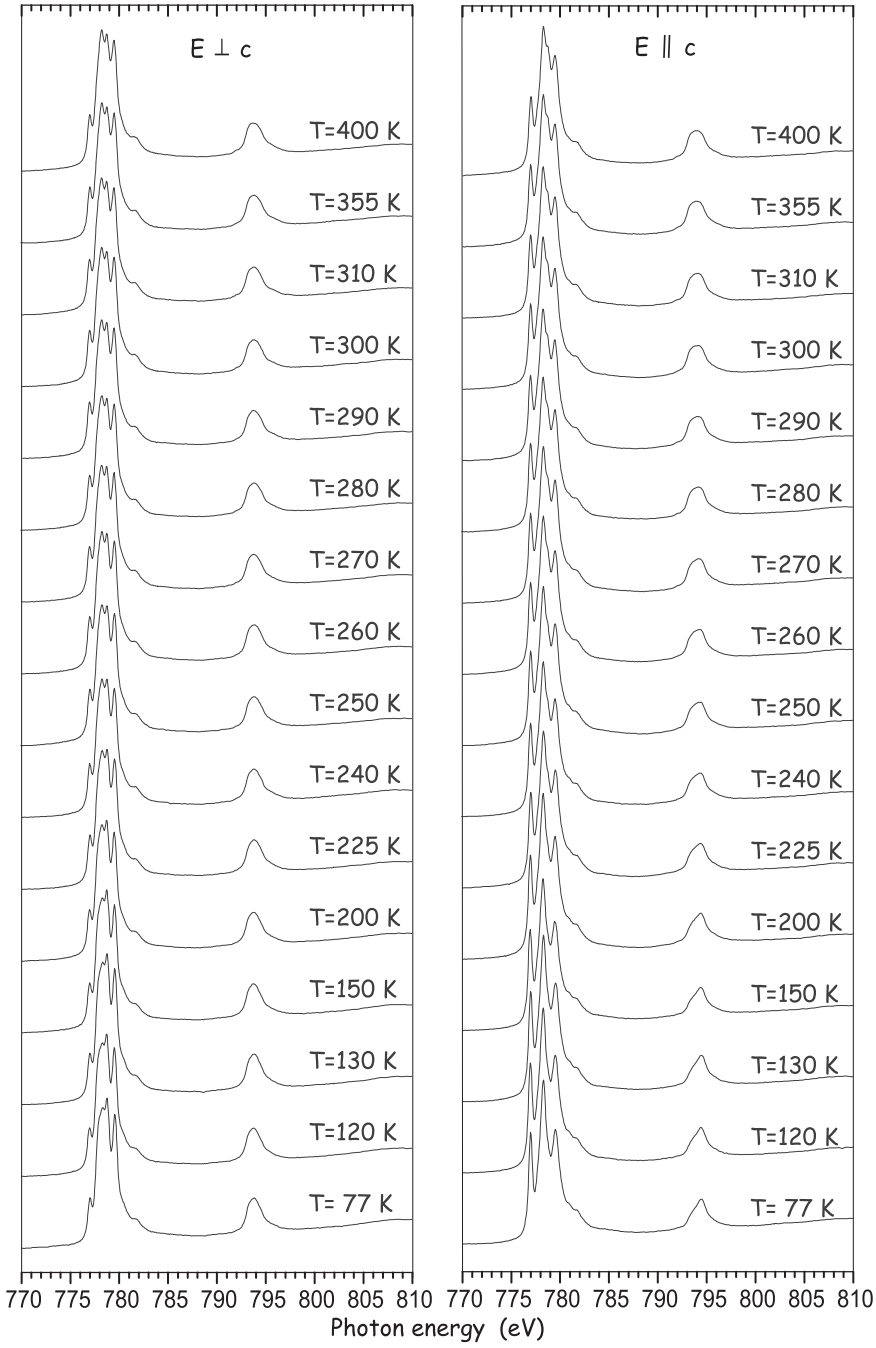

Figure 5.3: Temperature dependence of the 10 Å (5 ML) Co $L_{2,3}$ spectra in the sandwich structure.

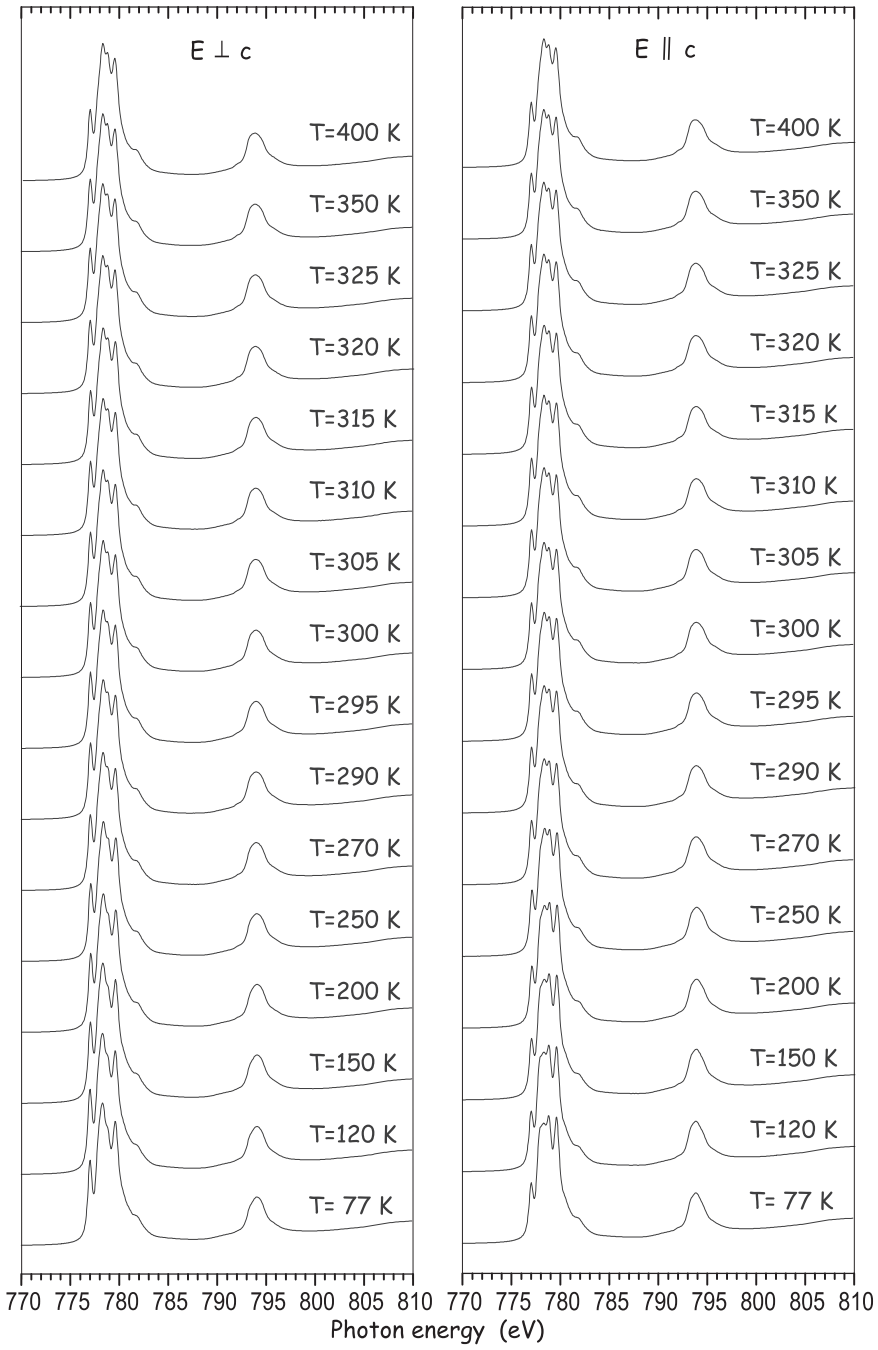

Figure 5.4: Temperature dependence of the 90Å(45 ML) Co $L_{2,3}$ film spectra grown on a Ag (001) single crystal for both polarizations.

the sign of the crystal field splittings is opposite in the two systems.

In order to analyze the Co $L_{2,3}$ spectra quantitatively, we performed calculations for the atomic-like $2p^6 3d^7 \rightarrow 2p^5 3d^8$ transitions using a similar method as described by Alders *et al.* [23], but now in a D_{4h} point group symmetry and including covalency. The method uses a CoO_6 cluster which includes the full atomic multiplet theory and the local effects of the solid [22, 24]. It accounts for the intra-atomic 3*d*-3*d* and 2*p*-3*d* Coulomb and exchange interactions, the atomic 2*p* and 3*d* spin-orbit couplings, the O 2*p* - Co 3*d* hybridization, local crystal field parameters $10Dq$, Ds and Dt, and a Brillouin type temperature dependent exchange field which acts on spins only and which vanishes at T_N. The calculations were carried out using the XTLS 8.0 program [24]. The results of the calculations are shown in Figure 5.2. We have used the parameters already known for bulk CoO [24, 25], and tuned only the parameters for Ds, Dt and the direction of the exchange field. For the CoO/MnO(100) system we find an excellent simulation of the experimental spectra for Ds = -40 meV, Dt = -13 meV and an exchange field parallel to the [001] surface normal. For the CoO/Ag(100) system we obtained the best fit for Ds = 13 meV, Dt = 4 meV and an exchange field perpendicular to the [001] surface normal. These two sets of parameters reproduce extremely well the spectra at all temperatures, as is also demonstrated in Figure 5.5 (a), which shows the excellent agreement between the calculated and measured temperature dependent polarization contrast of the first peak. Most important is obviously the information that can be extracted from these simulations. We find that the magnetic moments in CoO/MnO(100) are oriented out-of-plane, and, in strong contrast, those in CoO/Ag(100) to be in-plane. We also find for CoO/MnO(100) a 2.46 μ_B spin and 1.36 μ_B orbital contribution to the 3.82 μ_B total magnetic moment. By comparison, the values for CoO/Ag(100) are smaller: 2.14, 1.00, and 3.14 μ_B, respectively. The crystal field parameters give also a very different splitting in the t_{2g} levels: about -56 meV for CoO/MnO(100) and +18 meV for CoO/Ag(100), which is fully consistent with our structural data in that the CoO in CoO/MnO(100) experiences a *large* in-plane *expansion* (tensile strain) while the CoO in CoO/Ag(100) is only *slightly contracted* in-plane (compressive strain).

Shape anisotropy cannot explain why the spin of the thinner CoO film, i.e. CoO/MnO (100) is oriented out-of-plane while that of the thicker film, i.e. CoO/Ag(100), is in-plane. In order to understand intuitively the important interplay between strain and spin-orbit interaction for the magnetic properties of materials with a partially filled 3*d* t_{2g} shell, we will start with describing the energetics of the high spin Co^{2+} ($3d^7$) ion in a one-electron like picture.

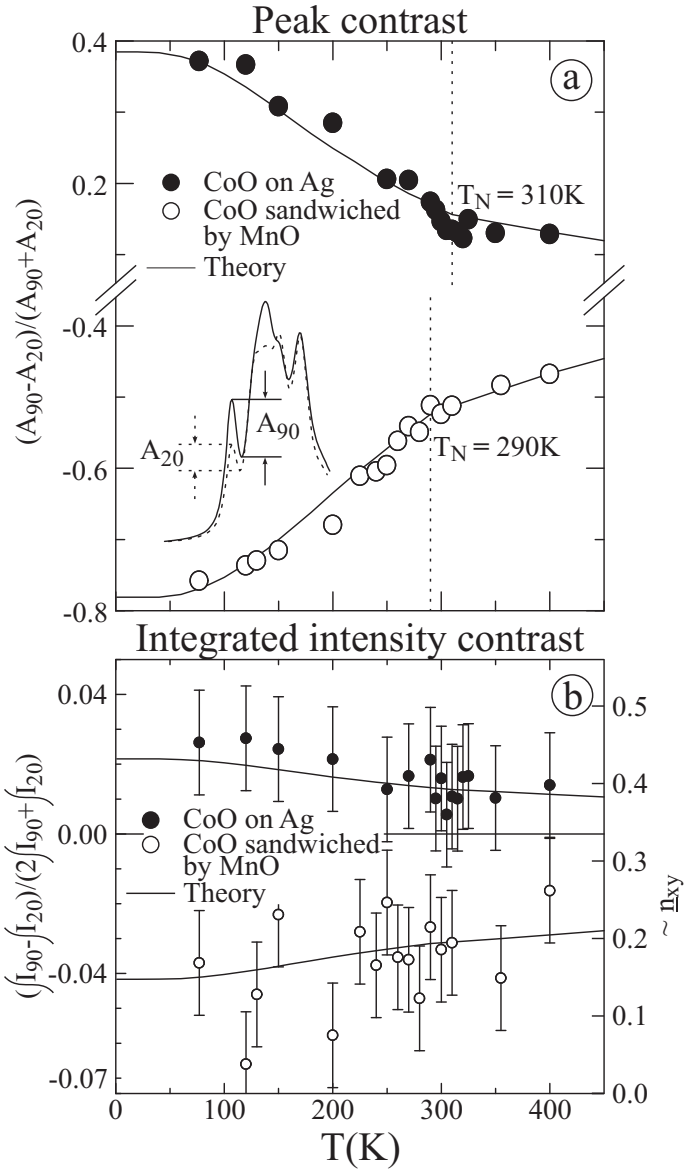

Figure 5.5: Temperature dependence of the polarization contrast in the Co $L_{2,3}$ spectra: a) peak contrast, defined as the difference divided by the sum of the height of the first peak at $h\nu = 777$ eV, taken with $\theta = 20°$ and $\theta = 90°$ polarizations; b) integrated intensity contrast, defined as the difference divided by the sum of the intensity, integrated over the entire $L_{2,3}$ range. Filled and empty circles are the experimental data. The solid lines are the theoretical simulations.

In O_h symmetry the atomic $3d$ levels are split into 3 t_{2g} and 2 e_g orbitals, so that two holes reside in the spin-down e_g orbitals and one hole in one of the spin-down t_{2g}. Introducing a tetragonal distortion, in which the c-axis (out-of-plane) is made different from the a-axis (in-plane), the t_{2g} levels also become split. In the limit that this splitting is much larger than the spin-orbit interaction, we will find for CoO with c/a$\ll$1, that the t_{2g} hole will occupy a linear combination of d_{xz} and d_{yz} orbitals. The spin-orbit interaction will then produce a $m_l = -1$ state, i.e. a state with an orbital moment of 1 μ_B directed perpendicular to the plane of the film. The spin moment will be also out-of-plane, since it is coupled via the spin-orbit interaction to the orbital moment. For CoO with c/a$\gg$1, we will get a t_{2g} hole in the d_{xy} orbital, i.e. a state with a quenched orbital momentum [26]. For the actual CoO/Ag(100) system, we find that c/a is indeed larger than 1, but only slightly and with a t_{2g} splitting which is smaller than the spin-orbit interaction. As a result, the orbital moment is not quenched [27]. In fact, it is directed in-plane, and thus also the spin moment. For the CoO/MnO(100) system, the c/a is smaller than 1, and the orbital and spin moment are indeed directed out-of-plane. The size of the orbital moment as calculated in the cluster model is somewhat larger than 1 μ_B, but this is merely due to the presence of Coulomb and exchange interactions in the multiplet structure [27, 28] not considered in the simple one-electron picture.

The fact that strain has a direct influence on the orbital occupation as revealed by our theoretical analysis, can also be verified experimentally. In Figure 5.5 (b) we plot the difference divided by the sum of the integrated Co $L_{2,3}$ intensities for the two polarizations for a wide range of temperatures. The integration is over the entire Co $L_{2,3}$ spectral region and a background has been subtracted following the prescription often used in evaluating orbital moment sum rules in soft-x-ray magnetic circular dichroism spectroscopy [29]. One can clearly observe that there is a significant non-zero polarization contrast in the integrated intensities, and that this contrast has opposite sign for the two systems studied here. It is important to realize that the integrated intensity for a particular polarization of the light merely depends on the symmetry of the $3d$ holes in the initial state. To illustrate this, let us make the simplification that 2 holes reside in the spin-down e_g orbitals and 1 hole in one of the spin-down t_{2g}. We then have [27]:

$$\frac{\int I_{90} - \int I_0}{2\int I_{90} + \int I_0} = \frac{\underline{n}_{xy} - \frac{1}{2}(\underline{n}_{xz} + \underline{n}_{yz})}{2\underline{n}_{total}} \tag{5.1}$$

where $\underline{n}$ denotes the hole number and the subscript the orbital type. For an isotropic orbital occupation, the integrated contrast would be 0 and $\underline{n}_{xy}$

= 1/3. One can now directly deduce from the data that the CoO/Ag(100) system has relatively more d_{xy} holes than the CoO/MnO(100), fully consistent with $c/a > 1$ in CoO/Ag(100), and $c/a < 1$ in CoO/MnO(100). The cluster calculations reproduce the measured integrated polarization contrast very well, and reveal that the actual $\underline{n}_{xy}$ [27] is about 0.4 and 0.2 for the two systems, respectively.

5.5 Single ion anisotropy of CoO in thin films

Based on the parameters extracted from the excellent quality of the simulations of the spectra, we have estimated the magnetocrystalline anisotropy within the CoO films. We calculated the single ion anisotropy by comparing the total energy of the CoO_6 cluster for different exchange field directions. This energy is expressed as $E = K_0 + K_1 sin^2(\eta) + K_2 sin^4(\eta) + K_3 sin^4(\eta) sin^2(\varphi) cos^2(\varphi)$, where η is the angle between the exchange field and the c-axis, and φ the azimuthal angle. We find for CoO/MnO(100) K_1 = 3.4 meV, K_2 = 1.4 meV and K_3 = 0.1 meV, while for CoO/Ag(100) we obtain K_1 = -1.7 meV, K_2 = 0.1 meV, and K_3 = 0.1 meV. In other words, for CoO/MnO(100) the energy difference between the spin directed parallel to the easy axis ($\eta = 0°$, perpendicular to the film) and parallel to the hard axis ($\eta = 90°$, lying in the film plane) amounts to about 4.8 meV. The same single ion anisotropy energy calculated for the CoO/Ag(100) is about -1.6 meV, i.e. the hard axis is perpendicular and the easy axis parallel to the film plane. These energies are more than 2 orders of magnitude larger than the dipolar anisotropy within the film [30]. The cubic anisotropy energy for bulk CoO was estimated by J. Kanamori an is of the order of 1.2 meV [31, 32].

5.6 Conclusions

To conclude, we have observed that CoO films grown on different substrates show dramatic differences in their magnetic properties. Using polarization dependent x-ray absorption spectroscopy at the Co $L_{2,3}$ edges, we revealed that the magnitude and orientation of the magnetic moments strongly depend on the strain in the films induced by the substrate. We presented a quantitative model to explain how strain together with the spin-orbit interaction determine the $3d$ orbital occupation, the magnetic anisotropy, as well as the spin and orbital contributions to the magnetic moments. Control over the sign and direction of the strain may therefore open new opportunities for applications in the field of exchange bias in multilayered magnetic films

References

[1] W. H. Meiklejohn and C. P. Bean, Phys. Rev. **102**, 1413 (1956); **105**, 904 (1957).

[2] See for review: J. Nogués and I. K. Schuller, J. Magn. Magn. Mater. **192** 203 (1999).

[3] See for review: A. F. Berkowitz and K. Takano, J. Magn. Magn. Mater. **200** 552 (1999).

[4] A. P. Malozemoff, Phys. Rev. B **35**, R3679 (1987).

[5] D. Mauri, H. C. Siegmann, P. S. Bagus, and E. Kay, J. Appl. Phys. **62**, 3047 (1987).

[6] N. C. Koon, Phys. Rev. Lett. **78**, 4865 (1997).

[7] T. C. Schulthess and W. H. Butler, Phys. Rev. Lett. **81**, 4516 (1998).

[8] M. D. Stiles and R. D. McMichael, Phys. Rev. B **59**, 3722 (1999).

[9] K. Takano, R. H. Kodama, A. E. Berkowitz, W. Cao, and G. Thomas, Phys. Rev. Lett. **79**, 1130 (1997).

[10] P. J. van der Zaag, Y. Ijiri, J. A. Borchers, L. F. Feiner, R. M. Wolf, J. M. Gaines, R. W. Erwin, and M. A. Verheijen, Phys. Rev. Lett. **84**, 6102 (2000).

[11] H. Ohldag, T. J. Regan, J. Stöhr1, A. Scholl, F. Nolting, J. Lüning, C. Stamm, S. Anders, and R. L. White, Phys. Rev. Lett. **87**, 247201 (2001).

[12] H. Ohldag, A. Scholl, F. Nolting, E. Arenholz, S. Maat, A. T. Young, M. Carey, and J. Stöhr, Phys. Rev. Lett. **91**, 017203 (2003).

[13] J. Camarero, Y. Pennec, J. Vogel, M. Bonfim, S. Pizzini, F. Ernult, F. Fettar, F. Garcia, F. Lançon, L. Billard, B. Dieny, A. Tagliaferri and N. B. Brookes, Phys. Rev. Lett. **91**, 027201 (2003).

[14] A. Scholl, M. Liberati, E. Arenholz, H. Ohldag, and J. Stöhr, Phys. Rev. Lett. **92**, 247201 (2004).

[15] M. J. Carey, A. E. Berkowitz, J. A. Borchers, and R. W. Erwin, Phys. Rev. B **47**, 9952 (1993).

[16] Y. Ijiri J. A. Borchers, R. W. Erwin, S.-H. Lee, P. J. van der Zaag and R. M. Wolf, Phys. Rev. Lett. **80**, 608 (1998).

[17] J. A. Borchers, Y. Ijiri, S.-H. Lee, and C. F. Majkrzak, J. Appl. Phys. **83**, 7219 (1998).

[18] H. Ohldag, A. Scholl, F. Nolting, S. Anders, F. U. Hillebrecht, and J. Stöhr, Phys. Rev. Lett. **86**, 2878 (2001).

[19] F. Radu, M. Etzkorn, R. Siebrecht, T. Schmitte, K. Westerholt, and H. Zabel, Phys. Rev. B **67**, 134409 (2003).

[20] S. I. Csiszar and T. Hibma (in preparation).

[21] R. Nakajima, J. Stöhr and Y. U. Idzerda, Phys. Rev. B, **59**, 6421 (1999).

[22] See review by F. M. F. de Groot, J. Electron Spectrosc. Relat. Phenom. **67**, 529 (1994).

[23] D. Alders, L. H. Tjeng, F. C. Voogt, T. Hibma, G. A. Sawatzky, C. T. Chen, J. Vogel, M. Sacchi, and S. Iacobucci, Phys. Rev. B **57**, 11623 (1998)

[24] A. Tanaka and T. Jo, J. Phys. Soc. Jpn. **63**, 2788 (1994).

[25] Parameters for CoO_6 cluster: Δ=6.5, U_{dd}=6.5, $U_{\underline{c}d}$=8.2, $pd\sigma$=-1.2, T_{pp}=0.7, $10Dq$=0.525, ζ=0.066, H_{ex}=0.0126; Slater integrals 80% of Hartree Fock values; CoO/MnO(100): Ds=-0.040, Dt=-0.013; CoO/Ag(100): Ds=0.013, Dt=0.004; all values in eV.

[26] T. Jo, T. Shishidou, J. Phys. Soc. Jpn., **67**, 2505 (1998).

[27] M. W. Haverkort *et al.*, in preparation.

[28] S. Sugano, Y. Tanabe, and H. Kamimura, *Multiplets of Transition-Metal Ions in Crystals* (Academic, New York, 1970).

[29] C. T. Chen, Y. U. Idzerda, H.-J. Lin, N. V. Smith, G. Meigs, E. Chaban, G. H. Ho, E. Pellegrin1, and F. Sette, Phys. Rev. Lett. **75**, 152 (1995).

[30] M. Finazzi and S. Altieri, Phys.Rev. B, **68**, 054420 (2003)

[31] P.J. van der Zaag, A.R. Ball, L.F. Feiner, R.M. Wolf, P.A.A. van der Heijden, J. Appl. Phys. 5103, **79** (1996)

[32] J. Kanamori in *Magnetism*, edited by G.T. Rado and H. Suhl (Academic, New York 1963), Vol. 1, pp. 198-199

Chapter 6

Aligning spins in antiferromagnetic films using antiferromagnets

6.1 Introduction

The study of the exchange bias phenomena in multilayered magnetic systems is a very active research field in magnetism, not the least motivated by the high potential for applications in information technology. Various combinations of antiferromagnetic (AFM) and ferromagnetic (FM) thin film materials have been fabricated and intensively investigated [1, 2]. There seems to be an agreement among the experimental and theoretical studies that the largest exchange bias effects can be found in systems containing AFMs with a high magnetocrystalline anisotropy, such as CoO. The simple underlying idea is that the anisotropy helps to fix the spin orientation in the AFM while switching the magnetization in the FM.

Our objective is to explore the possibilities to control and to pin the spin direction in AFM oxides having low magnetocrystalline anisotropy, e.g. transition metal oxides with the $3d^3$, $3d^5$, or $3d^8$ ionic configurations. If successful, this would help to extend the material basis for the AFMs used in exchange bias systems. One could then consider not only NiO, but also thin films of $LaCrO_3$, $LaFeO_3$, γ-Fe_2O_3, and $R_3Fe_5O_{12}$ [3].

At first sight, our chances may seem bleak since a recent study on ultra thin NiO films revealed that the magnetic anisotropy results from a detailed balance between the influence of strain and thickness on the already very weak dipolar interactions in the AFM [4, 5]. This sensitivity to details can easily

lead to a complete loss of macroscopic magnetic anisotropy if, for instance, the strain is (partially) released when the film is made thicker. We have, for example, grown 50 ML of NiO epitaxially on Ag (001) surface, and have not been able to detect any magnetic linear dichroism signal that otherwise was clearly visible for thinner NiO films, e.g. 3-20 ML. Another example is shown in Figure 6.1. Here we have tried to find magnetic linear dichroism in the Mn $L_{2,3}$ XAS spectrum of 50 ML MnO on Ag (001) at 30 K, well below the Néel temperature of bulk MnO (T_N=121 K). Apparently the absence of any dichroic signal indicates that the film breaks up in many magnetic domains without orientational preference within our 1×1 mm^2 beam spotsize.

However, an alternative approach seems to be possible. The few studies available in the literature on combinations of AFM/AFM films revealed that the interlayer exchange coupling can be very strong [6–12]. We took these findings as starting point of our work. We will use MnO as an ideal model for an antiferromagnetic system with negligible single-ion anisotropy and grow it epitaxially as a thin film on two different types of CoO single crystal films. In one CoO film the spin direction is oriented perpendicular to the surface, and in the other parallel to the surface [13]. Using soft X-ray absorption spectroscopy at the Mn $L_{2,3}$ edges, we will study the spin direction of these MnO films and try to find out whether the spin orientation of the CoO film plays an important role.[1]

Part of this chapter was submitted to Phys. Rev. B as *"Aligning spins in antiferromagnetic films using antiferromagnets"*, S. I. Csiszar, M. W. Haverkort, T. Burnus, Z. Hu, A. Tanaka, H. H. Hsieh, H.-J. Lin, C. T. Chen, T. Hibma and L. H. Tjeng

6.2 Sample details and measurement setup

The actual MnO/CoO systems studied are (14Å)MnO/(10Å)CoO/(100Å)MnO/ /Ag(001) and (22Å)MnO/(90Å)CoO/Ag(001). The two samples were grown on a Ag(001) single crystal by molecular beam epitaxy (MBE), evaporating elemental Mn and Co from alumina crucibles in a pure oxygen atmosphere of 10^{-7} to 10^{-6} mbar. The base pressure of the MBE system is in the low 10^{-10} mbar range. The thickness and epitaxial quality of the films are monitored by reflection high energy electron diffraction (RHEED) measurements. With the lattice constants of bulk Ag, CoO and MnO being 4.09Å, 4.267Å, and 4.445Å, respectively, we find from x-ray diffraction (XRD) and RHEED that the in-plane lattice constants in each film are essentially given by the thickest layer which is almost bulk like. Compared to the bulk, the 10Å CoO sandwiched by MnO is about 4% expanded in-plane ($a_{\parallel} \approx 4.424$Å), while the 90Å CoO directly on Ag is slightly compressed in-plane ($a_{\parallel} \approx 4.235$Å, $a_{\perp} \approx 4.285$Å). The MnO is compressed in both samples, but much more so for the one on the 90Å CoO film. Details about the growth was presented in Chapter 2, Section 2.5.1 of the present thesis. We have shown in the previous Chapter that the spin direction is oriented perpendicular to the surface in the CoO film under tensile in-plane stress, and that it is parallel to the surface in the film with the slightly compressive in-plane stress [13].

The XAS measurements were performed at the Dragon beamline of the NSRRC in Taiwan using *in-situ* MBE grown samples. The spectra were recorded using the total electron yield method in a chamber with a base pressure of 3x10^{-10} mbar. The photon energy resolution at the Mn $L_{2,3}$ edges ($h\nu \approx 635 - 655$ eV) was set at 0.3 eV, and the degree of linear polarization was $\approx 98\%$. The sample was tilted with respect to the incoming beam, so that the Poynting vector of the light makes an angle of $\alpha = 70^{\circ}$ with respect to the [001] surface normal. To change the polarization, the sample was rotated around the Poynting vector axis as depicted in Figure 6.2, so that θ, the angle between the electric field vector $\vec{E}$ and the [001] surface normal, can be varied between 20° and 90°. This measurement geometry allows for an optical path of the incoming beam which is independent of θ, guaranteeing a reliable comparison of the spectral line shapes as a function of θ. A MnO single crystal is measured *simultaneously* in a separate chamber to obtain a relative energy reference with an accuracy of better than 0.02 eV.

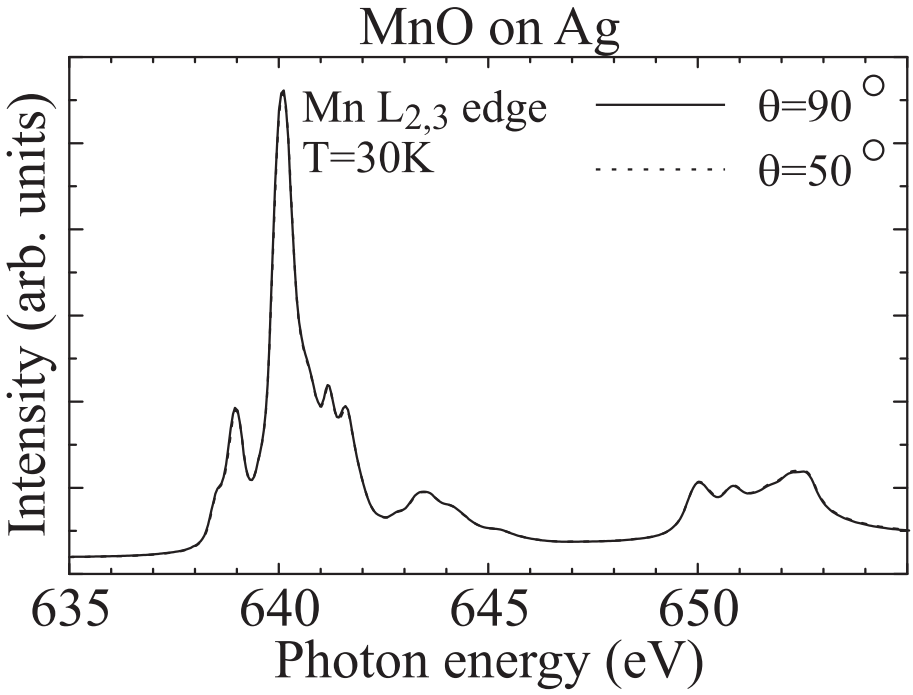

Figure 6.1: X-ray absorption spectra of 50 ML MnO on Ag. There is no magnetic linear dichroism visible although the spectra are taken well below the Neel temperature of the MnO.

6.3 X-ray absorption measurements

Figure 6.3 shows the polarization dependent Mn $L_{2,3}$ XAS spectra of the MnO/CoO samples with CoO spin-orientation perpendicular (left panels) and parallel (right panels) to the surface, taken at temperatures far below (top panels) and far above (bottom panels) the Néel temperature (T_N) of the MnO thin film, which is about 130 K as we will show below. The spectra have been corrected for electron yield saturation effects [15]. The general line shape of the spectra shows the characteristic features of bulk MnO [16], demonstrating the good quality of our MnO films. Very striking in the spectra is the clear polarization dependence, which is strongest at low temperatures. It is important to note that below T_N the dichroism, i.e. the polarization dependence, of the two samples are opposite: for instance, the intensity of the first peak at $h\nu = 639$ eV is higher for $\theta = 20°$ than for $\theta = 90°$ in MnO/CoO where the spin orientation of the CoO is out-of-plane, while it is smaller in the other

sample. Above T_N, the dichroism almost vanishes. Nevertheless, small but clear and reproducible shifts in the spectra as a function of polarization can be seen: the main peak at 640 eV has a shift of about 30 meV for the MnO sandwiching the 10Å CoO film, and 150 meV for the MnO grown on top of the 90Å CoO film.

In order to resolve the origin of the dichroism in the spectra, we have investigated the temperature dependence in more detail. Figure 6.4 and 6.5 show the Mn $L_{2,3}$ XAS spectrum for the two samples for a wide range of temperatures. Figure 6.6 provides a summary by depicting the polarization contrast of the peak at $h\nu = 639$ eV, defined as the difference divided by the sum of the peak height in the spectra taken with the $\theta = 20°$ and $\theta = 90°$ polarizations. In going from low to high temperatures, one can see a significant temperature dependence for both samples (with opposite signs), which flattens off at about 130 K, identified as the T_N of these MnO thin films. We therefore infer that at low temperatures the strong dichroic signal is caused by the presence of magnetic ordering. An important point here is that the opposite sign in the dichroism for the two samples implies that the orientation of the magnetic moments is quite different.

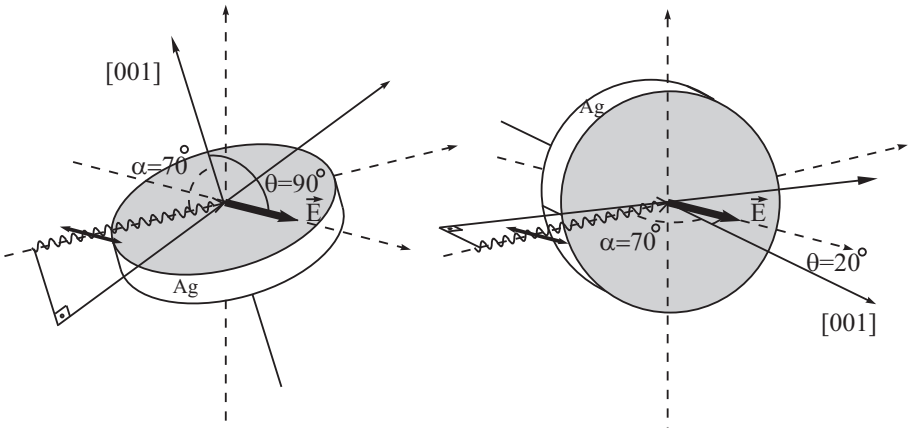

Figure 6.2: Experimental XAS geometry, with polarization of the light in the horizontal plane. θ is the angle between the electric field vector $\vec{E}$ and the [001] surface normal, and α the tilt between the Poynting vector and the surface normal.

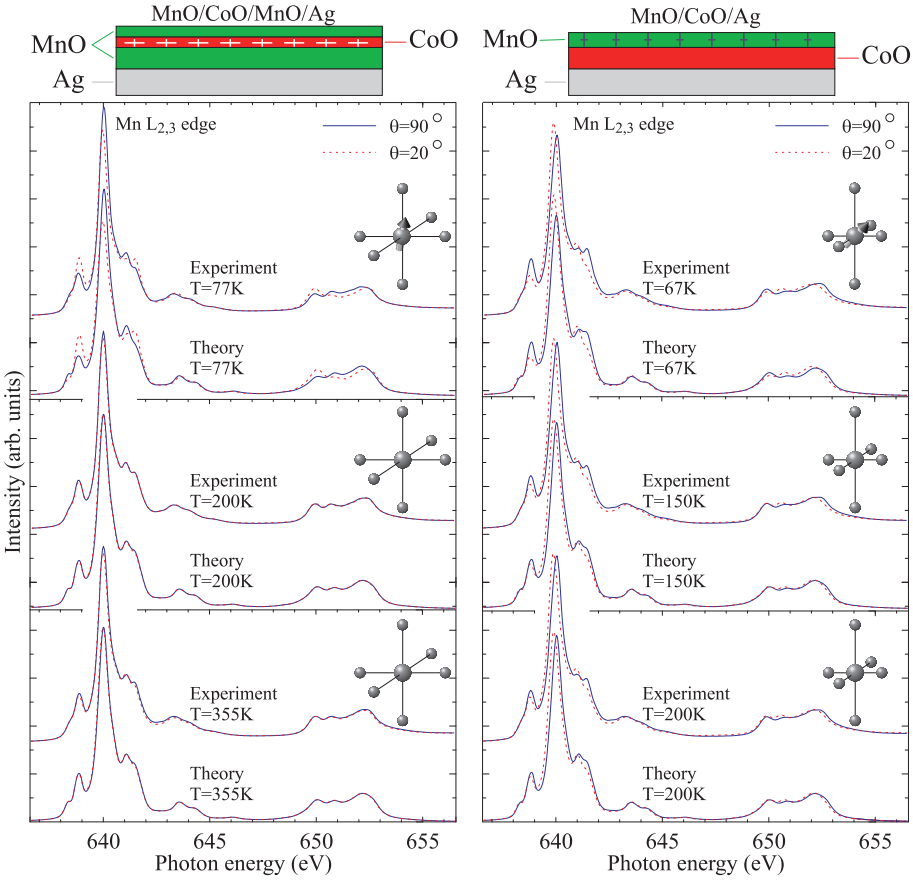

Figure 6.3: Experimental and calculated Mn $L_{2,3}$ XAS spectra of: **left panel** MnO in (14Å)MnO/(10Å)CoO/(100Å)MnO/Ag(001) for $\theta = 20°$ and $\theta = 90°$, far below (top panel, T=77K) and far above (middle panel, T=200K; bottom panel, T=355K) T_N of the MnO thin film, as well as above T_N of the CoO film (bottom panel; T=355K); **right panel** the same for MnO in (22Å)MnO/(90Å)CoO/Ag(001), below (top panel, T=67K) and above (middle panel, T=150K; bottom panel, T=200K) T_N of the MnO thin film.

6.4 Discussion and analysis

In order to analyze the Mn $L_{2,3}$ spectra quantitatively, we performed calculations for the atomic-like $2p^6 3d^5 \rightarrow 2p^5 3d^6$ transitions using a similar method as described by Kuiper *et al.* [17] and Alders *et al.* [18], but now in a D_{4h} point group symmetry and including covalency. The method uses a MnO_6

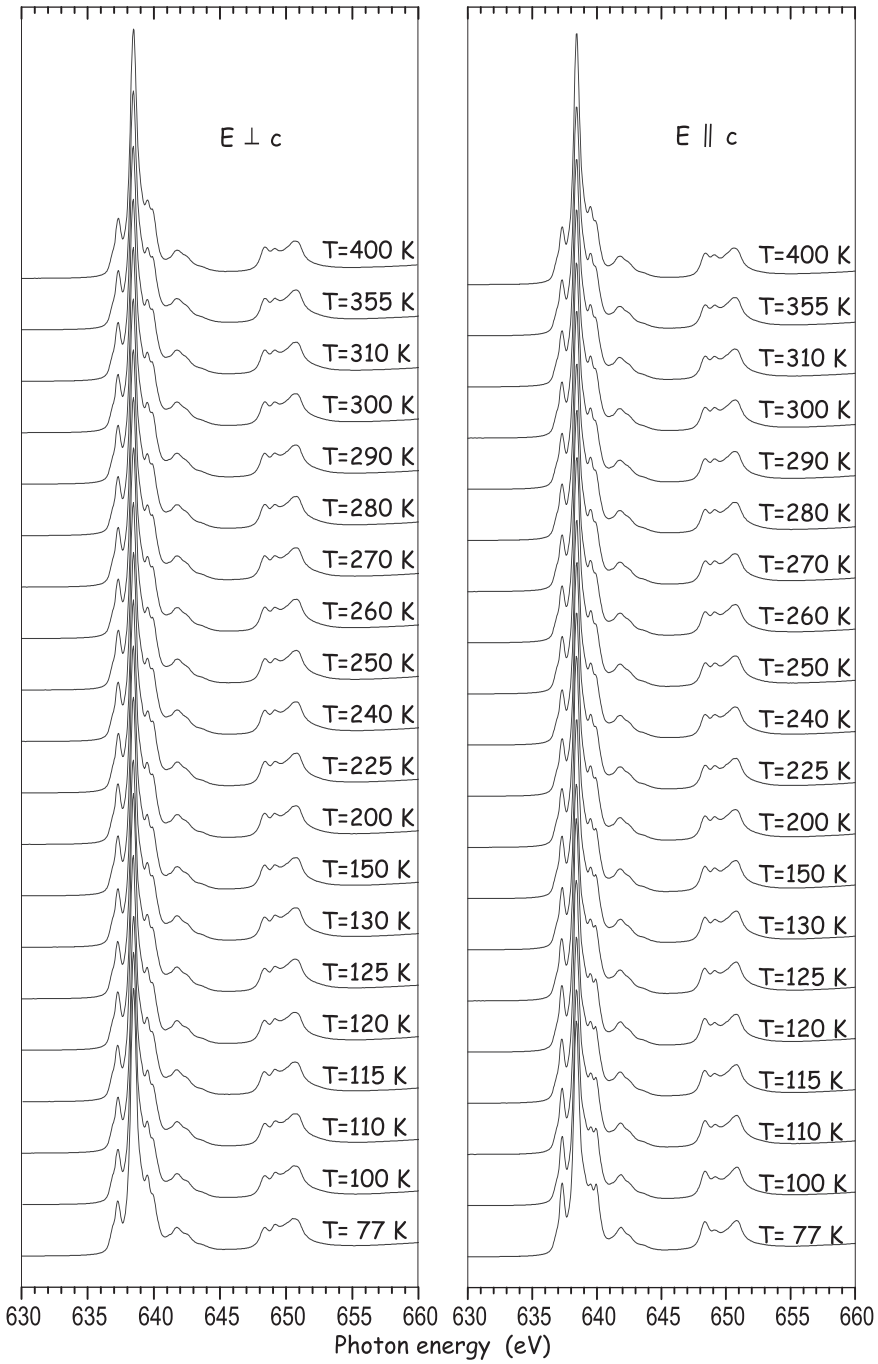

Figure 6.4: Temperature dependence of the Mn $L_{2,3}$ spectra of the MnO sandwiching the 10 Å CoO film.

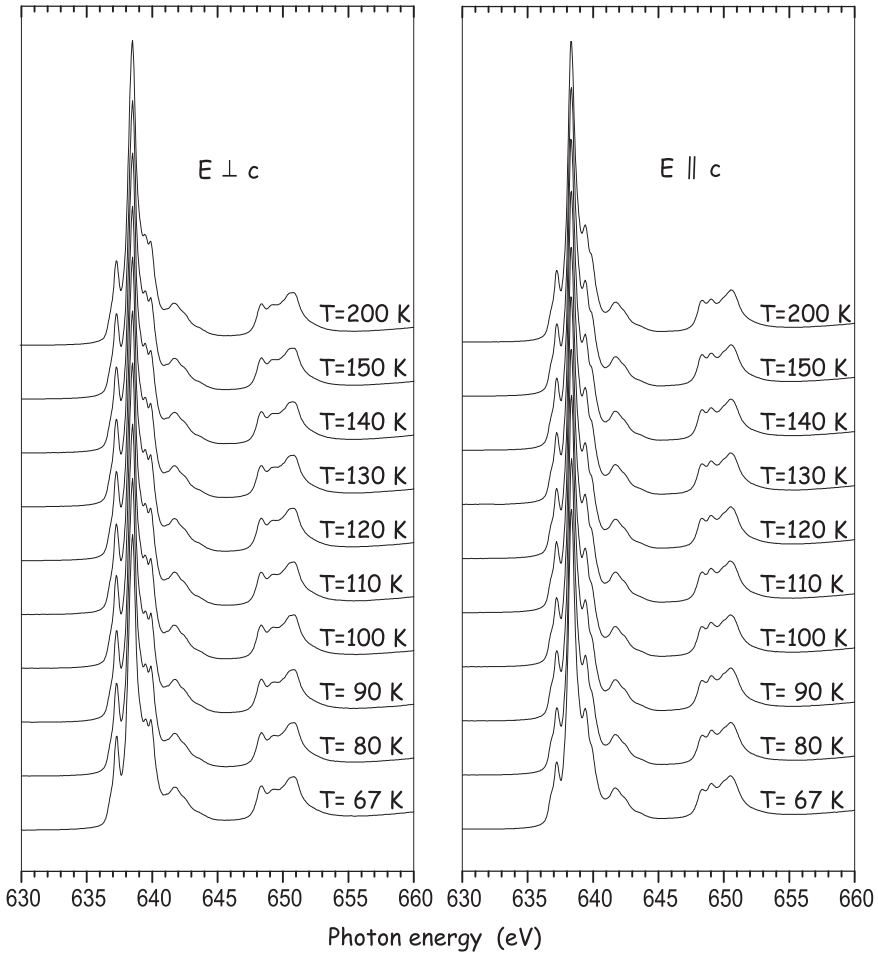

Figure 6.5: Temperature dependence of the Mn $L_{2,3}$ spectra of the MnO film grown on top of the 90 Å CoO film.

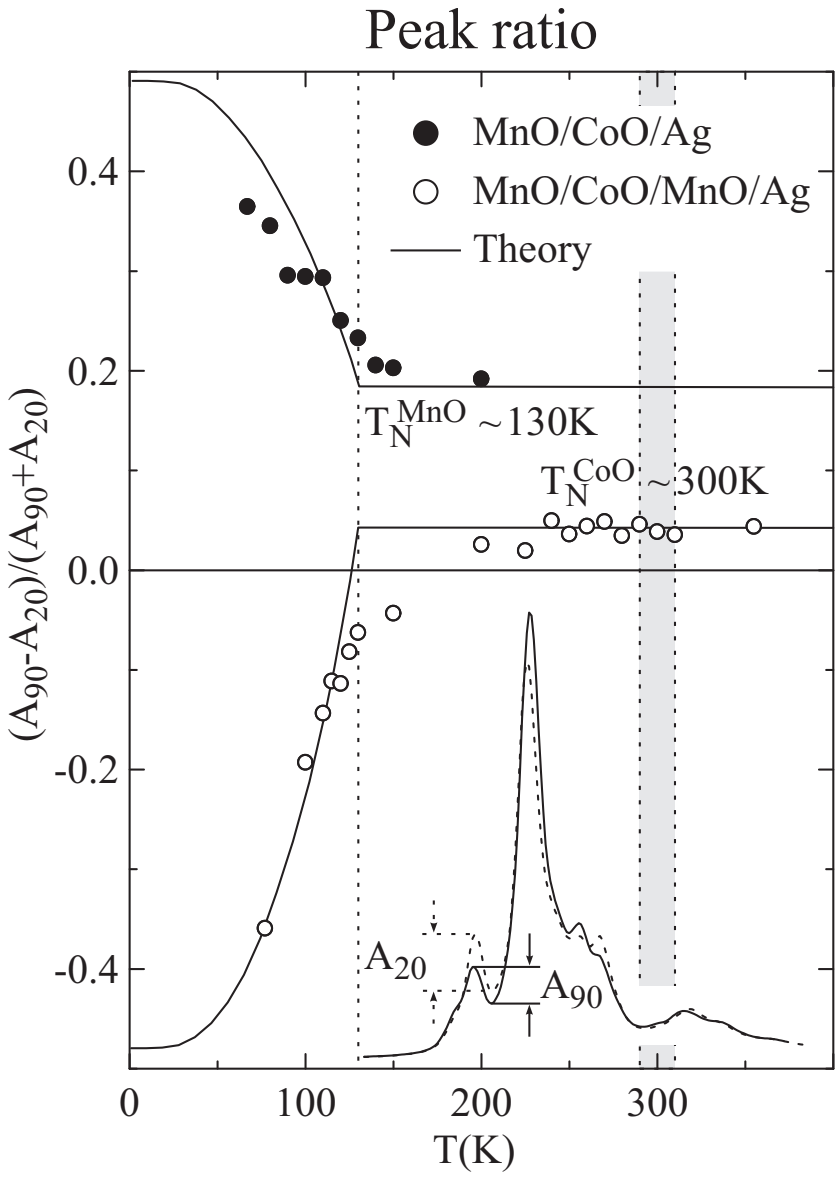

Figure 6.6: Temperature dependence of the polarization contrast in the Mn $L_{2,3}$ spectra, defined as the difference divided by the sum of the height of the first peak at $h\nu = 639$ eV, taken with $\theta = 20°$ and $\theta = 90°$ polarizations. Filled and empty circles are the experimental data. The solid lines are the theoretical simulations. The shaded area represents the T_N of the CoO layers under the MnO film.

cluster which includes the full atomic multiplet theory and the local effects of the solid [16, 19]. It accounts for the intra-atomic $3d$-$3d$ and $2p$-$3d$ Coulomb and exchange interactions, the atomic $2p$ and $3d$ spin-orbit couplings, the O $2p$ - Mn $3d$ hybridization, local crystal field parameters $10Dq$, Ds and Dt, and a Brillouin type temperature dependent exchange field which acts on spins only and vanishes at T_N. The calculations were carried out using the XTLS 8.0 program[19].

The results of the calculations are shown in Figure 6.3. We used the parameters already known for bulk MnO [19, 20], and tuned only the parameters for Ds, Dt and the direction of the exchange field. For the MnO sandwiching the 10Å CoO we find an excellent simulation of the experimental spectra for $Ds =$ 9.3 meV, $Dt = 2.6$ meV and an exchange field parallel to the [112] direction. For the MnO overlaying the 90Å CoO we obtained the best fit for $Ds = 48.6$ meV, $Dt = 11.1$ meV and an exchange field along the [211] direction. These two sets of parameters reproduce the spectra at all temperatures extremely well. This is also demonstrated in Figure 6.6, showing the excellent agreement between the calculated and measured temperature dependence of the dichroism in the first peak. Most important is obviously the information concerning the spin direction that can be extracted from these simulations. We find that the magnetic moments in the MnO are oriented towards the surface normal when it is grown on the CoO film which has the spin direction perpendicular to the surface, and that it is lying towards the surface when MnO is grown on the CoO film which has the parallel alignment. In other words, it seems that the MnO tries to follow the CoO magnetically.

In order to find out whether the spin direction in the MnO thin films is determined by the exchange coupling with the CoO, or whether it is given by strain and dipole interactions in the films as found for NiO thin films on non-magnetic substrates [4, 5], we now have to look more closely into the tetragonal crystal fields in the MnO films. The values for the tetragonal crystal field parameters Ds and Dt, which we have used to obtain the excellent simulations as shown in Figure 6.3, can actually be extracted almost directly from the high temperature spectra, where the magnetic order has vanished and does not contribute anymore to the polarization dependence.

The top panels of Figure 6.6 show a close-up of the spectra taken at 200K, i.e. above T_N. One can now observe small but clear and reproducible shifts in the spectra as a function of polarization: the shift in the first peak at 639 eV is denoted by Δ_A and in the main peak at 640 eV by Δ_B. In order to understand intuitively the origin of these shifts, we will start to describe the energetics of the high spin Mn^{2+} ($3d^5$) ion in a one-electron like picture. In

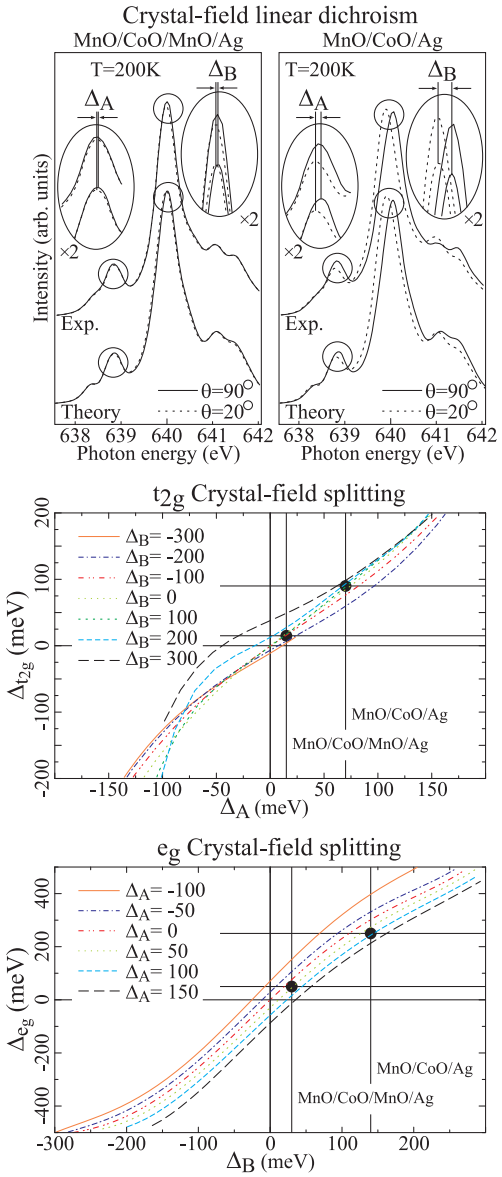

Figure 6.7: (top panel) Close-up of the experimental and calculated Mn L_3 XAS spectra at 200K, i.e. above T_N of (left) (14Å)MnO/(10Å)CoO/(100Å)MnO/Ag(001) and (right) (22Å)MnO/(90Å)CoO/Ag(001); Δ_A and Δ_B are the polarization dependent shifts in the peaks at 639 and 640 eV, respectively; (middle and bottom panels) Relationship between $\{\Delta_A, \Delta_B\}$ and the tetragonal $\{\Delta_{e_g}, \Delta_{t_{2g}}\}$ splittings.

O_h symmetry the atomic $3d$ levels are split into 3 t_{2g} and 2 e_g orbitals, so that three electrons reside in the spin-up t_{2g} orbitals and two in the spin-up e_g. Within the one-electron approximation, the L_3 edge of Mn^{2+} should consist of two peaks: in exciting an electron from the $2p$ core level to the $3d$, one can add an extra spin-down electron either to the lower lying t_{2g} or the higher lying e_g shell, producing the peaks at 639 and 640 eV, respectively. In the presence of a tetragonal distortion, both the e_g and t_{2g} levels will be split. For the e_g peak this will result in a polarization dependent energy shift in the same way as found for NiO [21]. With z polarized light one excites into the $d_{3z^2-r^2}$ orbital, but not in the $d_{x^2-y^2}$ orbital whereas with x or y polarized light one excites into the $d_{x^2-y^2}$ orbital with 3 times more intensity than into the d_{z^2} orbital. For the t_{2g} peak one can excite into the d_{xz} and into the d_{yz} orbitals with z polarized light, but not into the d_{xy} orbital. Therefore, within the one electron picture, the energy shifts Δ_A and Δ_B between the different polarizations are directly related to the crystal fields present in the MnO film.

Due to the intra-atomic $2p$-$3d$ and $3d$-$3d$ electron correlation effects, the relationship between the shifts in the spectra and the crystal field splittings become non-linear. Using the cluster model we are able to calculate this relationship for a Mn^{2+} $3d^5$ system and the results are plotted in Figure 6.7. With the help of this map, we find for the MnO sandwiching the 10Å CoO that $\Delta_{t_{2g}} = 15$ meV and $\Delta_{e_g} = 50$ meV, and for the MnO overlaying the 90Å CoO that $\Delta_{t_{2g}} = 90$ meV and $\Delta_{e_g} = 250$ meV (Ds=(Δ_{e_g}+$\Delta_{t_{2g}}$)/7, Dt=(3Δ_{e_g}-4$\Delta_{t_{2g}}$)/35). The crystal field splittings for the second sample are much larger than for the first sample. This is fully consistent with our structural data which indicate that in the second sample MnO experiences a much stronger compressive in-plane strain. It is important to recognize that the crystal field splittings for the two samples have the same sign, i.e. that both MnO films are compressed in-plane. This implies that strain together with the dipolar interactions cannot explain the quite different spin-orientations of the two MnO systems. We conclude that the magnetic anisotropy mechanism present in, for instance, NiO thin films on non-magnetic substrates [4, 5], is overruled by the stronger interlayer exchange coupling [6–12] between the CoO and MnO layers.

The T_N for these thin MnO layers is found to be at about 130 K. It is surprising that the Neél temperature is not reduced as compared to the bulk value of 121 K [22], since generally one would expect this to happen with decreasing thickness as was observed for NiO on MgO [18]. The origin for such a surprising behavior is not clear at this moment. It is possible that the in-plane compressive stress causes an increase in the Mn $3d$ - O $2p$ hybridization,

which in turn produces an increase of the superexchange interaction strength [3] and thus also of T_N. Another, more exciting, possibility emerges from the recent experimental and theoretical work on AFM/AFM multilayers such as FeF_2/CoF_2 and CoO/NiO [6–12]: these experiments have revealed that multilayers with very thin layers even might have a single magnetic ordering transition temperature lying in between the two T_Ns of the constituent materials. The phenomenon has been ascribed to the very strong interlayer exchange coupling in the multilayers.

6.5 Conclusions

In conclusion, we have explored the possibility to orient spins in antiferromagnetic thin films with low magnetocrystalline anisotropy via the exchange coupling to adjacent antiferromagnetic films with high magnetocrystalline anisotropy. We have used MnO as a prototype for a system with negligible single-ion anisotropy. We were able to control its spin direction very effectively by growing it as a film on antiferromagnetic CoO films with different predetermined spin orientations. This result may pave the way for tailoring antiferromagnets with low magnetocrystalline anistropy for applications in exchange bias systems. Very detailed information concerning the exchange-coupling and strain effects was obtained from Mn $L_{2,3}$ soft x-ray absorption spectroscopy.

References

[1] See for review: J. Nogués and I. K. Schuller, J. Magn. Magn. Mater. **192**, 203 (1999).

[2] See for review: A. F. Berkowitz and K. Takano, J. Magn. Magn. Mater. **200**, 552 (1999).

[3] J. B. Goodenough, *Magnetism and the Chemical Bond* (Wiley, New York, 1963)

[4] S. Altieri, M. Finazzi, H. H. Hsieh, H.-J. Lin, C. T. Chen, T. Hibma, S. Valeri, G. A. Sawatzky, Phys. Rev. Lett. **91**, 137201 (2003).

[5] M. Finazzi and S. Altieri, Phys.Rev. B **68**, 054420 (2003).

[6] C. A. Ramos, D. Lederman, A. R. King, and V. Jaccario, Phys.Rev. Lett. **65**, 2913 (1990).

[7] A. S. Carriço and R. E. Camley, Phys. Rev. B **45**, 13117 (1992).

[8] R. W. Wang and D. L. Mills, Phys. Rev. B **46**, 11681 (1992).

[9] D. Lederman, C. A. Ramos and V. Jaccarino, J.L. Cardy, Phys. Rev B, **48**, 8365 (1993).

[10] J. A. Borchers, M. J. Carey, R. W. Erwin, C. F. Majkzak, and A. E. Berkowitz, Phys. Rev. Lett. **70**, 1878 (1993).

[11] M. J. Carey, A. E. Berkowitz, J. A. Borchers and R. W. Erwin, Phys. Rev. B **47**, 9952 (1993).

[12] E. N. Abarra, K. Takano, F. Hellman, and A. E. Berkowitz, Phys. Rev. Lett. **77**, 3451 (1996).

[13] S. I. Csiszar, M. W. Haverkort, Z. Hu, A. Tanaka, H. H. Hsieh, H.-J. Lin, C. T. Chen, T. Hibma, L. H. Tjeng, (submitted Phys. Rev. Lett.).

[14] S. I. Csiszar and T. Hibma, (in preparation).

[15] R. Nakajima, J. Stöhr and Y. U. Idzerda, Phys. Rev. B, **59**, 6421 (1999).

[16] See review by F. M. F. de Groot, J. Electron Spectrosc. Relat. Phenom. **67**, 529 (1994).

[17] P. Kuiper, B. G. Searle, P. Rudolf, L. H. Tjeng, C. T. Chen, Phys. Rev. Lett. **70**, 1549 (1993)

[18] D. Alders, L. H. Tjeng, F. C. Voogt T. Hibma, G. A. Sawatzky, C. T. Chen, J. Vogel, M. Sacchi, S. Iacobucci, Phys. Rev. B **57**, 11623 (1998)

[19] A. Tanaka and T. Jo, J. Phys. Soc. Jpn. **63**, 2788 (1994)

[20] Parameters for MnO_6 cluster [eV]: Δ=8.0, U_{dd}=5.5, $U_{\underline{c}d}$=7.2, V_{e_g}=-2.1, T_{pp}=0.7, $10Dq$=0.5, ζ=0.066, H_{ex}=0.0135; Slater integrals 80% of Hartree Fock values; MnO/CoO/MnO/Ag(100): Ds=0.0093, Dt=0.0026; MnO/CoO/Ag(100): Ds=0.0486, Dt=0.0111. H_{ex} from G. Pepy, J. Phys. Chem. Solids **35**, 433 (1974).

[21] M. W. Haverkort, S. I. Csiszar, Z. Hu, S. Altieri, A. Tanaka, H. H. Hsieh, H.-J. Lin, C. T. Chen, T. Hibma, L. H. Tjeng, Phys. Rev. B **69**, 020408 (2004)

[22] C. G. Shull, W. A. Strauser, E. O. Wollan, Phys. Rev. **83**, 333, (1951)

Appendix A: Low density limit

```
Clear["Global`*"];
<< Graphics`Graphics`;
<< Graphics`Graphics3D`;
<< LinearAlgebra`MatrixManipulation`;
Off[General::"spell"]; Off[General::"spell1"];

QX0 = 0 * π;
QY0 = 0 * π;
QZ0 = 2 * π;

ν = 0.27;
α = 1 / (2 (1 - ν));
d = 4 0;
y = 0;
length = 401;
height = 4 0;
ω = 1;
l = (length - 1) / 2;
h = height;
atam := Arg[((z - d) + i x) e^(-i ArcTan[bz/bx])];
atap := Arg[(z + d + i x) e^(-i ArcTan[bz/bx])];
pu1x := -bx/(2 π) ((atam) + α x (z - d) / (x^2 + (z - d)^2));
pu1z := bx/(2 π) ((((1 - α)/2) Log[(x^2 + (z - d)^2)]) + α x^2 / (x^2 + (z - d)^2));
pu2x := bx/(2 π) ((atap) + α x (z + d) / (x^2 + (z + d)^2));
pu2z := -bx/(2 π) ((((1 - α)/2) Log[(x^2 + (z + d)^2)]) + α x^2 / (x^2 + (z + d)^2));
pu3x := bx d/π ((1 - α) x / (x^2 + (z + d)^2) - (2 α x z (z + d) / (x^2 + (z + d)^2)^2));
pu3z := -bx d/π ((z + d) / (x^2 + (z + d)^2) + (α z ((z + d)^2 - x^2) / (x^2 + (z + d)^2)^2));
nu1x := -bz/(2 π) ((((1 - α)/2) Log[(x^2 + (z - d)^2)]) + (α (z - d)^2 / (x^2 + (z - d)^2)));
nu1z := bz/(2 π) (atam + α x (z - d) / (x^2 + (z - d)^2));
nu2x := bz/(2 π) (((1 - α)/2) Log[x^2 + (x + d)^2] + α (z + d)^2 / (x^2 + (z + d)^2));
nu2z := -bz/(2 π) (atap + α x (z + d) / (x^2 + (z + d)^2));
nu3x := -bz d/π ((((1 - α) (z + d) / (x^2 + (z + d)^2))) + α (2 x^2 z + d (x^2 + (z + d)^2)) / (x^2 + (z + d)^2)^2);
nu3z := -bz d/π ((((1 - α) x / (x^2 + (z + d)^2))) + 2 α x z (z + d) / (x^2 + (z + d)^2)^2);
```

```
ξ = 10^-10;
ux[x_, z_] := If[(-(l + ξ) ≤ x ≤ (l + ξ)), pu1x + pu2x + pu3x + nu1x + nu2x + nu3x, 0];
uz[x_, z_] := If[(-(l + ξ) ≤ x ≤ (l + ξ)), pu1z + pu2z + pu3z + nu1z + nu2z + nu3z, 0];
bx = 1;
by = 0;
bz = -1;
uxp = Table[(Sum[e^(i qz z) (Exp[i (QX0 ux[x, z] + QZ0 uz[x, z])] - 1), {z, 0, d}]), {x, -ω l + ξ, ω l + ξ}]
 // MatrixForm;
uxn = Table[(Sum[e^(i qz z) (Exp[i (-QX0 ux[x, z] + QZ0 uz[x, z])] - 1), {z, 0, d}]), {x, ω l + ξ, -ω l + ξ, -1}]
 // MatrixForm;
iall = Log[(Abs[Table[Fourier[uxp[[1]], {qz, -.5, .5, 0.01}]])^2 +
     (Abs[Table[Fourier[uxn[[1]], {qz, -.5, .5, 0.01}]])^2] // MatrixForm;
i = Transpose[Join[Transpose[iall[[1]], Transpose[iall[[1]]]] // MatrixForm;
ListPlot3D[i[[1]]];
low = Floor[0.6 ω length];
high = Ceiling[1.4 ω length];
ipart = Transpose[Take[Transpose[i[[1]], {low, high}]] // MatrixForm;
ListPlot3D[ipart[[1]]];
qz = 0;
ipoz = (Abs[Fourier[uxp[[1]]])^2 + (Abs[Fourier[uxn[[1]]])^2 // MatrixForm;
i = Join[ipoz[[1]], ipoz[[1]] // MatrixForm;
ListPlot[Log[i[[1]]], PlotRange → All, PlotJoined → True];
low = Floor[0.6 ω length];
high = Ceiling[1.4 ω length];
ipart = Take[i[[1]], {low, high}] // MatrixForm;
ListPlot[Log[i part[[1]], PlotRange → All, PlotJoined → True];
low = Floor[0.92 ω length];
high = Ceiling[1.08 ω length];
ipart = Transpose[Take[Transpose[i[[1]], {low, high}]] // MatrixForm;
CMYKfromRGB[RGBColor[r_, g_, b_]] := CMYKColor[b, r b, 1 - b, (r + g + b)/3];
a = ListPlot3D[ipart[[1]], Mesh → False, Axes → False, Shading → True, ViewPoint → {2, 2, 3},
   Boxed → False, ColorFunctionScaling → False, ColorOutput -> CMYKfromRGB,
   AmbientLight → GrayLevel[-0.35], Lighting → True, Mesh → False];
b = Show[ContourGraphics[ipart[[1]]], ColorOutput → GrayLevel, Axes -> {False, False},
   Contours → 50];
xaxis = Table[N[d 2 ω π l / length], {l, -length + ξ, length + ξ}];
zaxis = i;
SetDirectory["c:\\export\\lowdensity\\002"];
Export["qx002", xaxis, "lines"];
Export["intensity002", zaxis[[1]], "lines"];
SetDirectory["c:\\export\\lowdensity\\002"];
Export["area002.jpg", b, ImageResolution → 400];
```

Appendix B: High density limit

```
Clear["Global`*"];
<< Graphics`Graphics`;
<< Graphics`Graphics3D`;
<< LinearAlgebra`MatrixManipulation`;
Off[General::"spell"]; Off[General::"spell1"];

QX0 = 0 * π;
QY0 = 0 * π;
QZ0 = 2 * π;

ν = 0.27;
α = 1 / (2 (1 - ν));
d = 100;
height = d + 1;
ρ = .043;
y = 0;

length = 201; (* odd number *)

l = (length - 1) / 2;
pu1x := -bx / (2 π) ((ArcTan[(z - (d)) / x]) + α x (z - d) / (x^2 + (z - d)^2));
pu1z := bx / (2 π) (((1 - α) / 2 Log[(x^2 + (z - d)^2)]) + α x^2 / (x^2 + (z - d)^2));

pu2x := bx / (2 π) ((ArcTan[(z + d) / x]) + α x (z + d) / (x^2 + (z + d)^2));
pu2z := -bx / (2 π) (((1 - α) / 2 Log[(x^2 + (z + d)^2)]) + α x^2 / (x^2 + (z + d)^2));

pu3x := bx d / π ((1 - α) x / (x^2 + (z + d)^2) - (2 α x z (z + d) / (x^2 + (z + d)^2)^2));
pu3z := -bx d / π ((z + d) / (x^2 + (z + d)^2) + (α z ((z + d)^2 - x^2) / (x^2 + (z + d)^2)^2));


nu1x := -bz / (2 π) (((1 - α) / 2 Log[(x^2 + (z - d)^2)]) + (α (z - d)^2 / (x^2 + (z - d)^2)));
nu1z := bz / (2 π) ((ArcTan[x / (z - (d + 10^-5))]) + α x (z - d) / (x^2 + (z - d)^2));

nu2x := bz / (2 π) ((1 - α) / 2 Log[x^2 + (x + d)^2] + α (z + d)^2 / (x^2 + (z + d)^2));
nu2z := -bz / (2 π) ((ArcTan[x / (z + d)]) + α x (z + d) / (x^2 + (z + d)^2));
```

$$\text{nu3x} := -\text{bz}\,\frac{d}{\pi}\left(\left((1-\alpha)\,\frac{(z+d)}{x^2+(z+d)^2}\right)+\alpha\,\frac{(2\,x^2\,z+d\,(x^2+(z+d)^2))}{(x^2+(z+d)^2)^2}\right);$$

$$\text{nu3z} := -\text{bz}\,\frac{d}{\pi}\left(\left((1-\alpha)\,\frac{x}{x^2+(z+d)^2}\right)+\frac{2\,\alpha\,x\,z\,(z+d)}{(x^2+(z+d)^2)^2}\right);$$

$$\text{yy1} := \frac{\text{by}}{2\,\pi}\,\text{ArcTan}\left[\frac{x}{z-d}\right];$$

$$\text{yy2} := \frac{-\text{by}}{2\,\pi}\,\text{ArcTan}\left[\frac{x}{z+d}\right];$$

```
bx = -1;
by = 0;
bz = -1;

uxzx1[x_, z_] = ∂x (pu1z + pu2z + pu3z);
uxxx1[x_, z_] = ∂x (pu1x + pu2x + pu3x);
uxzz1[x_, z_] = ∂z (pu1z + pu2z + pu3z);
uxxz1[x_, z_] = ∂z (pu1x + pu2x + pu3x);

uzzx1[x_, z_] = ∂x (nu1z + nu2z + nu3z);
uzzz1[x_, z_] = ∂z (nu1z + nu2z + nu3z);
uzxz1[x_, z_] = ∂z (nu1x + nu2x + nu3x);
uzxx1[x_, z_] = ∂x (nu1x + nu2x + nu3x);
uyxz1[x_, z_] = ∂z (yy1 + yy2);


bx = 1;
by = 0;
bz = -1;

uxzx2[x_, z_] = ∂x (pu1z + pu2z + pu3z);
uxxx2[x_, z_] = ∂x (pu1x + pu2x + pu3x);
uxzz2[x_, z_] = ∂z (pu1z + pu2z + pu3z);
uxxz2[x_, z_] = ∂z (pu1x + pu2x + pu3x);

uzzx2[x_, z_] = ∂x (nu1z + nu2z + nu3z);
uzzz2[x_, z_] = ∂z (nu1z + nu2z + nu3z);
uzxz2[x_, z_] = ∂z (nu1x + nu2x + nu3x);
uzxx2[x_, z_] = ∂x (nu1x + nu2x + nu3x);
uyxz2[x_, z_] = ∂z (yy1 + yy2);


QX := QX0 + qx;
QZ := QZ0 + qz;
s = 10^-5;
```

```
wxx[z_] := ρ/2
    (Sum_{i=-l+s}^{l+s} (QX^2 (uxxx1[i, z])^2 + QZ^2 (uxzx1[i, z])^2 + QX^2 (uzxx1[i, z])^2 + QZ^2 (uzzx1[i, z])^2 +
       QX^2 (uxxx2[i, z])^2 + QZ^2 (uxzx2[i, z])^2 + QX^2 (uzxx2[i, z])^2 + QZ^2 (uzzx2[i, z])^2));

wxz[z_] := ρ/2 QX QZ
    (Sum_{i=-l+s}^{l+s} (uxxx1[i, z] uxzz1[i, z] + uxxz1[i, z] uxzx1[i, z] + uzxx1[i, z] uzzz1[i, z] +
       uzxz1[i, z] uzzx1[i, z] + uxxx2[i, z] uxzz2[i, z] + uxxz2[i, z] uxzx2[i, z] +
       uzxx2[i, z] uzzz2[i, z] + uzxz2[i, z] uzzx2[i, z]));

wzz[z_] := ρ/2 (Sum_{i=-l+s}^{l+s} (QX^2 (uxxz1[i, z])^2 +
        2 QZ^2 (uxzz1[i, z])^2 + QX^2 (uzxz1[i, z])^2 + 2 QZ^2 (uzzz1[i, z])^2 +
        QX^2 (uxxz2[i, z])^2 + 2 QZ^2 (uxzz2[i, z])^2 + QX^2 (uzxz2[i, z])^2 +
        2 QZ^2 (uzzz2[i, z])^2) + Sum_{i=-l+s}^{l+s} (QX^2 ((uyxz1[i, z])^2 + (uyxz2[i, z])^2)));

w[z_] := wxx[z] wzz[z] - (wxz[z])^2;

invxx[z_] := wzz[z] / (-wxz[z]^2 + wxx[z] wzz[z]);
invxz[z_] := -wxz[z] / (-wxz[z]^2 + wxx[z] wzz[z]);
invzz[z_] := wxx[z] / (-wxz[z]^2 + wxx[z] wzz[z]);

i[qx_, qz_] =
   π Sum_{z=0}^{d} (1/Sqrt[w[z]] Exp[-0.25 (invxx[z] (qx)^2 + invzz[z] (qz)^2 + 2 invxz[z] (qx) (qz))]);
qz = 0;
itx = Table[i[qx, qz], {qx, -4, 4, 0.05}];
qx = 0;
itz = Table[i[qx, qz], {qz, -4, 4, 0.05}];
(*
 qx=0;
 Plot[i[qx,qz],{qz,-2,2}, PlotRange→ All];
 ContourPlot[Log[i[qx,qz]],{qx,-3,3},{qz,-3,3},PlotPoints→100, PlotRange→All,
  ContourShading→ True,Contours→ 40 ];
 Plot3D[i[qx,qz],{qx,-5,5},{qz,-5,5},
  PlotPoints→ 50, PlotRange→ All, ViewPoint→{-1,-1,1}];
 DensityPlot[Log[i[qx,qz]],{qxd,-150,150}, {qzd,-250,250}, PlotPoints→50,
  Mesh -> False,ColorFunction→Hue, ColorFunctionScaling→True, PlotRange→All,
  AspectRatio→Automatic];
 Plot3D[i,{qxd,-150,150}, {qzd,-150,150},
  PlotPoints→50, AspectRatio→Automatic, PlotRange→All];
 *)
```

```
ez = ListPlot[itx, PlotRange → All, PlotJoined → True, DisplayFunction → Identity];
az = ListPlot[itz, PlotRange → All,
   PlotJoined → True, PlotStyle → Hue[.6] , DisplayFunction → Identity];

Show[ez, az, DisplayFunction → $DisplayFunction];
ez = ListPlot[itx, PlotRange → All, PlotJoined → True, DisplayFunction → Identity];
az = ListPlot[itz, PlotRange → All,
   PlotJoined → True, PlotStyle → Hue[.6] , DisplayFunction → Identity];
Show[ez, az, DisplayFunction → $DisplayFunction];

xaxis = Table[d * qx, {qx, -4, 4, 0.05}];
SetDirectory["c:\\export\\highdensityCoO\\002"];

Export["xr0_043d100nu027", itx, "lines"];
Export["zr0_043d100nu027", itz, "lines"];
Export["qdr0_043d100nu027", xaxis, "lines"];
```

Appendix C: Orientation of an arbitrary off-specular peak in the high density limit

```
Clear["Global`*"];
<< Graphics`Graphics`;
Off[General::"spell"]; Off[General::"spell1"];
SetDirectory["c:\\export\\highdensity\\angle_of_area\\"];
```

$$\alpha := \frac{1}{2\,(1-\nu)};$$

$$pu1x := \frac{-bx}{2\pi}\left(\left(\text{ArcTan}\left[\frac{(z-(d))}{x}\right]\right)+\frac{\alpha\, x\,(z-d)}{x^2+(z-d)^2}\right);$$

$$pu1z := \frac{bx}{2\pi}\left(\left(\frac{1-\alpha}{2}\,\text{Log}\left[(x^2+(z-d)^2)\right]\right)+\alpha\,\frac{x^2}{x^2+(z-d)^2}\right);$$

$$pu2x := \frac{bx}{2\pi}\left(\left(\text{ArcTan}\left[\frac{(z+d)}{x}\right]\right)+\frac{\alpha\, x\,(z+d)}{x^2+(z+d)^2}\right);$$

$$pu2z := \frac{-bx}{2\pi}\left(\left(\frac{(1-\alpha)}{2}\,\text{Log}\left[(x^2+(z+d)^2)\right]\right)+\alpha\,\frac{x^2}{x^2+(z+d)^2}\right);$$

$$pu3x := bx\,\frac{d}{\pi}\left(\frac{(1-\alpha)\,x}{x^2+(z+d)^2}-\left(\frac{2\,\alpha\, x\, z\,(z+d)}{(x^2+(z+d)^2)^2}\right)\right);$$

$$pu3z := -bx\,\frac{d}{\pi}\left(\frac{z+d}{x^2+(z+d)^2}+\left(\frac{\alpha\, z\,((z+d)^2-x^2)}{(x^2+(z+d)^2)^2}\right)\right);$$

$$nu1x := \frac{-bz}{2\pi}\left(\left(\frac{(1-\alpha)}{2}\,\text{Log}\left[(x^2+(z-d)^2)\right]\right)+\left(\frac{\alpha\,(z-d)^2}{x^2+(z-d)^2}\right)\right);$$

$$nu1z := \frac{bz}{2\pi}\left(\left(\text{ArcTan}\left[\frac{x}{(z-(d))}\right]\right)+\alpha\, x\,\frac{(z-d)}{x^2+(z-d)^2}\right);$$

$$nu2x := \frac{bz}{2\pi}\left(\frac{(1-\alpha)}{2}\,\text{Log}\left[x^2+(x+d)^2\right]+\alpha\,\frac{(z+d)^2}{x^2+(z+d)^2}\right);$$

$$nu2z := \frac{-bz}{2\pi}\left(\left(\text{ArcTan}\left[\frac{x}{(z+d)}\right]\right)+\alpha\, x\,\frac{(z+d)}{x^2+(z+d)^2}\right);$$

$$nu3x := -bz\,\frac{d}{\pi}\left(\left((1-\alpha)\,\frac{(z+d)}{x^2+(z+d)^2}\right)+\alpha\,\frac{(2\,x^2\,z+d\,(x^2+(z+d)^2))}{(x^2+(z+d)^2)^2}\right);$$

$$nu3z := -bz\,\frac{d}{\pi}\left(\left((1-\alpha)\,\frac{x}{x^2+(z+d)^2}\right)+\frac{2\,\alpha\, x\, z\,(z+d)}{(x^2+(z+d)^2)^2}\right);$$

$$yy1 := \frac{by}{2\pi}\,\text{ArcTan}\left[\frac{x}{z-d}\right];$$

$$yy2 := \frac{-by}{2\pi}\,\text{ArcTan}\left[\frac{x}{z+d}\right];$$

$$uxzx[x\_, z\_] = \partial_x\,(pu1z+pu2z+pu3z);$$
$$uxxx[x\_, z\_] = \partial_x\,(pu1z+pu2z+pu3z);$$
$$uxxz[x\_, z\_] = \partial_z\,(pu1x+pu2x+pu3x);$$
$$uxzz[x\_, z\_] = \partial_z\,(pu1z+pu2z+pu3z);$$

$$uzzx[x\_, z\_] = \partial_x\,(nu1z+nu2z+nu3z);$$
$$uzzz[x\_, z\_] = \partial_z\,(nu1z+nu2z+nu3z);$$
$$uzxz[x\_, z\_] = \partial_z\,(nu1x+nu2x+nu3x);$$
$$uzxx[x\_, z\_] = \partial_x\,(nu1x+nu2x+nu3x);$$
$$uyxz[x\_, z\_] = \partial_z\,(yy1+yy2);$$

```
uxzx0 = ReplaceAll[Simplify[uxzx[x, z]], z → 0];
uzzx0 = ReplaceAll[Simplify[uzzx[x, z]], z → 0];

specZ = Symplify[Integrate[uxzx0^2 + uzzx0^2, {x, -∞, ∞}]];

uxzz0 = ReplaceAll[Simplify[uxzz[x, z]], z → 0];
uzzz0 = ReplaceAll[Simplify[uzzz[x, z]], z → 0];

specX = FullSymplify[Integrate[uxzz0^2 + uzzz0^2, {x, -∞, ∞}]];
ratiospec = specZ / specX;
(*___ ___ ___ ___ ___ ___ ___ ___ ___ ___ ___ ___ ___ ___ ___ ___ ___ ___ _*)

bex = 1;
bey = 0;
bez = 0;

uxzx0 = ReplaceAll[Simplify[uxzx[x, z]], {bz → bez, bx → bex }];
uzzx0 = ReplaceAll[Simplify[uzzx[x, z]], {bz → bez, bx → bex}];
uxzz0 = ReplaceAll[Simplify[uxzz[x, z]], {bz → bez, bx → bex }];
uzzz0 = ReplaceAll[Simplify[uzzz[x, z]], {bz → bez, bx → bex }];

uxxx0 = ReplaceAll[Simplify[uxxx[x, z]], {bz → bez, bx → bex }];
uxxz0 = ReplaceAll[Simplify[uxxz[x, z]], {bz → bez, bx → bex }];
uzxz0 = ReplaceAll[Simplify[uzxz[x, z]], {bz → bez, bx → bex}];
uzxx0 = ReplaceAll[Simplify[uzxx[x, z]], {bz → bez, bx → bex }];
uyxz0 = ReplaceAll[Simplify[uyxz[x, z]], {bz → bez, bx → bex, by → bey}];

z = 0;
d = 200;
ρ = 10;


QX = 1 π;
QY = 1 π;
QZ = 3 π;


offXX := ρ/2 NIntegrate[QX^2 (uxxx0^2 + uzxx0^2) + QZ^2 (uxzx0^2 + uzzx0^2), {x, -∞, ∞}]
offXZ := ρ/2 NIntegrate[
   QX * QZ * ((uxxx0 uxzz0 + uxxz0 uxzx0) + (uzxx0 uzzz0 + uzxz0 uzzx0)), {x, -∞ , ∞}]
offZZ := ρ/2 NIntegrate[QX^2 (uxxz0^2 + uzxz0^2) + 2 QZ^2 (uxzz0^2 + uzzz0^2) + QX^2 uyxz0^2,
   {x, -∞, ∞}]
ω := 1/2 ArcTan[(2 offXZ / (offZZ - offXX))] * 180/π;
ratio = offZZ / offXX;

nu = Table[ν, {ν, 0, 0.4, 0.01}];
omega = Table[ω, {ν, 0, 0.4, 0.01}];

Plot[ω, {ν, 0, 0.4}]

(*
  Plot[offXX, {z,0,100}, PlotPoints→ 50]
  Plot[offXZ, {z,0,100}, PlotPoints→ 50]
  Plot[offZZ, {z,0,100}, PlotPoints→ 50]
 *)

Export["(nu113)pure edge", nu , "lines"];
Export["(omega113)pure edge", omega, "lines"];
```

Summary

To summarize the results described in this thesis also for an unspecialized reader we will take the liberty of relaxing the scientific rigor in this last section. We therefore first apologize to the specialized reader for the use of, sometimes, physically not entirely correct examples or comparisons.

The constituent blocks of matter are the atoms. Atoms, besides the core which makes up almost all of their mass, also contain electrons. These electrons define the properties of all materials. Most of these negatively charged electrons are located very close to the positively charged core and only part of them are involved in the bonding with the outer electrons of other atoms in order to form all the matter that we see around us and which also we are made of. Electrons also behave like little magnets. Actually, electrons are the cause of all magnetism, including the well known earth magnetic field.[2] There are many ways that electrons choose to be involved in bonding. In the case of the compounds studied by us, namely CoO and MnO, the outmost electrons from the Co or Mn transition-metal (TM) atom will jump to a neighboring O atom. The positively (Co^{2+} and Mn^{2+}) and negatively (O^{2-}) charged ions formed in this way will attract each other and form a crystal. Different arrangements of these TM and O atoms can form and different stoichiometries can also exist. In this thesis we studied the CoO and MnO, both having a rock-salt structure, shown schematically in Figure 9.8.

The unexpected behavior of these compounds is that they are not conductive. This property could not be explained for a long time and calculations could not describe the strongly insulating nature of these materials, since it was expected that compounds having an unfilled shell of electrons behave as metals. In our case Co^{2+} has 7 and Mn^{2+} has 5 of the possible 10, 3d shell

Along the years many thinking and research hours have been spent to understand the behavior of these little particles and to be able to predict and describe the microscopic and macroscopic effects they produce. It must be said, at this point, that the present book is a vanishingly little part of this immense struggle to achieve this immense goal.

electrons, and both are, in fact, very good insulators. The solution of these discrepancies came with the recognition that the movement of an electron in the crystal is not independent from the other electrons but depends very much on the movement of the rest of the electrons, in other words the electrons are correlated, hence the name *strongly correlated electron systems*. The electrons on these TM ions become very localized, and being small magnets (also called *spins*), they want to be all pointing in the same direction. This latter property of spin alignment is the result of the so-called Pauli exclusion principle. Another important consequence of Pauli's principle is that for d electrons a maximum of 5 spins can orient in the same direction, the rest must have their spin in the opposite direction. This way a particular Co^{2+} (or Mn^{2+}) ion will have a magnetic moment of $5\uparrow+2\downarrow=3\uparrow$ (or $5\uparrow$).

It is at this point important to note that these materials are anti-ferromagnets. This property differs from the commonly known ferromagnets, where all the above mentioned magnetic moments on the TM sites are pointing in the same direction therefore creating a magnet known from everyday life. In anti-ferromagnets the total magnetic moment is zero because half of TM ions have spins pointing in the opposite direction of the other half. The arrangement of the moments around the TM ions is such that every little magnet is surrounded by six little magnets pointing in the opposite direction (this is illustrated in Figure 1.1 of the introductory chapter).

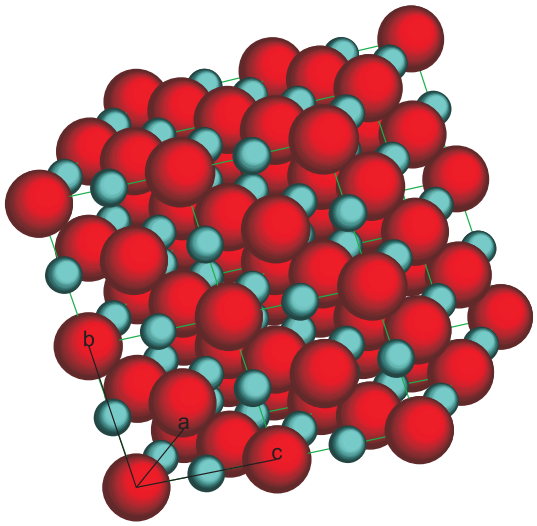

Figure 9.8: Structure of rock-salt CoO (or MnO). Large spheres represent the O^{2-} ions and small spheres represent the Co^{2+} (or Mn^{2+}) ions.

Interestingly enough, the magnetic moment of some the TM ions is not only composed by the spins but also by the so-called orbital angular momentum. In most of the TM oxides this extra component of the total magnetic moment is quenched because of the presence of the O^{2-} environment, but the Co^{2+} ion in CoO still retains a considerable amount of angular magnetic momentum. This makes CoO so much more complicated and interesting than others. The orbital angular momentum appears as a result of the fast rotation of the electrons around the nucleus. There is a substantial coupling between the axis of this rotation and the spin momentum, which is the result of the so-called spin-orbit coupling. The energy is minimized if these two momenta are parallel with each other. Therefore, the spin-orbit coupling phenomenon in a material having an unquenched orbital momentum will allow one to manipulate the orientation of the total momentum by altering in some way the rotation axis of the electrons. This is at the basis of the present thesis, in which we tried to find a way to gain control on the orientation of this rotation axis, thereby gaining control on the total momentum.

One way of achieving this was suggested by Takeo Jo and T. Shishidou (J. Phys. Soc. Jpn. **67**, 2505 (1998)) who predicted a quenching of the orbital momentum by imposing a biaxial compressive strain on a CoO crystal. They calculated X-ray absorption spectra of such an model system for both positive and negative biaxial strains.

How can one impose biaxial strain in a crystal? One might try to squeeze a single crystal of CoO simultaneously in two directions using two clamps perpendicular to each other and let the material expand in the third direction. The opposite strain, the stretching, would of course be more problematic since than one has to glue the clamps to the crystal. A more considerate way of doing this is using epitaxial strain by growing a thin film on a substrate having smaller (for compressive strain) or slightly larger (for tensile strain) lattice parameter. The advantage of this, above the previous method using clamps, lies not only in the experimental ease but also in the size of the distortion. By epitaxial stress massive strains can be induced in these thin layers.

Although this method is very popular in the semiconductor industry, there is no straight-forward theory describing the evolution of the strain as the thickness of the film is increased. It is generally accepted that at the initial stages of growth the film will have the in-plane lattice parameters identical with the ones of the substrate, but it is also recognized that above a certain thickness, the so-called critical thickness, the film will start to relax to its natural lattice parameters. This happens by the appearance of defects in the crystal which are called dislocations. To find the optimum thickness for the

films to be used in the spectroscopic experiments, we had to study the effects of thickness of the CoO film on the strain in these films. For this, CoO layers with different thickness have been grown by a technique called Molecular Beam Epitaxy on substrates chosen such that they imposed compressive or tensile strains in the films. The strain was determined using the easiest but also the most exact method, namely X-ray diffraction.

X-ray diffraction is a technique by which one can determine the exact distance between the atoms. The interatomic distances in the crystals can be determined from the angle at which the crystal scatters the X-rays. The relation that relates the two quantities is the so-called Bragg law: $2d\sin\theta = \lambda$. Here we know λ because it is the wavelength of the X-rays, we can measure the angle θ and the relation gives us d which can be easily related to the interatomic distance. By measuring this d for different film thicknesses we were able to determine the critical thickness. We also found that deformations in the lattice, caused by the dislocations that relieve the strain, contribute to the scattering but at different angles than the so-called coherent part, which is related to the ordered lattice without incoherent deformations. From such measurements we could determine the density of the dislocations in our films. Although well studied in the case of semiconductors, we performed these measurements for the first time for rock-salt ionic solids such as CoO or MnO. By simulating the measured data we were able to determine the type of dislocations that are present in our films.

In the next step the absorption of X-rays by CoO films having thicknesses just below the critical thickness had to be measured at the synchrotron in Taiwan. By comparing the measured spectra with calculations done by Maurits Haverkort, we found that the spin orientation in the CoO layers is very much dependent on the sign of the strain. For compressive strains we found that the spins are lying in the plane of the film, while for tensile strains the spin is oriented perpendicular to the film. We therefore gained control over the spin orientation in such anti-ferromagnetic films with unquenched orbital momentum. These results, if taken seriously, might change the way scientists approach the very much studied, but not yet entirely understood, effect called exchange-bias.

Finally we found that CoO layers with controlled spin orientation affect the spin orientation in adjacent anti-ferromagnets having no magnetocrystalline anisotropy such as MnO. Using the same method of X-ray absorption, we determined the spin orientation in the MnO layers. We found that the spin orientation in these films follows the spin orientation in the underlying CoO layers. Therefore, the control on one can be transmitted to other one. This

kind of interlayer coupling might help to extend the material basis to other, unused sofar, anti-ferromagnets for exchange-bias structures.

Samenvatting

Om de samenvatting van de resultaten in dit proefschrift ook begrijpelijk te maken voor de leek, zijn we zo vrij om het wetenschappelijke jargon in dit onderdeel even te laten voor wat het is. Daarom allereerst onze verontschuldiging aan de gespecialiseerde lezer voor het gebruik van fysisch gezien soms niet geheel correcte voorbeelden of vergelijkingen.

Atomen vormen de bouwstenen van alle materie. Atomen zelf bestaan uit een kern, waarin bijna al hun massa zit, en elektronen. Deze elektronen zijn bepalend voor de eigenschappen van alle materialen. De meeste van deze negatief geladen elektronen bevinden zich heel dicht bij de positief geladen kern en slechts een klein deel van alle elektronen (diegenen die zich wat verder van de kern bevinden) is betrokken bij de binding die wordt aangegaan met de buitenste elektronen van andere atomen. Die bindingen zijn essentieel om alle materie te vormen die om ons heen bestaat en waar ook wij uit opgebouwd zijn. Naast deze belangrijke rol van de elektronen gedragen zij zich ook als een soort kleine magneten. De elektronen zijn dan ook de oorzaak van alle magnetisme, met inbegrip van het alom bekende aardmagnetisch veld[3]. Er zijn veel manieren waarop elektronen bindingen veroorzaken. In de door ons bestudeerde verbindingen, CoO en MnO, springen de elektronen van het Co of Mn overgangsmetaal (OM) naar een naburig O atoom. De positief geladen ionen (Co^{2+} en Mn^{2+}) en negatief geladen ionen (O^{2-}) die hierbij gevormd worden zullen elkaar aantrekken en een kristal vormen. Er ontstaan hierbij verschillende schikkingen van de OM en O atomen en ook de daarmee gepaard gaande verschillende stoichiometrieën. De door ons bestudeerde verbindingen zijn CoO en MnO, allebei met een NaCl-structuur, toegelicht in Figure 9.9.

In de loop der jaren is veel studie gewijd aan en onderzoek verricht naar het begrijpen van het gedrag van deze kleine deeltjes. Het uiteindelijke doel is het voorspellen en beschrijven van de microscopische en macroscopische effecten die de elektronen veroorzaken. Er moet gezegd worden dat dit huidige boek een heel klein onderdeel is van de immense strijd om dit doel te bereiken.

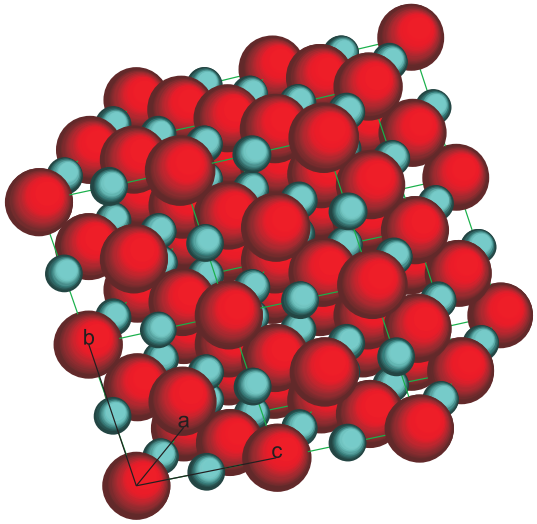

Figure 9.9: NaCl-structuur van CoO (of MnO). Grote bollen verbeelden de O^{2-} ionen en kleine bollen de Co^{2+} (of Mn^{2+}) ionen.

De onverwachte eigenschap van deze verbindingen is dat ze niet geleiden. Dit kon lange tijd niet worden verklaard en berekeningen konden het sterk isolerende gedrag van deze materialen niet beschrijven, aangezien verbindingen met niet volledig gevulde elektronenschillen zich als metalen gedragen. In ons geval heeft Co^{2+} 7 en Mn^{2+} 5 van de mogelijke 10 3d elektronen, maar beide zijn juist heel goede isolatoren. De oplossing voor deze discrepantie kwam met de erkenning van het feit dat de beweging van een elektron op het OM ion niet onafhankelijk is van de andere elektronen, maar juist heel erg afhangt van de bewegingen van de andere elektronen. Met andere woorden: de elektronen zijn gecorreleerd, vandaar ook de term *sterk gecoreleerde elektronsystemen.* De elektronen op de OM ionen zijn sterk gelokaliseerd en willen, als kleine magneten (ook *spins* genaamd), allemaal dezelfde kant op wijzen. Deze laatste eigenschap van spin-uitlijning is het resultaat van het zogenaamde Pauli principe. Een andere belangrijke consequentie van dit Pauli principe is dat voor d elektronen maximaal 5 spins in dezelfde richting kunnen wijzen. De rest zal in de tegenovergestelde richting moeten wijzen. Op deze manier heeft een bepaald Co^{2+} (of Mn^{2+}) ion een magnetisch moment van $5\uparrow+2\downarrow=3\uparrow$ (of $5\uparrow$).

Het is op dit moment van belang te vermelden dat deze materialen antiferromagneten zijn. Deze eigenschap verschilt van de bekende ferromagneten, die een macroscopisch magnetisch moment bezitten (bekend uit het dagelijks

leven), doordat bovengenoemde OM spins allen in dezelfde richting wijzen. In anti-ferromagneten is het totale magnetisch moment nul, omdat de ene helft van de spins rondom de OM ionen de ene kant op wijst, en de andere helft van de spins de tegenovergestelde kant. De ordening van de momenten op de OM ionen is zodanig dat elk magneetje omgeven is door zes magneetjes wijzend in de tegenovergestelde richting (zie Figure 1.1 in het inleidende hoofdstuk).

Een interessant punt is dat het magnetisch moment van sommige OM ionen niet alleen ontstaat door de spins, maar ook door het zogenaamde baan-impulsmoment. In de meeste OM oxides is dit extra component van het totaal magnetisch moment uitgedoofd door de O^{2-} omgeving, maar het Co^{2+} ion in CoO houdt nog steeds een aanzienlijke hoeveelheid van het baan-impulsmoment vast. Het maakt dit materiaal veel gecompliceerder en interessanter dan andere materialen. Het baan-impulsmoment vindt zijn oorsprong in de snelle rotatie van de elektronen om de kern heen. Er bestaat een substantiële koppeling tussen de rotatie-as en het spinmoment, wat het resultaat is van spin-baan koppeling. De energie wordt geminimaliseerd als deze twee momenten parallel aan elkaar zijn. Het spin-baan koppeling fenomeen in een materiaal met een niet-uitgedoofd impulsmoment stelt men in staat om de oriëntatie van het totale moment te manipuleren door op een bepaalde manier de rotatie-as van de elektronen te veranderen. Dit is de basis van dit proefschrift, waarin we een manier probeerden te vinden om grip te krijgen op de oriëntatie van deze rotatie-as, en daarmee op het totale moment.

Een van de manieren om dit te bereiken werd geopperd door Takeo Jo en T. Shishidou (J. Phys. Soc. Jpn. **67**, 2505 (1998)). Zij voorspelden dat het baanmoment uit zou doven wanneer biaxiale spanning wordt uitgeoefend op het CoO kristal door middel van compressie, en berekenden de röntgenstraling absorptiespectra voor een modelsysteem als dit, voor zowel positieve als negatieve biaxiale spanning.

Hoe kan men biaxiale spanning tot stand brengen in een kristal? Je zou een enkel CoO kristal gelijktijdig in twee richtingen kunnen bevestigen tussen twee klemmen, die loodrecht op elkaar staan, en het kristal de ruimte geven om uit te zetten in de derde richting. De tegenovergestelde spanning, uitrekking, zou iets ingewikkelder zijn om te bereiken. De klemmen zouden dan immers vastgelijmd moeten worden aan het kristal. Een meer doordachte manier om dit te bereiken is het gebruiken van de epitaxiale spanning wanneer een dunne laag groeit op een substraat met kleinere (voor de compressiespanning) of een beetje grotere (voor trekspanning) roosterparameters. De voordelen hiervan boven de methode met de klemmen zijn het experimentele gemak en de grootte van de vervorming. Met epitaxiale druk kunnen zeer grote spanningen worden

bereikt in de films.

Hoewel dit een erg geliefde methode is in de halfgeleider industrie, is er nog geen eenvoudige theorie die de ontwikkeling van spanning beschrijft wanneer de dikte van de laag toeneemt. Er wordt doorgaans aangenomen dat tijdens de eerste stappen van het groeien van de film de roosterparameters in het vlak gelijk zijn aan de roosterparameters van het substraat, maar er wordt ook erkend dat de film zich zal ontspannen tot zijn natuurlijke roosterparameters als de kritieke dikte wordt bereikt. Dit gaat gepaard met het ontstaan van defecten in het kristal. Deze defecten worden ook wel dislocaties genoemd. Om de optimale dikte voor de films te vinden, voor het gebruik in spectroscopische experimenten, bestudeerden wij de effecten van de dikte van CoO films op de spanning in deze films. Hiervoor werden CoO lagen gemaakt met verschillende dikten, met behulp van een techniek genaamd 'Molecular Beam Expitaxy'. De substraten werden zodanig gekozen dat ze compressiespanning of trekspanning teweeg brachten in de films. De spanning werd bepaald door de eenvoudigste en nauwkeurigste methode: röntgendiffractie.

Röntgendiffractie is een techniek waarmee de exacte afstanden tussen atomen bepaald kunnen worden. Zo kunnen deze afstanden in een kristal bepaald worden door te kijken naar de hoek waaronder röntgenstralen verstrooid worden wanneer ze op het kristal vallen. De relatie tussen deze twee waarden wordt gegeven in de wet van Bragg: $2d \sin\theta = \lambda$. In deze vergelijking is de waarde van λ bekend: het is de golflengte van de röntgenstralen. Vervolgens wordt hoek θ gemeten en de vergelijking geeft dan d, die gemakkelijk kan worden gerelateerd aan de afstand tussen atomen. Het bepalen van d voor verschillende filmdikten stelde ons in staat de kritieke dikte vast te stellen. We zagen ook dat de deformaties in het kristalrooster, veroorzaakt door de dislocaties die de spanning verminderen, bijdragen aan de verstrooiing. Deze dislocaties verstrooien de röntgenstralen echter wel onder een andere hoek dan het zogenaamde coherente gedeelte, welke is gerelateerd aan het geordende rooster zonder incoherente deformaties. Deze experimenten hielpen ons de dislocatiedichtheid te bepalen in onze films. Hoewel dit al uitvoerig is bestudeerd in halfgeleiders, hebben wij deze metingen voor het eerst uitgevoerd op ionische vaste stoffen met NaCl-structuur, zoals CoO en MnO. Door de gemeten data te simuleren waren we in staat de types dislocaties te bepalen die aanwezig zijn in onze films.

In de volgende stap werd de absorptie van röntgenstralen door CoO films, met een dikte net onder de kritieke dikte, gemeten bij de synchrotron voorziening in Taiwan. Uit de vergelijking van deze gemeten spectra met berekeningen van Maurits Haverkort vonden we dat de spinoriëntatie in de CoO lagen

zeer afhankelijk is van het teken van de spanning (positief of negatief). Bij compressiespanning zagen we dat de spins in richting van het vlak van de film lagen, terwijl ze bij trekspanning loodrecht op dit vlak stonden. Hierdoor hadden we controle verworven over de spinoriëntatie in zulke anti-ferromagnetische films met niet-uigedoofd baanmoment. Dit veel bestudeerde, maar niet volledig begrepen, effect heet ook wel exchange-bias. Als de resultaten van dit onderzoek serieus genomen worden, zouden ze de manier waarop wetenschappers dit onderwerp benaderen zeker kunnen veranderen.

Tenslotte hebben we ontdekt dat zulke CoO lagen met gecontroleerde spinoriëntatie de spinoriëntatie beïnvloeden in aangrenzende anti-ferromagneten, zonder magnetokristallijne anisotropie, zoals MnO. Door toepassing van dezelfde methode van röntgenstraling absorptie werd de spinoriëntatie in de MnO lagen bepaald. We vonden daarbij dat de spinoriëntatie in deze films de oriëntatie van spins in de ondergelegen CoO lagen overnamen. Daarom kan de controle op de oriëntatie van de ene overgedragen worden op de andere. Dit soort koppeling tussen verschillende lagen zou de materiële basis kunnen uitbreiden naar andere, nog niet gebruikte, anti-ferromagneten voor exchange-bias structuren.

Acknowledgements

Finally, after finishing this thesis, it is time to attend the part that, most possibly, will be the most read of all: the acknowledgements. As almost all PhD theses, this is no exception, as what the number of people that contributed to it is concerned and it is time to thank them for all they did for helping me to reach this goal.

To start with, I thank my first promotor Tjipke Hibma. Dear Tjip, you are amongst the very few people that truly impressed me, not only in the professional point of view, but also as a person. The latter probably because you reminded me very much of my father. Your approach to solve problems inspired me intensely and made me feel more confident about myself when trying to interpret experimental data. Thank you for your close guidance as a promotor, even after your retirement, as well as for the many funny moments we spent together. Also I am grateful for all the mails and letters you wrote to the bureaucratic Dutch and Romanian institutions (here included is the highly distinguished Romanian Army).

My second promotor was Hao Tjeng. Dear Hao, your practical guidance that led to all that beautiful data that constitutes the second part of the present thesis was irreplaceable. Simply, I am proud that I worked with you in the lab. You made me realize how difficult is to actually measure something meaningful and how much care one has to take in experimental physics to avoid all kind of unwanted artifacts. I feel very sorry that you moved so far from Groningen and so I could not embrace more of your vast knowledge and experimental expertise.

I acknowledge the reading comity: Petra Rudolf, Thom Palstra and Jeroen Goedkoop for reading and correcting the manuscript, I also praise your obser-

vations and constructive suggestions concerning my thesis.

Maurits Haverkort, I value all the impressively simple and transparent explanations you gave me every time I came up with a stupid question. My stay in Cologne would have been very boring without your company and our collaboration resulted in two nice works about the magnetic structure of CoO and MnO.

Dear Zhiwei Hu, I had the impression that there are no materials you didn't already measure, but Hao always came up with another one. Therefore, at the synchrotron in Taiwan, we had enough occasions to get to know each other quite a bit. I enjoyed a lot doing all those endless temperature dependent and (or) polarization dependent XAS measurements with you. The data we collected from CoO and MnO thin films became part of this thesis.

The scientists from Taiwan were always there when needed and made sure we have a pleasant stay there. Thank you: Roger Chang, Hui-Huang Hhsieh, Hong-Ji Lin and Di-Jing Huang. Thanks also for Harry Jonkman to let me use his MBE equipment. Also i am grateful for dr. Wim Arnold Bik for doing the RBS measurements.

Our group was little and it became even smaller as time passed, so at a certain point we evolved (as Alex pointed it out for me) into the perfect structure: one professor (Tjip), one technician (Henk) and one student (me). This though did last only for one month after which my contract ended. In the early days though the group was more numerous and it is time to mention some of the people here. Diana Rata, we had many nice discussions not only about science but also trying to figure out how western people think. Also, you're a good cook but I must say that your mother is still better than you. Wilma Eerenstein, you introduced me first to the actual practice of thin film growth. We grew several samples together and, even if it is hard to believe, already our second sample has made it into the present thesis and it is responsible for one point in Figure 3.8 (and this only because the film on the *first* sample was too thin). Beside work you also proved me several times that my initial belief, about myself, of being a well-endowed drinker was *entirely wrong*. Sjoerd Hak, with you I had probably the most fun, not only because you started your PhD virtually at the same time as I, but also because somehow we were at the same wavelength when all kinds of stupid jokes were concerned. I also esteem your patience and the technical insight into how things should work, or are working, in and outside the lab. Finally, Henk Bruinenberg, I enjoyed not only watching you repairing the old machine and learning about how things work but also I felt the most relaxed around you when talking about all sorts of personal matters. You did for me many things that only a friend would have

done and I truly appreciate all that.

The solid state chemistry group of Thom Palstra was our "brother group", we had many common work discussions which proved to be quite a success. People here were also always ready to help in any situation, so thank you all: Beatriz Noheda for accepting me into your group before my promotion, Jacob Baas for all sort of help in the lab, Graeme Blake, Umut Adem, Coen van den Brom, Gustau Catalan, Agung Nugroho, Oana Jurchescu, Gwilherm Nenert, Gijsbert Rispens, Mylene Sage, Vadim Volotchaev for all the joyful coffee breaks. Thanks also for our secretary Henriet van Mil-Boddeveld, who could manage to handle four (or five) groups at the same time and still having enough time to listen to all my weird problems. In addition to this, I had many pleasant moments with people from other groups: Yutao Pei, Xiaosong Du, Friso Jedema, Diana Dulic, Jochem Baselmans, Sense Jan van der Molen, Michele Zaffalon, Karina Schulte, Peter Steeneken, Henk Bron, Ole Goebel, Paul Bronsveld, Branislava, Steven Celotto, Bernd Struth, Radmir Gaynutdinov, Jens Seeger, Andrivo Rusydi, Seiji Yunoki, Yutaka Furubayashi, Sandra Mendoza, Monica Lubomska, Imad Arfaoui, Roberto Macovez, Ben, Frans van der Horst, Arend Heeres, Luc Venema, Bernard Wolfs, Siemon Bakker.

Beside work there was always time enough for other things. The group accountable for quite a large part of my time spent outside the lab is the "Romanian mafia". Since this group (harmless - for those who might think I am referring to criminals) increased considerably during my stay here, I will only mention some of the people here. Mişu Popinciuc, Magda Mandoc, Mirko Unipan, Nicoleta Voicu, Dan Cringus, Irina Fundeanu, Dana Borsa, Bogdan Craus, Mirela Folea, Gabi Blaj, Gabi Maris, Liviu Hozoi, Oana Jurchescu, Ana Arteni, Alex Lerescu, Alex Macridin, Dan Cozma, Diana Boar, Mihai Morariu, Tony Chezan, Vali Mihailetchi, Lacramioara Popescu, Józsa Csaba. Thank you all for all the dancing and drinking parties, as well as the fun during some other occasions we had together. Andrei Filip, you were a good organizer and since you left Groningen the group started to fall apart, this of course could also be attributed to the increased number of people. Before that though, we had a lot of fun together and I learned a lot from you. Sergey Grachev we spent many happy and sad moments together, during these sessions we even succeeded once (or twice) to rouse the attention of my grumpy neighbor (we thank her also for the understanding).

I'm also grateful to a few people not related to my work or the university. My father, in the first place, made me interested in science already starting from when I was little. Even though he past away during my PhD, he will forever occupy a special place in my heart. Thank you mother for all your

worries for me. Betty, Hein, Wendy and Lisa you all were, and still are, amazingly patient and encouraging with my improper Dutch. Moreover, I spent many unforgettable moments with you, also thank you for your moral support. Szabó Zoltán and Csiha Réka thank you for all the great time we spent together. Moni Dumitrescu thanks for helping me financially to get me started here.

Finally, sweet Marinda, your intelligence, simplicity and straightforwardness made me happier than ever before. Thank you for all your patience and love. Your support was crucial for finishing the present thesis.

Szili